THE UNIVERSITY OF ADELAIDE

An optical computed tomography scanner for three dimensional gel dosimetry of radiotherapy dose distributions

Daniel Paul Norman Ramm

A thesis submitted in fulfilment of the requirements
for the degree of Doctor of Philosophy

in the

School of Physical Sciences
The University of Adelaide

September 2017

Contents

Abstract

THE UNIVERSITY OF ADELAIDE
School of Physical Sciences

Doctor of Philosophy

An optical computed tomography scanner for three dimensional gel dosimetry of radiotherapy dose distributions

Daniel Paul Norman Ramm

Clinical radiotherapy treatments using linear accelerator (linac) generated megavoltage x-ray beams are planned using computer models that calculate patient specific three dimensional (3D) radiation dose distributions. Treatment planning system (TPS) calculated doses are evaluated by clinicians to ensure suitable dose coverage of targeted tumours and the avoidance of excessive doses to normal tissues. The accuracy of the TPS must be validated by measurement to ensure correct patient treatments. Traditional radiotherapy dosimeters do not measure dose entirely in 3D. They effectively ‘spot check’ accuracy at discrete points or planes, without the ability to fully visualise measured dose distributions in true 3D. True 3D dosimetry systems have been a subject of research for more than 3 decades. Gel dosimetry with optical computed tomography (CT) scanning using visible light wavelengths has been under investigation and development for much of this time. A lack of clinical uptake of the systems developed to date suggests that there are deficiencies or unappealing aspects, such as optical CT scanner maintenance and reliance upon optical expertise. Dosimetric accuracy of these systems also requires improvement, closer to accepted clinical dosimeters. In this work it was postulated that an optical CT scanner could be developed that is more efficient, practical and accurate than those demonstrated previously. This would address key aspects relating to clinical appeal. A specific application of stereotactic radiosurgery was targeted, where small dose distributions are delivered with high spatial accuracy to cranial tumours.

Improvements in the practicality and efficiency of optical CT scanning were initially sought by elimination of the need for a refractive index (RI) matching fluid bath for scanning gel dosimeter samples. Optical simulations were used to investigate and identify suitable optical geometry that would enable fluid-less scanning for tomographic reconstruction. A prototype fluid-less optical CT scanner was constructed and the proof of concept was demonstrated using ferrous xylenol orange gel (FXG). The next phase of work was to develop the dosimetry system further, striving for dosimetric accuracy. The properties of the FXG dosimeter were studied by characterising the dose response, dose development, ion diffusion and thermochromism. The scanner was refined by addressing imaging artefacts, the addition of a reference detector and the development of a cuvette based dose calibration procedure. Standard procedures for gel manufacturing and handling, and for optical CT operation were developed to improve reproducibility of results. The system's performance was assessed and its utility was demonstrated in the clinical application of linac radiosurgery and was also extended to brachytherapy ^{192}Ir source verifications.

Further improvements of system practicality and measurement quality were proposed by the concept of dual wavelength scanning. A second laser of a different wavelength could provide reference scan data instead of pre-irradiation scans. This would give a single scan procedure for greater practicality and could improve measurement quality by avoiding scan to scan artefacts. Dual wavelength feasibility was first investigated by revisiting optical simulations and the development of a design incorporating a second laser. Through the addition of the second wavelength further insights were gained into optical artefacts and image quality improvements were realised. An alternative calibration method using a reconstructed test pattern was compared to the cuvette method and resulted in improvements of calibration accuracy for dual wavelength scanning. The dual wavelength scanner dosimetry system was tested and benchmarked using a range of test irradiations, with comparison to reference dosimeters. This culminated in a true 3D dosimetry solution for radiotherapy dose verifications with accuracy of the order of 1 %, together with practical and efficient optical readout for clinical use.

Declaration

I certify that this work contains no material which has been accepted for the award of any other degree or diploma in my name in any university or other tertiary institution and, to the best of my knowledge and belief, contains no material previously published or written by another person, except where due reference has been made in the text. In addition, I certify that no part of this work will, in the future, be used in a submission in my name for any other degree or diploma in any university or other tertiary institution without the prior approval of the University of Adelaide and where applicable, any partner institution responsible for the joint award of this degree.

I acknowledge that copyright of published works contained within this thesis resides with the copyright holder(s) of those works.

I also give permission for the digital version of my thesis to be made available on the web, via the University's digital research repository, the Library Search and also through web search engines, unless permission has been granted by the University to restrict access for a period of time.

I acknowledge the support I have received for my research through the provision of an Australian Government Research Training Program Scholarship.

Signed: Date: 24/02/2018

Acknowledgements

I would firstly like to thank the organisations that provided me with the opportunity and support to conduct this work, The University of Adelaide and especially The Royal Adelaide Hospital where I was based for the duration of the project. My introduction to the area of gel dosimetry and optical CT scanning was provided by Madhava Bhat and I am extremely grateful to have received his advice and encouragement that would lead to my achievements and an ongoing interest in gel and related dosimetry techniques. I also thank Thomas Rutten for assisting me to establish in the area of optical CT research and for ongoing support and advice. I appreciate the supervisory input and thank Eva Bezak, Justin Shepherd and Scott Penfold for their assistance in conducting this research and completion of the PhD. I also appreciate the support of medical physics staff at The Royal Adelaide Hospital in carrying out this work over a number of years and thank you to John Schneider for manufacturing scanner parts in the workshop. Finally I thank my family, Kara-Lee, Isaac and Ethan for their understanding and support that made it possible to realise this accomplishment.

Abbreviations

1D	One dimensional
2D	Two dimensional
3D	Three dimensional
AAARA	As accurately as reasonably achievable
AAm	Acrylamide
ART	Algebraic reconstruction technique
BANANA	Bis AAm nitrous oxide agarose
BANG	Bis AAm nitrous oxide gelatin
Bis	N,N’-methylene-bis-acrylamide
CBCT	Cone beam computed tomography
CCD	Charge coupled device
CMOS	Complementary metal-oxide-semiconductor
CT	Computed tomography
DICOM	Digital imaging and communications in medicine
EBRT	External beam radiotherapy
FBP	Filtered back-projection
FBX	Ferrous benzoic acid xylenol orange
FDK	Feldkamp Davis Kress
FOV	Field of view
FXG	Ferrous xylenol orange gelatin
HDR	High dose rate
He-Ne	Helium Neon
HU	Hounsfield unit
ID	Inner diameter
IGRT	Imaged guided radiotherapy
IMRT	Intensity modulated radiotherapy
kV	Kilovoltage
LCV	Leuco crystal violet
LED	Light emitting diode
LMG	Leuco malachite green
MC	Monte Carlo
MLC	Multi-leaf collimator

MRI	Magnetic resonance imaging
MV	Megavoltage
NMR	Nuclear magnetic resonance
NTCP	Normal tissue complication probability
OBI	On board imaging
OD	Outer diameter
OSLD	Optically stimulated luminescence dosimetry
PAG	Polyacrylamide gel
PAGAT	Polyacrylamide gel in atmospheric conditions
nPAG	Normoxic polyacrylamide gel
PMMA	Polymethyl methacrylate
QA	Quality assurance
QC	Quality control
RI	Refractive index
ROI	Region of interest
RT	Radiotherapy
SABR	Stereotactic ablative radiotherapy
SBRT	Stereotactic body radiotherapy
SNR	Signal to noise ratio
SRS	Stereotactic radiosurgery
TCP	Tumour control probability
TLD	Thermo-luminescence dosimetry
TPS	Treatment planning system
VMAT	Volumetric modulated arc therapy
XO	Xylenol orange

Chapter 1

Introduction

1.1 True three dimensional dosimetry in radiotherapy

1.1.1 Radiotherapy

Radiotherapy is a clinical treatment option for a range of benign and malignant lesions. It is most commonly associated with the treatment of cancer. Ionising radiation is used to kill tumour cells by direct and indirect DNA damage. The response to radiation dose can be described by the tumour control probability (TCP) where a treatment dose is selected that gives a high probability of tumour control for the particular type of tumour. When tumours are targeted with radiation, normal tissue also receives some dose. It is kept to a minimum considering acceptable normal tissue complication probabilities (NTCP). There is therefore a trade-off between increasing dose for a higher TCP and decreasing dose for an improved NTCP. The ratio of TCP to NTCP is the therapeutic ratio and is optimised to achieve the best outcome for the patient. The therapeutic ratio is increased if the tumour cells are more radiosensitive and the normal tissue is less radiosensitive. Another way to increase the TCP is to improve the conformity of the dose distribution to the tumour. This means normal tissue receives less dose while maintaining the tumour dose or the tumour dose can be escalated while maintaining normal tissue dose.

Some tissues have an early response to radiation, resulting in greater cell killing at low doses compared to late responding tissues. Tumour cells are often early responding while normal tissues are often late responding. Late responding tissues repair sub-lethal DNA damage better than early responding tissues. These differences can be exploited by delivering many small doses that accumulate to the total prescribed dose in the approach called fractionation. This results in a greater overall differential in cell kill and therefore an improved therapeutic ratio. Fractionation has been a longstanding feature of conventional external beam radiotherapy (EBRT) with treatment regimes over a number of weeks. Not all tumours are necessarily early responding, nor are all normal tissues late responding, so varying fractionation schedules have been utilised. In recent times, hypo-fractionation has increased in use for particular, well defined smaller tumours resulting in many less treatment sessions. This is made possible by technological advances leading to improved abilities to reliably deliver more conformal dose distributions to targets, thus reducing doses to normal tissues for a given tumour dose and lessening the importance of differences in tumour and normal tissue radiobiological responses. In stereotactic radiosurgery (SRS), a single fraction treatment is used, made possible by precise localisation hardware. Traditionally in cranial SRS, a metal frame was attached to the patients' skull to provide a fixed frame of reference giving accurate localisation (within 1 mm). Modern IGRT and immobilisation techniques have provided the option of 'frameless' SRS where a relocatable mask is used in conjunction with the imaging systems to accurately position the patient. Hypo-fractioned treatments termed stereotactic body RT (SBRT) or stereotactic ablative RT (SABR) have also been used for extra-cranial targets.

The main sources of ionising radiation in cancer clinics are linear accelerators (linacs), producing MV energy x-rays and electrons. Lower kV x-rays are used for superficial lesions. These are the most common EBRT sources, while particle therapy using protons is increasing in use. Protons are an attractive option due to the nature of the dose deposition with depth. A relatively large peak of dose is deposited at depth, called the Bragg peak. This contrasts with photons that deposit maximum dose near the surface and progressively decrease with depth. Electron beams also deposit maximum dose near the surface, but have a sharper drop-off in dose with depth, and are utilised for more shallow lesions.

Radioisotopes are used in brachytherapy treatments where a small sealed source, typically ^{192}Ir, is inserted into catheters that are placed in intra-cavitary locations or implanted into or positioned near the surface of the body. The source is set in position for a programmed amount of time and stepped to other positions and catheters to deliver planned dose distributions. Since the source is placed inside or near the target and due to the sharp drop-off in dose with depth, conformal dose distributions can be achieved without the extra dose from entry and exit beam paths as in EBRT. However, brachytherapy is usually a somewhat invasive procedure.

Linac based EBRT is currently the main RT treatment modality and has a long history dating back to the 1950s (Thwaites and Tuohy 2006). Early 2D planning methods used planar x-ray imaging and manual calculations with subsequent progression to full 3D computerised planning and delivery technologies in the 1980s and 1990s. With the advent of sufficient computing power and 3D imaging systems, 3D conformal RT (3DCRT) was adopted with planned dose distributions computed in 3D and delivered via computer programmed control. The development of a programmable, shape adaptable collimator, the multi-leaf collimator (MLC), was a major step towards the ability to achieve dose conformity to irregular targets. This then led to intensity modulated RT (IMRT). Treatment planning systems (TPS) were developed with inverse planning optimisers to generate many MLC segments that when combined, give the resulting modulated photon fluence computed by the TPS. Later, additional degrees of freedom were introduced by allowing modulation of gantry rotation speed and dose-rate together with the MLCs. This became commonly known as volumetric modulated arc therapy (VMAT). These advancements in planning and delivery methods have led to improvements in dose distribution conformity and delivery efficiency.

Other major advancements in linac EBRT have been in patient positioning. Image guidance has been adopted using on board imagers (OBI) giving image guided RT (IGRT). These imaging units produce kV planar electronic images, calibrated to accurately position the patient. 3D imaging is also used in the form of cone beam CT (CBCT). These types of patient localisation systems can be capable of sub-millimetre positioning accuracy as required for SRS and SBRT. On board imaging also provides the possibility for adaptive RT where the treatment plan is adjusted to suit the patient geometry for each treatment session.

The implementation of real-time monitoring systems such as optical marker and surface tracking, or x-ray imaging has given the ability to gate linac beams such that targets are only irradiated when located within predefined ranges of position. Another step beyond this is to track to tumours' position and conform the beam to the real-time position or move the patient such that the target is 'followed' by the beam. This means target margins can be reduced and less normal tissue is irradiated. The introduction of MRI guided RT gives the best imaging quality to facilitate adaptive and tracking approaches.

Increases in sophistication and automation of modern linac RT planning and delivery systems can mean treatment plan parameters are less intuitive, and detailed commissioning and QA is required to validate accuracy. The dose to be delivered to the patient is calculated by the TPS, giving a full 3D dose distribution. The accuracy of computed doses needs to be confirmed by measurements using dosimeters. The required accuracy depends upon the steepness of the TCP curve and relationship to NTCP, which is dependent on radiobiology and the RT techniques employed. The historical general statement of required dose accuracy of ± 5 % (ICRU 1976) does not necessarily apply to contemporary RT. New guidelines have emerged with IAEA (2016) recommending the principle of 'as accurately as reasonably achievable' (AAARA), considering technical and biological factors. For low dose gradient regions, accuracy is quantified by dose difference, while in high gradient regions, spatial accuracy in terms of distance to agreement is used. Dosimetry instrumentation and methods with appropriate accuracy, precision, spatial resolution and practicality are required to validate RT patient treatments.

1.1.2 Radiotherapy dosimetry

The quantity measured in radiation dosimetry is absorbed dose which is the energy absorbed in a medium per unit mass. Energy is deposited in ionisation events as the incident radiation interacts with the medium. The most common direct measurement of absorbed dose is by calorimetry where the temperature rise in the medium is measured. The absorbed energy is determined by the temperature rise and the known specific heat capacity for the medium. This absolute dosimetry method is not practical for clinical dosimetry and is used for reference dosimetry in standards laboratories. Other dosimeters are 'relative' dosimeters with calibration achieved using a radiation beam calibrated by a reference dosimeter, traceable to a primary standard (eg. calorimeter). Detection of absorbed energy can be made by measurement of ionisation of gases, liquids and solids. Other mechanisms of detection include chemical reactions and light emission by scintillation or luminescent materials. A recent review has been conducted by Kron *et al* (2016) summarising radiation dosimetry methods and applications.

Dosimeters can be classified according to their dimensional extent, that is, 0D (point detector), 1D, 2D or 3D. Most detectors are inherently point detectors such as ion chambers, diodes, diamonds, TLDs and OSLDs. A small volume of medium is the radiation sensitive volume providing a signal - electrical for ionisation (ion chambers, diodes, diamonds) or light output for luminescence (TLDs, OSLDs), measured by instrumentation such as electrometers and photometers. Point detectors are commonly used in scanning water tank phantoms. The detector can be scanned in 3D to characterise static radiation beams, however time varying beams (eg. modulated) cannot be readily integrated in 3D.

Multiple point detectors (ion chambers and diodes in particular) have been arranged in arrays to produce 2D and semi-3D dosimeters. Commercial products include MapCheck and ArcCheck (Sun Nuclear Corp), the Octavius suite of products (PTW Freiburg), Delta4 Phantom (ScandiDos AB), and MatriXX (IBA Dosimetry). These dosimetry solutions have become popular for clinical use, partly due to their efficiency through use of integrated software for instrument control and analysis of results. The validity and reliability of quasi-3D measured dose distributions need to be verified since they do not completely sample 3D measurement space and are often indirectly derived.

Detector arrays can have issues with water equivalence since ionisation based detector elements are usually air or silicon, and a comprehensive array can result in a substantial amount of the phantom that is far from water equivalent. Water equivalence is important since radiation dosimeters are calibrated to dose to water, as water is the standard reference medium in radiotherapy. Water has similar radiological properties to a range of tissues in the body. Phantoms that differ from water need to have well characterised radiological properties for them to be useful for dosimetry purposes. Inaccuracies can also result from detector angular dependence. Most point detectors suffer from some degree of angular dependence due to shape of the sensitive volume, as it is not really a ‘point’ but a finite volume being sampled. The volume may be the shape of a thin chip, thus there are large changes of detector cross-section from the beams’ eye view. Volume averaging is also an issue for point detectors of substantial size relative to the spatial features of the dose distribution.

Some detectors are a continuous medium that can sample radiation beams in 2D. Film is a longstanding 2D radiation detector. Historically, radiographic silver emulsion type films were used. Now, radiochromic films are used, since the wet processing step is not required and they have improved energy independence. Chemical reactions (reduction of silver ions for radiographic and polymerisation for radiochromic) in the film active layer result in changes to visible light transmission that can be related to radiation dose. The spatial resolution of film dosimetry is dictated by the film scanning readout method. The most common current scanners are standard office flatbed document transmission scanners adapted for dosimetry purposes. As these scanners are not purpose designed scientific instruments for film dosimetry, they suffer from issues such as non-uniformity due to light polarisation and optical geometry effects, and they typically cannot be recalibrated like measurement instruments often are to maintain a high level of accuracy (in 2D).

Other detectors that are inherently 2D include OSLDs and plastic scintillators in sheet form. Light emission is spontaneous for scintillators and stimulated for OSLDs. Thus scintillators require a light detection system at the location of irradiation and OSLDs are read out post-irradiation. Neither of these approaches has been significantly developed for radiotherapy dosimetry purposes. In diagnostic radiology, computed radiography (CR) has been extensively used, which is a form of OSL. CR systems have been succeeded by direct reading flat panel detectors using semiconductor technologies. Flat panel detectors have also been used for the OBI systems on linacs. On board MV imaging panels have been utilised for RT dosimetry and have provided virtual 3D dosimetry by reconstruction of the exit dose measured at the panel to a 3D volume in the patient or phantom (Mijnheer *et al* 2013).

Approaches to give 3D measured doses as mentioned above have been by arrangements of lower dimension detectors to give semi-3D dose or by calculations using entry and/or exit measurements to give virtual-3D dose. Dosimeters that are inherently 3D would be useful since arrays and calculation based methods have experimental and calculation complexities that give uncertainties that cannot be necessarily avoided or corrected in all conditions of use. Film dosimeters can be stacked to give a 3D dosimeter, however the practicalities of the labour required for readout and registration make this unattractive for routine use.

It is logical that radiation dose calculated in 3D for patient treatment would be verified by measurement in full 3D instead of point dose, 2D or quasi-3D dosimetry. This is particularly the case as delivery methods now provide modulated dose distributions in 3D. For example, clinical proton beam treatment units now use active beam steering systems, thus 3D dosimetry would ideally be used to verify the results of the beam's motions. High resolution 3D dosimetry not only provides the benefit of verifying dose calculation accuracy at every point of interest, but also the positioning accuracy of the treatment system can be quantified. The entire treatment process can be mimicked with a 3D dosimeter in a phantom, providing verification that the correct dose is delivered to the correct location. De Wagter (2004) provided a concept of 4 levels of dosimetric QA (for IMRT) with “3D dosimetry of entire treatment delivery” at the final step of level 4. With the advent of modulation of an increased number of parameters, motion management techniques, adaption and automation, there is an increasing need to conduct end to end tests with all components of the delivery system to verify a final combined result. Thus an accurate and reliable true 3D dosimetry technique with practical operation for clinical use would be extremely useful for end to end RT verifications.

1.1.3 True 3D dosimeters

A true 3D dosimeter can provide a full 3D dose map with high resolution (eg. < 2 mm spatial resolution). Dose gradients in RT can exceed 30 % / mm, so high spatial resolution capabilities are desired to accurately represent RT dose distributions. True 3D measurements can provide complete visualisation and quantification of the dose distribution instead of just particular points or planes. Gel dosimetry was proposed as an inherently 3D dosimeter in the 1980s by the use of MRI 3D scanning technology (Gore *et al* 1984). The gel was a chemical dosimeter where ferrous ions were oxidised to ferric ions, a change detected by MR relaxation rate measurements. This prompted interest in gel dosimetry and a number of researchers started investigating the possibilities of gel dosimeters, which led to the establishment of the 1st International Workshop on Radiation Therapy Gel Dosimetry, held in Kentucky, USA (DosGel’99 1999). A series of subsequent conferences followed, DOSGEL (2001, 2004, 2006, 2008). Then in 2010, the conference scope was broadened by renaming to the International Conference on 3D dosimetry (IC3DDose). By then, gels were not the only form of 3D dosimeters. Further meetings have been conducted, IC3DDose (2010, 2012, 2014, 2016). The proceedings of these conferences are a vast source of information on 3D dosimetry, particularly the numerous reviews and ‘refresher’ papers.

The developments in 3D dosimetry are summarised here by categorisation of dosimeter physical state and mechanism of radiation induced change. Readout systems for chemical dosimeters are outlined. As with film dosimetry, the readout system dictates the spatial resolution and plays a major role in the overall measurement quality.

1.1.3.1 Semi-solids – Gel dosimeters

The first true 3D dosimeters were manufactured using gels formed by gelatine, agarose and sephadex (Schreiner 1999) from as early as the 1950s (Day and Stein 1950). Chemical solutions known to provide a physically detectable change due to ionising radiation were spatially fixed in a gel matrix. Development of this idea would only really gain interest when 3D scanning technologies became available in the 1980s.

1.1.3.1.1 Ferrous sulphate gels

An aqueous ferrous sulphate solution chemical dosimeter known as the Fricke dosimeter (Fricke and Morse 1927) formed the chemical basis for early gel dosimeters. A typical Fricke solution comprised 1 mM ferrous ammonium sulphate and 1 mM sodium chloride in a 0.4 M sulphuric acid solution (Shortt 2001). Upon irradiation, radiolysis of water produced ions and radicals that caused oxidation of the ferrous (Fe^{2+}) ions to ferric (Fe^{3+}) ions as follows (Shortt 2001):

$$Fe^{2+} + HO_2 \rightarrow Fe^{3+} + HO_2^- \tag{1.1}$$

$$HO_2^- + H^+ \rightarrow H_2O_2 \tag{1.2}$$

$$Fe^{2+} + H_2O_2 \rightarrow Fe^{3+} + OH + OH^- \tag{1.3}$$

$$Fe^{2+} + OH \rightarrow Fe^{3+} + OH^- \tag{1.4}$$

For gel dosimeters the yield of Fe^{3+} ions is increased substantially from that indicated by the above simplified equations due to impurities introduced by gelatin or agarose, and sodium chloride is not required, since its role is to suppress oxidation due to contaminants (Shortt 2001). The increase of Fe^{3+} ions gives increased optical absorption at 304 nm so radiation dose can be related to optical transmission measurements using spectrophotometry. The addition of a metal indicator dye, xylenol orange (XO), resulted in the formation of Fe^{3+}- XO complexes with peak radiation induced absorption at 540 nm (Gupta *et al* 1978). This was called a ferrous, benzoic acid, XO (FBX) dosimeter. The benzoic acid increased Fe^{3+} yield, however was not necessary when a gelling agent was added such as agarose (Appleby and Leghrouz 1991). An FBX gelatin dosimeter was used in the first example of an optical CT scanned FX dosimeter (Kelly *et al* 1998). Further optimisations of the chemical constituents would result in the ferrous, XO, gelatin (FXG) dosimeter (Bero *et al* 2001).

Even though the original Fricke solution was probed by optical methods, the first 3D scanning method was not optically based but MRI based (Gore *et al* 1984). Since the Fe^{2+} and Fe^{3+} ions had different paramagnetic characteristics, NMR relaxation rate measurements ($1/T_1$) could determine the concentration on Fe^{3+} ions and hence dose deposited.

Whilst FX gels were promising for 3D dosimetry, there was the significant shortcoming of Fe^{3+} ion diffusion resulting in blurring of the dose distribution (Olsson et al 1992). Characterisations of diffusion were conducted and it was found that XO also acted as a chelator to reduce the diffusion coefficient to about half of that observed without XO (Rae *et al* 1996). Many attempts to reduce diffusion further have been made including recently (Penev and Mequanint 2013) with only minor improvements. A significant decrease of diffusion was achieved using polyvinyl alcohol as the gelling agent (Chu et al 2000). A hydrogel was formed by refrigeration and cryogel by freezing. The cryogel was opaque, thus read by MRI and the hydrogel could be optically read. Diffusion was about 1/3 of that reported by Rae *et al* (1996). Recent further attempts have not yielded significantly improved results (Smith et al 2015). PVA gels have only seen minor use compared to gelatin gels due to manufacturing difficulties regarding viscosity during mixing. The issue of diffusion remains the main limitation of FX gels.

A version of FX gel has been commercialised by Modus Medical Devices Inc. (Canada) called TrueView. It is marketed as reusable by virtue of diffusion blurring the dose distribution over 2 days, and is then ready for reuse. This approach presents calibration complications for subsequent usages.

1.1.3.1.2 Polymer gels

Alternatives to FX gels were investigated and a polymer 3D dosimeter was proposed (Maryanski *et al* 1993). The dosimeter comprised acrylamide (AAm) and N,N'-methylene-bis-acrylamide (Bis) monomers in an agarose gel, and was named BANANA (Bis, AAm, nitrous oxide, agarose). The monomers polymerise upon irradiation and oxygen needed to be removed since it would inhibit polymerisation, hence the nitrous oxide. The agarose was replaced with gelatin to give a Bis, AAm, nitrogen, gelatin (BANG) dosimeter (Maryanski *et al* 1994). 3D readout of the BANG gel was first considered using MRI (Maryanski *et al* 1994) and then optical CT (Maryanski *et al* 1996). Radiation induced polymerisation gave differences in NMR relaxation rates and optical attenuation via optical scattering. As BANG gel was patented, a generic name of polyacrylamide gel (PAG) was adopted by researchers producing their own versions of the gel. BANG gel was commercialised by MGS Research Inc. (USA).

The issue of having to prepare and maintain polymer gels in a hypoxic environment was addressed by the addition of antioxidants (Fong *et al* 2001). Many normoxic variants were investigated and one using tetrakis (hydroxymethyl) phosphonium chloride (THPC) as the antioxidant (De Deene *et al* 2002) provided improved dose rate dependence and cooling rate effects (De Deene *et al* 2006, De Deene *et al* 2007). This was called PAGAT (PAG in ATmospheric conditions). A drawback to PAG type gels is that acrylamide is a toxic substance and is dangerous to work with. A less toxic version was proposed using N-isopropylacrylamide instead of acrylamide, named NIPAM (Senden *et al* 2006). Leakage of oxygen into prepared gel containers remains an issue and even minor leaks can cause substantial errors (Sedaghat *et al* 2011).

Proposals of MRI and optical CT readout of polymer gels were followed by x-ray CT (Hilts *et al* 2000). Regions of greater polymerisation have increased physical density that can be detected by conventional clinical x-ray CT scanners, however dose sensitivity is low.

There has been much work done in polymer gel dosimetry, with MRI in particular, and a major review was done in 2010 by a number of the prominent researchers in the field (Baldock *et al* 2010).

1.1.3.1.3 Other gel dosimeters

1.1.3.1.3.1 Micelle gels

A radiochromic, non-toxic, low diffusion, transparent hydrogel for optical CT scanning was sought by Jordan and Avvakumov (2009) when they developed a micelle gel dosimeter with leuco malachite green (LMG) dye. LMG converts to malachite green upon irradiation, giving a change in colour by increased optical absorption at around 600 nm. Micelles are aggregates of surfactant molecules with hydrophobic and hydrophilic parts. The insoluble leuco dye is emulsified in the aqueous solution by situating at the hydrophobic centre of the micelles. Since the micelles have substantial size they do not readily diffuse in the gelatin matrix. An alternative dye was also used, leuco crystal violet (LCV) which converts to crystal violet (Babic *et al* 2009a). Low diffusion was confirmed, however dose sensitivity was 10 times less than FXG. LCV gels were preferred due to linear dose response, higher dose sensitivity and lower diffusion.

Further investigations into optimisation of LCV micelle gels resulted in an increase of dose sensitivity by a factor of 1.5, but at the expense of introducing significant dose rate dependence (Nasr *et al* 2015). LCV micelle gels are a promising option, and alternative reporter molecules may be possible in micelles.

1.1.3.1.3.2 Genipin gels

The use of a plant extract, genipin was found to be a potential option in a 3D gel dosimeter (Jordan 2008). Genipin was known to form cross-links with substances such as gelatin, so Jordan (2008) developed a method of preparing a genipin gel by blending a heated genipin and gelatin solution until it darkened and then sulphuric acid was added. When the genipin gel was irradiated it bleached in proportion to radiation dose. The change in optical density could be measured at its peak of about 600 nm. Due to the structural stability provided by the genipin-gelatin crosslinking, a wall-less gel was optical CT scanned (Jordan 2009).

Further characterisations of genipin gel provided indication of some favourable properties such as low dose rate and temperature dependence, and no detectable diffusion (Davies *et* *al* 2013). The main issues for implementation as a 3D dosimeter are high optical density of unirradiated gel and low dose sensitivity of around 1/20 of FXG.

1.1.3.1.3.3 Fluorescent gels

The process of radio-fluorogenic co-polymerisation (RFCP) has been applied to a gelatin gel (Warman *et al* 2011) to give a gel that exhibits radiation induced UV stimulated fluorescence. A monomer, tertiary-butyl acrylate (tBuA) was used with a fluorogenic compound, N-(1-pyrenyl)maleimide (MPy) to give an RFCP product within a gel matrix. The fluorogenic response was shown to be proportional to radiation dose, however only 2D photographs were obtained for quantitative analysis. The development of an optical emission tomographic scanner with suitable UV stimulation light system is required for this radio-fluorogenic gel to become a true 3D dosimeter.

1.1.3.2 Solid dosimeters

True 3D dosimeters of a solid form are more recent developments than the previously established gel approaches. Solid dosimeters benefit from a more rigid and stable form, while uniform material and dosimetric properties throughout the volume are important to maintain in manufacture.

1.1.3.2.1 Presage

Presage is a tradename for a commercial 3D dosimeter by Heuris Inc. (USA). It is a rigid solid plastic, polyurethane, doped with the radiochromic leuco dye LMG (Adamovics and Maryanski 2004). A radical initiator such as a halocarbon is required to produce free radicals upon irradiation to cause oxidisation of the dye. A peak optical absorption dose response is observed at about 630 nm. Presage is scanned by optical CT for 3D readout (Guo *et al* 2006). It can be moulded into various shapes and machined in its solid form, and a variety of formulations have been used (Oldham 2015). Water equivalence and optical quality (homogeneity) has been improved in later versions and there is no significant diffusion. The manufacturing process is more involved than gels, but it is available commercially. The high RI compared to gels can make optical scanning more difficult due to RI matching (Doran 2013).

1.1.3.2.2 Silicone

A flexible solid radiochromic dosimeter material was recently proposed, using silicone (Sylgard 184 silicone elastomer kit) and LMG dye (De Deene *et al* 2015, Hoye *et al* 2015). Chloroform is another ingredient to generate radiation induced radicals to oxidise the LMG dye. As with Presage, the peak optical dose response is around 630 nm. Optical CT readout using dual wavelengths was demonstrated by De Deene *et al* (2015). Pre-irradiation reference scanning was avoided by referencing the dose responsive red channel to the blue which has little dose response. This was due to the dosimeter being deformable, meaning accurate localisation for pre and post-irradiation scans would not be possible. Dose rate and temperature dependencies were detected, while diffusion was not (De Deene *et al* 2015). Dose rate dependence was improved by investigations of ingredient concentrations (Hoye *et al* 2015).

1.1.3.2.3 Other solids

Film dosimetry can provide high resolution 2D dose maps, and by construction of a stack of films in a phantom, 3D dosimetry is possible. This was investigated in detail by McCaw *et al* (2014). It was found that the radiochromic film stack dosimeter was accurate with an estimated uncertainty of 3 % (k=1), and was utilised in the application of IMRT verification. The practicalities of preparation and readout of multiple films may not be an attractive option for clinical physicists, however, for current film users with film equipment and procedures in place, it could be readily adopted.

Plastic scintillator material has potential to be a real-time reusable 3D dosimeter as it is a transparent solid that emits light upon irradiation. Additionally plastic scintillator materials have good water equivalence for RT applications (Beddar *et al* 1992). Plastic scintillators have an organic fluorophore that is excited by charged particles and results in spontaneous visible light emission upon decay to the ground state. Kroll *et al* (2013) used plastic scintillator BC-408 (Saint-Gobain Crystals) in a hexagonal block shape with 3 CCD cameras facing 3 of the hexagonal faces and a fourth camera facing the end. The 4 camera views were used to generate a tomographic reconstruction. A significant limitation was that only a fixed beam orientation could be used due to the camera arrangement. Another approach was to use a plenoptic camera viewing one side of a plastic scintillator cube (EJ-260, Eljen technology, USA) embedded in a PMMA phantom (Goulet *et al* 2014). The linac portal imager was used to obtain another distinct view. A 3D iterative reconstruction algorithm was devised and IMRT and VMAT deliveries were measured. These early results indicate potential for plastic scintillators, however further work is required.

1.1.3.3 Liquid dosimeters

3D dosimeters of a liquid form could potentially be realised by using real-time imaging systems capable of 3D representations of light emissions from radio-luminescent liquids. This would result in time resolved dosimetry that could be integrated to give a composite dose distribution from a time varying delivery such as IMRT or VMAT. This is an area of recent development and is briefly outlined in the following sections.

1.1.3.3.1 Scintillators

The feasibility of liquid scintillators for 3D dosimetry was investigated using BC-531 (Saint-Gobain Crystals) scintillator in a rectangular tank with a CCD camera facing one wall (Beddar *et al* 2009). This would only provide 2D dosimetry of proton Bragg peaks but it was proposed to add a second camera to facilitate 3D dosimetry. Further work was conducted, however, it was still only proposed that 3D imaging was possible (Archambault *et al* 2012). A simulation study of 3D reconstruction using limited views was conducted, indicating that 3 camera views would be a feasible approach by using an iterative reconstruction method (Hui *et al* 2014). Robertson *et al* (2013) has studied Bragg peak quenching in the 3D volume scintillator.

1.1.3.3.2 Cherenkov light

The Cherenkov effect is the emission of light due to electrons travelling faster than the local speed of light in a dielectric medium. Cherenkov light generated by linac MV irradiations of plastic scintillator dosimeters has been challenging to avoid (Beddar *et al* 1992). In recent work Cherenkov light itself has been utilised to visualise radiation dose in a water phantom (Glaser *et al* 2013a). Cherenkov emissions were used to induce fluorescence of quinine sulphate added to the water. A CMOS camera gave 2D images of 6

MV beams that were proportional to dose, and it was suggested that extension to 3D dosimetry was possible. A 3D tomographic reconstruction method was demonstrated by rotating the linac collimator to give multiple 2D views of Cherenkov light without a fluorophore (Glaser *et al* 2013b). A telecentric lens helped with quantitative imaging of the anisotropic light emission. A similar 3D reconstruction method was used for isotropic quinine fluorescence without the telecentric lens (Glaser *et al* 2015). Multiple projection views were generated by collimator and couch rotations and a cone beam reconstruction was used to generate 3D dose maps of several MLC fields. Whilst useful to demonstrate 3D dosimetry is possible, the collimator and couch rotations are impractical for clinical verifications where collimator, couch and gantry angles are defined by treatment plans.

1.1.4 Three dimensional readout methods for chemical dosimeters

Three dimensional passive dosimeters require a 3D imaging modality to interrogate the dosimeter and generate 3D dose maps. In modern medical diagnostic imaging, 3D imagers are commonplace. X-ray CT and MRI scanners are standard imaging technologies and have both been associated with 3D dosimetry. The other major imaging technique used for 3D dosimetry has been optical CT scanning, which is a cheaper, dosimetry dedicated solution. Other methods such as ultrasound (Mather and Baldock 2003) have only been of minor interest due to imaging quality limitations. Readout methods for optical emission dosimeters are less mature than those for chemical 3D dosimeters and were briefly described in the dosimeters section 1.1.3.

1.1.4.1 MRI

The first 3D imaging modality used for 3D dosimetry was MRI (Gore *et al* 1984). It was found that the Fricke dosimetry solution radiation induced conversion of Fe^{2+} to Fe^{3+} could be quantified by NMR relaxation rate measurements. The spin-lattice relaxation rate R_1 ($1/T_1$) and spin-spin relaxation rate R_2 ($1/T_2$) of protons in water were found to be proportional to ferric ion concentration, and hence dose. The R_1 relaxation rate was found to be more reliable. This was also the case for Fricke solution with a gelling agent added to form a 3D gel dosimeter. Due to the diffusion limitation of Fricke gels, polymer gels soon became of interest with MRI scanning (Maryanski *et al* 1993). Many formulations of polymer gels have followed, using the scanning method of MRI, and numerous applications involving IMRT, VMAT, brachytherapy and proton therapy have been studied (Baldock *et al* 2010).

An advantage of MRI scanning is that gel dosimeter shape can be varied from the typical cylindrical shape used by optical scanning, thus providing the ability to scan human shaped gel dosimeters (De Deene *et al* 1998). This study gave mean absolute dose differences of 8 % when compared to film dosimetry. This led to further studies to improve MRI quantitative imaging for polymer gel dosimetry. Issues that were noted include the following: eddy currents can cause the R2 response to be slice orientation and sequence parameter dependant (De Deene *et al* 2000a), and inhomogeneities in the magnetic field (B_0) can cause geometric distortions (De Deene *et al* 2000b). With attention to these issues, improved polymer gel dosimetry was demonstrated for an IMRT application (De Deene *et al* 2000c). Furthermore, non-uniformities in imaged volumes can be caused by temperature drift due to the imaging workload (De Deene *et al* 2001). To assist other workers, suitable quantitative imaging sequences for polymer gel scanning have been suggested (De Deene 2013).

A recent comprehensive study of MRI scanning of polymer gels revealed that temperature variations in the MRI scanner room were responsible for large dose deviations of 15 %, so dosimeter temperatures needed active control to reduce absolute dose uncertainty to 2.6 % (Vandecasteele and De Deene 2013a). The effects of inhomogeneous main magnetic (B_0) and RF (B_1) fields were investigated and compensated by scanning blank gel phantoms.

While MRI is a highly developed imaging modality for the general purpose of imaging human anatomy, it is not dedicated to the purpose of dosimetry and is largely the domain of the specialist MRI staff operating such equipment. Therefore it can be difficult to generate the expertise required to familiarise and develop suitable imaging techniques for quantitative dosimetry. Additionally, MRI machines are an important clinical resource for diagnostic imaging purposes, so access for scanning dosimeters can be problematic compared to a dedicated dosimetry scanner. However, RT treatment machines with integrated MR imagers have become a clinical reality (MRIdian, ViewRay USA) and MRI-linacs are following, so interest in MRI based 3D dosimetry may increase.

1.1.4.2 Optical CT

Optical CT scanning was perhaps an overdue development by the time Gore *et al* (1996) provided clear demonstration of the feasibility of optical CT scanning for 3D dosimetry. X-ray CT scanning had been developed decades earlier, which shares the same basis of tomographic reconstruction except using x-ray beams and detectors suited for these higher photon energies. Another optical scanner was developed in 1996 for the purpose of imaging 3D chemical structures using a CCD camera and LED light source (Winfree et al 1996). With specific applications in mind, in an era of progress in photonics (lasers, LEDs and detectors), researchers in multiple fields were able to develop 3D optical CT scanning techniques.

1.1.4.2.1 Optical CT scanning principles

Optical CT scanners measure the change of optical attenuation, $\Delta\mu$ of a dosimeter. Light is attenuated exponentially (as with x-rays) when passing through a medium. The Beer-Lambert law describes this behaviour with transmitted light intensity, I as a function of the wavelength, λ of the light:

$$I(\lambda) = I_0(\lambda)e^{-\mu(\lambda)x} \tag{1.5}$$

where I_0 is the incident light intensity, x is the pathlength and μ is the linear optical attenuation coefficient. Transmittance is defined as:

$$T = \frac{I(\lambda)}{I_0(\lambda)} \tag{1.6}$$

and absorbance is:

$$A = -log\left(\frac{I(\lambda)}{I_0(\lambda)}\right) \tag{1.7}$$

In spectrophotometry, transmittance is measured at a given wavelength using a light source with monochromator and a detector. The same principle is used for optical CT with a laser or LED light source and photodiode or CCD detector. Measured transmittance is used to determine the optical attenuation coefficient per unit pathlength:

$$\mu = -ln(T)/x \tag{1.8}$$

If the pathlength comprises a number of various levels of optical attenuation, as with a 3D dosimeter, they are summed to give the total for the ray path:

$$\mu x_n = \sum_{i=1}^{n} \mu_i \Delta x_i \tag{1.9}$$

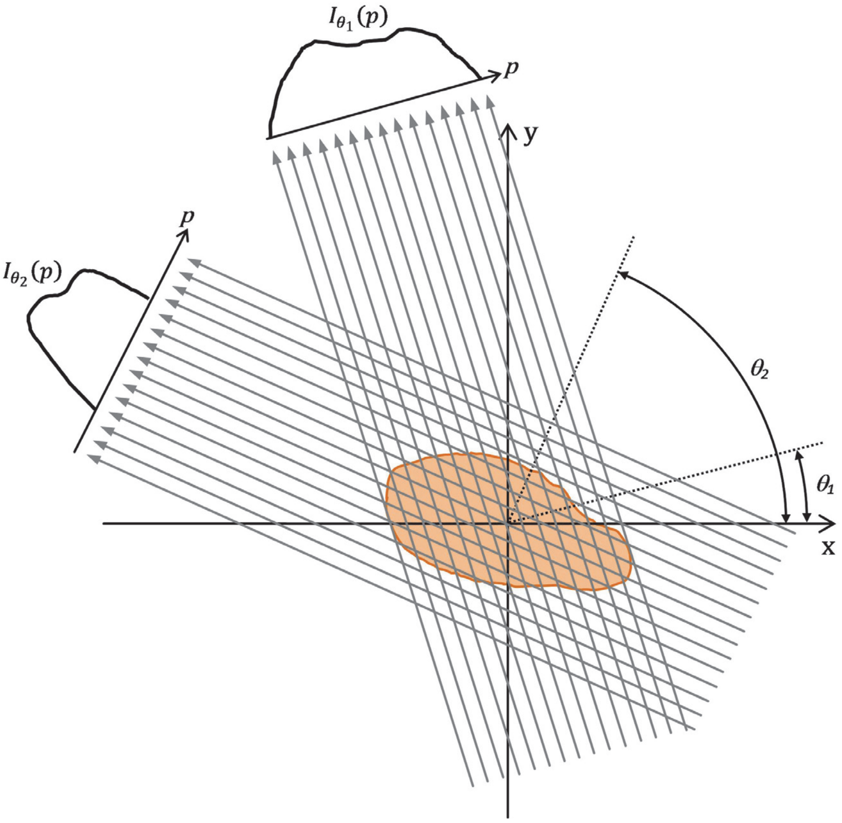

Figure 1.1. Schematic diagram of 1D projections $I_\theta(p)$ at different angles of rotation. The projections are the Radon transform of the 2D object. A set of projections are inverse Radon transformed to reconstruct the 2D cross section of the 3D object.

Multiple ray paths through a dosimeter form a projection as shown in figure 1.1. For a laser pencil beam with a point detector, translation across the sample gives a projection with parallel rays through the sample, that is, a profile across the sample with each point being the line integral of the optical attenuation over the pathlength at a given point. Tomographic reconstruction methods are used to reconstruct a 2D map of optical attenuation coefficients. After one projection is obtained, the sample (or source and detector) is then rotated and another projection is acquired. This is repeated for many angles of rotation over 180 or 360°. This set of projections can be plotted as intensity values as a function of rotation angle and translation distance, giving a 'sinogram'. This is the Radon transform of the original image of the 2D slice of the sample. To reconstruct the original image from the sinogram, it is inverse Radon transformed or 'back-projected'. Back-projection involves taking one projection at a given angle in real space and propagating the intensity values in the direction perpendicular to the projection. This is done for all projections at their given angles, where overlapping regions result in higher values, thus a 2D map of the original sample image is produced. The reconstructed image will be blurred since the backprojection is not a perfect mathematical transformation with low spatial frequencies more dominant. This is addressed with filtering using a high pass filter in the spatial frequency domain. Therefore this process of image reconstruction is named 'filtered back-projection' (FBP).

Parallel ray geometry through the sample is the simplest case. Methods have also been extended to fan beam geometry, and then further developed to cone beam reconstruction, for example the Feldkamp, Davis, Kress (FDK) algorithm (Feldkamp *et al* 1984). Other approaches to tomographic reconstruction include iterative algorithms such as algebraic reconstruction techniques (ART). Here the difference between measured sinogram data and calculated estimate from a current iteration of the estimated reconstructed matrix is minimised to produce the final reconstruction. An advantage of ART is the ability to include known physical processes (ie. modelling) that can account for deviations from standard assumptions required in FBP reconstructions.

1.1.4.2.2 Development of optical CT for dosimetry

The first generation optical CT scanner for radiation dosimetry by Gore *et al* (1996) used a He-Ne laser and large area photodiodes for measurement and reference detectors. The beam was translated across the sample by a pair of translating mirrors, ie. translate-rotate geometry. This scanner was used to measure optical attenuation by scattering in polymer gel dosimeters. The cylindrical gel sample was immersed in a RI matching fluid bath. The bath walls were perpendicular to the incident light beam to avoid refraction and give parallel rays through the sample. The translation mechanism resulted in slow scan speeds for the first generation scanner. Kelly *et al* (1998) developed a first generation scanner with FX gels. The sample was translated instead of the light beam and acquisition was slow at 1 hour per slice. Oldham *et al* (2001) also constructed a first generation scanner with a 20 min per slice acquisition time for a 1 mm pixel size. A first generation scanner was commercialised with the name 'Octopus' (MGS Research Inc. USA), and was evaluated by Islam et al (2003). Imaging artefacts were apparent with 3 - 5 % relative dose errors for BANG gels, due to optical scattering effects. Scan speed was 12 min per slice for 1.4 mm pixels. Studies of scanner performance were ongoing (Oldham *et al* 2003, Xu *et al* 2003, Oldham and Kim 2004).

With the scan speed limitations of first generation scanners, faster methods were devised by using a rotating mirror to sweep the beam across the sample (Maryanski and Ranade 2001, van Doorn *et al* 2005). Acquisition as fast as 2.4 sec per slice was reported by van Doorn *et al* (2005), although quantitative imaging accuracy was not detailed. Another approach for increased scan speed was by broad beam scanning with a 2D camera detector. Tarte *et al* (1997) used a CCD camera to image FX gels in 2D and Wolodzko *et al* (1999) described a CCD cone beam scanner without fully addressing the optical geometry in terms of beam divergence and refraction. A parallel beam CCD camera system was developed with investigations into the ray paths by simulations (Doran *et al* 2001), and later further characterised (Krstajic and Doran 2006, 2007a). Jordan *et al* 2001 conducted initial investigations into cone beam scanning by re-sorting projection data.

A cone beam scanner was commercialised by Modus Medical Devices Inc. (Canada) named Vista, with characterisations soon following (DeJean *et al* 2006, Jordan *et al* 2006). Artefacts due to scatter were found to be notable as may be expected from the broad beam geometry (DeJean *et al* 2006). Scattering polymer gels were most problematic. Later characterisations would follow, and efforts to refine the system using FXG to make clinical use more viable (Olding *et al* 2010a, Olding and Schreiner 2011). The Vista scanner utilised 633 or 590 nm LED diffuse light sources, a RI matching fluid bath, a 12 bit CCD camera and acquisition times of 5 minutes. In the work of Olding *et al* (2010a, 2011), optical CT absorbance measurement accuracy was 3 - 4 %, using spectrophotometer measurements as a reference.

Another broad beam approach was implemented by Sakhalkar and Oldham (2008) with parallel beam geometry using a telecentric lens with a < 0.1° acceptance angle. Presage was scanned in a RI matching fluid. This was further developed into the Duke Large field of view Optical-CT Scanner (DLOS) (Thomas and Oldham 2010). A LED light source was collimated to give parallel rays passing through the sample to the telecentric lens and CCD camera. This scanner was prepared for clinical application by testing with a range of test fields and comparison to a TPS and some previous measurements (Thomas *et al* 2011). Scan time was 15 minutes and good quality relative dosimetry was achieved, however, absolute dosimetry using spectrophotometer cuvette calibration measurements gave discrepancies up to 5 % compared to the reference TPS data.

Among other novel prototypes, a method of laser beam fast scanning was proposed by using multiple galvo mirrors to raster scan the sample in 20 minutes (Krstajic and Doran 2007b). Promising preliminary results were provided. A prototype laser fan beam scanner was described using a RI fluid tank with curved walls to maintain perpendicular incidence for all angles of the fan beam (Campbell *et al* 2013). Although steps were taken to address artefacts, image quality remained a problem. Improved performance of the Octopus scanner was proposed by the addition of a beam splitter to route a second laser beam to a second set of translating mirrors and detector, giving double the data acquisition rate (Qian *et al* 2013). Scan time was reduced from around 8 hours to 2 hours, however there were a number of additional components and moving parts.

A standard design feature of optical CT scanners has been the use of RI matching fluid to avoid unwanted refraction at the dosimeter walls. Maryanski and Ranade (2001) did not use RI matching fluid, however, only a small central area of the dosimeter could be irradiated and read. Interest in fluid-less scanning became topical with simulation studies showing potentially feasible options of scanning Presage in air and using an ART (Doran and Yatigammana 2012, Rankine and Oldham 2013). Simulations showed that up to 65 % of the Presage diameter could be acquired. An approach of minimising the amount of RI fluid was investigated by simulations (Chisholm *et al* 2015) and then realised as a prototype scanner using Fresnel lenses (Bache *et al* 2016). Reduction of fluid is not as beneficial as complete elimination of fluid since issues of RI matching and cleanliness will still be present.

Developments have continued in recent times with the following reports: optical geometry with a convergent light source to reduce the effects of stray light for cone beam scanning (Dekker *et al* 2016), a laser beam scanner for large volumes using off-axis ray paths and a novel RI matching fluid tank (Dekker *et al* 2017), dual wavelength scanning to avoid the need for pre-irradiation scanning since the second wavelength is used as the reference scan (De Deene 2015), a cone beam scanner with reconstruction using an ART with refraction corrections and investigation of RI matching with water and dry scanning (Manjappa *et al* 2016), and a fast cone beam scanner with projection data acquisition times of less than 1 minute (Chang *et al* 2016).

1.1.4.3 X-ray CT

The use of the established imaging modality of x-ray CT was investigated by Hilts *et al* (2000). Polymer gels exhibit an increase in physical density upon polymerisation which can be detected by x-ray attenuation measurements. The sensitivity was only approximately 1 HU/Gy and therefore SNR was a significant limitation. Later refinements of scan techniques, phantoms and data processing yielded noise reductions and identification of various sources of noise (Hilts et al 2005). Further efforts to improve the SNR by adaptive mean filtering gave increases in the SNR, however the level of filtration needed to be appropriate for the given application to avoid excessive spatial distortion (Hilts and Jirasek 2008). Another method was by extrapolation to a ‘zero-scan’ image (Kakakhel *et al* 2011). Pixel values as a function of scan number were curve fitted and extrapolated to a zero scan value. An alternative method was developed to reduce ‘structured’ noise by use of a signal removal method named remnant artefact removal (RAR) (Jirasek *et al* 2012). This was used in conjunction with the previous adaptive mean filtering that would only reduce stochastic noise.

The low dose sensitivity of polymer gel x-ray CT scanning remains a limitation compared to higher dose sensitivity methods of MRI and optical CT. Image averaging, filtering and additional artefact removal techniques improve results, but the image quality for a given dose is still inferior. However, since clinical RT departments usually have a CT scanner for treatment planning, and access is readily available, CT scanned polymer gels may be of interest to medical physicists to provide some form of true 3D dosimetry.

1.1.5 Applications of true 3D dosimetry

The utility of true 3D dosimetry has been demonstrated for many radiotherapy applications. While not widely adopted as a standard clinical tool, researchers have shown that there are many feasible options to generate useful true 3D dosimetry. Feasibility may provide indication of the possibilities for use, however issues such as practicality and accuracy may still be considered questionable for some methods, limiting translation to routine clinical use.

Further to the applications noted in the following sections, there are a number of earlier (pre-2007) examples of applications in the polymer gel review paper by Baldock *et al* (2010). Additionally, the DOSGEL / IC3DDOSE conference series proceedings include further examples.

1.1.5.1 External beam radiotherapy

Linac based EBRT is the most common RT treatment modality and there are a number of aspects of interest for 3D dosimetry as follows.

SRS has been long established as a treatment technique, and 3D dosimetry can provide analysis of the accuracy of the small conformal dose patterns delivered with high spatial accuracy. Small fields were characterised by Babic *et al* (2009b) using FXG and optical CT scanning. Wang *et al* (2010) used optical CT scanned Presage for verifications of the very small field, high dose treatments of trigeminal neuralgia. Thomas *et al* (2013) measured 3D dose distributions of multi-target, single isocenter VMAT SRS deliveries with Presage and optical CT. Teng *et al* (2014) assessed the significance of setup errors for SRS deliveries using Presage and a Vista optical CT scanner.

IMRT treatment plans are verified to ensure the modulation provided by the MLC is correct. IMRT verifications have been demonstrated by; Wuu and Xu (2006) with BANG gel scanned by an Octopus optical CT, Babic *et al* (2008) with optical CT and FXG, Oldham *et al* (2008) by Presage and Octopus optical CT, Olding *et al* (2010b) with a Vista optical CT and FXG, and Vandecasteele and De Deene (2013b) with both MRI read PAGAT and optical CT scanned micelle gel. VMAT deliveries have also been assessed by

Ceberg *et al* (2010) using nPAG read by MRI, and Jackson *et al* (2015) with Presage and optical CT scanning.

For SABR lung treatments where motion of the target is significant, causing dose blurring and the potential for interplay of motions to give dose delivery errors, 3D dosimetry may be useful and was demonstrated by Olding *et al* (2015) with optical CT scanned micelle gel. The accuracy of deliveries assisted by motion management systems such as gating were assessed using PAG with MRI and Presage with optical CT by Ceberg *et al* (2008) and Brady *et al* (2010) respectively. Skyt *et al* (2013) used nPAG and BANG gels scanned by optical CT to verify both dose painting and tracking motions.

One of the latest RT developments is the realisation of MRI guided treatments where an MRI scanner is integrated into the RT machine. The first commercial and clinical example is the MRIdian (ViewRay USA) ^{60}Co teletherapy machine. Rankine *et al* (2017) used Presage and a Duke University optical CT scanner to demonstrate the use of 3D dosimetry to validate IMRT delivered by a MRIdian. In the future, 3D dosimetry using passive chemical dosimeters may prove to be useful for MRI-linacs since they may be less affected by MRI magnetic fields than electrically based detectors.

The Gamma Knife (Elekta) treatment system for SRS uses many small ^{60}Co sources to give precise conformal doses to cranial tumours. Examples of 3D dosimetry have been given (Ma *et al* 2009, Moutsatsos *et al* 2013, Klawikowski *et al* 2014).

Assessment of the validity of software deformed doses is an application of rising interest. Dose deformation is useful for adaptive RT where changing anatomy can be registered and dose accumulated for repeated treatments or fractions. As dosimetric gels are naturally deformable they would appear to have potential for deformable dose measurements. PAG gels have been investigated as deformable dosimeters with MRI (Niu *et al* 2012) and optical CT readout (Yeo *et al* 2012). Solid dosimeters can also be deformable with Presage-Def proposed (Juang *et al* 2013), together with silicone dosimeters developed for the purpose (De Deene *et al* 2015, Hoye *et al* 2015).

Another application for proven 3D dosimetry systems with known accuracy is the verification of quasi-3D dosimeters such as virtual reconstructed 3D dosimetry and semi-

3D array detectors. An example of 3D assessment of a diode array (ArcCheck, Sun Nuclear Corp.) with 3D calculation software (3DVH, Sun Nuclear Corp.) using BANG3 gel scanned by MRI has been conducted (Watanabe and Nakaguchi 2013).

1.1.5.2 Brachytherapy

The radiation sources used for brachytherapy can make RT dosimetric verifications difficult due to very steep dose gradients and dosimeter energy dependencies. True 3D dosimeters sampling 3D space in high resolution can be useful for large gradients and are typically more energy independent than conventional detectors such as TLDs, ion chambers and diodes. Brachytherapy treatments are commonly provided by an ^{192}Ir source positioned by an afterloader. 3D measurements have been made using PAG scanned by MRI (Lin *et al* 2009) and Presage with optical CT (Wai et al 2009, Palmer *et al* 2013). Other radiation sources used in brachytherapy include sealed seed sources as permanent implants such as ^{103}Pd, ^{125}I and ^{131}Cs. Adamson *et al* (2014) used Presage and optical CT scanning to obtain 3D dose measurements for comparisons to planning data. Another type of source, ^{90}Sr/^{90}Y used for intravascular brachytherapy, was assessed with BANG gel and a high resolution optical CT scanner (Massillon-JL *et al* 2009).

1.1.5.3 Proton beam therapy

Proton beam therapy can provide more conformal dose distributions than photon EBRT due the nature of proton dose deposition with the Bragg peak. There are also proton scanning beam technologies that need to be verified for accurate performance. Presage has been investigated (Zhao *et al* 2012) together with polymer gels (Zeidan *et al* 2010, Su *et al* 2012) however, as with many dosimeters for protons, questions remain over accuracy especially regarding quenching of the Bragg peak (Doran *et al* 2015). Other particle beams such as carbon ions have also been investigated with Presage (Yates *et al* 2011).

1.1.6 Conclusions

Technological advances in radiotherapy have been rapid in the last 20 years with the implementation of IMRT, VMAT, IGRT, gating, tracking, and leading into adaptive RT with on board MRI imaging. There are also the treatment modalities of brachytherapy and proton beam therapy delivering very conformal dose distributions. Methods and equipment to verify the 3D dose distributions delivered by increasingly sophisticated techniques have not developed to the point that true 3D dosimetry has been widely adopted in clinics. The feasibility of a number of approaches to 3D dosimetry has been demonstrated, however, the reliability and practicality remains questionable. It could be argued that such techniques are not required, as evidenced by the acceptance of new treatment techniques without them, but if the shortcomings can be improved, they may be considered more valuable in the future. Gel dosimetry has a long history of being ‘under development’ and improvements, particularly in practicality, are required to become a more commonly practiced form of dosimetry. Solid chemical dosimeters have been developed that have some improved dosimetric properties, but 3D scanning issues are similar. Newer methods using plastic and liquid scintillators, and luminescent dosimeters are in the early stages of development.

The original 3D dosimeter readout method of MRI may have been limited by access to these machines, but with their increasing presence in RT departments, this may change. Optical CTs are a relatively cheap option and have shown promise in the quality of results. If practicality and accuracy could be further developed, optical CT scanning could become a more viable option for clinical medical physicists. An undesirable aspect of most optical CT scanners is the use of a RI matching fluid bath. An accurate fluid-less scanner would be a good advancement for the technique. In developmental work of an optical CT, an established gel dosimeter such as FXG could be beneficial as it has many desirable properties such as being optically absorbing, dose rate independent, tissue equivalent, good dose sensitivity, non-toxic and easy to manufacture without specialised equipment. Ferric ion diffusion is the main drawback, but a fast scanning method can mitigate this to a degree. Further improvements of gel dosimeters particularly the dose sensitivity of inexpensive, non-diffusing radiochromic hydrogels would be a welcome addition to a more practical optical scanner.

1.2 Objectives of this research

The overall aim was to develop an optical CT scanner with improved practicality and suitable accuracy and reliability to increase the likelihood of use in clinical radiotherapy dosimetry. To develop new scanning techniques, fundamental optical interactions were considered in investigations of optical ray paths for tomographic reconstructions and factors relating to accurate measurements of optical transmittance. Specific objectives were identified to achieve the overall aim as follows:

1. Design optical CT scanner optical geometry such that RI matching fluid is eliminated and a high likelihood of quantitative accuracy is possible.
2. Construct a prototype scanner and demonstrate the feasibility of the optical design.
3. Refine the scanner and develop a dosimetry system using a radiosensitive gel.
4. Demonstrate the clinical utility for specific RT applications.

During the work of addressing the above objectives, further ideas on improving both scanner practicality and performance were introduced, resulting in additional objectives as follows:

5. Design and development of a dual wavelength optical CT scanner.
6. Identify the advantages and weaknesses of the various modes of scanner operation.
7. Validate the fluid-less dual wavelength scanner performance as part of a dosimetry system, ready for clinical use.

1.3 Structure of the thesis

The body of this thesis comprises a combination of conventional narrative and published research papers. The narrative provides details of unpublished work and background details for the publications, together with further discussions and linkage to the subsequent work. Thus an account is provided of progression from concepts through development and realisation of objectives in chronological order occurring during the research.

The general research topic of true 3D dosimetry in radiotherapy was introduced in Chapter 1. Techniques used to date were reviewed to identify areas of improvement that could assist in the development of a true 3D dosimetry solution for radiotherapy clinical applications. Chapters 2 to 6 comprise the body of the thesis, documenting the development of a new optical CT scanner and 3D dosimetry system, suitable for clinical use. In Chapter 7, final conclusions are drawn and the possibilities for further work are discussed.

1.4 References

Adamovics J and Maryanski M J 2004 A new approach to radiochromic three-dimensional dosimetry-polyurethane *J. Phys. Conf. Ser.* **3** 172–175

Adamson J, Yang Y, Juang T, Chisholm K, Rankine L, Adamovics J, Yin F F and Oldham M 2014 On the feasibility of polyurethane based 3D dosimeters with optical CT for dosimetric verification of low energy photon brachytherapy seeds *Med. Phys.* **41** 071705

Appleby A and Leghrouz A 1991 Imaging of radiation dose by visible color development in ferrous-agarose-xylenol orange gels *Med. Phys.* **18(2)** 309-314

Archambault L, Poenisch F, Sahoo N, Robertson D, Lee A, Gillin M T, Mohan R and Beddar S 2012 Verification of proton range, position, and intensity in IMPT with a 3D liquid scintillator detector system *Med. Phys.* **39** 1239-46

Bache S, Malcolm J, Adamovics J and Oldham M 2016 Optical-CT 3D Dosimetry Using Fresnel Lenses with Minimal Refractive-Index Matching Fluid *PLoS ONE* **11**(3): e0152606 doi:10.1371/journal.pone.0152606

Babic S, Battista J and Jordan K 2008 Three-dimensional dose verification for intensity-modulated radiation therapy in the radiological physics centre head-and-neck phantom using optical computed tomography scans of ferrous xylenol-orange gel dosimeters *Int. J. Radiat. Oncol. Biol. Phys.* **70** 1281-1291

Babic S, Battista J J and Jordan K 2009a Radiochromic leuco dye micelle hydrogels: II. Low diffusion rate leuco crystal violet gel *Phys. Med. Biol.* **54** 6791–6808

Babic S, McNiven A, Battista J and Jordan K 2009b Three-dimensional dosimetry of small megavoltage radiation fields using radiochromic gels and optical CT scanning *Phys. Med. Biol.* **54** 2463-81

Baldock C, De Deene Y, Doran S, Ibbott G, Jirasek A, Lepage M, McAuley K B, Oldham M and Schreiner L J 2010 Polymer gel dosimetry *Phys. Med. Biol.* **55** R1-63

Beddar A S, Mackie T R and Attix F H 1992 Water-equivalent plastic scintillation detectors for high energy beam dosimetry: I. Physical characteristics and theoretical consideration *Phys. Med. Biol.* **37** 1883‑900

Beddar S, Archambault L, Sahoo N, Poenisch F, Chen G T, Gillin M T and Mohan R 2009 Exploration of the potential of liquid scintillators for real-time 3D dosimetry of intensity modulated proton beams *Med. Phys.* **36** 1736‑43

Bero M A, Gilboy W B and Glover P M 2001 Radiochromic gel dosemeter for three-dimensional dosimetry *Rad. Phys. Chem.* **61** 433-435

Brady S L, Brown W E, Clift C G, Yoo S and Oldham M 2010 Investigation into the feasibility of using PRESAGE/optical-CT dosimetry for the verification of gating treatments *Phys. Med. Biol.* **55** 2187–201

Campbell W G, Rudko D A, Braam N A, Wells D M and Jirasek A 2013 A prototype fan-beam optical CT scanner for 3D dosimetry *Med. Phys.* **40** 061712

Ceberg S, Karlsson A, Gustavsson H, Wittgren L and J Back S A 2008 Verification of dynamic radiotherapy: the potential for 3D dosimetry under respiratory-like motion using polymer gel *Phys. Med. Biol.* **53** N387–N396

Ceberg S, Gagne I, Gustafsson H, Scherman J B, Korreman S S, Kjaer-Kristoffersen F, Hilts M and Bäck S A 2010 RapidArc treatment verification in 3D using polymer gel dosimetry and Monte Carlo simulation *Phys. Med. Biol.* **55** 4885-98

Chang K H et al 2016 Development of a 3D optical scanner for evaluating patient-specific dose distributions *Phys. Med.* **31** 553 - 559

Chisholm K, Miles D, Rankine L and Oldham M 2015 Investigations into the feasibility of optical-CT 3D dosimetry with minimal use of refractively matched fluids *Med. Phys.* **42** 2607-2614

Chu K C, Jordan K J, Battista J J, Van Dyk J and Rutt B K 2000 Polyvinyl alcohol-Fricke hydrogel and cryogel: two new gel dosimetry systems with low Fe+3 diffusion *Phys. Med. Biol.* **45** 955–69

Davies J B, Bosi S G, Baldock C 2013 Dosimetry aspects of a non-diffusing genipin-gelatin gel *Rad. Phys. Chem.* **83** 19-27

Day M J and Stein G 1950 Chemical effects of ionizing radiation in some gels *Nature* **166** 146-147

De Deene Y, De Wagter C, Van Duyse B, Derycke S, De Neve W, Achten E 1998 Three-dimensional dosimetry using polymer gel and magnetic resonance imaging applied to the verification of conformal radiation therapy in head-and-neck cancer *Radiother. Oncol.* **48**(3) 283-291

De Deene Y, De Wagter C, De Neve W and Achten E 2000a Artifacts in multi-echo T2 imaging for high-precision gel dosimetry: I. Analysis and compensation of eddy currents *Phys. Med. Biol.* **45** 1807–23

De Deene Y, DeWagter C and De Neve W 2000b Artifacts in multi-echo T2 imaging for high-precision gel dosimetry: II. Analysis of B1 field inhomogeneity *Phys. Med. Biol.* **45** 1825–39

De Deene Y, De Wagter C, Van Duyse B, Derycke S, Mersseman B, De Gersem W, Voet T, Achten E, De Neve W 2000c Validation of MR-based polymer gel dosimetry as a preclinical three-dimensional verification tool in conformal radiotherapy *Magn Reson Med.* **43**(1) 116-25

De Deene Y and De Wagter C 2001 Artifacts in multi-echo T2 imaging for high-precision gel dosimetry: III. Effects of temperature drift during scanning *Phys. Med. Biol.* **46** 2697–711

De Deene Y, Hurley C, Venning A, Vergote K, Mather M, Healy B J and Baldock C 2002 A basic study of some normoxic polymer gel dosimeters *Phys. Med. Biol.* **47** 3441–3463

De Deene Y, Vergote K, Claeys C and De Wagter C 2006 The fundamental radiation properties of normoxic polymer gel dosimeters: a comparison between a methacrylic acid based gel and acrylamide based gels *Phys. Med. Biol.* **51** 653–673

De Deene Y, Pittomvils G and Visalatchi S 2007 The influence of cooling rate on the accuracy of normoxic polymer gel dosimeters *Phys. Med. Biol.* **52** 2719–2728

De Deene Y 2013 How to scan polymer gels with MRI? *J. Phys.: Conf. Ser.* **444** 012003

De Deene Y, Skyt P S, Hill R and Booth J T 2015 FlexyDos3D: a deformable anthropomorphic 3D radiation dosimeter: radiation properties *Phys. Med. Biol.* **60** 1543–63

De Deene Y 2015 Dual wavelength optical CT scanning of anthropomorphic shaped 3D dosimeters *J. Phys.: Conf. Ser.* **573** 012058

DeJean P, Senden R J, McAuley K B, Rogers M and Schreiner L J 2006 Initial Experience with a commercial cone beam CT unit for polymer gel dosimetry: I. optical dosimetry issues *J. Phys.: Conf. Ser.* **56** 179–82

Dekker K H, Battista J J and Jordan K J 2016 Stray light reduction in cone beam optical computed tomography: II. Reduction using a convergent light source *Phys. Med. Biol.* **61** 2910–25

Dekker K H, Battista J J and Jordan K J 2017 Scanning laser optical computed tomography system for large volume 3D dosimetry *Phys. Med. Biol.* **62** 2636–2657

De Wagter C 2004 The ideal dosimeter for intensity modulated radiation therapy (IMRT): What is required? *J. Phys.: Conf. Ser.* **3** 4-8

Doran S J, Koerkamp K K, Bero M A, Jenneson P, Morton E J and Gilboy W B 2001 A CCD-based optical CT scanner for high-resolution 3D imaging of radiation dose distributions: equipment specifications, optical simulations and preliminary results *Phys. Med. Biol.* **46** 3191-213

Doran S J and Yatigammana D N B 2012 Eliminating the need for refractive index matching in optical CT scanners for radiotherapy dosimetry: I. Concept and simulations *Phys. Med. Biol.* **57** 665–683

Doran S J 2013 How to perform an optical CT scan: an illustrated guide *J. Phys.: Conf. Ser.* **444** 012004

Doran S, Gorjiara T, Kacperek A, Adamovics J, Kuncic Z and Baldock C 2015 Issues involved in the quantitative 3D imaging of proton doses using optical CT and chemical dosimeters *Phys. Med. Biol.* **60** 709–726

DosGel'99 Schreiner L J 1999 Proceedings of the 1st International Workshop on Radiation Therapy Gel Dosimetry. Lexington, Kentucky. *Canadian Organisation of Medical Physicists*

DOSGEL 2001 Baldock C and De Deene Y 2001 Proceedings of the 2nd International Conference on Radiotherapy Gel Dosimetry. Brisbane, Qld. *Queensland University of Technology. Centre for Medical, Health and Environmental Physics*

DOSGEL 2004 De Deene Y and Baldock C 2004 Third International Conference on Radiotherapy Gel Dosimetry *J. Phys.: Conf. Ser.* **3**

DOSGEL 2006 Schreiner L J 2006 4th International Conference on 3D Radiotherapy Gel Dosimetry *J. Phys.: Conf. Ser.* **56**

DOSGEL 2008 Maris T G and Pappas E 2009 5th International Conference on 3D Radiotherapy Gel Dosimetry *J. Phys.: Conf. Ser.* **164**

Feldkamp L A, Davis L C and Kress J W 1984 Practical cone-beam algorithm *J. Opt. Soc. Am. A/Vol.* 1 **6** 612-619

Fong P M, Keil D C, Does M D and Gore J C 2001 Polymer gels for magnetic resonance imaging of radiation dose distributions at normal room atmosphere *Phys. Med. Biol.* **46** 3105–3113

Fricke H and Morse S 1927 The chemical action of Roentgen rays on dilute ferrosulphate solutions as a measure of dose *Am. J. Roent. Radium Ther. Nucl. Med.* **18** 430-432

Glaser A K, Davis S C, Voigt W H, Zhang R, Pogue B W and Gladstone D J 2013a Projection imaging of photon beams using Cerenkov-excited fluorescence *Phys. Med. Biol.* **58** 601–19

Glaser A K, Voigt W H A, Davis S C, Zhang R X, Gladstone D J and Pogue B W 2013b 3D Cerenkov tomography of energy deposition from ionizing radiation beams *Opt. Lett.* **38** 634–6

Glaser A K, Andreozzi J M, Zhang R, Pogue B W and Gladstone D J 2015 Optical cone beam tomography of Cherenkov-mediated signals for fast 3D dosimetry of x-ray photon beams in water *Med. Phys.* **42** 4127-4136

Gore J C, Kang Y S and Schulz R J 1984 Measurement of radiation dose distributions by nuclear magnetic resonance (NMR) imaging *Phys. Med. Biol.* **29** 1189-97

Goulet M, Rilling M, Gingras L, Beddar S, Beaulieu L and Archambault L 2014 Novel, full 3D scintillation dosimetry using a static plenoptic camera *Med. Phys.* **41** 082101 1‑13

Guo P, Adamovics J, and Oldham M 2006 A practical three-dimensional dosimetry system for radiation therapy *Med. Phys.* **33(10)** 3962–3972

Gupta B L, Bhat R M, Gomathy K R and Susheela B 1978 Radiation Chemistry of the Ferrous Sulfate-Benzoic Acid-Xylenol Orange System *Radiation Research* **75(2)** 269-277

Hilts M, Audet C, Duzenli C and Jirasek A 2000 Polymer gel dosimetry using x-ray computed tomography: a feasibility study *Phys. Med. Biol.* **45** 2559–71

Hilts M, Jirasek A and Duzenli C 2005 Technical considerations for implementation of x-ray CT polymer gel dosimetry *Phys. Med. Biol.* **50** 1727–1745

Hilts M and Jirasek A 2008 Adaptive mean filtering for noise reduction in CT polymer gel dosimetry *Med. Phys.* **35** 344-355

Høye E M, Balling P, Yates E S, Muren L P, Petersen J B B and Skyt P S 2015 Eliminating the dose-rate effect in a radiochromic silicone-based 3D dosimeter *Phys. Med. Biol.* **60** 5557–5570
IC3DDose 2010 Oldham M 2010 6th International Conference on 3D Radiation Dosimetry *J. Phys.: Conf. Ser.* **250**

Hui C, Robertson D and Beddar S 2014 3D reconstruction of scintillation light emission from proton pencil beams using limited viewing angles - a simulation study *Phys. Med. Biol.* **59** 4477-92

IC3DDose 2012 Thwaites D and Baldock C 2013 7th International Conference on 3D Radiation Dosimetry (IC3DDose) *J. Phys.: Conf. Ser.* **444**

IC3DDose 2014 Olsson L E, Bäck S and Ceberg S 2015 8th International Conference on 3D Radiation Dosimetry (IC3DDose) *J. Phys.: Conf. Ser.* **573**

International Atomic Energy Agency (2016) Accuracy Requirements and Uncertainties in Radiotherapy, *IAEA Human Health Series No.* **31**, Vienna, Austria

International Commission on Radiation Units and Measurements (1976) Determination of Absorbed Dose in a Patient Irradiated by Beams of X or Gamma Rays in Radiotherapy Procedures, *ICRU Rep.* **24**, Bethesda, MD

Islam K T, Dempsey J F, Ranade M K, Maryanski M J and Low D A 2003 Initial evaluation of commercial optical CT-based 3D gel dosimeter *Med. Phys.* **30** 2159-68

Jackson J, Juang T, Adamovics J and Oldham M 2015 An investigation of PRESAGE 3D dosimetry for IMRT and VMAT radiation therapy treatment verification *Phys. Med. Biol.* **60** 2217-2230

Jirasek A, Carrick J and Hilts M 2012 An x-ray CT polymer gel dosimetry prototype: I. Remnant artefact removal *Phys. Med. Biol.* **57** 3137–3153

Jordan K 2008 Zero diffusion radiochromic genipin–gelatin dosimeter *Med. Phys.* **35** 3413

Jordan K and Avvakumov N 2009 Radiochromic leuco dye micelle hydrogels: I. Initial investigation *Phys. Med. Biol.* **54** 6773–6789

Jordan K 2009 Optical CT scanning of cross-linked radiochromic gel without cylinder wall *J. Phys.: Conf. Ser.* **164** 012029

Jordan K J, Pajak T M, Piontek C and Battista J J 2001 Optical cone beam tomography with low pressure sodium light *Queensland University of Technology, Conference Proceedings DOSGEL 2001* 166-168

Jordan K and Battista J 2006 Linearity and image uniformity of the Vista optical CT scanner *J. Phys.: Conf. Ser.* **56** 217–20

Juang T, Das S, Adamovics J, Benning R and Mark Oldham 2013 On the Need for Comprehensive Validation of Deformable Image Registration, Investigated With a Novel 3-Dimensional Deformable Dosimeter *Int. J. Radiation. Oncol. Biol. Phys.* **87** 414-421

Kakakhel M B, Kairn T, Kenny J and Trapp J V 2011 Improved image quality for x-ray CT imaging of gel dosimeters *Med. Phys.* **38** 5130–5

Kelly R G, Jordan K J and Battista J J 1998 Optical CT reconstruction of 3D dose distributions using the ferrous-benzoic-xylenol (FBX) gel dosimeter *Med. Phys.* **25** 1741-50

Klawikowski S J, Yang J N, Adamovics J and Geoffrey S Ibbott G S 2014 PRESAGE 3D dosimetry accurately measures Gamma Knife output factors *Phys. Med. Biol.* **59** N211–N220

Kroll F, Pawelke J and Karsch L 2013 Preliminary investigations on the determination of three dimensional dose distributions using scintillator blocks and optical tomography *Med. Phys.* **40** 082104

Kron T, Lehmann J and Greer P B 2016 Dosimetry of ionising radiation in modern radiation oncology *Phys. Med. Biol.* **61** R167–205

Krstajic N and Doran S J 2006 Focusing optics of a parallel beam CCD optical tomography apparatus for 3D radiation gel dosimetry *Phys. Med. Biol.* **51** 2055–75

Krstajic N and Doran S J 2007a Characterization of a parallel-beam CCD optical-CT apparatus for 3D radiation dosimetry *Phys. Med. Biol.* **52** 3693–3713

Krstajic N and Doran S J 2007b Fast laser scanning optical-CT apparatus for 3D radiation dosimetry *Phys. Med. Biol.* **52** N257–N263

Lin M-H, Huang T-C, Kao M-J, Wu J, Chen C-L, Wu T-W 2009 Three-dimensional dosimetry in brachytherapy: A MAGAT study *Appl. Rad. Isot.* **67** 1432-1437

Ma L, Kjall P, Novotny J, Nordstrom H, Johansson J and Verhey L 2009 A simple and effective method for validation and measurement of collimator output factors for Leksell Gamma Knife Perfexion *Phys. Med. Biol.* **54** 3897–907

Manjappa R, Makki S S, Kumar R, Vasu R M and Kanhirodan R 2016 Fully 3D refraction correction dosimetry system *Phys. Med. Biol.* **61** 1722-1737

Maryanski M J, Gore J C, Kennan R P and Schulz R J 1993 NMR relaxation enhancement in gels polymerized and cross-linked by ionizing radiation: a new approach to 3D dosimetry by *MRI Magn. Reson. Imaging* **11** 253–258

Maryanski M J, Schulz R J, Ibbott G S, Gatenby J C, Xie J, Horton D and Gore J C 1994 Magnetic resonance imaging of radiation dose distributions using a polymer-gel dosimeter *Phys. Med. Biol.* **39** 1437–1455

Maryanski M J, Zastavker Y Z and Gore J C 1996 Radiation dose distributions in three dimensions from tomographic optical density scanning of polymer gels: II. Optical properties of the BANG polymer gel *Phys. Med. Biol.* **41** 2705–2717

Maryanski M J and Ranade M K 2001 Laser micro-beam CT scanning of dosimetry gels *Proc. of SPIE Int. Soc. Optic. Eng.* **4320** 764-767

Massillon-JL G, Minniti R, Mitch M G, Maryanski M J and Soares C G 2009 The use of gel dosimetry to measure the 3D dose distribution of a 90Sr/90Y intravascular brachytherapy seed *Phys. Med. Biol.* **54** 1661-72

Mather M L and Baldock C 2003 Ultrasound tomography imaging of radiation dose distributions in polymer gel dosimeters: preliminary study *Med. Phys.* **30** 2140–8

McCaw T J, Micka J A and DeWerd L A 2014 Development and characterization of a three-dimensional radiochromic film stack dosimeter for megavoltage photon beam dosimetry *Med. Phys.* **41** 052104

Mijnheer B, Beddar S, Izewska J and Reft C 2013 In vivo dosimetry in external beam radiotherapy *Med. Phys.* **40** 070903

Moutsatsos A, Karaiskos P, Petrokokkinos L, Sakelliou L, E. Pantelis, E. Georgiou, Torrens M and Seimenis I 2013 Assessment and characterization of the total geometric uncertainty in Gamma Knife radiosurgery using polymer gels *Med. Phys.* **40** 031704

Nasr A T, Alexander K M, Olding T, Schreiner L J and McAuley K B 2015 Leuco-crystal-violet micelle gel dosimeters: II. Recipe optimization and testing *Phys. Med. Biol.* **60** 4685–4704

Niu C J, Foltz W D, Velec M, Moseley J L, Al-Mayah A and Brock K K 2012 A novel technique to enable experimental validation of deformable dose accumulation *Med. Phys.* **39** 765-776

Oldham M, Siewerdsen J H, Shetty A and Jaffray D A 2001 High resolution gel-dosimetry by optical-CT and MR scanning *Med. Phys.* **28** 1436-45

Oldham M, Siewerdsen J H, Kumar S, Wong J and Jaffray D A 2003 Optical-CT gel-dosimetry. I: basic investigations *Med. Phys.* **30** 623-634

Oldham M and Kim L 2004 Optical-CT gel-dosimetry. II: Optical artifacts and geometrical distortion *Med. Phys.* **31** 1093-104

Oldham M, Sakhalkar H, Guo P and Adamovics J 2008 An investigation of the accuracy of an IMRT dose distribution using two- and three-dimensional dosimetry techniques *Med. Phys.* **35** 2072-2080

Oldham M 2015 Radiochromic 3D detectors *J. Phys. Conf. Ser*. **573** 012006

Olding T, Holmes O and Schreiner L J 2010a Cone beam optical computed tomography for gel dosimetry I: scanner characterization *Phys. Med. Biol.* **55** 2819-40

Olding T, Salomons G, Darko J and Schreiner L J 2010b A Practical Use for FXG Gel Dosimetry *J. Phys.: Conf. Ser.* **250** 012003

Olding T and Schreiner L J 2011 Cone beam optical computed tomography for gel dosimetry II: imaging protocols *Phys. Med. Biol.* **56** 1259-79

Olding T, Alexander K M, Jechel C, Nasr A T and Joshi C 2015 Delivery validation of VMAT stereotactic ablative body radiotherapy at commissioning *J. Phys.: Conf. Ser.* **573** 012019

Olsson L E, Westrin B A, Fransson A and Nordell B 1992 Diffusion of ferric ions in agarose dosimeter gels *Phys. Med. Biol.* **37(12)** 2243-2252

Palmer A L, Di Pietro P, Alobaidli S, Issa F, Doran S, and Bradley D and Nisbet A 2013 Comparison of methods for the measurement of radiation dose distributions in high dose rate (HDR) brachytherapy: Ge-doped optical fiber, EBT3 Gafchromic film, and PRESAGE radiochromic plastic *Med. Phys.* **40** 061707

Penev K I and Mequanint K 2013 Controlling sensitivity and stability of ferrous–xylenol orange–gelatin 3D gel dosimeters by doping with phenanthroline-type ligands and glyoxal *Phys. Med. Biol.* **58** 1823–1838

Qian X, Adamovics J and Wuu CS 2013 Performance of an improved first generation optical CT scanner for 3D dosimetry *Phys. Med. Biol.* **58** N321–N331

Rae W I D et al 1996 Chelator effect on ion diffusion in ferrous-sulphate-doped gelatin gel dosimeters as analysed by MRI *Med. Phys.* **23(1)** 15-23

Rankine L and Oldham M 2013 On the feasibility of optical-CT imaging in media of different refractive index *Med. Phys.* **40** 051701

Rankine L J et al 2017 Three-Dimensional Dosimetric Validation of a Magnetic Resonance Guided Intensity Modulated Radiation Therapy System *Int. J. Radiation Oncol. Biol. Phys.* **97** 1095-1104

Robertson D, Mirkovic D, Sahoo N and Beddar S 2013 Quenching correction for volumetric scintillation dosimetry of proton beams *Phys. Med. Biol.* **58** 261‑73

Sakhalkar H S and Oldham M 2008 Fast, high-resolution 3D dosimetry utilizing a novel optical-CT scanner incorporating tertiary telecentric collimation *Med. Phys.* **35** 101-111

Schreiner L J 1999 Gel dosimetry: Motivation and historical foundation *Canadian Organisation of Medical Physicists, Conference Proceedings DosGel99* 1-10

Sedaghat M, Bujold R and Lepage M 2011 Severe dose inaccuracies caused by an oxygen-antioxidant imbalance in normoxic polymer gel dosimeters *Phys. Med. Biol.* **56** 601–625

Senden R J, De Jean P, McAuley K B and Schreiner L J 2006 Polymer gel dosimeters with reduced toxicity: a preliminary investigation of the NMR and optical dose–response using different monomers *Phys. Med. Biol.* **51** 3301–3314

Shortt K R 2001 Fundamentals of Fricke Dosimetry *Queensland University of Technology, Conference Proceedings DOSGEL 2001* 10-14

Skyt P S, Petersen J B B, Yates E S, Poulsen P R, Ravkilde T L, Balling P and Muren L P 2013 Dosimetric verification of complex radiotherapy with a 3D optically based dosimetry system: Dose painting and target tracking *Acta Oncol.* **52** 1445-50

Smith S T et al 2015 Technical Note: Preliminary investigations into the use of a functionalised polymer to reduce diffusion in Fricke gel dosimeters *Med. Phys.* **42(12)** 6798-6803

Su Z, Lopatiuk-Tirpak O, Zeidan O, Sruprisan S I, Meeks S L, Slopsema R, Flampouri S and Li Z 2012 An experimental investigation into the effect of periodic motion on proton dosimetry using polymer gel dosimeters and a programmable motion platform *Phys. Med. Biol.* **57** 649–663

Tarte B J, Jardine P A, van Doorn T, Nitschke K N and Poulsen M G 1997 Development of a CCD array imaging system for measurement of dose distributions in doped agarose gels *Med. Phys.* **24** 1521–1525

Teng K, Gagliardi F, Alqathami M, Ackerly T, and Geso M 2014 Dose variations caused by setup errors in intracranial stereotactic radiotherapy: A PRESAGE study *Med. Dosim.* **39** 292-299

Thomas A and Oldham M 2010 Fast, large field-of-view, telecentric optical-CT scanning system for 3D radiochromic dosimetry Journal of Physics: Conference Series **250** 012007

Thomas A, Newton J, Adamovics J and Oldham M 2011 Commissioning and benchmarking a 3D dosimetry system for clinical use *Med. Phys.* **38** 4846-4857

Thomas A, Niebanck M, Juang T, Wang Z, and Oldham M 2013 A comprehensive investigation of the accuracy and reproducibility of a multitarget single isocenter VMAT radiosurgery technique *Med. Phys.* **40** 121725

Thwaites D I and Tuohy J B 2006 Back to the future: the history and development of the clinical linear accelerator *Phys. Med. Biol.* **51** R343–R362

Vandecasteele J and De Deene Y 2013a On the validity of 3D polymer gel dosimetry: III. MRI-related error sources *Phys. Med. Biol.* **58** 63–85

Vandecasteele J and De Deene Y 2013b Evaluation of radiochromic gel dosimetry and polymer gel dosimetry in a clinical dose verification *Phys. Med. Biol.* **58** 6241–6262

van Doorn T, Bhat M, Rutten T P, Tran T and Costanzo A 2005 A fast, high spatial resolution optical tomographic scanner for measurement of absorption in gel dosimetry *Australas. Phys. Eng. Sci. Med.* **28** 76-85

Wai P, Adamovics J, Krstajic N, Ismail A, Nisbet A and Doran S 2009 Dosimetry of the microSelectron-HDR Ir-192 source using PRESAGE and optical CT *Appl. Rad. Isot.* **67** 419-422

Wang Z, Thomas A, Newton J, Ibbott G, Deasy J and Oldham M 2010 Dose verification of stereotactic radiosurgery treatment for trigeminal neuralgia with presage 3D dosimetry system *J. Phys. Conf. Ser.* **250** 012058

Warman J M, Luthjens L H and de Haas M P 2011 High-energy radiation monitoring based on radio-fluorogenic co-polymerization II: fixed fluorescent images of collimated x-ray beams using an RFCP gel *Phys. Med. Biol.* **56** 1487–1508

Watanabe Y and Nakaguchi Y 2013 3D evaluation of 3DVH program using BANG3 polymer gel dosimeter *Med. Phys.* **40** 082101

Winfree A T, Caudle S, Chen G, McGuire P, and Szilagyi Z 1996 Quantitative optical tomography of chemical waves and their organizing centers *Chaos* **6** 617-626

Wolodzko J G, Marsden C and Appleby A 1999 CCD imaging for optical tomography of gel radiation dosemeters *Med. Phys.* **26** 2508–13

Wuu C-S and Xu Y 2006 Three-dimensional dose verification for intensity modulated radiation therapy using optical CT based polymer gel dosimetry *Med. Phys.* **33** 1412-1419

Xu Y, Wuu C S and Maryanski M J 2003 Performance of laser CT scanning of polymer gels as a tool for three dimensional dose verification *Med. Phys.* **30** 1426-1426

Yates E S, Balling P, Petersen J B, Christensen M N, Skyt P S, Bassler N, Kaiser F J and Muren L 2011 Characterization of the optical properties and stability of Presage following irradiation with photons and carbon ions *Acta Oncol.* **50** 829–34

Yeo U J, Taylor M L, Dunn L, Kron T, Smith R L and Franich R D 2012 A novel methodology for 3D deformable dosimetry *Med. Phys.* **39** 2203-2213

Zeidan O A, Sriprisan S I, Lopatiuk-Tirpak O, Kupelian P A, Meeks S L, Hsi W C, Li Z, Palta J R and Maryanski M J 2010 Dosimetric evaluation of a novel polymer gel dosimeter for proton therapy *Med. Phys.* **37** 2145–52

Zhao L, Newton J, Oldham M, Das I J, Cheng C-W and Adamovics J 2012 Feasibility of using PRESAGE for relative 3D dosimetry of small proton fields *Phys. Med. Biol.* **57** N431

Chapter 2

Initial investigations into a new optical CT scanner

2.1 Introduction

A new optical CT scanner design was sought to provide a more practical solution than those previously described for the verification of RT dose distributions in full 3D. The specific application targeted was the small dose distributions of SRS. The planning and delivery of dose to small cranial tumours requires the highest degree of spatial accuracy in photon based EBRT. Positioning uncertainty for point or even 2D detectors results in uncertainty in the dosimetry, since it is unclear which exact points of the dose distribution have been sampled. True 3D dosimetry provides the entire dose distribution, thus identifying spatial delivery accuracy and dose accuracy at all points.

Broad beam scanners appeared to be the state of the art around the time of 2010 due to the speed of data acquisition, however broad beam geometry presents challenges relating to optical scatter (De Jean *et al* 2006). Fast laser beam scanners had been described giving scan acquisition times comparable to those of broad beam scanners (Van Doorn *et al* 2005). A laser beam approach was therefore selected, giving likely advantages in inherent scatter rejection and a narrow bandwidth of He-Ne lasers to avoid preferential attenuation of different wavelengths in the dosimeter. He-Ne lasers can also have a small enough spot size to give suitable spatial resolution of less than 0.5 mm, without having to focus the beam using lenses. The laser used initially had a wavelength of 540 nm which was close to the peak dose response of FXG. To move the beam across the sample while generating adequate scan speed, a rotating mirror design was chosen (Van Doorn *et al* 2005).

Existing scanner designs used RI matching fluid baths to provide light ray paths through gel samples appropriate to the reconstruction algorithm. The requirement of a fluid bath was deemed to be a significant impediment in changing the perception of optical CT scanning being a specialised technique requiring knowledge in RI matching. In addition, RI fluid could be a source of optical artefacts due to particles in the fluid and RI inhomogeneities (Doran 2009). Lastly, RI fluid was considered too messy and time consuming to maintain. Thus a fluid-less design was sought.

The choice of dosimeter for the 3D dosimetry system influences the design of the optical scanning arrangement. In this case, the chosen dosimeter was a gel based radiochromic option. Radiochromic gels utilise optical absorption as the mechanism for optical attenuation and gel provides advantages of cheap ingredients and simplicity of preparation. Usually for gels, a rigid container is required to maintain the shape of the dosimeter, except where the dosimeter is intentionally deformable such as in dose deformation studies. Since a plastic structure to contain the gel was a requirement for this work, it would be desirable to use the container as the main optical lens if possible. This would avoid additional optical components that add cost and increase the number of optical interfaces. Minimising the number of interfaces in the imaging path helps to reduce the potential effects of inter-reflections, alignment issues and contaminant particles and marks on surfaces.

The major design problem was to simplify the arrangement of lenses to provide parallel light ray paths through gel samples and avoid the use of a RI matching fluid bath. Parallel rays are required for straightforward tomographic reconstruction using the Radon transform. A previously developed scanner was noted to have used the gel container as the lens (Maryanski and Ranade 2001), although performance was severely limited by projection data acquisition of only the central 1/3 of gel diameter.

Alternative options were investigated using simulations of light ray paths and varying the dimensions of the gel cylindrical container. It was anticipated that a greater extent of light ray collection (than 1/3 of the gel diameter) could be achieved with a single point (large area) photodiode detector. Ray tracing using first principles was adopted to ensure there were no approximations of any form that could affect the accuracy of the calculated ray paths.

2.2 Ray tracing calculations

A set of equations were developed to propagate light rays from a fixed point representing the rotation centre of a rotating mirror, through the 4 interfaces of a gel filled plastic cylinder, converging to a detection point. This is shown schematically in figure 2.1. An example of the equations and refractive indices used to calculate ray paths is given in Appendix A. The RI value for PMMA was obtained from material specifications and the FXG (4 % gelatin) RI was measured in previous unpublished work with an Abbe refractometer at 589 nm. Snell's Law was used to give the angles of refraction, and geometry provided the intersection points at each of the interfaces. Numerical solutions for ray paths were obtained while varying the cylinder ID and distance from rotating mirror to the cylinder. The results for a standard 3 mm wall thickness container with 76 mm OD as used by Maryanski and Ranade (2001) showed that close to 50 % of the central rays would be within 0.1 mm of parallel at the gel centre. This could be achieved by decreasing the mirror to cylinder distance such that rays nearer to the centre would be compromised with up to 0.1 mm deviation from parallel to then provide additional outer rays for collection. Results illustrating this were included in the paper of Chapter 3 (section 3.1) and figure 2.2(a) herein.

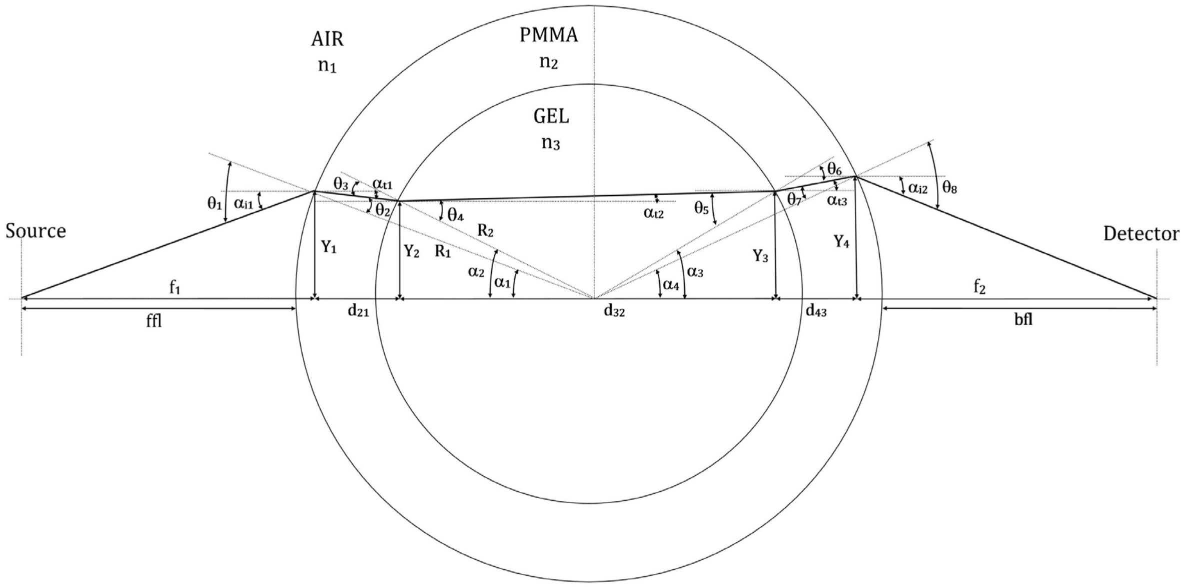

Figure 2.1. Schematic diagram with variables used for ray tracing calculations (refer to Appendix A for example). A light ray originating at the left (source) is refracted as it passes through a gel filled cylinder in air. The light rays are required to be close to parallel when passing through the gel and converge to a point for collection by a photodiode detector.

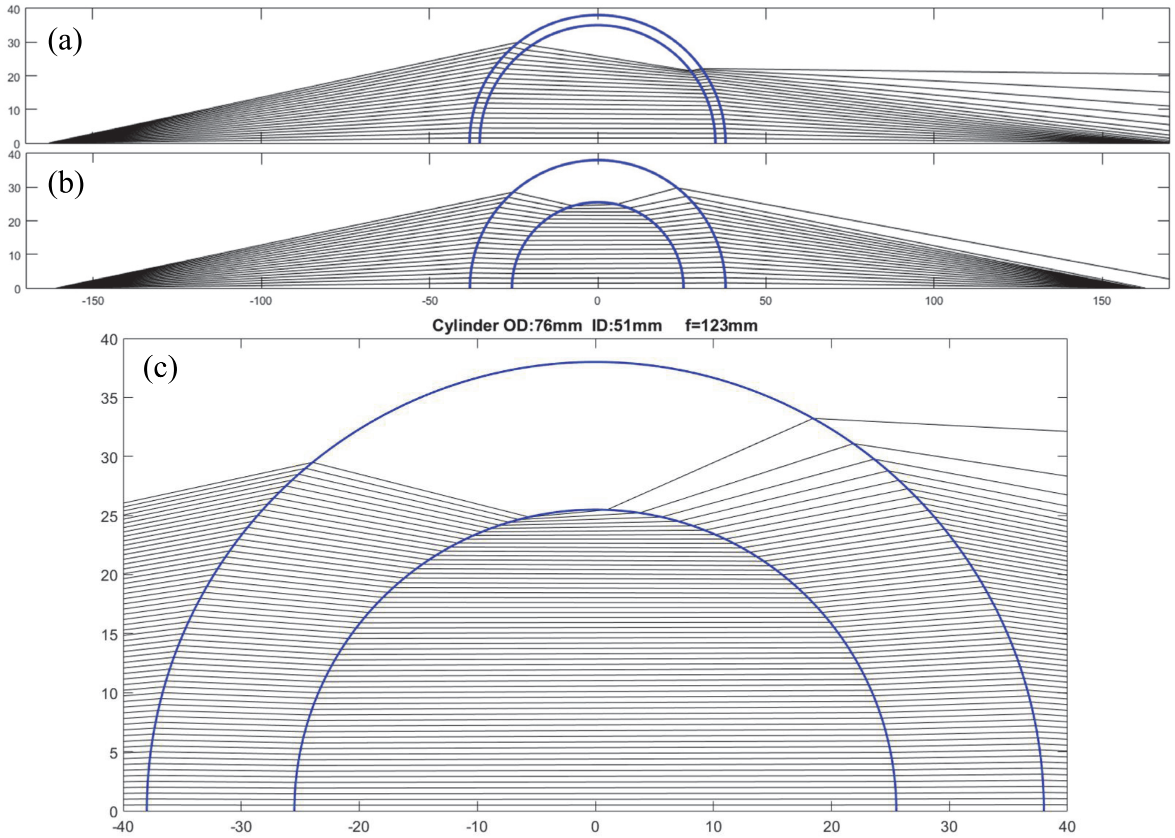

Figure 2.2. Ray tracing calculations for gel filled PMMA cylinders in air. **(a)** 76 mm OD, 70 mm ID cylinder. **(b)** 76 mm OD, 51 mm ID cylinder. **(c)** Magnified view of (b). All axes are distances in mm.

It was discovered that when the cylinder ID was reduced there were additional parallel rays that could be collected by the detector. Figure 2.2 illustrates the ray paths and further details are given in the paper of Chapter 3 (section 3.1).

It was found that a 76 mm OD, 51 mm ID PMMA cylinder would provide projection data within 0.1 mm of parallel at the gel centre for around 90 % of the gel diameter. Prior to the manufacture of such a cylinder, the ray tracing calculation methodology was verified using a readily available PMMA cylinder with 63 mm OD and 50 mm ID. Ray tracing calculations were made for the cylinder filled with water and 2 different distances from the rotating mirror to the cylinder. Measurements were made of ray position in the water at the cylinder centre for different positions laterally off the central ray axis (ie. x = 0 and y = 0 to 25 mm in figure 2.3). Ray positions as a function of Y_1 (figure 2.1) were obtained by a metal plate drilled with 1 mm holes corresponding to Y_1 distances 5, 10, 15, 20 and 25 mm. The ray positions in the water were measured using a target mounted on a micrometer stage. Results are shown in figure 2.3(a) for 104 mm and 81.5 mm mirror to cylinder surface distances. These results confirmed the validity of the ray tracing calculations. When the ideal cylinder of 76 mm OD and 51 mm ID had been manufactured, the ray position measurements were repeated with results as shown in figure 2.3(b). Calculated ray positions in gel were also shown in figure 2.3(b), illustrating the small differences compared to water.

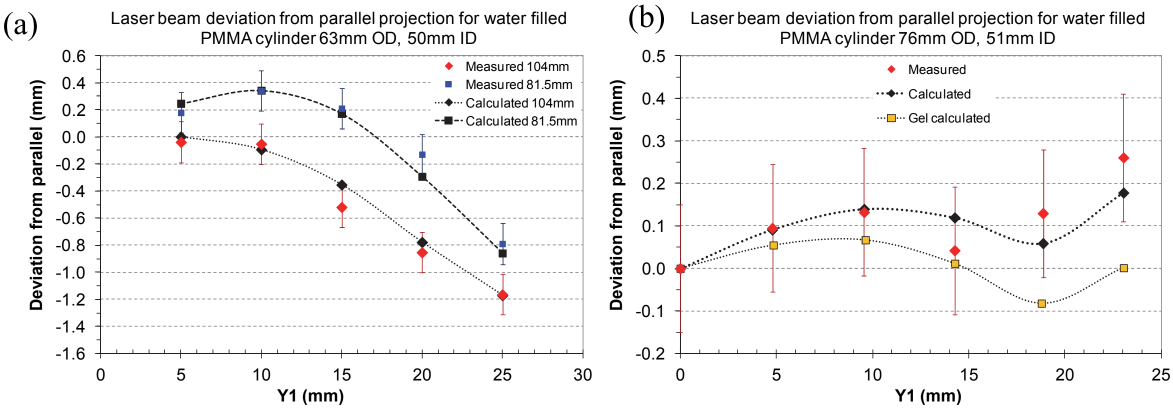

Figure 2.3. Measured and calculated 540 nm light ray positions in water filled PMMA cylinders. Results shown as deviations from parallel rays versus radial location. **(a)** 63 mm OD, 50 mm ID cylinder with mirror to cylinder distances of 104 mm and 81.5 mm. **(b)** 76 mm OD, 51 mm ID cylinder with 127 mm mirror to cylinder distance. Gel filled cylinder calculated paths shown for reference.

The sensitivity of ray positions to change in distance from mirror to cylinder, cylinder ID, cylinder refractive index and gel refractive index were examined by calculations. The results were included in the paper of Chapter 3 (section 3.1). It was found that the design was robust and it would take relatively large changes in the mentioned parameters to significantly change the ray paths from the intended. Even changing from the gel refractive index of 1.34 to water at 1.33 resulted in less than 0.2 mm changes of ray location.

2.3 Interface reflections

With a cylinder in air as described in section 2.2, angles of incidence range from 0° up to about 60° at the air to PMMA interfaces. It was noted that light transmission would vary significantly due to reflection losses. It was also noted that the losses are light polarisation dependent. To understand the consequences of differing polarisations and the extent of losses, calculations were conducted using Fresnel's equations to obtain reflection coefficients. The angles of incidence were obtained from ray tracing calculations and used to calculate the reflection coefficient at each interface. The coefficients were summed to give the total transmission loss for a given ray path from source to detector. It was found that p-polarised light would be the preferable polarisation orientation since the losses were less than s-polarised as the ray path approaches the gel periphery. Figure 2.4 shows the calculated transmission through a PMMA cylinder considering interface reflection losses only.

The lasers used for the optical CT were linearly polarised, and apart from investigations of reflection losses as a function of polarisation orientation, p-polarisation was always used. It was observed that an intermediate polarisation angle could be used to ‘flatten’ the appearance of the projection, however, the clearly defined reproducible condition of full p-polarisation was preferred for experimental setup reasons, given that the losses would be corrected. Figure 2.4 shows the ‘horns’ of the p-polarised transmission profile that can be reduced with intermediate polarisation, by moving towards the other extreme of s-polarisation.

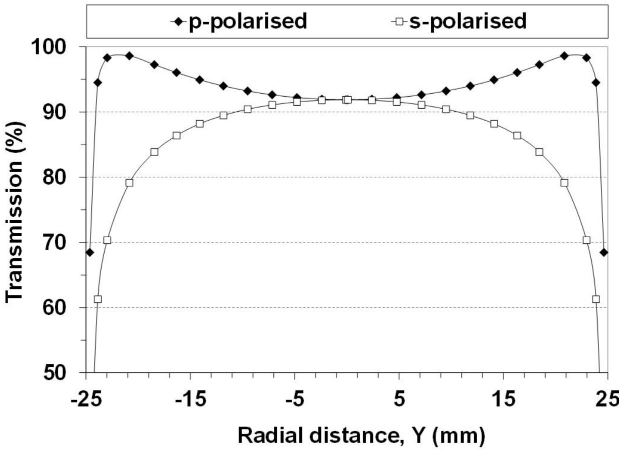

Figure 2.4. Calculated transmission through the gel filled 76/51 mm PMMA cylinder (with zero internal optical attenuation) as a function of radial distance in the gel sample. Data for p and s-polarised beams are shown, while intermediate polarisation gives a transmission profile within the bounds of the extremes of p and s-polarisation.

Reflection losses ranging from 1 to 8 % over a projection needed to be corrected. This was considered to be straightforward, since pre-irradiation scans would be required to provide a zero dose reference for the gel and would also result in cancellation of the differences in reflection losses in projection data. For the initial prototype and the work in Chapter 3, the pre-irradiation scan was averaged to provide a single reference projection to normalise all post-irradiation projections. The reason for this was to avoid noise, as the averaged projection was a smooth low noise curve.

2.4 Incomplete projection data and simulated reconstructions

The ray tracing results indicated that close to 90 % of the gel diameter would be imaged, giving truncated projections with 5 % missing at each end. The effects of missing projection data was previously shown by Jordan (1999). The missing data can cause a cupping artefact in reconstructions that propagates into the reconstructed volume. To address this issue a number of options were considered. Low optical attenuation in the sample periphery would help avoid artefacts, so ideas included: transparent non-gel material with gel refractive index, a transparent gel layer (ie. minus Fe & XO) and a more transparent gel. Increasing the wavelength from 540 nm green light to 594 nm yellow light would give a more transparent dosimeter, as shown by the absorption spectra of figure 2.5. The addition of a non-active layer of material with the refractive index of gel may have been achievable however, this would have introduced complications to gel or cylinder manufacturing.

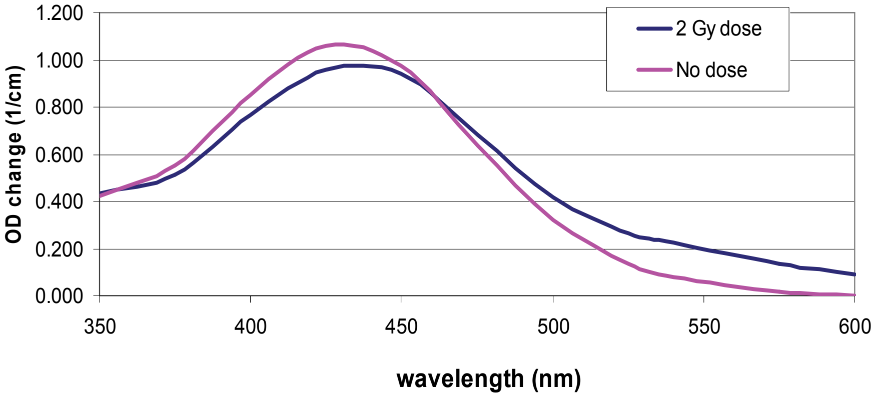

Figure 2.5. FXG absorption spectra showing a decrease of OD with increasing wavelength from 450 nm.

An alternative approach was considered by extrapolating the missing data. The thick walled precision cylinder gave a well-known gel diameter to extrapolate to. The extrapolated data was calculated by considering the gel pathlength for each ray in the extrapolated region and by using the optical attenuation coefficient of the last measured projection data point. The equation for this was given in the paper of Chapter 5 (equation (5), section 2.1.2). It was considered that curve fitting of some form may give better results for the case of dose gradients in the gel periphery however, the main aim was just to avoid the cupping artefact from propagating into the measured data.

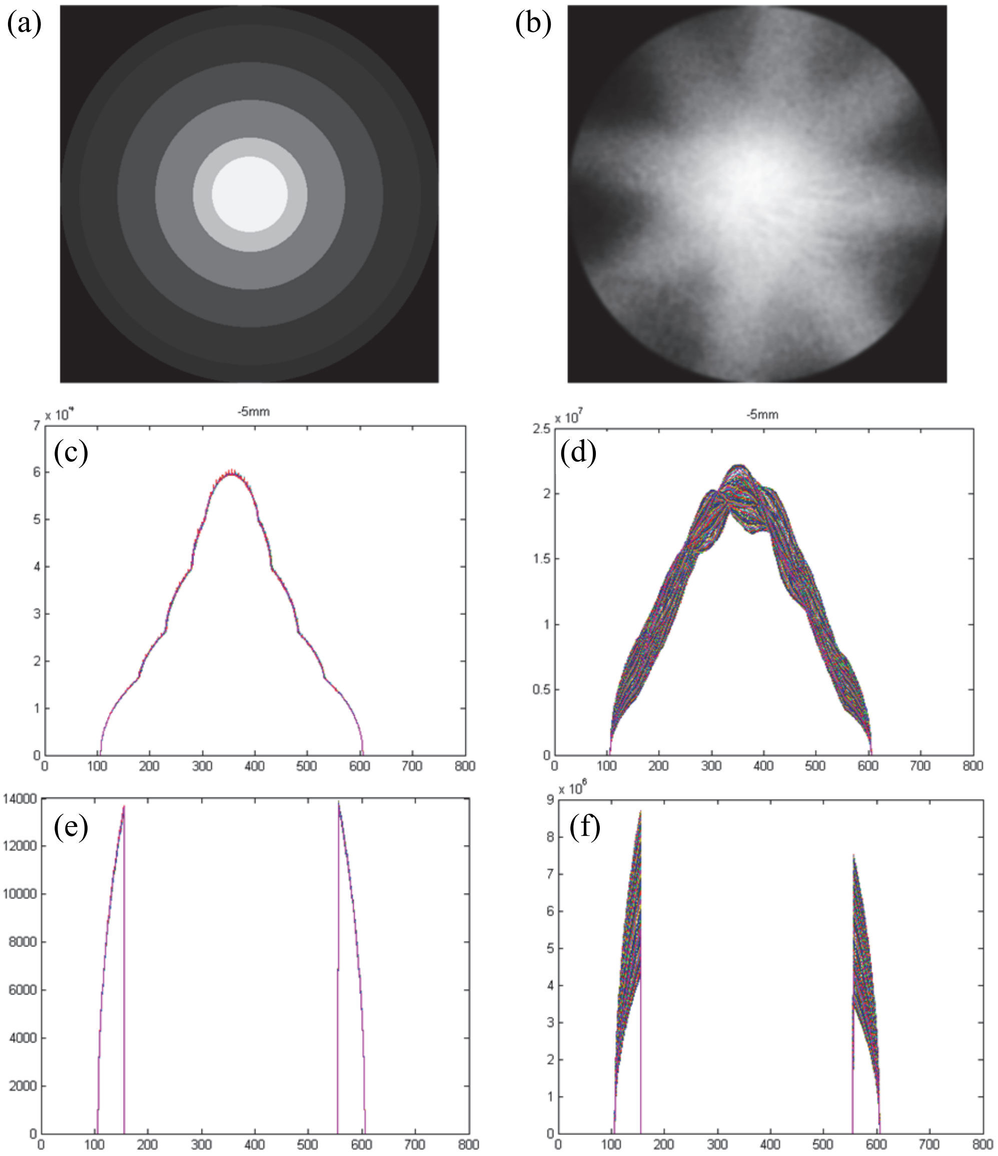

Figure 2.6. Test images used to test the extrapolation method to account for missing projection data. Arbitrary units used for optical attenuation and distances. **(a)** Test image with concentric circles of increasing levels. **(b)** Test image of a star dose pattern. **(c)** Optical attenuation projection data for image of (a) with 10 % of the total data extrapolated at each end. **(d)** Optical attenuation projection data for image of (b) with 10 % of the total data extrapolated at each end. **(e)** Extrapolated ends for (c). **(f)** Extrapolated ends for (d).

The proposed extrapolation method was tested by simulations. Test images were Radon transformed using Matlab (The Mathworks) to obtain projections that were then manipulated by truncating projection ends to varying degrees such as 5 and 10 % of the diameter. These projections were extrapolated back to the original diameter and inverse

Radon transformed to reconstruct the image. Examples of test images are shown in figure 2.6 with a simple artificial image and a semi-realistic image of a dose distribution with gradients in the periphery. Projection data and the extrapolated ends are shown for 288 projections. These examples illustrate extrapolation of 10 % of the diameter at each end, meaning 80 % of the projections' extent was 'measured'. In practice the acquired data should be around 90 % of the diameter, thus this test case had double the amount of extrapolated data.

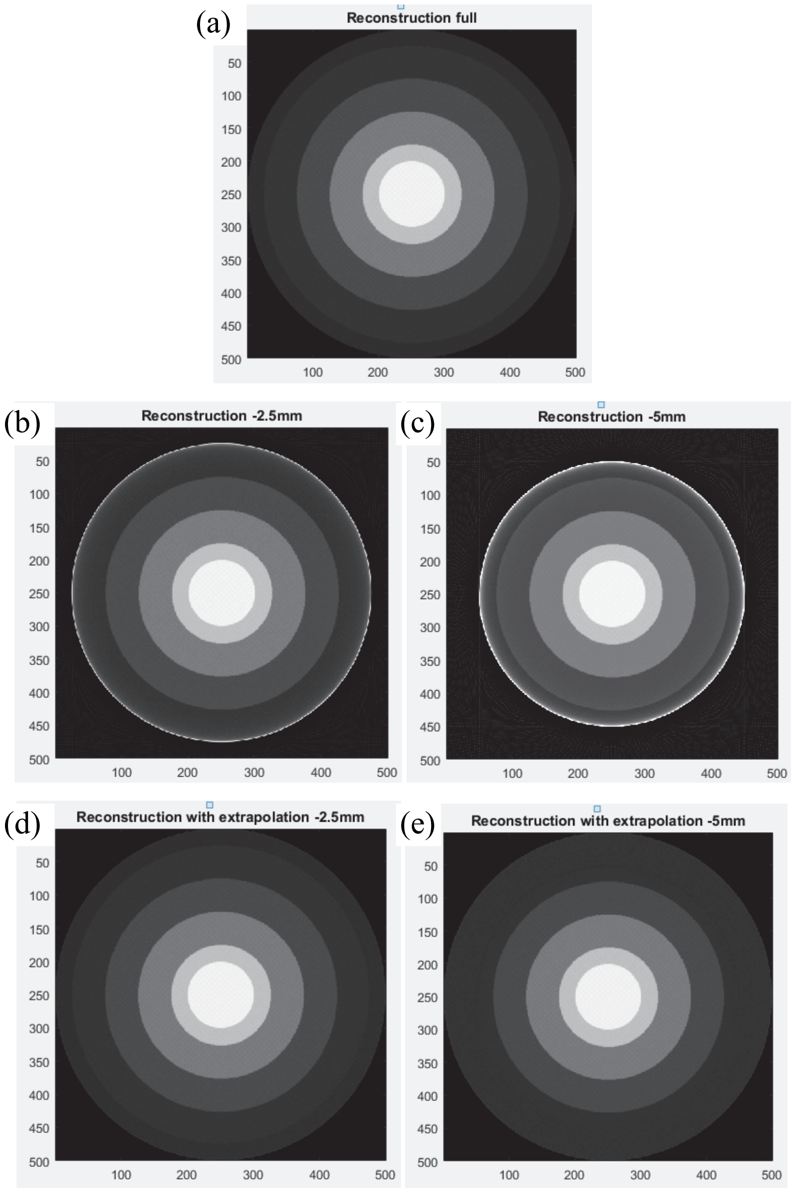

Figure 2.7. (a) Test Image reconstructed with full projections (true image). **(b)** Reconstruction with 5 % (2.5mm/50mm) missing projection data at each end. **(c)** Reconstruction with 10 % (5mm/50mm) missing projection data at each end. **(d)** Reconstruction with 5 % of missing projection data at each end and extrapolation applied. **(e)** Reconstruction with 10 % of missing projection data at each end and extrapolation applied.

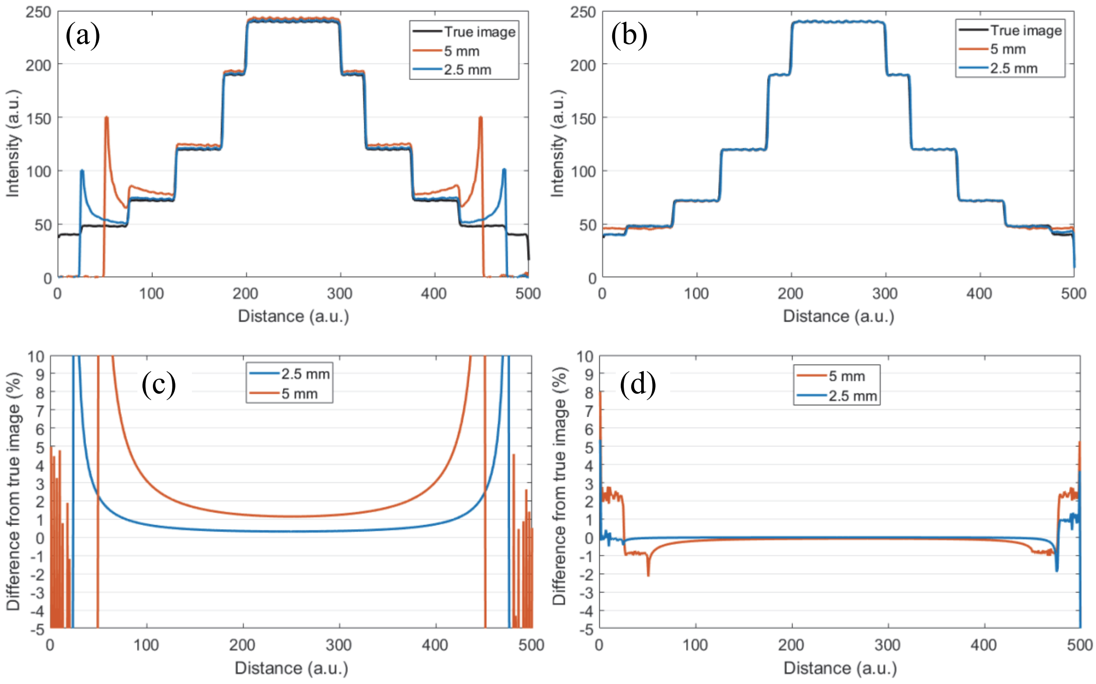

Figure 2.8. Line profiles from the images of figure 2.7. **(a)** Profiles without extrapolation. **(b)** Profiles with extrapolation **(c)** Differences in profiles without extrapolation. **(d)** Differences in profiles with extrapolation.

The consequences of the extrapolation for reconstructed images were assessed by comparison of profiles across the reconstructed data and difference maps. Figures 2.7 and 2.8 show the improvements given by the extrapolation method. Without extrapolation, differences extend into the FOV, while the differences are small with extrapolation applied. Similar results were obtained for the star pattern with further details included in the paper of Chapter 3 (section 3.2).

2.5 Prototype scanner construction

The basis of the prototype scanner construction was from a previously designed fast laser beam optical CT scanner (van Doorn *et al* 2005). The existing rotating mirror was used but the remainder was redesigned. The optical design was developed from the ray tracing outlined in section 2.2. The light source and detector were replaced with a new photodiode with adjustable gain. The He-Ne laser was 540 nm green with random polarisation which would later be changed to 594 nm yellow polarised. The motion control for gel cylinder rotation and translation was programmed using National Instruments Labview software, which also controlled the detector data acquisition. This enabled reliable synchronisation of motion and data acquisition. A screenshot of the scanner user interface is given in figure 2.9. Further details of the components, a schematic diagram and photograph of the initial scanner prototype are given in the paper of Chapter 3 (section 2.2).

Slice distance 55 mm

Number of steps 1

Acquisition type
● Measurement scan
○ Reference scan

Slice distance 1 mm

Number of slices 55

Samples 450 Rate (S/sec) 300000

Slice 55

Distance 54 mm

Projection number 288

Projection number 20

Figure 2.9. Optical CT scanner user interface with manual translate/rotate motions, automated multi-slice acquisition and cuvette calibration acquisition sequence (partially visible). This was the later version with dual wavelength acquisition as used at the stage of development in Chapter 5. Display of raw projection data was used for prototype development to assist with troubleshooting and alterations. Two projections are shown in the screenshot of an unirradiated gel, the left is 594 nm and the other is 633 nm.

The sole optical lens component was the gel container that was custom made. Different plastics were considered and PMMA was selected by consideration of radiological, optical and mechanical properties. Together with the gel itself, the cylinder would form part of a dosimetry phantom, so ideally the plastic would be approximately water equivalent. This is desired to avoid the introduction of additional uncertainties in TPS dose calculations. For MV photon beam applications, Compton scatter is the dominant interaction and therefore, the electron density of the material is most important for a dosimetry phantom. PMMA has an electron density of 1.15 and physical density of 1.19, thus there is greater x-ray attenuation than the same physical thickness of water. In the application of comparing gel measurements to TPS calculated doses, the TPS uses x-ray CT scan data of the phantom, calibrated to relative electron densities to compute dose. This means that the PMMA inhomogeneity will be accounted for, depending on TPS modelling accuracy. Given PMMA is a well know material in dosimetric uses, and it forms a ‘shell’ that the MV beams pass through to the gel dosimeter, it was considered to be a suitable option for the gel cylinder. The other key properties of PMMA given that it would form a lens are optical clarity and the suitability for machining and polishing to customise the size and shape. It is also a readily available material of various sizes.

The first gel cylinder of the particular size of 76 mm OD, 51 mm ID was machined with a standard workshop lathe and finished with polishing compounds to give highly polished optical surfaces. Tolerances of 0.2 mm were used for the diameters and 0.05 mm for concentricity. A PMMA base plate for the cylinder was machined for an interference fit on the cylinder OD and a recess to reproducibly locate the cylinder on the scanner rotating mount.

Projection data was processed into matrices using Matlab and then normalised to pre-irradiation scan projections. The net transmission data was converted to attenuation and the missing projection ends were extrapolated. The inverse Radon transform function was used for tomographic reconstruction.

2.6 First tomographic reconstructions

Simple optically opaque objects with known dimensions were scanned to begin with. The rotating mirror was set to 36.2 revolutions/second. The data acquisition rate was 560k samples/second and this resulted in 0.097 mm/pixel in the gel sample. Acquisition time per slice was 8 seconds for 288 projections at 0.625 degree increments. These angular increments would give approximately 0.3 mm projection spacing at the periphery of the dosimeter, which was smaller than the spatial resolution of the system due to laser beam spot size. This was deemed adequate for scanning dose distributions since high spatial frequencies are not present as in other objects for imaging such as human anatomy with x-ray CT scanning. Artefacts due to aliasing are of lesser concern for the relatively smoothly varying image objects of dose distributions in gel.

Metal rods of known dimensions were scanned as shown in figure 2.10. Reconstructed slices of the rods provided immediate indication of the validity of the optical geometry. The spacing of the rods was accurately represented in the reconstructions to within 0.5 mm compared to direct measurements using digital calipers. Metal items do not provide ideal test objects for optical scanning since photon extinction artefacts result. Some streaking can be seen in figure 2.10 even though the image had windowing and levelling set to indicate the circular cross-sections of the rods.

Figure 2.10. Reconstruction of three 2.5 mm diameter metal rods, with 15 mm centre to centre spacing in water.

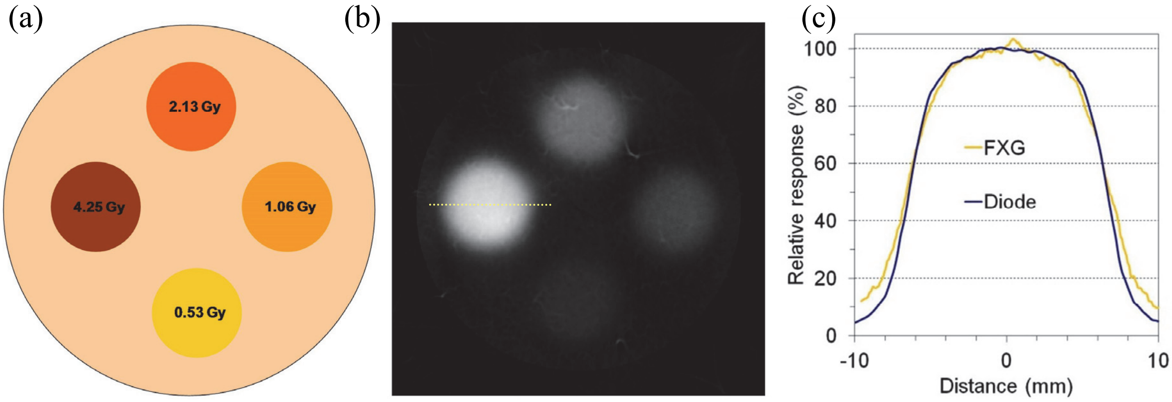

Figure 2.11. Irradiation of FXG with a 13 mm diameter cone and 6 MV beam at four dose levels. **(a)** Schematic diagram of the irradiation with doses. **(b)** Reconstructed slice of FXG with the four circular doses. **(c)** A relative profile through the high dose beam compared to a diode scan.

After accurate imaging of metal objects, an FXG sample was irradiated to provide a test object relevant to the intended imaging application. The FXG comprised 4 % gelatine, 25 mM H_2SO_4, 0.1 mM Fe^{2+} and 0.05 mM XO. The irradiation comprised four 6 MV beams collimated by circular cones, directed down the cylinder axis, with four dose levels as shown in figure 2.11. The circular beams appeared to be qualitatively well represented in the FXG reconstructions, with some artefacts due to particles in the gel. The mean reconstructed relative optical attenuation coefficients in a 2 mm diameter ROI at the centre of each beam were 100, 49, 26 and 12 %, compared to the relative doses delivered of 100, 50, 25 and 12.5 %. This indicated a near linear dose response for the FXG, which was consistent with cuvette studies of dose response also conducted. The shape of the beam profile was similar to a diode scan as shown in figure 2.11(c), with ferric ion diffusion evident. These results provided promising indications that the optical design of the scanner could provide accurate dosimetry.

Projection data for the reconstructed slice of figure 2.11(b) is shown in figure 2.12. Viewing the data in this way was useful in identifying scanning issues. For example the data shown had a problem in that the first projection was de-synchronised with the remainder of projections. This could be seen in figure 2.12(a) in what appears to be a 'stray' projection and the first vertical line of the sinogram of figure 2.12(b). Rectification was made by amendment of the motion control and data acquisition programming.

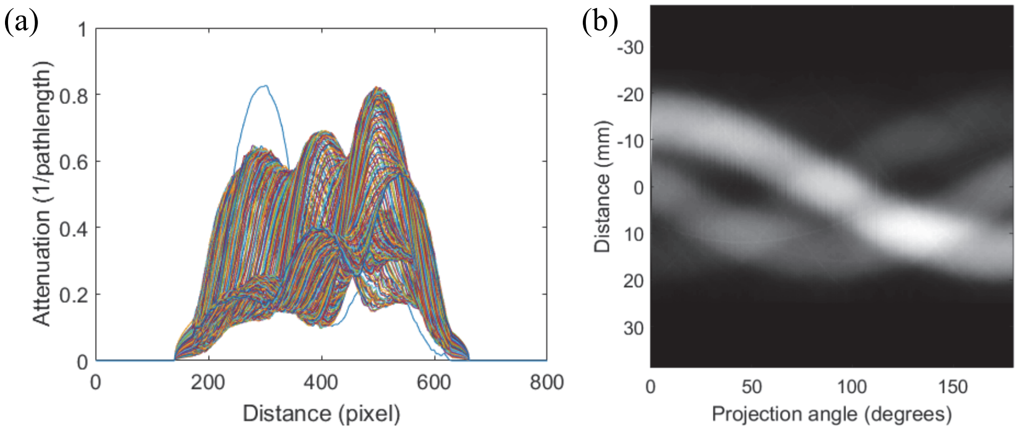

Figure 2.12. Projection data for the reconstructed slice shown in figure 2.11. **(a)** Line plot of all projections, and **(b)** in the form of a sinogram.

2.7 Conclusions

New optical geometry for optical CT scanning was devised with parallel ray paths through the gel sample, without the use of RI matching fluid. The gel cylinder forms the optical lens that provides parallel light rays. Optical ray tracing calculations were validated by measurements. Calculations yielded an optimal gel cylinder size with ID to OD ratio of 0.67 to give projection data to 90 % of the sample diameter. Extrapolation of the missing projection ends was investigated to avoid artefacts in the non-extrapolated FOV. A PMMA cylinder was machined to 76 mm OD and 51 mm ID and a prototype scanner was constructed.

The initial testing of the scanner using solid objects gave correct geometry of reconstructed images of the objects, within 0.5 mm. Imaging of FXG irradiated with beams of various doses indicated a linear change in optical attenuation with dose, and profiles across the beams were comparable to reference data. These early results indicated that the scanning approach was viable and the prototype scanner and processing code was operating satisfactorily. Further testing was conducted to demonstrate the proof of concept with results for distortion, spatial resolution, uniformity, noise and dose response as given in the following Chapter 3.

2.8 References

De Jean P, Senden R, McAuley, Rogers M and Schreiner L J 2006 Initial experience with a commercial cone beam optical CT unit for polymer gel dosimetry I: Optical dosimetry issues *J Phys: Conf Series* **56** 179-82

Doran S J 2009 The history and principles of optical computed tomography for scanning 3-D radiation dosimeters: 2008 update *J Phys: Conf Series* **164** 012020

Jordan K 1999 Developmental issues for optical CT and gel dosimetry, *Canadian Organisation of Medical Physicists, Conference Proceedings DosGel99* 91-97

Maryanski M J and Ranade M K 2001 Laser micro-beam CT scanning of dosimetry gels *Proc. SPIE* **4320** 764–7

Van Doorn T, Bhat M, Rutten T P, Tran T and Costanzo A 2005 A fast, high spatial resolution optical tomographic scanner for measurement of absorption in gel dosimetry *Australas. Phys. Eng. Sci. Med.* **28** 76–85

Chapter 3

Fluid-less optical CT scanner proof of concept

3.1 Introduction

Following the initial design, construction and preliminary testing, the prototype fluid-less optical CT scanner was set up with a 594 nm polarised yellow He-Ne laser. The 540 nm He-Ne laser used initially, was replaced with a 594 nm version to lower optical attenuation with only minor reduction of dose sensitivity. This reduces the detector dynamic range and may improve the SNR. Linear polarisation was useful to set the polarisation angle to verify and control reflection losses. The rotating mirror and detector distances were set to give the desired ray paths as determined from ray tracing calculations. Ray tracing calculations had been conducted with ranges of RIs, focal distances and cylinder ID/OD ratios. Data acquisition over a full 360° sample rotation was adopted since the redundant data provided improved reconstructions of the optically opaque metal objects by the averaging effect of having 2 projections for each view through the sample. To maintain the scan speed of 8 seconds per slice, the angular intervals were increased from 0.625° to 1.25°. This was considered adequate since the angular resolution gave approximately 0.5 mm spacing at the periphery of the non-extrapolated FOV, similar to the spatial resolution due to laser spot size. The laser spot size is the dominant influence on intrinsic spatial resolution. In the work presented in the publication following, the native pixel size of 0.1 mm was used to present raw data without any re-sampling or filtering. In later work, a lower spatial resolution was used to increase the SNR. An axial pixel size smaller than, but closer to, the laser spot size reduces the effects of stochastic noise while not degrading spatial resolution due to use of a pixel size greater than the intrinsic resolution.

A number of tests were devised to evaluate the imaging capabilities of the prototype scanner and give indication of the potential for accurate quantitative imaging. With unique optical geometry, spatial distortion was one of the first questions to be addressed, as to whether the reconstructed geometry was accurate. Spatial resolution was assessed, with particular interest in the most limiting factor. Uniformity and noise were assessed using a dosimeter uniform in axial slices to within 1 %. Optical artefacts can be quantified by uniformity and noise metrics to a degree, however often a qualitative evaluation is also useful in attempting to determine the source of artefacts. Finally a demonstration of the ability to reconstruct a dose pattern from an FXG gel sample was conducted and compared to commissioned TPS data. The FXG composition was: 4 % gelatine, 50 mM H_2SO_4, 0.3 mM Fe^{2+} and 0.05 mM XO.

For this initial study, single slice scanning had only been developed, with automated multi-slice scanning to be further developed. The motion control coding in LabView was a ‘ground up’ development without the use of a commercial motion control package. This approach provided financial benefits and freedom in customising a solution at the expense of greater developmental effort.

3.2 Research publication on the fluid-less scanner

The following research paper was published in Physics in Medicine and Biology in 2012.

Optical CT scanner for in-air readout of gels for external radiation beam 3D dosimetry

Daniel Ramm, Thomas P Rutten, Justin Shepherd and Eva Bezak

Physics in Medicine and Biology **57** (2012) 3853–3868

https://doi.org/10.1088/0031-9155/57/12/3853

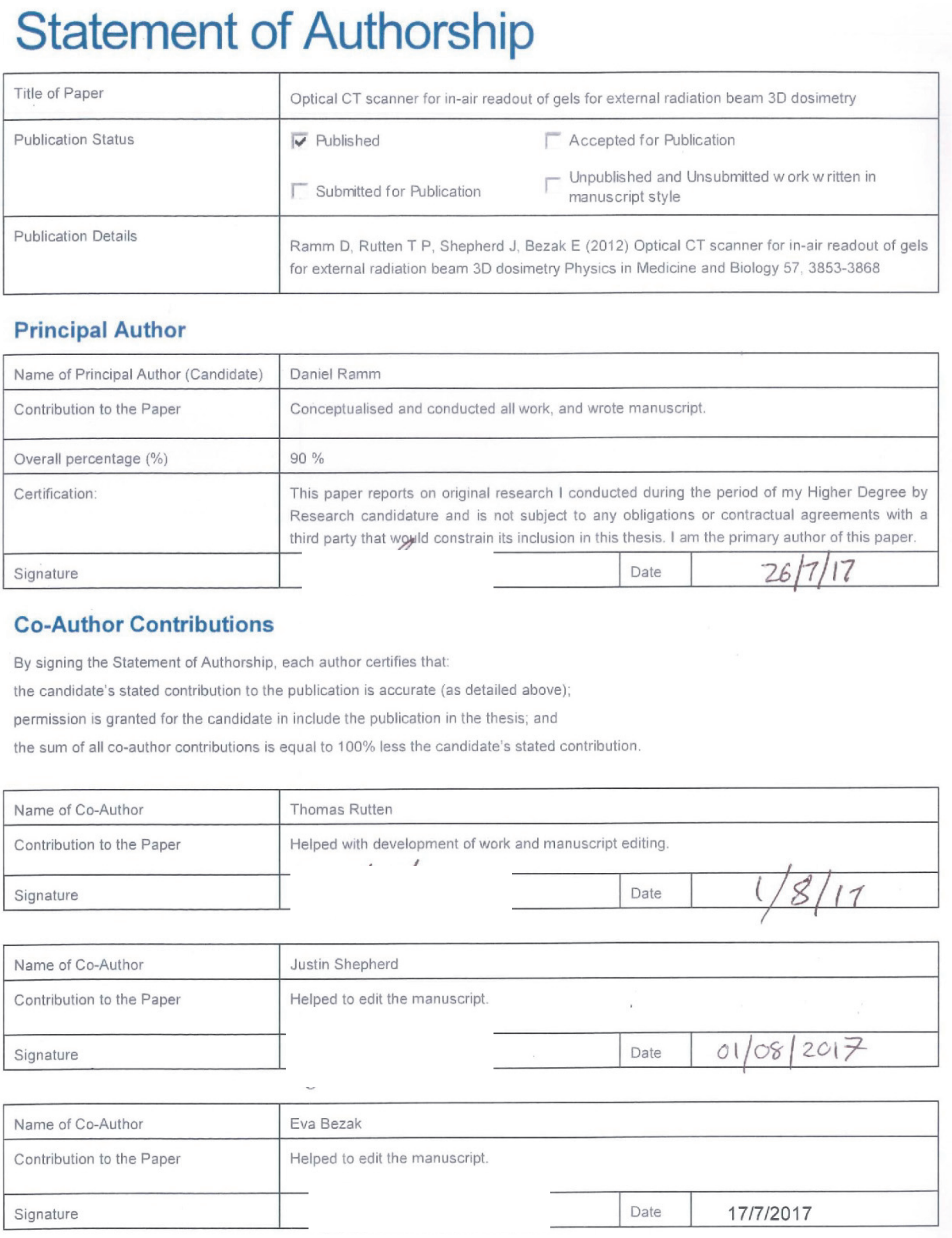

Statement of Authorship

Title of Paper	Optical CT scanner for in-air readout of gels for external radiation beam 3D dosimetry	
Publication Status	☑ Published ☐ Submitted for Publication	☐ Accepted for Publication ☐ Unpublished and Unsubmitted w ork w ritten in manuscript style
Publication Details	Ramm D, Rutten T P, Shepherd J, Bezak E (2012) Optical CT scanner for in-air readout of gels for external radiation beam 3D dosimetry Physics in Medicine and Biology 57, 3853-3868	

Principal Author

Name of Principal Author (Candidate)	Daniel Ramm		
Contribution to the Paper	Conceptualised and conducted all work, and wrote manuscript.		
Overall percentage (%)	90 %		
Certification:	This paper reports on original research I conducted during the period of my Higher Degree by Research candidature and is not subject to any obligations or contractual agreements with a third party that would constrain its inclusion in this thesis. I am the primary author of this paper.		
Signature		Date	26/7/17

Co-Author Contributions

By signing the Statement of Authorship, each author certifies that:

the candidate's stated contribution to the publication is accurate (as detailed above);

permission is granted for the candidate in include the publication in the thesis; and

the sum of all co-author contributions is equal to 100% less the candidate's stated contribution.

Name of Co-Author	Thomas Rutten		
Contribution to the Paper	Helped with development of work and manuscript editing.		
Signature		Date	1/8/17

Name of Co-Author	Justin Shepherd		
Contribution to the Paper	Helped to edit the manuscript.		
Signature		Date	01/08/2017

Name of Co-Author	Eva Bezak		
Contribution to the Paper	Helped to edit the manuscript.		
Signature		Date	17/7/2017

IOP PUBLISHING PHYSICS IN MEDICINE AND BIOLOGY

Phys. Med. Biol. **57** (2012) 3853–3868 doi:10.1088/0031-9155/57/12/3853

Optical CT scanner for in-air readout of gels for external radiation beam 3D dosimetry

Daniel Ramm[1,2], **Thomas P Rutten**[1], **Justin Shepherd**[1] **and Eva Bezak**[1,2]

[1] Department of Medical Physics, Royal Adelaide Hospital Cancer Centre, South Australia, Australia
[2] School of Chemistry and Physics, University of Adelaide, South Australia, Australia

E-mail: daniel.ramm@health.sa.gov.au

Received 11 January 2012, in final form 5 April 2012
Published 30 May 2012
Online at stacks.iop.org/PMB/57/3853

Abstract
Optical CT scanners for a 3D readout of externally irradiated radiosensitive hydrogels currently require the use of a refractive index (RI) matching liquid bath to obtain suitable optical ray paths through the gel sample to the detector. The requirement for a RI matching liquid bath has been negated by the design of a plastic cylindrical gel container that provides parallel beam geometry through the gel sample for the majority of the projection. The design method can be used for various hydrogels. Preliminary test results for the prototype laser beam scanner with ferrous xylenol-orange gel show geometric distortion of 0.2 mm maximum, spatial resolution limited to beam spot size of about 0.4 mm and 0.8% noise (1 SD) for a uniform irradiation. Reconstruction of a star pattern irradiated through the cylinder walls demonstrates the suitability for external beam applications. The extremely simple and cost-effective construction of this optical CT scanner, together with the simplicity of scanning gel samples without RI matching fluid increases the feasibility of using 3D gel dosimetry for clinical external beam dose verifications.

(Some figures may appear in colour only in the online journal)

1. Introduction

Development of 3D gel dosimetry has been progressing for more than two decades, striving to give high quality inherently 3D, near tissue equivalent, integrated dose measurement techniques (Baldock *et al* 2010). Some recent examples of the utilization of gel dosimetry in external beam radiotherapy include small field dosimetry for stereotactic radiosurgery (SRS) and stereotactic radiotherapy (Babic *et al* 2009), intensity modulated radiotherapy (IMRT) (Sakhalkar *et al* 2009) and volumetric modulated arc therapy (VMAT) (Ceberg *et al* 2010). These advanced treatment techniques can deliver increasingly modulated 3D dose distributions that would ideally be verified by more comprehensive means than the conventional point and 2D detectors. Reports on IMRT dosimetric verification (Low *et al* 2011, Mijnheer and Georg 2008) indicate the need for a 3D dosimetry verification method. Considering IMRT is well established in clinical use, 3D dosimetry is perhaps under-utilized. Doran (2009a) suggested further refinement of techniques and materials in gel dosimetry is required to allow more prevalent use in the clinical setting. Likely factors that limit the attractiveness for clinical use include the manufacture and handling of gel, and secondly, complicated and tedious readout techniques.

3D readout of gels using optical CT was proposed (Gore *et al* 1996) as a cheaper, dedicated alternative to MRI (Gore *et al* 1984). Optical CTs have been developed in varying forms: first generation laser beam scanning, fast laser beam scanning and parallel or cone beam scanners with area detectors, as reviewed recently (Doran 2009b). Laser beam scanners accept limited stray light and typically have slow scan times due to the scanning motions of the beam, while area detector scanners are generally quicker since all projections for a given sample angle of rotation are acquired simultaneously. Area detection introduces issues with stray light where scattering artefacts may result, particularly with polymer gels (Islam *et al* 2003). The so-called fast laser scanners incorporate the stray light rejection of the scanning laser beam while replacing laser translation with faster options such as a rotating mirror that fans the beam across the sample (Maryanski and Ranade 2001, van Doorn *et al* 2005).

A common aspect of the various optical CT scanner designs is a tank containing a refractive index (RI) matching fluid into which the gel sample is immersed. The matching fluid helps maintain the desired beam paths through the sample by minimizing refraction and reflection effects at the sample container and gel interfaces. An exception is the design of Maryanski and Ranade (2001) where a rotating mirror laser beam scanner used the cylindrical walls of the gel container to generate parallel beam paths through a central portion of the gel, without the use of a RI matching tank. This design has been utilized for the measurement of centrally localized brachytherapy source dose distributions (Wuu *et al* 2003, Massillon-JL *et al* 2009) and a central small Co^{60} field (Massillon-JL *et al* 2010). MGS Research Inc. (Madison, CT, USA) has commercialized the scanner as the DRYSCANNER. This scanner is typically not suited to external beam dosimetry since the projection data are limited to the central one-third of the gel sample which can lead to inaccurate reconstruction where there is significant optical attenuation in the regions of missing data. This is usually the case for external beam irradiation through the walls of the cylindrical gel container.

This paper presents the development of a gel dosimetry system aimed at being more accessible for routine use by designing a simple, robust and practical optical CT scanner. The prototype scanner presented here has overcome the cylindrical aberration effects that severely limit the projection data for a cylindrical gel container in air. This has been achieved by the use of a cylindrical gel container of specific dimensions and material, designed to give effectively parallel rays and allow at least 90% of the projection to be acquired. Removal of the need for a carefully maintained RI matching fluid tank provides an extremely simple scanner with a minimal number and complexity of optical components. The scanning process is as simple as placing the gel container on the scanner locating platform after wiping over the cylinder surface to remove any marks or dust. No knowledge, capability or time is required for accurate RI matching. No time is required for cleaning in the advent of dust or other contaminants in RI fluid or on tank walls. The importance of cleanliness and optimization of RI fluid were highlighted in a recent review by Doran (2010). A typical clinical radiotherapy facility may have less scope for the designation of an ideal clean room than a dedicated research laboratory type environment. Simplification of the scanning process may assist with the transition from the use of optical CT for research purposes in laboratory settings with experimental optics expertise, to more routine verification applications in clinical radiotherapy departments.

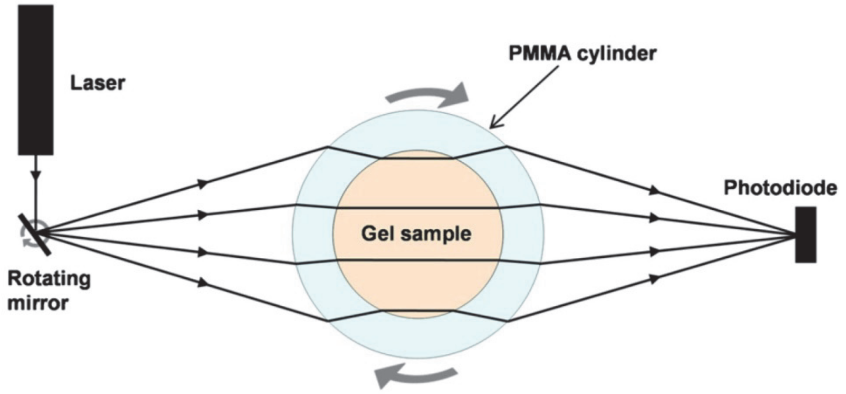

Figure 1. Schematic diagram of the scanner optics. A He–Ne 594 nm laser is fanned by a rotating mirror across a PMMA cylinder containing a gel sample, giving parallel beam geometry through the gel, and then converges at a silicon photodiode detector.

2. Materials and methods

2.1. Gel dosimeter

The type of gel selected for use should be matched to the capabilities of the scanner for best results (Lepage and Jordan 2010). The mechanism of object contrast generation in the dosimeter should be compatible with the scanner, and in this case either an optically absorbing or scattering gel would be suitable. The well-established ferrous xylenol-orange gelatine (FXG) dosimeter was selected for its favourable properties of optical attenuation by absorption, low cost, low toxicity, readily available raw materials, basic manufacturing, and known characteristics (Schreiner 2004, Babic *et al* 2008a). The use of an optically absorbing gel combined with a laser beam scanner means potential artefacts due to scattered light are minimized by both gel and scanner. The main drawback of ion diffusion leading to a blurred dose distribution can be minimized by avoiding prolonged irradiation times, fast scan acquisition conducted as soon as possible after irradiation, and diffusion correction methods (Babic *et al* 2008a). The formulation of FXG used in this work is similar to that of Babic *et al* (2009) and the dose threshold effect reported by Babic *et al* (2008b) for yellow lasers, around 590 nm, has been noted. Other hydrogels such as more stable radiochromic versions (Jordan 2010) or polymer types (Baldock *et al* 2010) may be preferable depending on the clinical treatment application (e.g. higher dose gradients such as SRS). However, for the purpose of this work in demonstrating the feasibility of the scanner design, FXG is sufficient.

2.2. Optical CT scanner design

Figure 1 schematically shows the scanner optical design. A laser beam is fanned by a rotating mirror across the PMMA (acrylic) cylindrical gel container that has a specific inner diameter (ID) to outer diameter (OD) ratio, which combined with the RI of gel inside, provides parallel beam paths through the gel sample. The rays then converge at the photodiode detector. The amount of projection acquired is limited by refraction and reflection as the beam approaches the edges. Edge effect issues are also present in the matching fluid bath designs and the significance depends on gel container size, thickness and material (refractive index), in addition to the RI of gel and bath fluid (Doran *et al* 2001). For the scanner described here, the amount of projection

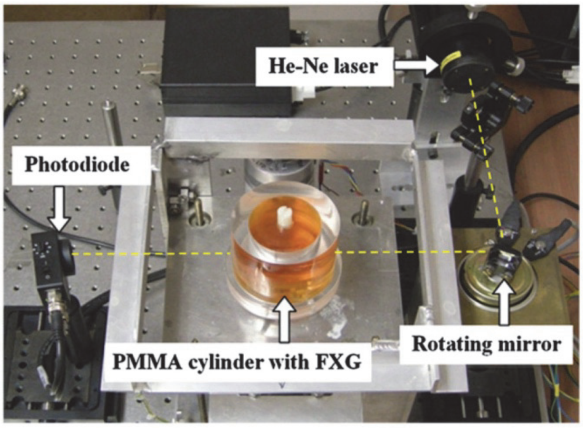

Figure 2. Photograph of the prototype scanner with the FXG filled cylinder in position. Laser beam path is illustrated by the dashed lines.

data affected by the edge effects (approx. 10%) is actually comparable to that of earlier reports of scanners with RI matching baths (Gore *et al* 1996, Kelly *et al* 1998, Oldham and Kim 2004). A correction is applied to the ends of the projection data to reduce the effects of incomplete data on backprojection as detailed in section 2.5.

2.3. Components of the scanner

Shown in figure 2 is the prototype scanner setup developed in this work. The He-Ne laser (Melles Griot model 25 LYP 173–230) provides a 594 nm linearly polarized beam of diameter 0.8 mm (1/e^2). While not at the peak response of FXG gel, the yellow wavelength was chosen to give reasonable sensitivity while minimizing the optical attenuation of un-irradiated FXG. This is beneficial for the signal-to-noise ratio of the transmitted beam on highly attenuating paths, which is particularly relevant for larger gel samples. The detector is a Thorlabs model PDA100A amplified silicon photodiode with 9.8 mm diameter and 600 kHz bandwidth on the gain setting (2) used. This detector was of sufficient size to capture the beam after passing through the cylinder for the whole projection. The temporal response was adequate to allow fast data acquisition of at least 0.8 ms per projection with 0.1 mm sample resolution. A reference detector to account for laser fluctuations has not been incorporated initially, but is a planned addition prior to future work on accuracy and precision of the scanner. A beam splitter was already located in the beam between the laser and rotating mirror to direct approximately 1% of the beam to a reference detector.

A continuously rotating mirror with a constant angular speed was used so that the data samples acquired per unit time could be easily related to the distance in the sample. The only other optical component in the beam path is the machined and polished cylindrical PMMA gel container which provided the desired beam geometry through the gel. For this prototype, a 76 mm OD gel cylinder was manufactured with an ID of 51 mm, with a tolerance of ±0.2 mm for the OD and ID.

Stepper motors providing the cylinder axial rotation and longitudinal translation were driven by LabVIEW (National Instruments) software, which also synchronously acquired 288 projections over a 360° sample rotation in approximately 8 s. A National Instruments model PCIe-6251 16 bit, 1.25 MS/s multifunction data acquisition card was used to control output signals and acquire the projection data. Data were processed with Matlab (The MathWorks) including backprojection reconstruction using the inbuilt Radon transform function.

2.4. Gel cylinder

The cylinder material needs to form a reliable optical component with suitable RI, surface finish, light transmission, dimensions and rigidity. Glass would meet the optical requirements; however, it is far from being water equivalent which is typically undesirable for a radiotherapy phantom. PMMA was selected since it is readily machined and polished, giving good optical properties, and has been commonly used in radiotherapy as an approximate water equivalent phantom. The cylinder OD was constrained to 76 mm to fit inside a SRS head phantom, while the ID was varied to give optimum beam paths.

In designing the cylinder, the effects of refraction and reflection as the light beam passes through the gel filled cylinder were considered separately. Beam paths due to refraction were calculated by ray tracing using Snell's law at each of the air to PMMA and PMMA to gel interfaces. This determined the parallelism of the beam path through the gel sample in an endeavour to achieve parallel beam geometry suitable for standard backprojection. The ray tracing calculations were conducted with various focal distances of the light source (rotating mirror) to the cylinder and a range of RIs for the gel (n_{gel}) and cylinder (n_{PMMA}).

Reflections at each of the interfaces were calculated to determine the amount of light intensity lost at the interfaces. These losses must be accounted for in the measured transmission intensity signal to accurately measure the transmission due to optical attenuation of the gel sample. Reflection depends upon the laser beam polarization and the calculations were made for the extremes of a linearly polarized beam, s-polarized (parallel to cylinder axis) and p-polarized beams (perpendicular to cylinder axis). The Fresnel reflection equations were used to calculate the reflectance for s- and p-polarizations. The reflectance is the fraction of reflected beam intensity of the incident, and by combination of the losses at each interface the expected transmission intensity was determined as a function of the projection distance.

Instances of optical modelling considering gel container edge effects for optical CTs with a RI matching fluid bath have been reported previously (Gore *et al* 1996, Kelly *et al* 1998, Doran *et al* 2001).

2.5. Incomplete projection data

As the laser beam approaches the edges of the cylinder in its sweep across the cylinder, the angles of incidence at the interfaces are increasing. There comes a point, before reaching the edge, when refraction and reflection effects put a limit on useful projection data. The cylinder was designed so that the effects of both refraction (beam path deviation) and reflection (beam intensity losses) would become limiting at similar points on the cylinder, i.e. a similar extent of projection data of greater than 90%.

The consequences of missing data at the extremities of projections were verified by simulation. Various test images were artificially generated and Radon transformed using Matlab to obtain projection data. These projections were modified by deleting data at the ends (5% at each end) to simulate measured data with missing projection ends. The modified projections were inverse Radon transformed to examine the reconstructed result. Next tested was the method to be employed on actual acquired projection data to minimize the effects of missing data. The projection ends were extrapolated by calculation using ray tracing and the assumption that the optical attenuation coefficient at the last measured point was constant for the remainder of projection. The simulated reconstructions were repeated with the deleted

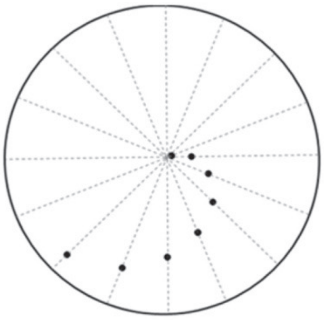

Figure 3. Top view of the locations of 0.5 mm diameter pins in the distortion test phantom. Nominal radial pin distances were 1, 4, 7, 10, 13, 16, 19 and 22 mm, every 22.5°.

projection ends being determined by the extrapolation method. Kelly *et al* (1998) used an interpolation of missing data due to the gel container wall effects in the RI fluid bath to give an improved result.

2.6 Data processing and image reconstruction

Prior to irradiation of the gel sample, a reference scan of the gel cylinder was taken by scanning a slice with 360 degrees rotation and then averaging the projections to obtain a reference projection. All post-irradiation projections were normalized to the reference projection. This accounts for the reflection effects in section 2.4; any asymmetry in the projection is due to the photodiode being non-orthogonal to the beam (to avoid back reflection), photodiode area response and any minor losses in the cylinder material. Reference scans were used by Kelly *et al* (1998) to correct for non-uniformities in the walls of the RI matching tank.

The normalized projection data gave the net change in the transmission between pre and post scans. After conversion to attenuation, extrapolation of missing projection ends was applied and then back projected by Matlab inverse Radon transformation. The resultant image of attenuation coefficients was calibrated to a dose by calibration sample data, including subtraction of auto-oxidation induced increases in attenuation of all FXG samples. Pre-irradiation scans of gel calibration samples in 1 cm pathlength cuvettes were made at the same time as the cylinder sample reference pre-scan. Post-irradiation, the gel cylinder sample was scanned together with 0, 2 and 4 Gy calibration samples. A Varian 600C/D linear accelerator 6 MV x-ray 10×10 cm^2 beam was used for all calibration irradiations with the centre of the cuvette being at $d_{\max}$ in a full scatter phantom with a source to surface distance (SSD) of 100 cm. The centre of the cuvette was scanned by the optical CT.

The reconstructed pixel size was 0.1 mm as per the raw projection data sampling rate. No filtering or smoothing was applied to the raw or reconstructed data.

2.7. Geometrical distortion

To demonstrate the parallel beam geometry achieved by the scanner in this work, a geometrical test phantom was used, similar to those used in previous studies (Oldham and Kim 2004, Olding *et al* 2010). As shown in figure 3, a spiral pattern of 0.5 mm diameter steel pins was located in a PMMA base with positions measured to be within 0.1 mm by digital callipers. The cylinder was filled with FXG and scanned adjacent to the plastic base after the gel had set. Using

ImageJ (National Institutes of Health, USA) software, the radial distance from the cylinder centre to each of the pins was measured in the optical CT reconstructed images.

2.8. Spatial resolution

For the scanner in this work, spatial resolution primarily depends on the laser spot size, photodiode response time and data acquisition rate. The detector response time and acquisition rate were sufficiently fast to measure several data points in the transition of the beam swept across a sharp edge, for the mirror rotation rate of 2170 rpm. To verify that the laser spot size was the limiting factor, fine wires of diameter 0.1 mm were positioned with one approximately in the centre and four about 20 mm from the centre. The FXG filled cylinder with wires was scanned and reconstructed. Line profiles of the wire cross sections were extracted using ImageJ. The modulation transfer function (MTF) was calculated using Matlab fast Fourier transforms. Both the object (wire) size of 0.1 mm and the pixel size of 0.1 mm were sufficiently small to give minimal degradation of the intrinsic MTF of the imaging system.

2.9. Uniformity, noise and artefacts

Dose uniformity and the extent of noise and artefacts were examined using the gel cylinder with FXG irradiated by a single 6 MV 10 × 10 cm^2 x-ray beam from a Varian 600C/D linear accelerator, directed down the cylinder axis. The cylinder was positioned in a small water tank with the top surface of the cylinder flush with the water surface at 100 cm SSD. A 400 cGy dose at 1.3 cm depth was delivered, where according to ion chamber beam data, the uniformity is within 1% over the central 5 × 5 cm^2 region. This dose level would be at the upper end of the range planned for use with FXG. At the maximum dose, there is a minimum of transmission signal due to the high optical attenuation, which is likely to lead to lower signal-to-noise ratios. The reconstructed images from post-irradiation scans were assessed using ImageJ.

2.10. Dose response

The ability of this scanner to reconstruct a dose pattern delivered by an external beam through the cylinder walls was illustrated by a four beam star pattern. The cylinder was filled with fresh FXG and irradiated isocentrically by a Varian 600C/D linear accelerator 6 MV x-ray beam with a SRS cone of about 10 mm diameter, perpendicular to the cylinder axis. A total dose of 400 cGy was delivered to the isocentre at the cylinder centre with gantry angles: 0°, 45°, 90° and 135°. The cylinder was optically scanned at 25 min post-irradiation, and an axial slice central to the star pattern was reconstructed. This measured slice was compared to the exported dose from BrainLAB iPlan (version 4.1.2) where the star pattern delivery was planned on a CT scan of the FXG filled cylinder. Sun Nuclear MapCheck software was used in dose comparisons.

3. Results and discussion

3.1. Cylinder design

Calculated laser beam paths through two different cylinders are shown in figure 4. Nominal RIs of $n_{\mathrm{PMMA}} = 1.49$ and $n_{\mathrm{gel}} = 1.34$ for FXG were used. Focal distances were selected to give a split of beam deviations in both the positive and negative directions. The first case, as shown in figure 4(a), shows beam paths for a cylinder with ID 70 mm and OD 76 mm, i.e. 3 mm wall thickness. The beam deviation from parallel to the central axis increases with the

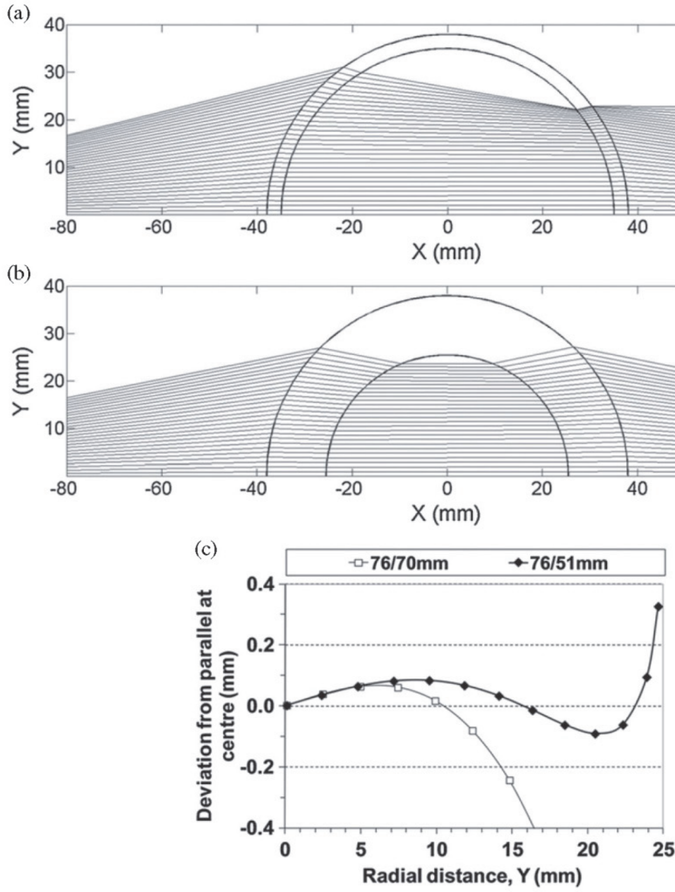

Figure 4. Calculated beam paths through PMMA cylinders in air with FXG in the centre, (a) for cylinder OD 76 mm, ID 70 mm and (b) OD 76 mm, ID 51 mm. (c) Beam displacements from parallel paths at the centre of cylinder.

radial distance, *Y*, from the cylinder centre as shown graphically in figure 4(c). The deviation exceeds 0.1 mm at $Y = 13$ mm (37% of radius) and increases to give the severe cylindrical aberration effect, as shown in figure 4(a). This corresponds to a previous design (Maryanski and Ranade 2001) where the projection data were limited to about 33% of the radius for a similarly sized 3 mm wall thickness cylinder.

By variation of the cylinder ID (wall thickness), it was found that the PMMA to gel interface can correct for the increasingly severe refraction (with beam angle of incidence) at the air to PMMA interface. At an ID to OD ratio of about 67%, the ray paths are parallel to within ± 0.1 mm for about 24 mm of the 25.5 mm radius (94% of the radius). This is shown in figures 4(b) and (c) for cylinder OD 76 mm and ID 51 mm. The front focal distance was set at 125 mm. In varying the ID there is a trade-off between the reduction of the beam deviations by decreasing the ID and the reduction of the extent of parallel rays. For example, with ID 49 mm, a beam deviation of ±0.05 mm is maintained, but for only about 85% of the ID. Conversely, if larger deviations were allowed by using a greater ID, the quasi-parallel rays would cover closer to the full diameter; however, reflection may become the limiting factor approaching the edges of the ID.

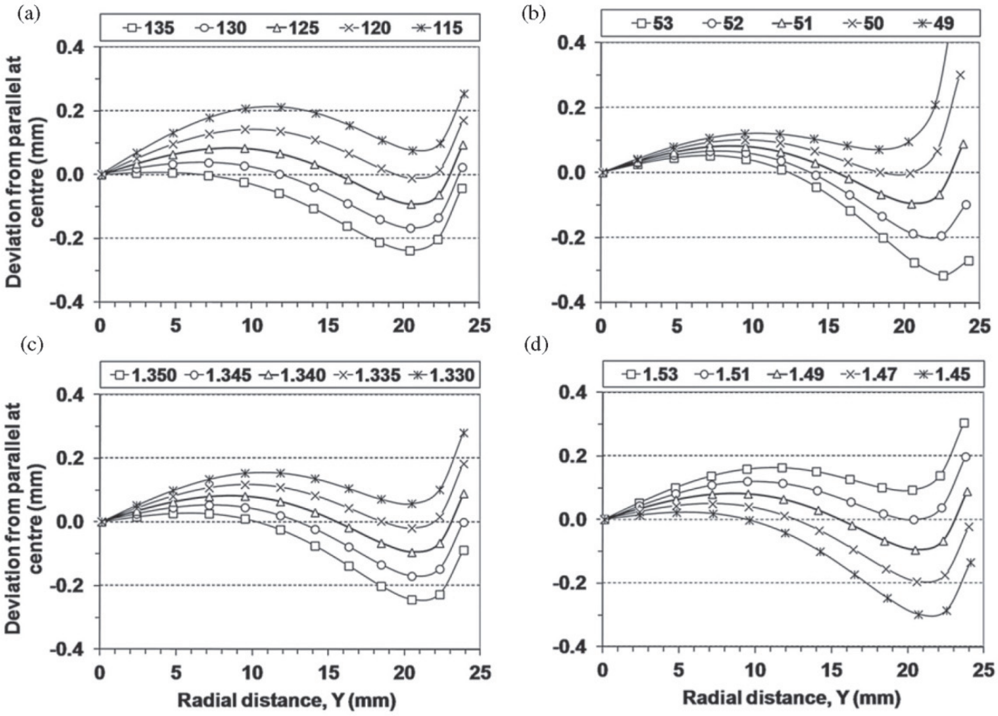

Figure 5. Calculated deviations from parallel beam paths for OD 76/ID 51 mm PMMA cylinder with various: (a) focal distances (mm) from the front surface of cylinder to the light source, (b) cylinder IDs (mm), (c) RIs of the gel and (d) RIs of the cylinder material.

Beam deviations were calculated and shown in figure 5 as a function of the focal distance figure 5(a), cylinder ID figure 5(b), RI of gel figure 5(c) and RI of cylinder figure 5(d). This shows the sensitivity of beam deviation to cylinder design parameters. Adjustment of the focal distance allows the deviations to be evenly divided as positive and negative. Changing the ID relative to a fixed OD gives the trade-off between the minimization of beam deviations and the extent of projection as mentioned. Different gel RIs can be accommodated within a given cylinder, and even scanning with water instead of gel is possible with appropriate minor adjustments such as focal distances. Cylinder RI is not critically sensitive for beam path deviations.

The transmitted beam intensity is affected by interface reflections as the beam scans across the cylinder, and the laser polarization determines the reflection characteristics. Calculated transmissions for p- and s-polarization orientations are shown in figure 6 for the 76 mm OD/51 mm ID PMMA cylinder. While s-polarization results in greater losses as the beam approaches the cylinder extremities, the p-polarized beam approaches Brewster's angle for the air–PMMA interface, improving the transmission, and then finally decreasing as the angles become more severe. This means projection data are lost at around 24 mm of the 25.5 mm radius, corresponding with the beam deviation limit.

p-polarization was utilized for its reduced variation in transmission and for convenience of establishing a known setup condition. Considering the reflection and refraction effects as discussed, the projection data limits were set at a conservative 23.5 mm (92%) of the 25.5 mm radial total. Additionally, shown in figure 6 is normalized measured data from a reference scan

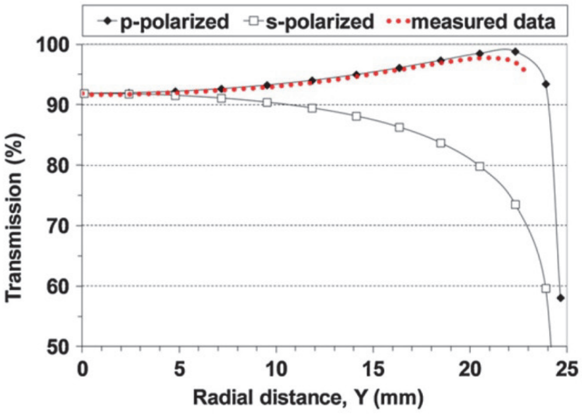

Figure 6. Calculated transmission due to reflections for *p*- and *s*-polarized laser beams with PMMA cylinder OD 76/ID 51 mm. Measured data are for the laser beam in the p-polarization orientation.

with water and the laser beam orientated for p-polarization. There is good agreement and the deviation at the extremity is mainly due to the lower RI of water used in the measurements compared to the gel used in the calculations.

The off-axis decrease in the transmission of s-polarization (or intermediate) could potentially be used to offset the increase in transmission usually obtained due to decreased pathlengths through the optically attenuating cylindrical gel sample. Potentially, this could reduce the dynamic range required by the detection system.

Hydrogels other than FXG can be readily implemented using the scanner cylinder design principles outlined in this report. Minor changes such as the focal distance adjustment and projection data end points may be sufficient to accommodate a gel change; however, optimization of the cylinder ID/OD ratio for a particular gel would give the best results. For example, polymer gels of higher RI would require a slightly reduced ID/OD ratio. Polymer gels would benefit from the scatter rejection of the single point detector design. Although other hydrogels can be adopted with this scanner design, the promising solid 3D dosimeter PRESAGE® (John Adamovics, USA) would not be suitable due to its high RI.

The disadvantage of the major optical component, the gel cylinder, being routinely handled possibly leading to scratching, needs to be minimized by appropriate handling. Re-polishing may be useful to repair minor scratching due to routine handling and cleaning, and the application of scratch resistant coatings to the PMMA surfaces is possible. In addition, precise indexing of the cylinder position on the scanner could allow the correction of cylinder imperfections (Doran *et al* 2001).

While the prototype scanner was sized for the small fields in SRS, a larger gel cylinder has been designed for future IMRT and VMAT applications.

3.2. Incomplete projection data simulation

The reconstruction results for a test image with 5% of projection data deleted at each end followed by extrapolation are shown in figure 7. This gives simulated projections of 90% of the gel sample diameter similar to the 92% of those acquired in practice. Horizontal profiles were extracted from each of the images in figures 7(a), (b) and (c) and plotted in figure 7(d). The percentage differences in the profiles are shown in figure 7(e), which reveals a substantial

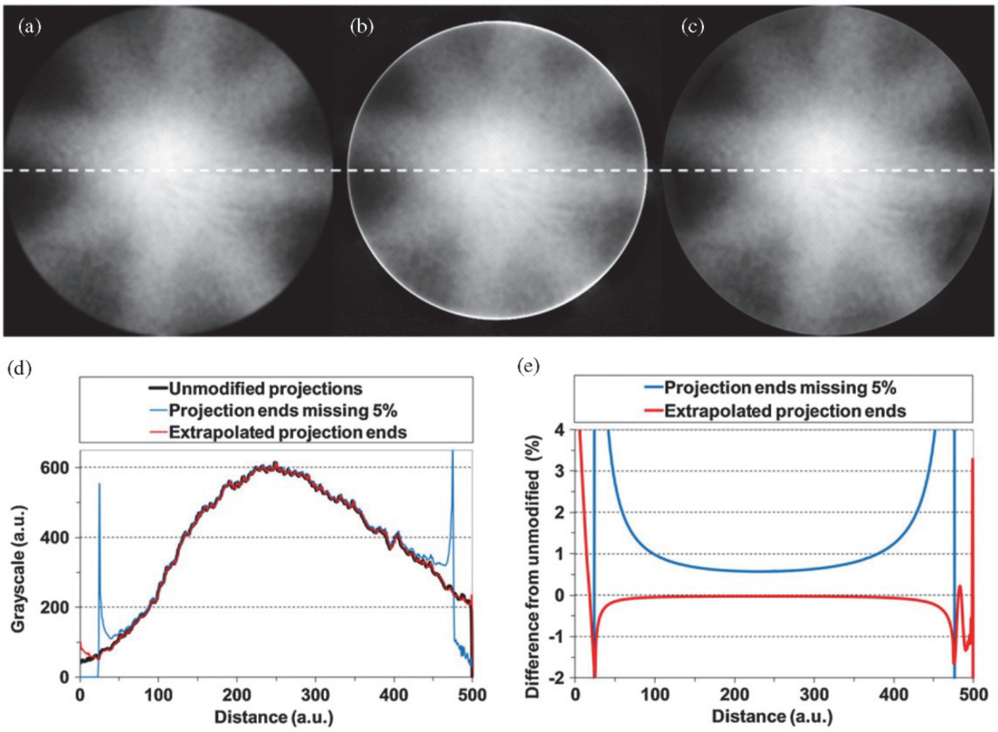

Figure 7. Simulation of the projection extrapolation method. (a) Reconstruction of test image with full unmodified projections. (b) Reconstruction using projections with 5% deleted each end. (c) Reconstruction with projections from (b) but with the extrapolation method applied. (d) Horizontal profiles through (a), (b) and (c). (e) Difference in the profiles of (d) between the deleted end projection data and the unmodified, without and with extrapolation.

global cupping artefact for the missing data case relative to the unmodified. For the extrapolated case, the differences have been reduced to 0.2% or less within the central 80% of the total image diameter. This means that if another 5% is added to the extrapolated 5% as a margin, the error within the central area is negligible. Therefore, in terms of incomplete projection data, a conservative accurate reconstruction FOV is about 40 mm for the 76 mm OD/51 mm ID cylinder.

Kelly *et al* (1998), Doran *et al* (2001) and Oldham and Kim (2004) showed that a global cupping artefact can occur as a result of gel container edge effects for a RI liquid bath scanner. One approach in the application of corrections to projection data has been by calculation to replace the edge affected data (Kelly *et al* 1998, Oldham and Kim 2004). Another approach has been the optimization of the matching fluid RI and container dimensions to avoid edge effects as much as possible (Doran *et al* 2001).

3.3. Geometrical distortion

The pin distortion phantom was scanned with the optical CT, and a reconstructed slice of the eight pins is shown in figure 8(a). Measurements of the radial distance to the pin centres for four separate scans were made with the mean optical CT image measurements, as shown in figure 8(b), together with the physically measured distances by digital callipers. The maximum

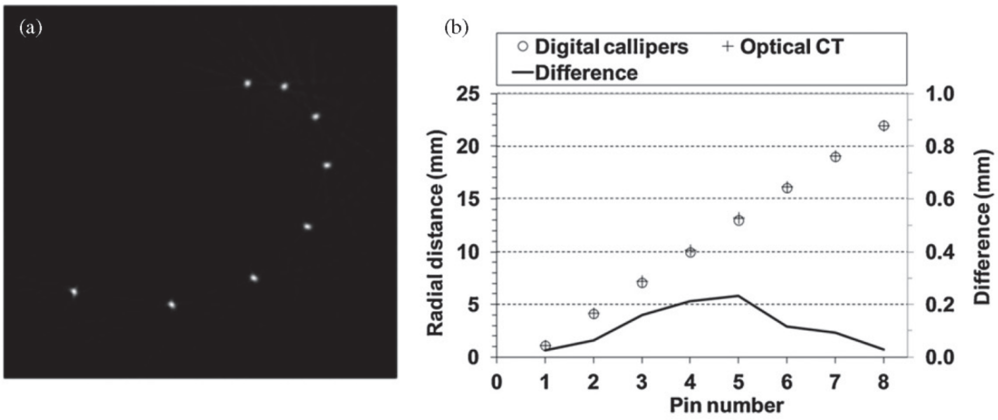

Figure 8. (a) Reconstructed axial slice for scans of the pin phantom to assess distortion. (b) Measured radial distances to the centre of the pins for both digital callipers directly and optical CT reconstructed images.

difference between the physical radial measurements and optical CT was 0.23 mm for pin 5, while the maximum standard deviation for all pin measurements was 0.02 mm. Similar results were obtained with the cylinder filled with water instead of FXG.

Generally for an optical CT scanner without a RI matching bath, geometric distortion would be a primary concern. However, the distortion results reported here are comparable to a recent report of the commercial Vista^{TM} (Modus Medical Devices Inc) cone beam optical CT scanner with a RI matching bath (Olding *et al* 2010). A test pin phantom showed typical deviations of 0.2–0.3 mm and up to 0.6 mm for the Vista scanner. Scaling up the cylinder size of the free-air scanner in this report can increase the geometrical deviations, however, acceptable results of less than 0.5 mm deviations are still possible for a doubling in size.

3.4. Spatial resolution

A reconstructed axial slice of a 0.1 mm diameter wire approximately centrally located in FXG is shown in figure 9(a). The outer four wires, located about 20 mm from the centre, provided similar profiles to that of the central wire shown in figure 9(b). The FWHM measured 0.4 mm in the reconstructed images. The raw projection data was also examined and the wire had a 0.47 mm FWHM when in a position closest to the light source. At the furthermost location the FWHM was 0.36 mm, while near the centre it was 0.40 mm. This was as expected since the front wall of the cylinder acts as a converging lens for the laser beam, and therefore the beam FWHM of 0.5 mm in air at the same point is reduced to around 0.4 mm on average within the cylinder. Additional focusing elements have been avoided to enhance simplicity, however, improvements in spatial resolution are possible by further beam focusing as demonstrated previously (Maryanski and Ranade 2001). The line profile of figure 9(b) represents a one-dimensional point spread function (PSF) produced by the 0.1 mm diameter object. The intrinsic normalized MTF for the imaging system is shown in figure 9(c). The relative modulation is 10% for the spatial frequency of 2.2 cycles/mm.

3.5. Uniformity, noise and artefacts

Figure 10 shows the reconstructed axial slice at a depth of 1.3 cm from the surface for the 400 cGy uniform (<1%) irradiation of FXG. Figure 10(a) was windowed to show 0–400 cGy

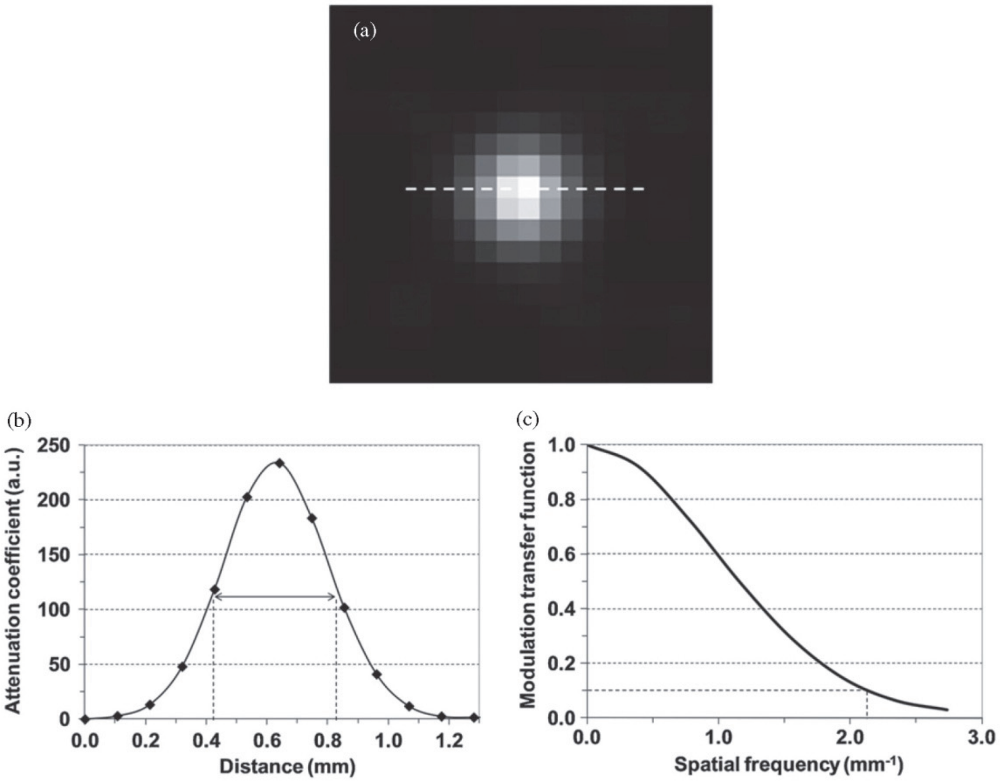

Figure 9. (a) Reconstructed axial slice of a 0.1 mm diameter wire, with 0.1 mm pixel size, (b) profile extracted from (a) giving a one-dimensional PSF with a FWHM of 0.4 mm and (c) normalized MTF calculated from the PSF.

irradiation (centre 200), while figure 10(b) has a window of 80 cGy centred on the mean value of 387 cGy (−3.3% from expected). The mean value was determined by a circular ROI of diameter 41 mm, i.e. excluding the outer 5 mm that is not considered reliable due to the 2 mm extrapolation. The standard deviation in this ROI was 3 cGy (0.8%). Figure 10(c) is the horizontal profile showing the uniformity across the centre of the reconstructed slice within the reliable FOV (41 mm) indicated by the dashed lines. A similar profile is shown for a scan depth of 2.5 cm.

The 80 cGy windowing of figure 10(b) reveals the three main types of artefact as follows. Firstly, the light outer ring artefact is due to mechanical rotation imprecision and variation of the projections at the extremities relative to the reference projection. Secondly, dust particles within the gel and on the cylinder inner wall surface are observed as small light spots. Thirdly, faint streaking is due to dust particles and scratches on the cylinder outer wall. Multiple low-level streaking intersects and causes a slight mottled appearance. All three sources of artefacts (mechanical precision, foreign particles and scratches on the cylinder surface) can be improved upon since the causes were readily determined and strategies for their minimization are anticipated in further work.

3.6. Dose response

A four beam star pattern was delivered by 10 mm diameter SRS cone beams through the cylinder walls to the FXG inside. Figure 11 displays the central axial slice through the centre

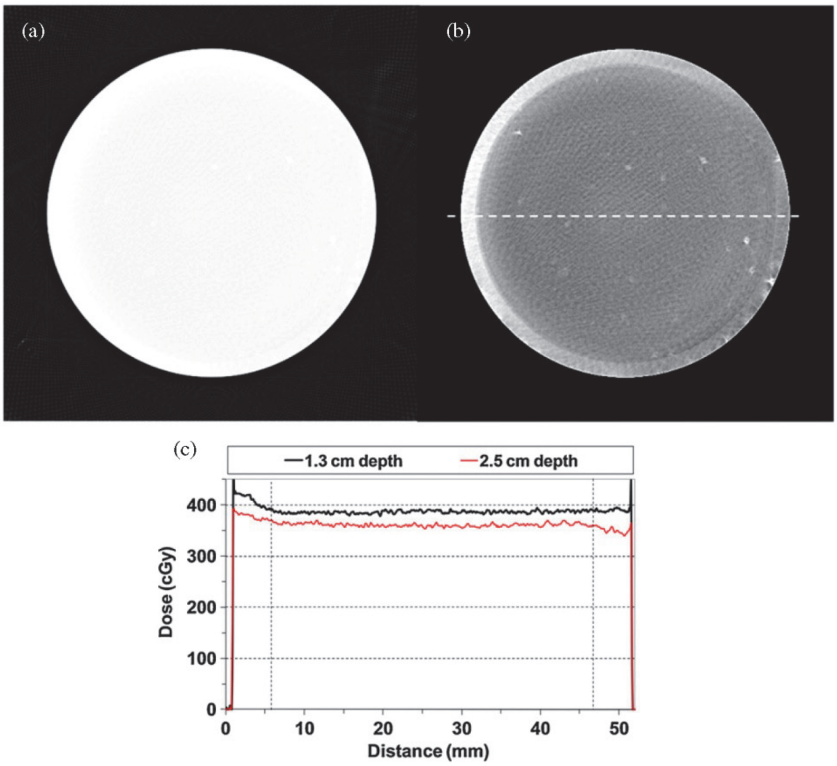

Figure 10. Reconstructed slice of uniform 400 cGy irradiated FXG sample at 1.3 cm depth. (a) Viewed with window 400, centre 200, and (b) window 80, centre 387 (mean value) to enhance the defects. (c) Extracted profiles for scan depths 1.3 and 2.5 cm. The dashed lines indicate the reliable FOV as determined from simulations of projection extrapolation.

of the star pattern. The BrainLAB iPlan calculated dose distribution is shown in figure 11(a), with 400 cGy being prescribed to the isocenter. The optical CT reconstruction with dose normalized to the isocentre is shown in figure 11(b). The dose difference between optical CT and iPlan is shown in figure 11(c). The use of gamma analysis using distance to agreement criteria was avoided to provide a more revealing comparison. The greatest differences within the reliable FOV occur at the beam penumbral overlap regions, and profiles were extracted through the worst region, shown in figure 11(d).

Generally there is agreement within 3% except for the regions of overlapping penumbra where there are differences of up to 5–6%. These larger differences may be due to FXG ion diffusion or iPlan penumbra inaccuracies, however, detailed investigation had not been conducted since this test was merely intended to be an example of the viability of this optical CT for external beam irradiation. Validation and dose accuracy of the optical CT is the subject of further work.

4. Conclusions

A viable approach to optical CT scanning of dosimetric hydrogels without a RI matching fluid bath for external beam applications has been demonstrated. A PMMA cylinder of an

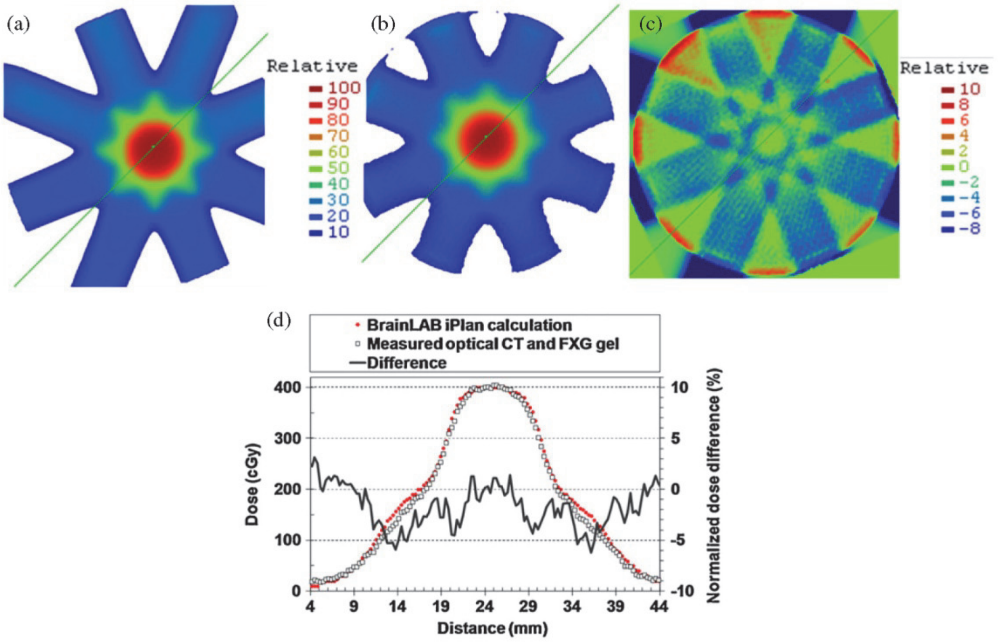

Figure 11. Slice through the centre of a four beam star pattern irradiation. (a) BrainLAB iPlan calculated dose. (b) Optical CT reconstructed relative dose. (c) Difference map between optical CT and iPlan. (d) Profiles through (a) and (b) in the regions of greatest disagreement.

appropriate ID to OD ratio containing gel was employed to achieve parallel ray geometry through the gel sample allowing straightforward CT reconstruction. The preliminary test results reported for the prototype scanner indicate that optical CT scanning for an external beam application such as SRS dose verification may be achieved without the use of a RI matching fluid bath. Further work is required to establish the dosimetric accuracy and precision after scanner refinements to minimize known sources of artefacts and to implement other improvements including the adoption of other hydrogels.

Scanning without a RI fluid represents a significant simplification of the optical CT scanning process that could assist in 3D gel dosimetry becoming more routinely adopted for clinical use.

Acknowledgments

The authors thank John Schneider and Trevor Waterhouse of the Royal Adelaide Hospital, Department of Medical Physics and The University of Adelaide, School of Chemistry and Physics workshops respectively for the fabrication of components for the optical CT scanner.

References

Babic S, Battista J and Jordan K 2008a Three-dimensional dose verification for intensity-modulated radiation therapy in the radiological physics centre head-and-neck phantom using optical computed tomography scans of ferrous xylenol-orange gel dosimeters *Int. J. Radiat. Oncol. Biol. Phys.* **70** 1281–91

Babic S, Battista J and Jordan K 2008b An apparent threshold dose response in ferrous xylenol-orange gel dosimeters when scanned with a yellow light source *Phys. Med. Biol.* **53** 1637–50

Babic S, McNiven A, Battista J and Jordan K 2009 Three-dimensional dosimetry of small megavoltage radiation fields using radiochromic gels and optical CT scanning *Phys. Med. Biol.* **54** 2463–81

Baldock C, De Deene Y, Doran S, Ibbott G, Jirasek A, Lepage M, McAuley K B, Oldham M and Schreiner L J 2010 Polymer gel dosimetry *Phys. Med. Biol.* **55** R1–63

Ceberg S, Gagne I, Gustafsson H, Scherman J B, Korreman S S, Kjaer-Kristoffersen F, Hilts M and Bäck S A 2010 RapidArc treatment verification in 3D using polymer gel dosimetry and Monte Carlo simulation *Phys. Med. Biol.* **55** 4885–98

Doran S J 2009a The history and principles of chemical dosimetry for 3-D radiation fields: gels, polymers and plastics *Appl. Radiat. Isot.* **67** 393–8

Doran S J 2009b The history and principles of optical computed tomography for scanning 3-D radiation dosimeters: 2008 update *J. Phys.: Conf. Ser.* **164** 012020

Doran S J 2010 Imaging and 3D dosimetry: top tips for MRI and optical CT *J. Phys.: Conf. Ser.* **250** 012086

Doran S J, Koerkamp K K, Bero M A, Jenneson P, Morton E J and Gilboy W B 2001 A CCD-based optical CT scanner for high-resolution 3D imaging of radiation dose distributions: equipment specifications, optical simulations and preliminary results *Phys. Med. Biol.* **46** 3191–213

Gore J C, Kang Y S and Schulz R J 1984 Measurement of radiation dose distributions by nuclear magnetic resonance (NMR) imaging *Phys. Med. Biol.* **29** 1189–97

Gore J C, Ranade M, Maryañski M J and Schulz R J 1996 Radiation dose distributions in three dimensions from tomographic optical density scanning of polymer gels: I. Development of an optical scanner *Phys. Med. Biol.* **41** 2695–704

Islam K T, Dempsey J F, Ranade M K, Maryanski M J and Low D A 2003 Initial evaluation of commercial optical CT-based 3D gel dosimeter *Med. Phys.* **30** 2159–68

Jordan K 2010 Review of recent advances in radiochromic materials for 3D dosimetry *J. Phys.: Conf. Ser.* **250** 012043

Kelly R G, Jordan K J and Battista J J 1998 Optical CT reconstruction of 3D dose distributions using the ferrous-benzoic-xylenol (FBX) gel dosimeter *Med. Phys.* **25** 1741–50

Lepage M and Jordan K 2010 3D dosimetry fundamentals: gels and plastics *J. Phys.: Conf. Ser.* **250** 012055

Low D A, Moran J M, Dempsey J F, Dong L and Oldham M 2011 Dosimetry tools and techniques for IMRT *Med. Phys.* **38** 1313–38

Maryanski M J and Ranade M K 2001 Laser micro-beam CT scanning of dosimetry gels *Proc. SPIE* **4320** 764–7

Massillon-JL G, Minniti R, Mitch M G, Maryanski M J and Soares C G 2009 The use of gel dosimetry to measure the 3D dose distribution of a ^{90}Sr/^{90}Y intravascular brachytherapy seed *Phys. Med. Biol.* **54** 1661–72

Massillon-JL G, Minniti R, Soares C G, Maryanski M J and Robertson S 2010 Characteristics of a new polymer gel for high-dose gradient dosimetry using a micro optical CT scanner *Appl. Radiat. Isot.* **68** 144–54

Mijnheer B and Georg D 2008 Guidelines for the verification of IMRT *Booklet No. 9 (ESTRO, Brussels, Belgium)*

Oldham M and Kim L 2004 Optical-CT gel-dosimetry: II. Optical artefacts and geometrical distortion *Med. Phys.* **31** 1093–104

Olding T, Holmes O and Schreiner L J 2010 Cone beam optical computed tomography for gel dosimetry: I. Scanner characterization *Phys. Med. Biol.* **55** 2819–40

Sakhalkar H, Sterling D, Adamovics J, Ibbott G and Oldham M 2009 Investigation of the feasibility of relative 3D dosimetry in the Radiologic Physics Center Head and Neck IMRT phantom using presage/optical-CT *Med. Phys.* **36** 3371–7

Schreiner L J 2004 Review of Fricke gel dosimeters *J. Phys.: Conf. Ser.* **3** 9

van Doorn T, Bhat M, Rutten T P, Tran T and Costanzo A 2005 A fast, high spatial resolution optical tomographic scanner for measurement of absorption in gel dosimetry *Australas. Phys. Eng. Sci. Med.* **28** 76–85

Wuu C-S, Schiff P, Maryanski M J, Liu T, Borzillary S and Weinberger J 2003 Dosimetry study of Re-188 liquid balloon for intravascular brachytherapy using polymer gel dosimeters and laser-beam optical CT scanner *Med. Phys.* **30** 132–7

3.3 Conclusions

The study presented in the preceding section provided indications that the prototype scanner had potential for good imaging quality with a completely fluid-less design. There was minimal distortion and spatial resolution was 0.5 mm. First indication of absolute dose accuracy was a 3.3 % difference from linac ion chamber reference dosimetry (section 3.5, Ramm *et al* 2012), using cuvette calibration samples. Scanner and processing code performance, together with gel limitations would need further investigation and improvements to yield the anticipated absolute dose accuracy (eg. < 2 %, k=1 measurement uncertainty). The addition of a reference photodiode detector was planned but had not been implemented prior to the study. This would correct for laser output variations observed to be up to 1 %.

Non-uniformity was dominated by the appearance of the extrapolated region. It was speculated at the time that cylinder rotational accuracy and projection data asymmetry played a role in the inaccurate extrapolation region. This was later determined to be the case in addition to pixel size calibration being a contributing factor. The other apparent artefacts were particulate matter in the gel which could be easily solved by filtration. A more significant concern was the issue of cylinder scratching or defects and the implications on reconstructed image quality. Only low level streak artefacts were observed with visually near pristine cylinder polished surfaces, and were probably more to do with dust on the optical surfaces. Nevertheless with repeated use the PMMA surfaces would almost certainly degrade. A solution was proposed of hard coating the cylinder optical surfaces to provide much greater scratch resistance.

The reconstructed dose star pattern gave good general agreement with TPS data. The largest discrepancies were areas of overlapping penumbrae. At the time it was not known whether the dominant cause was TPS data or ion diffusion. Further work and experience with FXG would later indicate that ion diffusion would certainly be problematic in that instance.

Chapter 4

Development of the optical CT dosimetry system

4.1 Introduction

The basis of a fluid-less optical CT scanner had been previously constructed and assessed by preliminary testing (Ramm *et al* 2012). The gel container formed the main optical lens to give parallel rays through the gel dosimeter, and the optical geometry was shown to provide geometrically accurate reconstructions. Further scanner refinements and gel dosimeter studies were required, with an overall aim of producing a 3D dosimetry system of dosimetric accuracy rivalling other established dosimeters such as film. The next stages of development would focus initially on minimising previously observed artefacts. Then improvements of scanner operation were addressed by the implementation of a reference photodiode, fully automated 3D data acquisition and validation of transmittance measurement accuracy. The dose response of FXG was characterised and calibration methodology developed for gel calibration using cuvettes under linac reference conditions.

To validate the scanner / gel dosimetry system, benchmarking against reference dosimeters was conducted by measurements of simple radiation fields. This would indicate the accuracy of the system and provide understanding of the limitations of FXG gel in particular. Then clinical application of SRS was demonstrated by end to end testing of planned dose distributions using the SRS TPS and localisation systems. The gel dosimeter was fixed inside a head shaped phantom and the normal treatment process was carried out. Another application was addressed using gel dosimetry by irradiation with a brachytherapy ^{192}Ir source. The gel measured dose distribution produced by a ^{192}Ir surface applicator was compared to the Monte Carlo computed planning data.

4.2 Imaging artefacts

The artefact previously observed in the extrapolated region in Chapter 3 (Ramm *et al* 2012) had only minor impact on the non-extrapolated FOV however, it was expected that it could be readily improved. Upon investigation, it was found that the gel cylinder rotation axis was slightly off vertical, resulting in the horizontally scanning laser being non-perpendicular to the cylinder axis, and cylinder position relative to the fixed light source and detector would change as the cylinder was translated vertically. A new bearing design was implemented giving a cylinder axis of rotation within 0.1° of vertical, and < 0.1 mm deviation of cylinder position when scanned from top to bottom. This reduced the extrapolation artefact to a more subtle effect as shown in figure 1 of the publication in section 4.2.1. Other sources of artefacts, dust and other particles in the sample, were addressed by a filtration method using a syringe filter (2 μm). This was used with dyed water solutions and gel in all subsequent work.

The issue of cylinder optical surface scratching or defects from repeated use was investigated. It was considered that a hard coating process similar to that used to give improved scratch resistance of optical or industrial plastic components may be beneficial. The implementation of a hard coating was reported in the publication in section 4.2.1. An undesirable effect was found where small variations in transmission were caused by thin film interference effects since the thin hard coating was not exactly RI matched to the PMMA and there were small variations of film thickness. This resulted in an artefact pattern in reconstructed slices. The use of point by point normalisation of the measurement scan projections to the reference scan projections instead of an averaged reference scan projection cancelled out the optical interference effects. These issues were reported in more detail in section 4.2.1. The point by point normalisation approach would become an important aspect in later work with regards to achieving good imaging uniformity over the entire 3D volume. The hard coating, even with the RI mismatch, was found to be useful and subsequent work utilised both the hard coated cylinder and a bare PMMA version. The main benefit of hard coating would be the increased working life of a cylinder, assuming failure of the coating did not occur (eg. delamination, crazing).

4.2.1 Publication on imaging artefacts

The following conference paper was published in Physics the IOP Journal of Physics Conference Series in 2013.

Laser beam optical CT scanner for in-air gel readout: imaging artefacts

D Ramm

Journal of Physics: Conference Series **444** (2013) 012078

doi:10.1088/1742-6596/444/1/012078

7th International Conference on 3D Radiation Dosimetry (IC3DDose) IOP Publishing
Journal of Physics: Conference Series **444** (2013) 012078 doi:10.1088/1742-6596/444/1/012078

Laser beam optical CT scanner for in-air gel readout: imaging artefacts

D Ramm
Department of Medical Physics, Royal Adelaide Hospital Cancer Centre, South Australia, Australia
School of Chemistry and Physics, University of Adelaide, South Australia, Australia

E-mail: daniel.ramm@health.sa.gov.au

Abstract. Ongoing progress on development of an in-air scanning optical CT is reported, specifically dealing with the minimization of scanner imaging artefacts. Improved scratch resistance of the PMMA gel cylinder was a primary goal, so that routine cleaning would not degrade the polished surfaces. This was achieved by the addition of a hard coating to the cylinder surfaces. New artefacts were introduced and subsequently reduced by alternative processing of projection data. The outcome was a gel cylinder of much greater practicality for routine use while maintaining similar signal to noise ratios and uniformity in the image reconstruction field of view.

1. Introduction

Optical CT scanning of dosimetric gels [1] usually requires the use of a RI matching fluid bath to reduce refraction and reflection effects at the surface of the cylindrical gel container. Recently we have developed an 'in-air scanner' that avoids the use of a fluid bath while obtaining effectively parallel ray projection data for 90 % of the gel sample diameter [2]. Previously Maryanski and Ranade developed the 'dry scanner' intended mainly for brachytherapy source applications [3]. This scanner cannot accurately image optical attenuation outside a small central region of the gel dosimeter since it only acquires projection data for about 36 % of the gel diameter. Another approach using the PRESAGE [4] dosimeter has been proposed, using algebraic reconstruction to account for non-parallel light rays [5]. Limited projection data (65 % of PRESAGE diameter) was still a limiting issue for that simulation study. Our in-air scanning approach is the only one realized to demonstrate the feasibility of scanning external beam irradiated gels without RI matching fluid.

While the principle of the prototype in-air scanner's operation has been shown, further developments are required in preparation for radiotherapy clinical application. One aspect is imaging artefacts [6, 7] that degrade 3D dosimetric data and can present a significant obstacle in gaining high quality measured data and general acceptance of the dosimetry method. Preliminary results indicated some readily observable artefacts [2]. These artefacts have been under investigation, together with some others that have become apparent.

7th International Conference on 3D Radiation Dosimetry (IC3DDose) IOP Publishing
Journal of Physics: Conference Series **444** (2013) 012078 doi:10.1088/1742-6596/444/1/012078

2. Methods

2.1. Optical CT scanner

The scanner is detailed in [2], with brief summary as follows. A He-Ne laser beam is fanned by a rotating mirror across the key component, a machined and polished PMMA cylinder (76 mm outer diameter (OD), 51 mm inner diameter (ID)). Inside the cylinder is the gel, and after the laser beam passes through with close to parallel ray geometry, it is refracted by the cylinder walls to a focal point at a silicon photodiode detector. With the ID/OD ratio of around 67 % and FXG inside, parallel rays extend to about 90 % of the gel diameter. Extrapolation of the missing projection ends is applied prior to back-projection.

Changes to the original scanner details include the following: (i) A revised bearing assembly for the sample rotation mechanism, giving improved rotational precision. (ii) The PMMA cylinder internal and external walls were hard coated with a scratch resistant coating (Crystalcoat MP-101, SDC Technologies). This polysiloxane based coating had a measured thickness of 3.8 ± 0.1 μm over the cylinder surfaces. (iii) Improved gel optical quality by using a syringe with filter (2 μm nominal pore size) to fill the gel containers. (iv) An option for low pass filtering of projection data and re-sampling to 0.4 mm. (v) An option for point by point division of measurement projection data by reference scan data for the entire cylinder, as opposed to the original method of a single averaged reference scan projection for normalization.

2.2. Imaging artefacts

The three most apparent artefacts identified previously were: (i) An outer ring in the extrapolation region due, in part, to mechanical imprecision of the sample rotation. (ii) Small spots in the sample due to foreign particles (dust). (iii) Low level streaking due to scratches or dust on the cylinder walls. Additionally, cylinder wall scratching through routine cleaning was a chief concern because severe streak artefacts can result. Attempts to improve these artefacts have been made by the aforementioned changes to the scanner.

Another potential source of artefacts is inter-reflection, ie. multiple reflections between optical components. One instance was reflected light from the photodiode surface back-reflected to itself by the cylinder. This was previously addressed by tilting the photodiode so that the reflection was not incident upon the cylinder. There is a more subtle effect where the beam is reflected from the exit wall of the cylinder (PMMA-air interface) back to the entry wall, and then towards the photodiode. Since air-PMMA interface reflectance is about 4 % in the worst case (for the acquired range of data) this signal can only amount to 0.2 %, and less with gel attenuation.

Optical interference effects are particularly important to avoid because signal modulation of several percent may be introduced. This has been observed at the central axis of the cylinder where cylinder inter-reflections can, at times, result in constructive and destructive interference. A significant transient waveform in the centre of projection data can occur, particularly when there is minimal attenuation in the cylinder. Interference effects can also be introduced where coatings are applied to components, such as the hard coating on the PMMA cylinder. With the current hard coating there is a mismatch in RI ($n_{coating} = 1.45$, $n_{PMMA} = 1.49$), leading to a change in transmission at an air-coating-PMMA interface of about 0.5 % for a 0.1 μm (typical) change in coating thickness ($\lambda = 594$ nm).

To investigate and illustrate the artefacts, the cylinder was filled with filtered distilled water and green dye water solutions. Undyed scans were used as the reference scan throughout, and an undyed measurement scan was used to examine low level effects (mainly interference). These effects are more evident in this case than scans with significant optical attenuation in the cylinder. Scans of water samples with uniform attenuation were made with dye solutions of moderate ($OD_{moderate} = 0.18$ cm^{-1}) and high ($OD_{high} = 0.50$ cm^{-1}) levels. Reconstructed dose images were viewed and analyzed using ImageJ (National Institutes of Health, USA).

7th International Conference on 3D Radiation Dosimetry (IC3DDose) IOP Publishing
Journal of Physics: Conference Series **444** (2013) 012078 doi:10.1088/1742-6596/444/1/012078

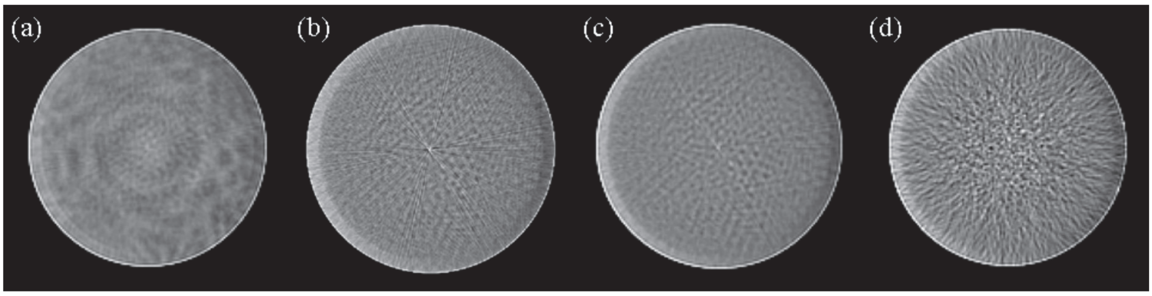

Figure 1: Reconstructed images of one slice for the green dye water filled cylinder, with viewing window widths of 20 % of the mean and centred on the mean value. (a) $OD_{moderate}$, 0.4 mm pixel size and averaged normalizing reference projection. (b) $OD_{moderate}$, 0.2 mm pixel and point by point reference scan normalization. (c) Same as 1(b) except for projection filtering and 0.4 mm pixel. (d) Same as 1(c) except for OD_{high}.

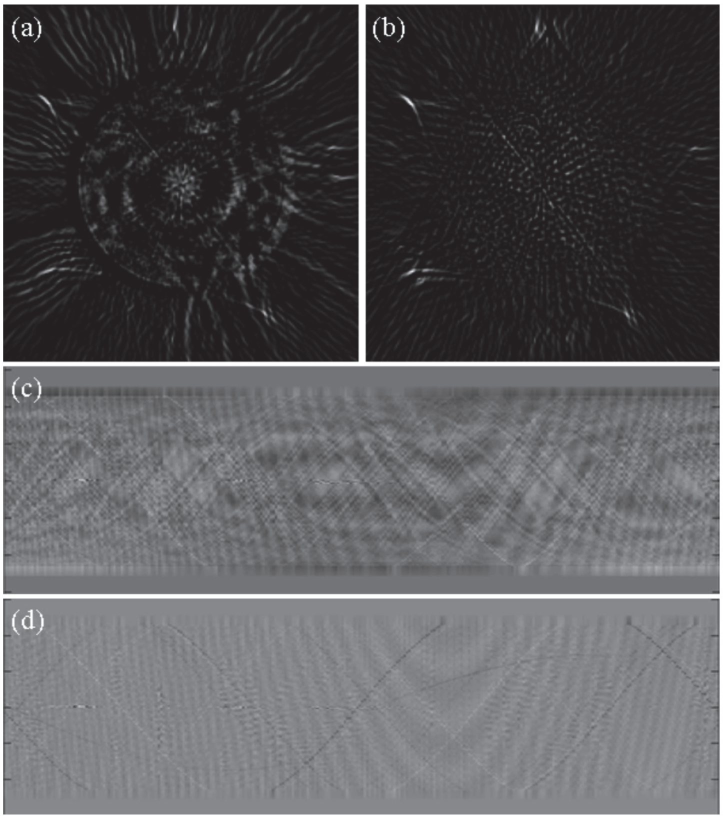

Figure 2: Undyed water scan normalized to another undyed water scan, where the ideal result would be a blank image. (a) Reconstructed slice using an averaged reference projection. Viewing window width 5 % of mean pixel value for $OD_{moderate}$. Interference artefacts appear inside and outside the internal volume of the cylinder. (b) Same as 2(a) except for point by point reference division, giving reduced interference artefacts. (c) Sinogram for 2(a) showing superimposed multiple interference patterns. (d) Sinogram for 2(b) with less interference patterns. The thin lines (dark from reference scan and light from measurement scan) are due to dust specks on the outer cylinder surface.

3. Results and discussion

A reconstructed slice of dyed water ($OD_{moderate}$) is shown in figures 1(a), 1(b) and 1(c). The same projection data was used for these three images, just differing in data processing. The most obvious non-uniformity feature of figure 1(a) was the patterned appearance that was new to this version of the scanner. The reason for this was due to interference effects from the addition of the hard coating on

7th International Conference on 3D Radiation Dosimetry (IC3DDose) IOP Publishing
Journal of Physics: Conference Series **444** (2013) 012078 doi:10.1088/1742-6596/444/1/012078

the cylinder. Figure 2 shows more detail of these interference patterns. Figures 2(a) and 2(b) are reconstructed slices of undyed water scans normalized to another undyed scan with averaged reference projection (2(a)) and point by point reference projections (2(b)). The sinograms are shown in figures 2(c) and 2(d) where optical interference patterns become more discernible, particularly figure 2(c). Figure 2(b) and the corresponding sinogram, figure 2(d), show that the point by point reference division largely removes the coating interference effects. Figures 1(b) and 1(c) confirm the minimization of this interference effect. The hard coating is substantially more durable than a PMMA surface, meaning the cylinder surfaces can be routinely cleaned with reduced scratching concerns.

Another optical interference effect was an interference signal on the central axis shown in the sinograms of figure 2(c) and 2(d). There is a broken line of signals of high and low relative intensities running down the central axis. These manifest in reconstructions as radial lines as shown in figure 1(b). Since these interference waveforms in the projection data are of high frequency, filtering assists in their minimization as shown by figure 1(c). This interference effect is dependent upon the degree of attenuation by the sample with the worst case occurring for undyed water as used here for all reference projection data. When gel is used, the presence of attenuation even in FXG pre-irradiation reference scans, means this effect is usually minimal.

Figure 1(d) is a high OD example with central axis OD of about 2.5 (0.3 % transmission). Noise in the projection data becomes more significant, hence a random noise appearance dominates the residual artefacts of figure 1(c). The residual artefacts mainly comprise a mottled appearance originally thought to be caused by multiple low level streaking, however further investigation is required to confirm the source(s). There is still a remaining artefact in the extrapolation region, however it is not considered reliable FOV in any case, and does not affect the full data FOV.

To put the fluctuations observed in the images of figure 1 into perspective, 1(a) had a standard deviation in the FOV of 0.8 % of the mean value, 1(b): 1.3 %, 1(c): 0.8 % and 1(d): 2.0 %.

4. Conclusions

Optical interference has been found to be a source of artefacts in the process of continued development of an in-air optical CT scanner. The addition of a hard coating to the gel cylinder provided greater scratch resistance, reducing the likelihood of streak artefact inducing scratches. However interference artefacts were also introduced. Point-by-point reference scan division helped minimize these effects. RI matched hard coating is planned for the future. A remaining structured mottle artefact in the FOV requires further investigation, however presently a signal to noise ratio of around 130 is obtained for a uniform moderate optical density.

5. Acknowledgements

Application of the cylinder hard coating by Colin Hall, University of South Australia, and support by John Schneider, Royal Adelaide Hospital, Medical Physics workshop is gratefully acknowledged.

5. References

[1] Baldock C *et al* 2010 *Phys. Med. Biol.* **55** R1-63
[2] Ramm D *et al* 2012 *Phys. Med. Biol.* **57** 3853-68
[3] Maryanski M J and Ranade M K 2001 *Proc. of SPIE Int. Soc. Optic. Eng.* **4320** 764-767
[4] Gorjiara T *et al* 2011 *Med. Phys.* **38** 2265-74
[5] Doran S J and Yatigammana D N 2012 *Phys. Med. Biol.* **57** 665-83
[6] Bosi S *et al* 2007 *Phys. Med. Biol.* **52** 2893–2903
[7] Bosi S G *et al* 2009 *Phys. Med. Biol.* **54** 275-83

4.3 Scanner refinements

Improvements of scanner performance were realised in the investigations of artefacts however a distinct mottle pattern residual artefact remained. It was suspected that laser output variations could be a contributing factor. The method to correct changes of laser output was by the use of a second photodiode measuring the output provided by a beam splitter. This was implemented after the prototype development in Chapter 3 and prior to the work of section 4.2. It was noted that the earlier work showed a finer mottle pattern when a higher data density (ie. higher spatial frequency data acquisition) was used. This indicated that data sampling was an influence factor. When the reference photodiode was added, the maximum acquisition rate was limited since the data acquisition card only had one analogue to digital converter scanning the multiple channels. The raw signals from the photodiodes were examined, with examples shown in figure 4.1. There were cyclical signals observed on varying time scales that were largely corrected by normalising the measurement signal to the reference. Sources of noise and interference were investigated and it was found that laser output instability appeared to be the largest contributor. With the reference signal correction applied, there were still some residual signals in the corrected measurements however, these fluctuations and the reconstructed mottle artefact were low level effects and were therefore not investigated further. It was concluded that the interplay between laser output fluctuations, data acquisition, detector response times and reconstruction would require significant further work to reduce the low level effect. A final point of note was from observations in later work with another laser (633 nm) which had more stable output than the 594 nm version. The mottle pattern was clearly reduced for the more stable laser when using exactly the same acquisition and processing methods. Thus further improvements could involve investigation of more stable light sources and better data acquisition with improved synchronisation of multi-channel acquisition.

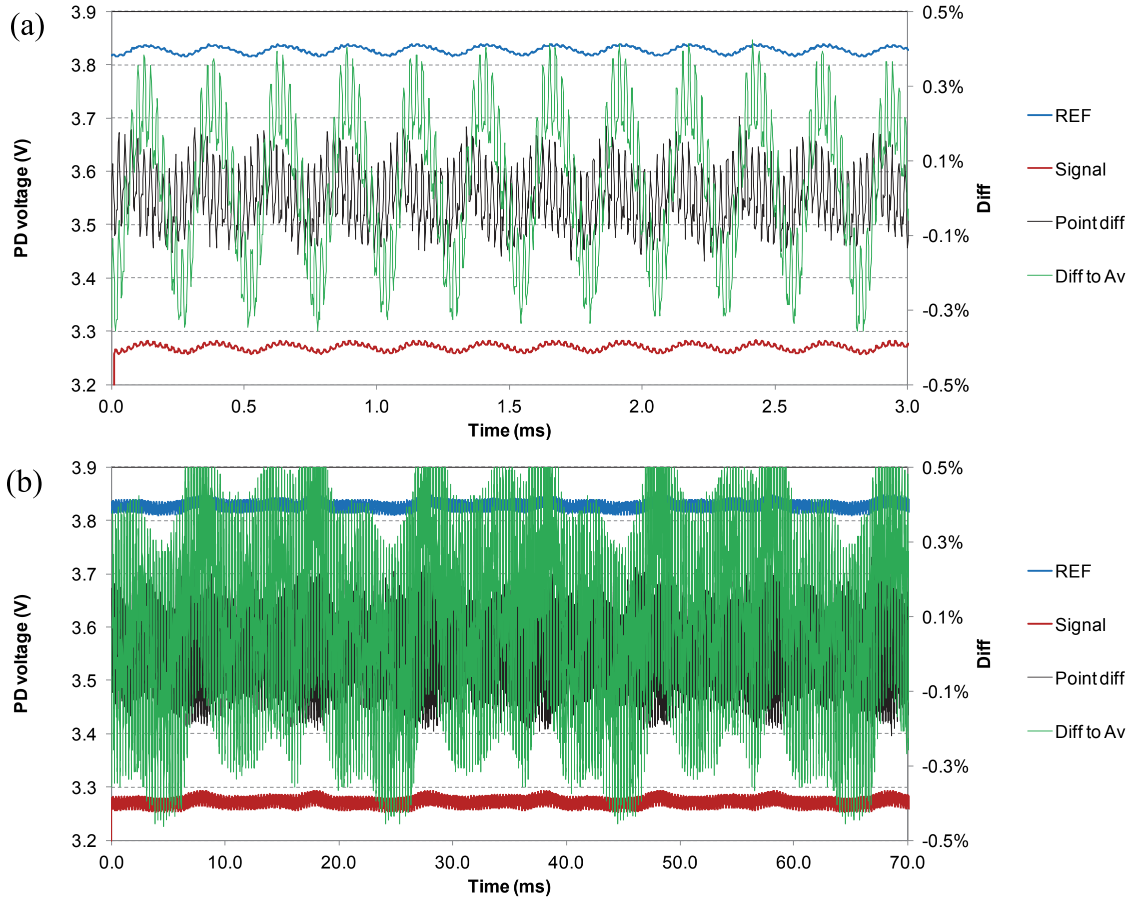

Figure 4.1. Raw photodiode signals for the measurement (signal) and reference (ref), and differences when referenced point by point (point diff) and measurement point to the average of the reference (diff to av). **(a)** On a time scale of the order of one projection and **(b)** a few projections.

Another significant change was the increase of rotating mirror speed from 2170 to 3620 rpm for quicker scan times (17 ms per projection). Standard scan parameters were now, 288 projections over a 360° rotation, giving 5 sec per slice at a data acquisition rate of 450 kS/sec and 0.2 mm sample spacing (in gel). Thus the scanning rate for the cylinder was 10 slices per minute, so a typical 3D acquisition would be 50 (1 mm) slices in 5 minutes to cover the 50 mm length and diameter.

A major technical development was the progression from single slice to 3D fully automated scanning. A priority was set on the robustness of the acquisition, ensuring precise alignment of projection data independent of the driving computer's state of performance. This was achieved by coding that used hardware position triggers on the rotating mirror motor to initiate acquisition of projection data each mirror rotation. If the timing of the loop controlling the acquisition was late, the acquisition would wait for the next mirror rotation as would the next step increment of sample rotation. The integrity of the data was tested by imaging metal rod and pin objects as shown in figure 4.2. Analysis of the sinogram data would be an alternative method to verify the accuracy of the data acquisition.

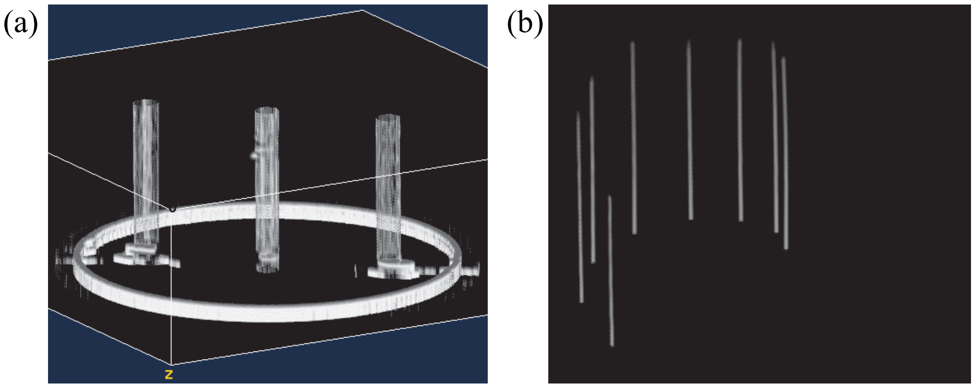

Figure 4.2. Reconstructed metal objects for verification of the integrity of the multi slice projection data. **(a)** Three 2.5 mm diameter metal rods (circular base partially included), with air bubble observed on the central rod, and **(b)** eight 1 mm diameter metal pins as used for spatial distortion testing.

With any developments of the scanning system there is the fundamental question of whether transmittance measurements are accurate. This is often addressed by cuvette measurements using an independent spectrophotometer compared to the optical CT (Olding *et el* 2010) and there has been the use of known optical density filters (Thomas *et al* 2011). The favoured method for this work was the use of independently calibrated filters to verify transmittance accuracy. Since the scanner was designed to have a cuvette measurement mode of operation, filters for the purpose of calibrating spectrophotometers would be ideal. A set of 4 filters were used with certified transmission values: 0.8174, 0.5237, 0.3374 and 0.1111 (at 590 nm) traceable to NIST (CF-VIS-ND, CVI Melles Griot). They were scanned on the optical CT with the rotation platform stationary and positioned in a cuvette dedicated mount with a recess machined for accurate localisation. The transmittance measurement results are shown in figure 4.3. This provided confidence in the ability to accurately measure transmittance since all results were within 0.5 % of expected.

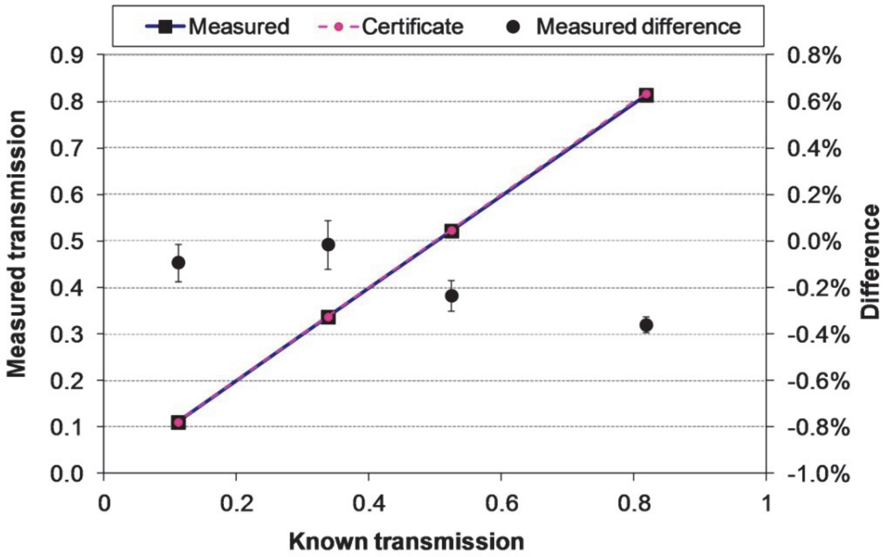

Figure 4.3. Measured transmission for NIST traceable spectrophotometer calibration filters using the optical CT 594 nm laser beam and photodiode. The differences between the measured and certified values are shown as indicated by the right side axis, including the 2σ uncertainties (n=10).

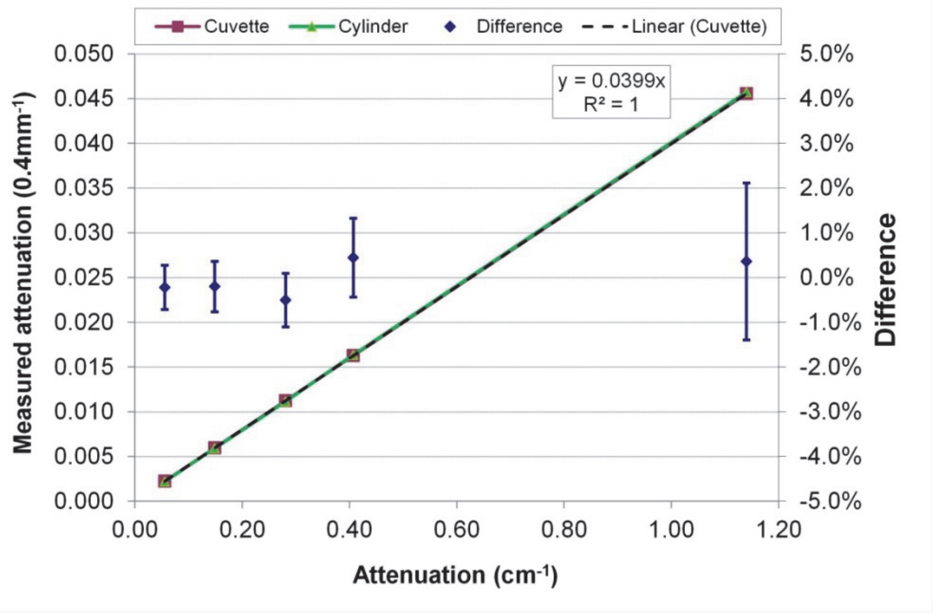

Figure 4.4. Optical attenuation of green dye water solutions measured in cuvettes and by optical CT reconstruction as a function of nominal attenuation values. The difference between CT cylinder and cuvette values are shown by the right side y-axis. The normal range of values is up to about 0.40 cm^{-1} and the high attenuation value at 1.14 cm^{-1} shows extended correlation. Uncertainties shown were 1σ (n=3) relative to the 0.4 cm^{-1} attenuation value.

The next step was to compare cuvette measured attenuation to 3D reconstructed optical attenuation measurements. Test solutions of water dyed to various levels using green food dye (Queen Fine Foods, Aust.) were prepared and measured in both cuvettes and the optical CT scanning cylinder. Results in figure 4.4 indicated a high level of correlation. Measurement points up to attenuation levels of 0.4 cm^{-1} were the intended range for standard operation while a much higher value of 1.14 cm^{-1} also provided good agreement.

The scanner had been shown to provide accurate absolute transmittance and hence optical attenuation measurements over the range of interest for samples contained in both cuvette and optical CT cylinder. These were independent methods with one being a simple transmission measurement at a point and the other used transmission measurements to form projections that were then reconstructed to provide voxels of optical attenuation in the cylinder. This would form a reliable basis for the cuvette gel calibration method to be used.

4.4 FXG dosimeter

A standard FXG recipe was used, similarly to others (Bero *et al* 2001, Babic *et al* 2008a). Some experimentation of different ingredient concentrations was conducted however, no significant gains were made in terms of reduction of auto-oxidation, diffusion or increased sensitivity. The standard recipe comprised 4 % w/v gelatin dissolved in 50 mM H_2SO_4 (3/4 of total) by heating to 40°C on a hotplate stirrer, then 0.05 mM XO, 0.3 mM ammonium ferrous sulphate added with the remainder of the 50 mM H_2SO_4. The liquid gel is syringed (via filter) into the optical CT scanning cylinder and calibration cuvettes (shown in figure 4.5) and refrigerated overnight to set.

The cylinder and cuvettes are stored together as a set as shown in figure 4.5(c), since the thermal history is an important issue for accurate FXG dosimetry. The most significant effect is the temperature of the gel during optical scanning. This has been reported to be a 2.5 % change in optical attenuation per °C (Olding and Schreiner 2011). For this work a temperature dependence of 1.1 % / °C was determined. While this is far from the 2.5 % / °C value, it is a significant effect that must be dealt with effectively since large temperature variations are possible due to the fact that the gel is refrigerated to set. Some detailed results of the experiment to determine temperature dependence were given in the publication in Chapter 6 (figure 4, section 3.1). For these temperature studies, cuvettes and a cylinder were fitted with fine wire (dia. 0.25 mm) type K thermocouples to minimally perturb the gel samples. A thermocouple was located at the centre of each cylinder or cuvette. The temperature monitored samples were not used for optical attenuation measurements. An identical sample, handled in the same way (ie. removed from water bath or storage box at the same time as the temperature monitored sample) was scanned to measure optical attenuation through the location of temperature measurement. After removal from the refrigerator, sample temperatures slowly increased by approximately 10°C up to room temperature over a 5 hour period, while repeat scanning was conducted.

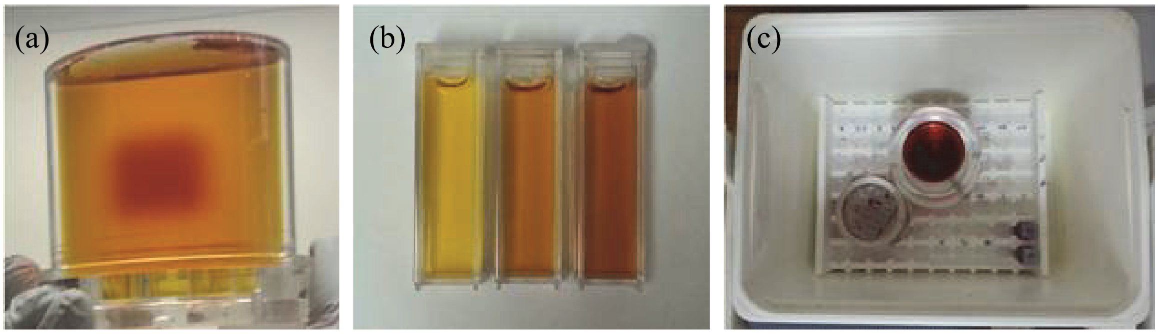

Figure 4.5. FXG in **(a)** a 76 mm diameter optical CT PMMA cylinder, with a 4 Gy 2 x 2 cm irradiation, and **(b)** 4 ml polystyrene 10 mm pathlength cuvettes for calibration of dose with 0, 2 and 4 Gy irradiations. **(c)** Gel sample storage conditions with the calibration cuvettes in a water bath of similar size to the cylindrical gel sample, giving comparable thermal load. All samples were located in an insulated box with lid.

The issue of Fe^{3+} ion diffusion imposes time constraints on irradiation time and the time between irradiation and gel scanning. While minimising the time from irradiation to the start of scanning for diffusion reasons, dose development must also be taken into consideration. The change in optical attenuation with time was largely stabilised from 20 minutes post irradiation (details included in the Chapter 6 publication). Thus the ideal scanning time is around 20 to 30 min post irradiation.

The FXG dose response was characterised by cuvette studies with 3 cuvettes for each of 8 dose points up to 5 Gy. The cuvettes were positioned in solid water at the linac calibration reference point. The cuvettes were located such that the axial plane of the beam at the cuvette centre was the effective point of measurement since it would be the path scanned by the laser beam. Irradiation was delivered by a 6 MV linac with a 10x10 cm field and 100 cm SSD. The cuvettes were scanned on the optical CT at 20, 40 and 60 minutes post irradiation, giving optical attenuation values for the centre of the cuvette using equation 1.8. Dose response curves are shown in figure 4.6. For this particular example, Fe^{2+} concentration was decreased from the standard 0.3 mM to 0.1 mM. The main effect of this was to cause slower development of Fe^{3+} ions. Thus optical attenuation changed by 5 % from 20 to 60 min scan time points. Auto-oxidation was accounted by subtraction of the zero dose cuvette optical attenuation from all other samples. All samples were scanned as a set with the same post-irradiation time, ± 1 minute.

FXG dose response is usually assumed to be linear even though non-linear response has been observed (Babic *et al* 2008b). In this work, initially a polynomial was used to fit the data then, it was found that a power fit gave improved fitting and simplicity of fit function. The reason for lower dose response at low doses for yellow light (eg. 594nm as used here) has been attributed to rate of formation of XO-Fe^{3+} double complexes (Babic *et al* 2008b). It was beyond the scope of this work to investigate the validity of the curve fit function's representation of the mechanism. Differences between inverse and reverse regression to obtain calibration curves were found to be negligible, thus reverse regression was routinely used. Low measurement uncertainties of each data point are beneficial in this case.

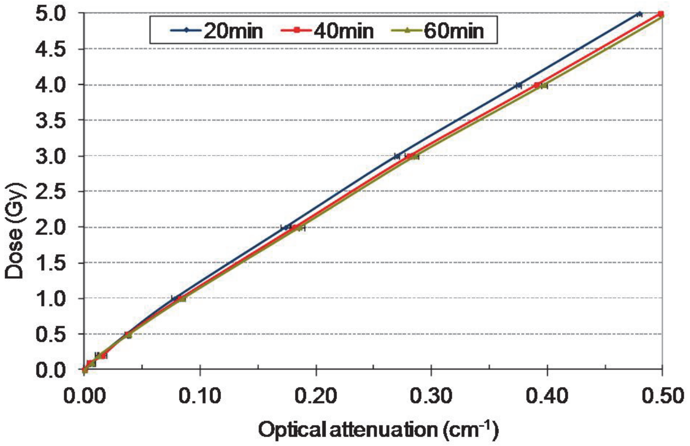

Figure 4.6. FXG optical attenuation (594 nm) dose response at 20, 40 and 60 min post irradiation. The uncertainties are 1σ (n=3). The differences in curves are due to dose development. This particular gel had a reduced concentration of Fe^{2+} (0.1 mM instead of 0.3 mM) giving slower dose development, and a relatively large change from 20 to 40 min (4%).

For routine calibrations a more practical number of dose points were desired. A 3 point fit using only the 1, 2 and 4 Gy dose points provided results as shown in figure 4.7. The 3 point fit was within ± 0.5 % up to the 4 Gy nominal maximum.

These results helped to determine FXG standard operation and handling procedures. A cuvette based dose calibration procedure for each batch of gel was developed and the importance of gel temperature during scanning had been established. The following sections detail the testing and use of the system.

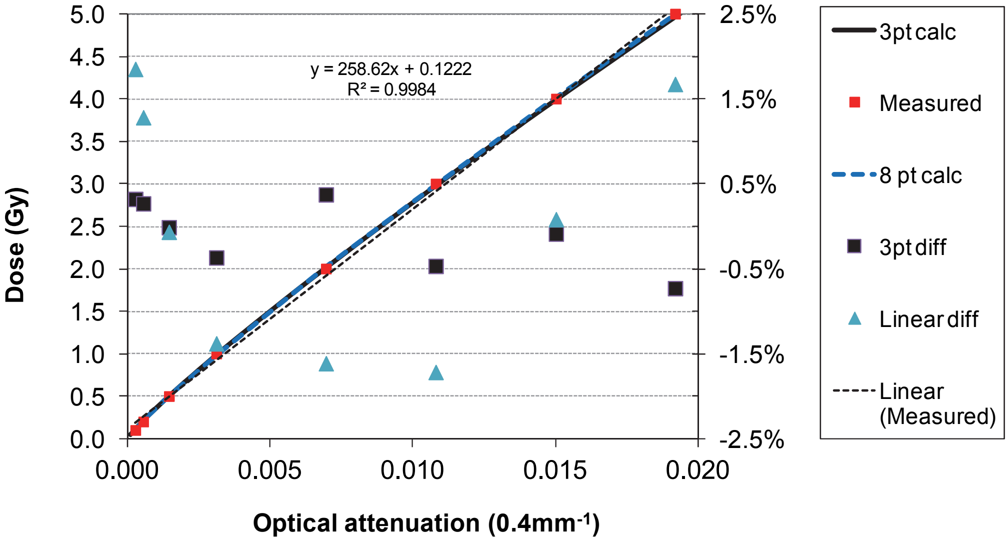

Figure 4.7. FXG Measured dose response (20 min post irradiation) and calculated dose using a 3 dose point (4, 2, 1 Gy) power fit, $dose = a(\Delta\mu)^b$. The full 8 point fit is also shown. Global differences between calculated and measured are shown by the right side y-axis. The linear fit is included for reference.

4.5 3D dosimetry system performance

The performance of the FXG / optical CT system was tested by 6 MV linac irradiations of well-known simple fields. Firstly a 10x10 cm field size reference beam was used with a gel cylinder immersed in a water phantom to provide a full scatter condition to compare to ion chamber data scanned in a 3D scanning water phantom. The beam was directed down the cylinder axis in one experiment and perpendicularly through the cylinder wall in another. A small field of 2x2 cm was also used, which was of a typical size of field in the application of SRS. The gel measured DICOM dose files were viewed in ImageJ (National Institutes of Health, USA) software, and routinely filtered with a 5x5 pixel median filter. FXG dose calibration was by cuvette optical attenuation coefficient measurements using the optical CT laser beam and detector. Three dose points and non-linear dose response fit were used as described in the preceding section

Figure 4.8 gives a 3D representation of a 2x2 cm measured dose distribution, providing a qualitative indication of the quality of imaging achieved. Dosimetric accuracy was quantified by comparison with ion chamber scans as shown in figure 4.9. The gel measured depth dose curves were not renormalised and dose values presented are those calibrated via the cuvette calibration procedure. The ion chamber data was the calibrated dose delivered, accounting for daily output variations. The gel results were typically within 0.5 % of the ion chamber beyond d_{max}, with maximum deviations of up to 1.2 % for the 2x2 cm field. Measurements of the side entry irradiations were in good agreement with the reference data given that the depth was corrected with the electron density of the 12.5 mm thick PMMA wall of 1.146. The depth correction was a 1.8 mm shift applied to the physical depth.

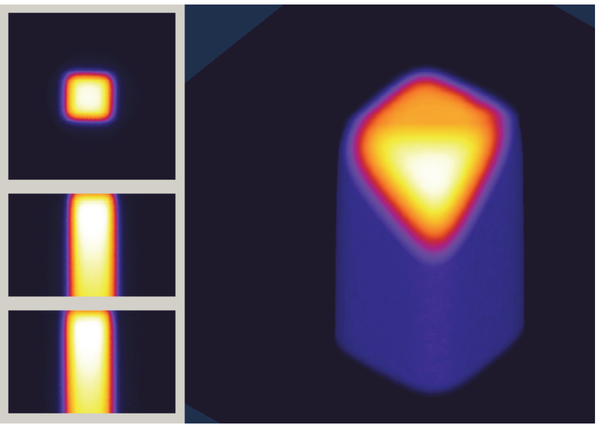

Figure 4.8. FXG measured 3D dose for a 6 MV 2x2 cm jaw field size, with voxel size 0.4 x 0.4 x 1.0 mm. The dose delivered at d_{max} was 3.57 Gy. Axial, coronal and sagittal 2D views (left) and 3D render with cutaway corner (right).

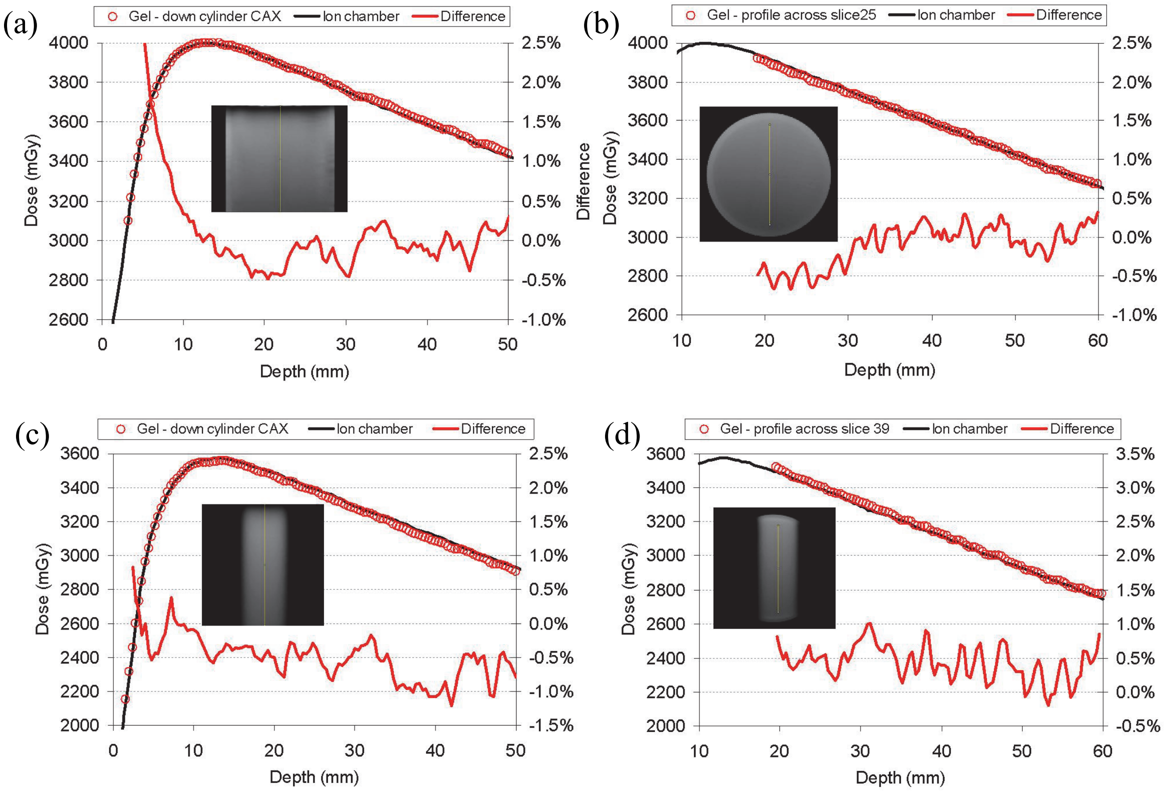

Figure 4.9. FXG measured depth dose curves compared to ion chamber for **(a)** 10x10 cm field size directed down the cylinder axis, **(b)** 10x10 cm field size directed through the side wall of the cylinder, **(c)** 2x2 cm field size directed down the cylinder axis, and **(d)** 2x2 cm field size directed through the side wall of the cylinder.

Line profiles were extracted from the 2x2 cm field 3D measured datasets in the axial plane of the beam as shown in figure 4.10. Multiple post irradiation scans were conducted to give a time sequence of data. With the higher dose gradients of around 20 % / mm in the penumbra of the beam, the effects of Fe^{3+} diffusion become clearly apparent. Figure 4.10(b) quantifies the effect in terms of change of the 80-20 % penumbra distance. A diffusion corrected curve was also shown. This was a point by point linear extrapolation to a zero post irradiation time. A PinPoint (PTW Freiburg) ion chamber gave an 80-20 % distance of 3.5 mm. Film and diode measured profiles, without the issue of volume averaging like ion chambers, give reduced penumbra distances by 0.5 to 1 mm. Thus for a steep gradient of a single beam, diffusion would cause up to a 0.5 mm deviation at a given dose point in the penumbra such as the 80 %. If a time sequence of post irradiation scan data were not available, a 20 minute scan would give a marginally greater deviation.

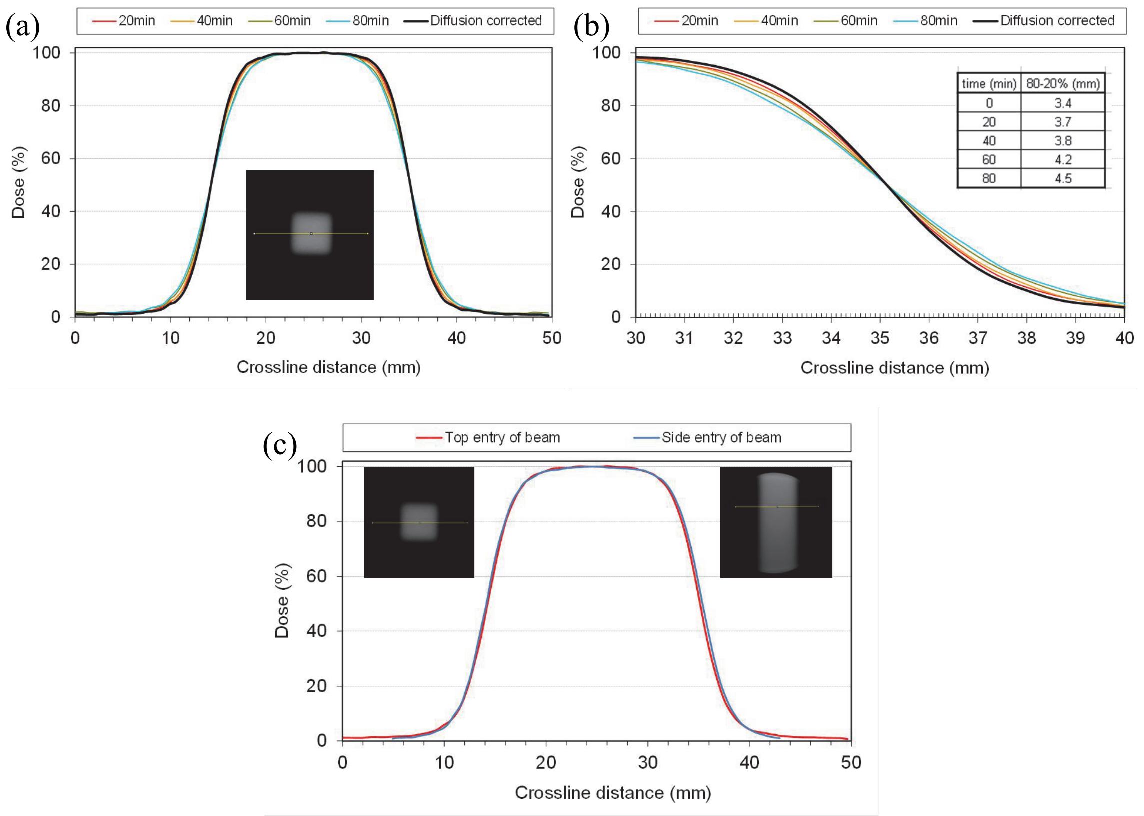

Figure 4.10. FXG measured crossline profile for a 2x2 cm jaw defined field. **(a)** The (top entry) full profile obtained with post irradiation scan times 20, 40, 60 and 80 min, showing the effects of Fe^{3+} ion diffusion. From the multiple time point data, a diffusion corrected curve is also shown. **(b)** Close-up view of the penumbral region of (a). The measured 80-20 % penumbra distance is shown on the table inset. **(c)** Comparison of the 20 min top entry profile of (a) with a separate side entry irradiation.

Figure 4.10(c) compares profiles of a 2x2 cm field delivered via top entry versus side entry. This shows that there are no significant differences in the integrity (scaling and distortion) of the axial image plane compared to lateral. There is also no notable distortion of the dose profile due to the MV beam transmission through the curved PMMA wall.

The FXG / optical CT system measured external beam 6 MV doses typically within 1 %, with reproducibility within 1 %. Larger (10x10 cm) and smaller (2x2 cm) field sizes had been studied to date. The major limitation of FXG, ion diffusion, was addressed by limiting the post irradiation scan time and fast optical scanning. Spatial resolution was 0.4 mm in axial slices and slice distance user configurable. Typical scan time was 5 minutes for the 51 mm diameter by 50 mm length 3D gel volume with 1 mm slices. This satisfies the resolution, time, accuracy and precision criteria (RTAP) proposed by Oldham *et al* (2001) for 3D dosimetry of: 1 mm^3, 60 min, 3 % and 1 % respectively.

4.6 Applications

Testing of the FXG / optical CT system indicated that it would be useful for verification of typical SRS dose distributions of around 1 to 3 cm in size. In addition, 3D dose distributions measured for ^{192}Ir HDR sources at distances greater than 20 mm from the source could be of value.

4.6.1 Stereotactic radiosurgery

The application of SRS was the original targeted use of the prototype optical CT scanner in this work. The gel cylinder was specifically sized to fit inside an existing water filled head phantom (RSVP Phantom Head, The Phantom Laboratory, USA). A mounting system for the gel cylinder was fabricated such that it could be reliably located inside the head phantom. Figure 4.11(a) shows the head phantom with gel, mounted to a linac couch with Brainlab SRS frame hardware. This was the delivery stage of end to end testing of the entire clinical treatment chain following the standard clinical process of CT scanning, treatment planning (Brainlab iPlan) and delivery on the linac. The final positioning of the phantom was by laser alignment to Brainlab target positioners attached to the frame, as per clinical use.

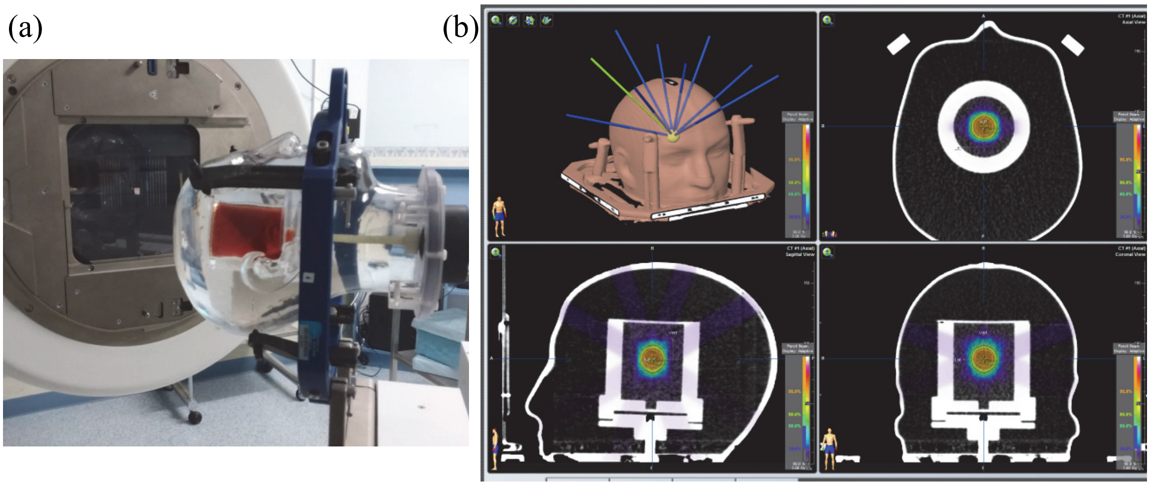

Figure 4.11. (a) FXG cylinder mounted inside the water filled head phantom, mounted to Brainlab SRS frame localisation hardware for end to end testing. **(b)** Brainlab iPlan TPS screenshot with the gel cylinder centre targeted for a 3 Gy spherical dose with a 10 beam treatment plan.

A 10 static beam treatment plan was generated using 2.5 mm MLCs to conform the 80 % isodose to a spherical target of 20 mm diameter. The 80 % dose was 3 Gy, giving 3.75 Gy to the centre of the target. A TPS screenshot is shown in figure 4.11(b). The planned spherical target was positioned to within 0.2 mm accuracy of the cylinder geometric centre, according to the TPS. The TPS dose distribution was carefully cropped to the gel volume (to sub-pixel level), and centred on the cylinder. Similar was done for the measured dose distribution. Thus the planned dose distribution had known registration to the cylinder and since the measured dose distribution would be inherently registered to the cylinder walls, an accurate analysis of dose distribution delivery accuracy in terms of both dose levels and localisation could be made. The delivery was provided by a Varian Trilogy linac 6 MV beam with HDMLC.

Figure 4.12 shows a dose slice through the target centre for iPlan calculated and FXG measured. Also shown are 3D surface rendered images of the 20 % and 80 % isodoses to illustrate the true 3D nature of the measurements. Positional accuracy was assessed by measurement of the centroid of the 80% isodose. Results are given in table 4.1, with the greatest deviation of measured to planned being 0.5 mm. The measured dose at the target centre with a 2 mm diameter ROI was 373.5 cGy compared to the 375 cGy planned, giving a -0.4 % difference.

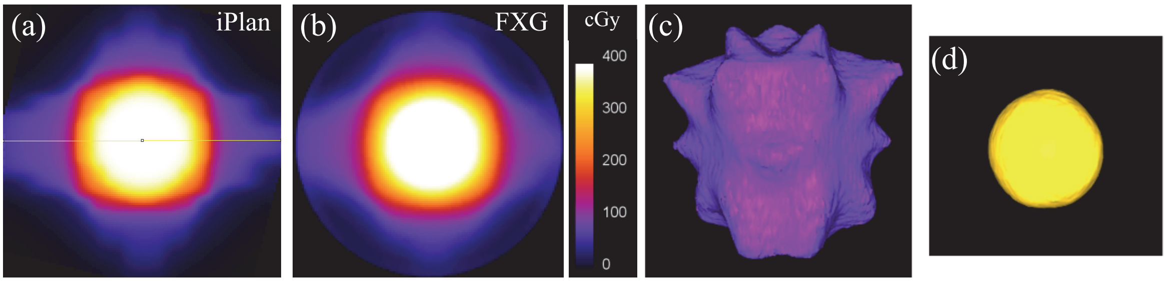

Figure 4.12. Treatment plan and delivery of a 20 mm diameter spherical dose. **(a)** iPlan TPS calculated 2D dose plane through the target centre. **(b)** FXG measured dose for the same plane as (a). **(c)** A 3D rendered image of the measured 20 % isodose surface, and **(d)** the 80 % isodose surface.

Table 4.1. Delivery positional accuracy of a 20 mm diameter spherical dose. Positioning determined by the centroid of the 3 Gy 80 % isodose.

	Axial plane (mm)		Sagital plane (mm)	
	X (L-R)	Z (A-P)	Y (S-I)	Z (A-P)
Measured centre	40.71	40.72	24.63	40.50
Target centre	40.20	40.20	24.20	40.20
Difference	0.5 (Rt)	0.5 (P)	0.4 (S)	0.3 (P)

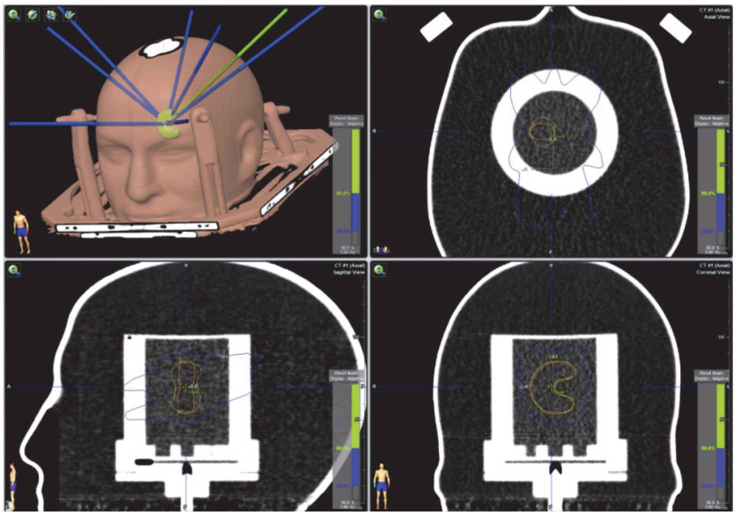

Figure 4.13. Brainlab iPlan TPS screenshot with the gel cylinder targeted with a c-shape dose using an 8 beam treatment plan.

Another treatment plan was produced with a c-shaped target as shown in figure 4.13. Results are given in figure 4.14 showing the c-shaped dose distribution. There was good agreement of absolute dose and alignment as illustrated by the line profiles. Absolute dose agreement was within 2.5 % in the high dose areas and within 1 mm DTA in the high gradient regions.

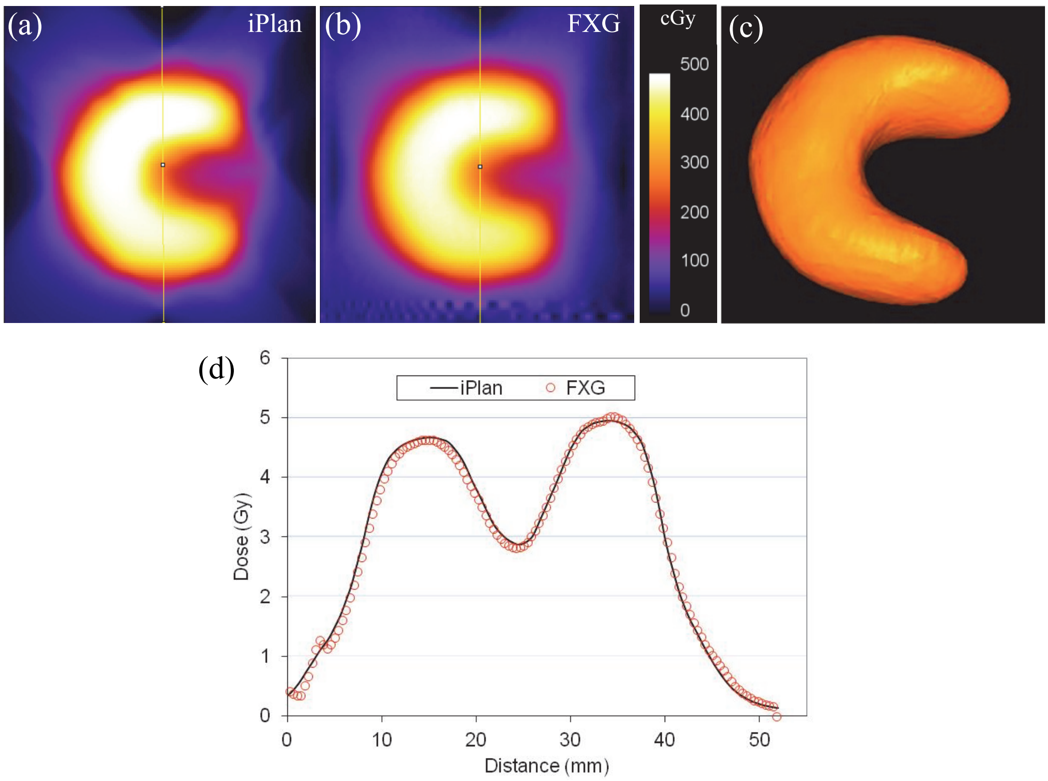

Figure 4.14. Treatment plan and delivery of a c-shaped dose. **(a)** iPlan TPS calculated dose 2D plane through the target centre. **(b)** FXG measured dose for the same plane as (a). **(c)** A 3D rendered image of the measured 80 % isodose surface. **(d)** Line profiles extracted from (a) and (b). Note that the artefact at the bottom of the FXG image and also seen on the profile was the result of a mark on the cylinder wall, added for registration purposes.

4.6.2 Brachytherapy source

The 3D dose distribution delivered by a 20 mm H Leipzig applicator and ^{192}Ir afterloader (Nucletron B.V. The Netherlands) was measured using the FXG / optical CT system. This provided visualisation and detailed comparisons of measured dose to the Monte Carlo (MC) derived values used for treatment planning. Leipzig applicators are a treatment option for superficial leisons. Figure 4.15 shows the experimental setup with water phantom and the applicator. The gel cylinder was immersed in the water phantom with top surface flush with the water surface. The lid was removed from the gel sample giving a flat gel surface. The applicator was positioned just in contact with the gel surface using micrometer stages with estimated accuracy of 0.1 mm. The source dwell time was calculated to deliver 2.705 Gy to the reference point at the depth of 3 mm. Calibration of the FXG dosimeters was by the standard cuvette calibration procedure using a 6 MV beam, and thus independent of the HDR equipment. Since the HDR source has a 380 keV gamma emission, dosimeter energy dependence should be considered. It has been shown previously that FXG has low energy dependence and good water equivalence above 100 keV (Keall *et al* 1999, Kron *et al* 1993).

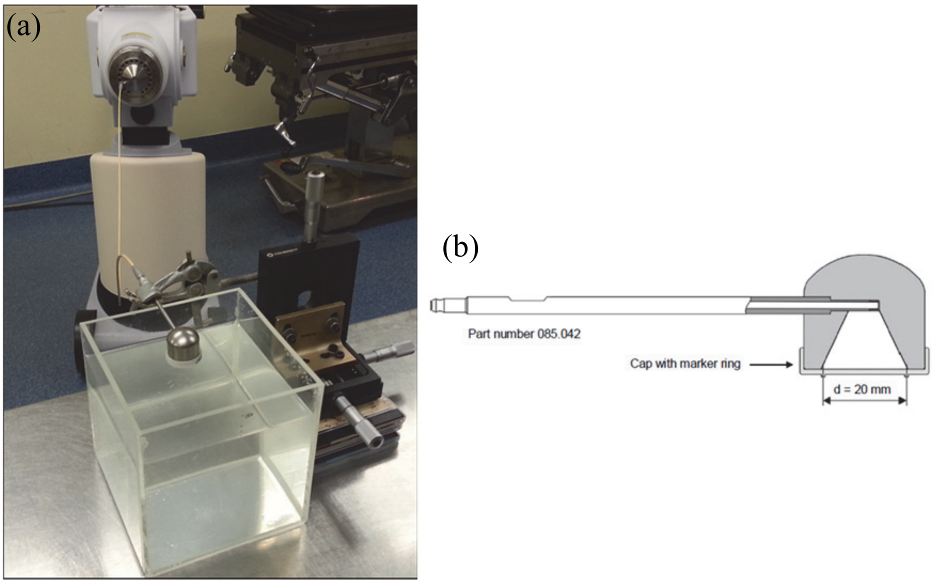

Figure 4.15. (a) Measurement setup with Leipzig applicator positioned by 3 axis micrometer stages. The gel cylinder was immersed in the 15 x 15 x 15 cm water phantom. HDR afterloader is shown in the background. **(b)** HDR Leipzig surface applicator (Nucletron B.V. The Netherlands).

The FXG measured 3D dose distribution is illustrated in figure 4.16. Data could be extracted from close to the surface since the scanner scanned slice by slice. The first scanned slice was at a 2 mm depth in the gel since the gel was level with the top of the cylinder and the first 1 mm of the cylinder was not suitable for scanning. The depth of the first slice was measured from the gel surface to the centre of the scanning laser beam using the distance calibrated motion of the vertical translation stage.

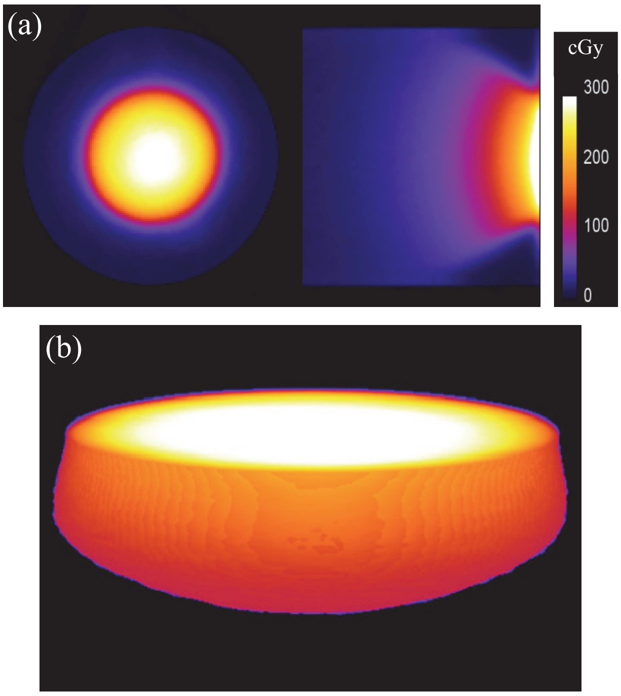

Figure 4.16. Visualisation of FXG 3D measured dose for a 20 mm Leipzig applicator with ^{192}Ir source. The first slice was a 2 mm depth in gel. **(a)** Cylinder axial view (left) and lateral view (right). **(b)** 3D render of the 50 % isodose surface.

Depth dose curves at the central axis are shown in figure 4.17(a) for the full cylinder length of 50 mm. There was good agreement with the manufacturer data which was based upon the work of Perez-Calatayud *et al* (2005) from the University of Valencia. Deviations were within 1 % except at depths < 10 mm where there were up to 5 % differences. Dose accuracy in this high dose gradient region is highly sensitive to positioning accuracy, and a further study was conducted to more closely investigate. To reduce the positional uncertainty (due to the scanning process) a higher resolution scan was taken by decreasing slice thickness to 0.2 mm. This would give an estimated 0.1 mm positioning uncertainty (0.14 mm when combined with setup uncertainty). At the 3 mm depth reference point, 0.1 mm corresponds to about 1 % difference in dose. Figure 4.17(b) shows the depth dose curves from around 3 to 10 mm depths. There was a 1.3 % difference at the 3 mm depth and the other depths were within 1 % thus providing good validation of the planning data at these clinically relevant depths.

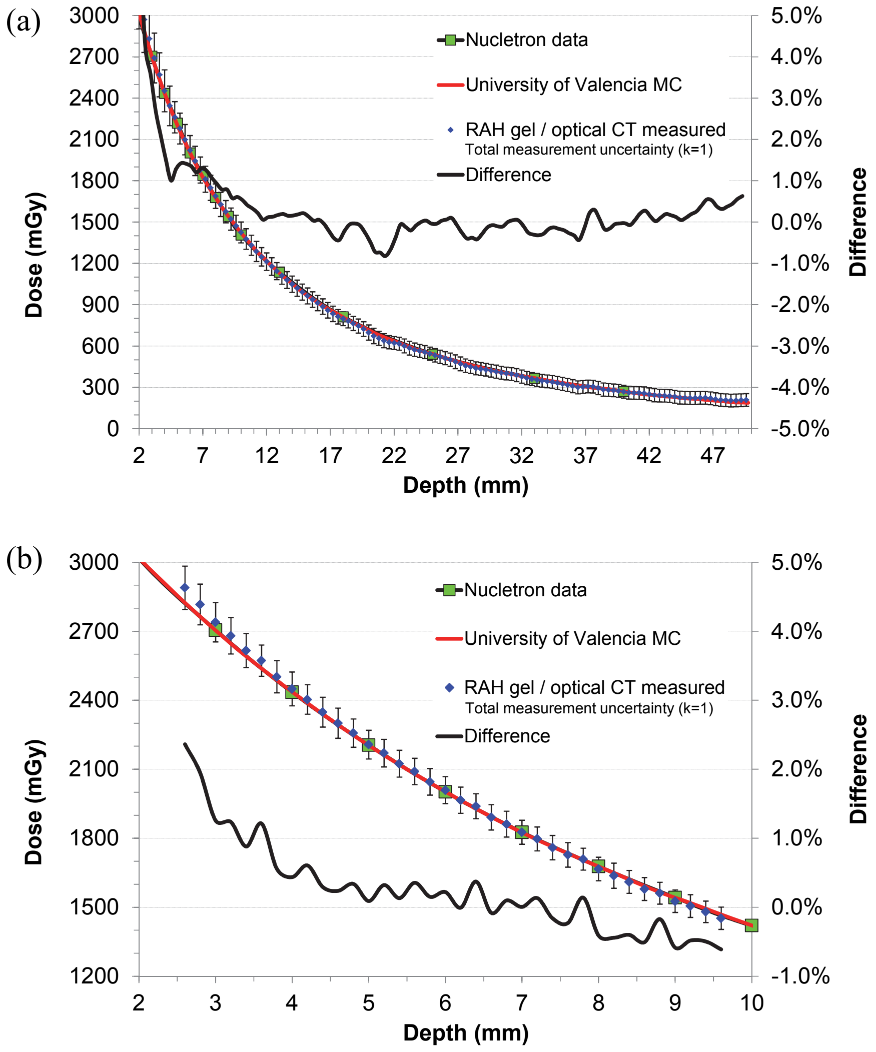

Figure 4.17. FXG measured depth dose for a 20 mm Leipzig applicator. (a) Optical CT scan from 2 to 50 mm depths with a 1.0 mm slice step size. (b) Optical CT slice step size was reduced to 0.2 mm for high resolution data to the 10 mm depth.

Profiles of the 20 mm Leipzig ^{192}Ir beam for the 6 mm depth are shown in figure 4.18. The in-plane direction was parallel to the source travel and cross-plane perpendicular. Measured data was not renormalised, similar to the depth dose data. Figure 4.18(a) shows reasonable agreement between measured and MC in the high dose regions, with some asymmetry noted. Diffusion effects are obvious in the penumbral regions due to the very steep gradients. The cross-plane profiles in figure 4.18(b) give better agreement with MC than the in-plane profiles. Asymmetric in-line profiles are likely to be due to source dwell position uncertainty.

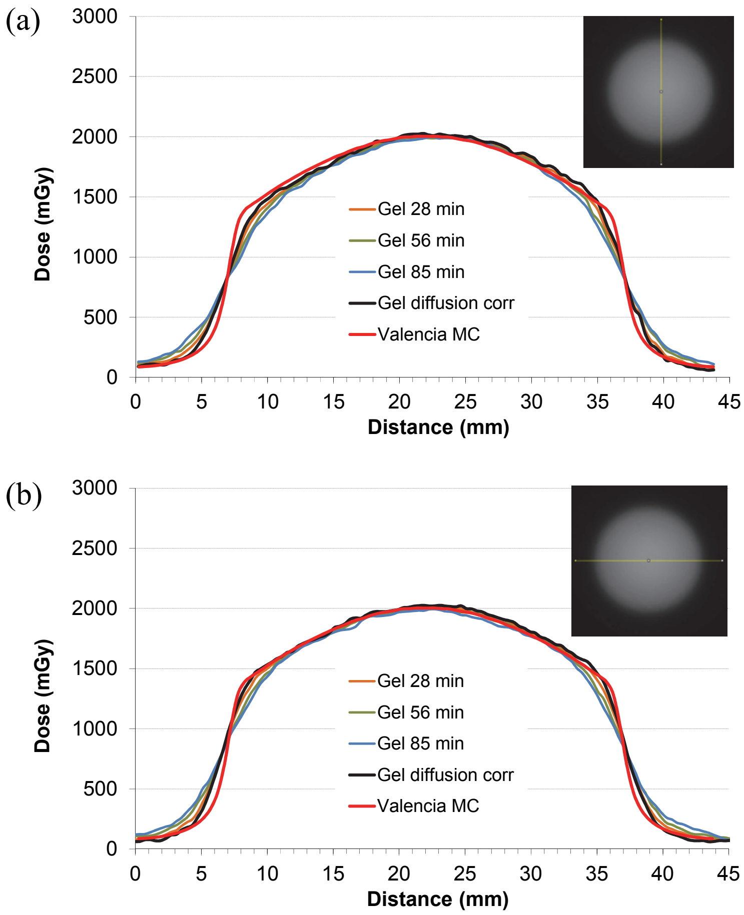

Figure 4.18. FXG measured dose profiles at 6 mm depth for a 20 mm Leipzig applicator. **(a)** In-plane profile, and **(b)** cross-plane profile. The gel was scanned at multiple time points to show Fe^{3+} diffusion, and was compared to Monte Carlo calculated treatment planning data.

4.7 Conclusions

The FXG / optical CT dosimetry system was shown to provide useful true 3D dosimetry. The system was refined by improvements of scanning artefacts, giving improved image quality. FXG dose response and temperature dependence were quantified and a cuvette calibration process was established using the optical CT. A power curve fit was used to improve calibration accuracy for the slightly non-linear FXG dose response at 594 nm. Measurement quality was assessed using simple well defined linac beams. FXG measurements were compared to reference data for depth dose curves, profiles and beam output. Typical agreement was within 1 % except for penumbral regions where Fe^{3+} diffusion limits the accuracy. A simple diffusion correction method was used however, differences of up to 0.5 mm still occur at dose points in high gradients. The application of end to end testing of a clinical SRS system was demonstrated, providing verification of dose levels and positioning accuracy. The true 3D measured dose datasets can be used to extract data in a variety of ways. Another application was demonstrated using an ^{192}Ir brachytherapy surface applicator on the surface of the gel. The MC calculated doses used for treatment planning were validated with the FXG dose measurements, with 1.3 % agreement at the 3 mm reference depth and < 1% for depths greater than 10 mm.

4.8 References

Babic S, Battista J and Jordan K 2008a Three-dimensional dose verification for intensity-modulated radiation therapy in the radiological physics centre head-and-neck phantom using optical computed tomography scans of ferrous xylenol-orange gel dosimeters *Int. J. Radiat. Oncol. Biol. Phys.* **70** 1281-1291

Babic S, Battista J and Jordan K 2008b An apparent threshold dose response in ferrous xylenol-orange gel dosimeters when scanned with a yellow light source *Phys. Med. Biol.* **53** 1637-50

Bero M A, Gilboy W B and Glover P M 2001 Radiochromic gel dosemeter for three-dimensional dosimetry *Rad. Phys. Chem.* **61** 433-435

Keall P and Baldock C 1999 A theoretical study of the radiological properties and water equivalence of Fricke and polymer gels used for radiation dosimetry *Australas. Phys. Eng. Sci. Med.* **22** 85–91

Kron T, Metcalfe P and Pope J M 1993 Investigation of the tissue equivalence of gels used for NMR dosimetry *Phys. Med. Biol.* **38** 139–150

Oldham M, Siewerdsen J H, Shetty A and Jaffray D A 2001 High resolution gel-dosimetry by optical-CT and MR scanning *Med. Phys.* **28** 1436-1445

Olding T, Holmes O and Schreiner L J 2010 Cone beam optical computed tomography for gel dosimetry I: scanner characterization *Phys. Med. Biol.* **55** 2819-40

Olding T and Schreiner L J 2011 Cone beam optical computed tomography for gel dosimetry II: imaging protocols *Phys. Med. Biol.* **56** 1259-79

Pérez-Calatayud J, Granero D, Ballester F, Puchades V, Casal E, Soriano A, and Crispín V 2005 A dosimetric study of Leipzig applicators *Int. J. Radiat. Oncol. Biol. Phys.* **62** 579–584

Ramm D, Rutten T P, Shepherd J, Bezak E 2012 Optical CT scanner for in-air readout of gels for external radiation beam 3D dosimetry *Phys. Med. Biol.* **57** 3853-3868

Thomas A, Newton J, Adamovics J and Oldham M 2011 Commissioning and benchmarking a 3D dosimetry system for clinical use *Med. Phys.* **38** 4846-4857

Chapter 5

Design and development of a dual wavelength optical CT scanner

5.1 Introduction

The process of optical CT scanning had been improved by negating the need for RI matching fluid as an integral part of the scanner. This also makes the scanner largely maintenance free. The fluid-less scanner with FXG gel dosimeters was demonstrated to provide reliable absolute 3D dosimetry and practical operation for clinical applications. Pre-irradiation scanning of the gel dosimeters is required for best results. If this requirement could be avoided there would be further simplification of the scanning process. The use of a second wavelength to provide a reference scan instead of a pre-irradiation scan was considered in this work. Near simultaneous acquisition of the two different beams could also help to minimise artefacts and improve image quality. With sufficient beam matching, artefacts that vary from scan to scan such as dust or marks on gel cylinder may be corrected. Therefore the feasibility of a dual wavelength scanner was initially investigated as described in the following section 5.2, and the development of a prototype dual wavelength scanner is detailed in the section 5.3.

5.2 Feasibility of dual wavelength scanning

The following conference paper was published in the IOP Journal of Physics Conference Series in 2015.

Feasibility of a dual wavelength laser optical CT scanner with in-air gel readout

D Ramm and T P Rutten

Journal of Physics: Conference Series **573** (2015) 012057

doi:10.1088/1742-6596/573/1/012057

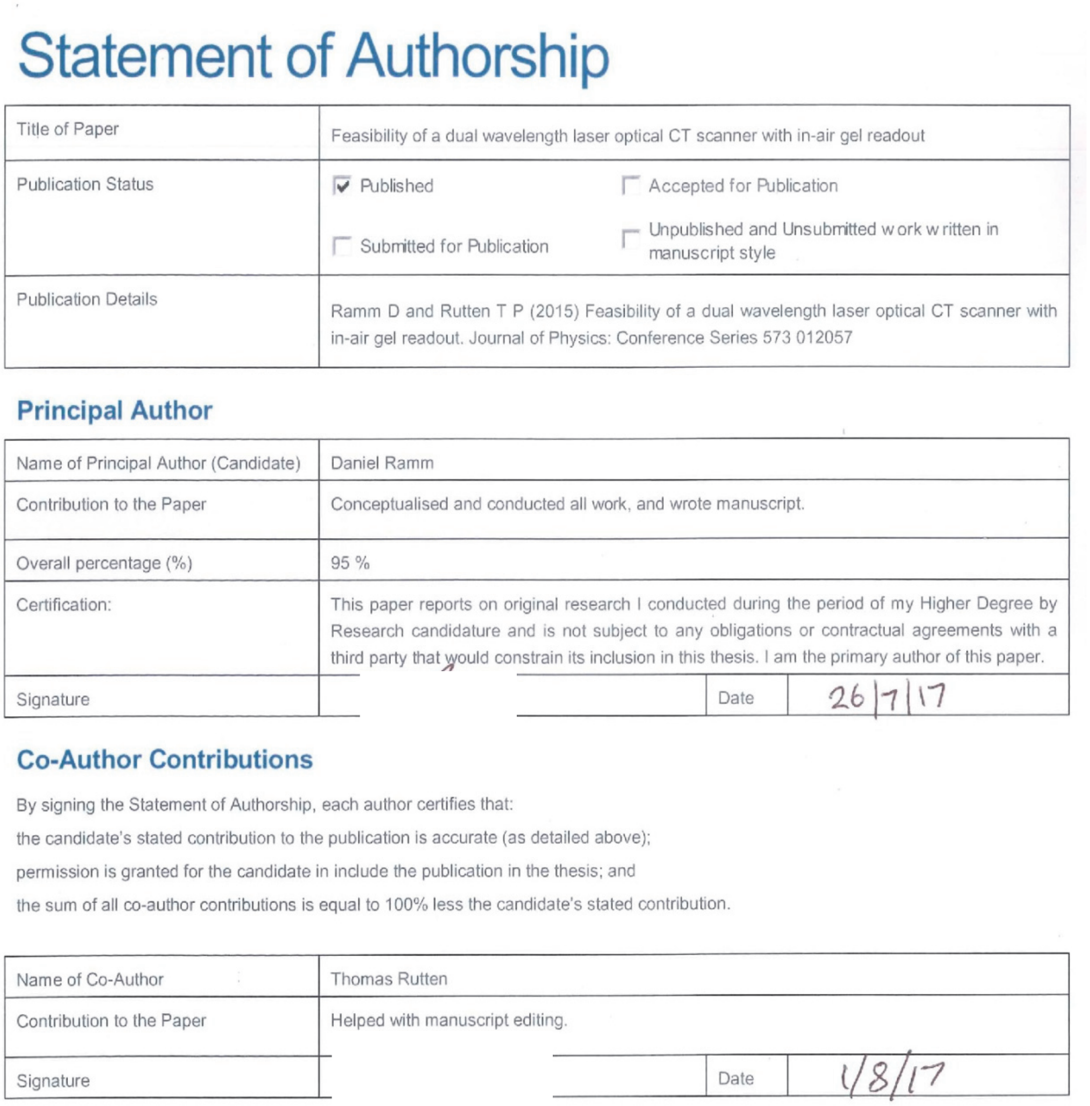

Statement of Authorship

Title of Paper	Feasibility of a dual wavelength laser optical CT scanner with in-air gel readout	
Publication Status	☑ Published ☐ Submitted for Publication	☐ Accepted for Publication ☐ Unpublished and Unsubmitted w ork w ritten in manuscript style
Publication Details	Ramm D and Rutten T P (2015) Feasibility of a dual wavelength laser optical CT scanner with in-air gel readout. Journal of Physics: Conference Series 573 012057	

Principal Author

Name of Principal Author (Candidate)	Daniel Ramm		
Contribution to the Paper	Conceptualised and conducted all work, and wrote manuscript.		
Overall percentage (%)	95 %		
Certification:	This paper reports on original research I conducted during the period of my Higher Degree by Research candidature and is not subject to any obligations or contractual agreements with a third party that would constrain its inclusion in this thesis. I am the primary author of this paper.		
Signature		Date	26/7/17

Co-Author Contributions

By signing the Statement of Authorship, each author certifies that:

the candidate's stated contribution to the publication is accurate (as detailed above);

permission is granted for the candidate in include the publication in the thesis; and

the sum of all co-author contributions is equal to 100% less the candidate's stated contribution.

Name of Co-Author	Thomas Rutten		
Contribution to the Paper	Helped with manuscript editing.		
Signature		Date	1/8/17

8th International Conference on 3D Radiation Dosimetry (IC3DDose) IOP Publishing
Journal of Physics: Conference Series **573** (2015) 012057 doi:10.1088/1742-6596/573/1/012057

Feasibility of a dual wavelength laser optical CT scanner with in-air gel readout

D Ramm[1,2] and T P Rutten[1]
[1]Department of Medical Physics, Royal Adelaide Hospital Cancer Centre, South Australia, Australia
[2]School of Chemistry and Physics, University of Adelaide, South Australia, Australia

E-mail: daniel.ramm@health.sa.gov.au

Abstract. Net optical attenuation in optical CT scanning is usually determined by pre and post-irradiation scans. Replacement of the pre-irradiation scan by a scan of different wavelength, acquired concurrently with the post irradiation scan is proposed. This would result in greater practicality of gel dosimetry and potentially improved image quality. This study indicates that the approach may be viable, however experimental investigation is required for analysis of the prospective benefits of removing inter-scan variations.

1. Introduction

Contemporary optical CT scanners typically require the use of refractive index matching fluid and pre-irradiation scans [1-3][1-4]. Removing both of these requirements simplifies the scanning process and may help make optical CT scanning a more attractive option for dosimetry in the radiotherapy clinic. In this work, the viability of a dual wavelength scanner is investigated for the case of a previously developed fluid-less optical CT at the Royal Adelaide Hospital (RAH) [4][5]. A laser beam of different wavelength scanned sequentially to the measurement laser could provide more relevant reference data than pre-irradiation scanning as dust, fingerprints and other scattering particles are sampled at the time of readout.

2. Dual wavelength concepts and methods

Differential absorption measurements require two wavelengths, λ_1 and λ_2 giving significantly different responses to dose. As refractive index is wavelength dependant, the difference in λ_1 and λ_2 is minimized to mitigate the effects of refractive index change. Therefore the gel dose response absorption spectrum was searched for a steep gradient where λ_1 gives near maximum response to dose, while λ_2 gives a substantially reduced response. Ferrous, xylenol orange gel (FXG) is scanned with the existing RAH scanner using a He-Ne 594 nm laser, providing a suitable λ_1. At increased wavelengths the dose response decreases. For example, at 633 nm the response is approx. 1/3 of that at 594 nm, and drops further to 1/6 at 650 nm. A λ_2 of 633 nm (He-Ne laser) is considered in this work however laser diodes can provide other wavelength options.

The second laser is directed at the rotating mirror as shown in figure 1, resulting in a λ_1 scan across the cylinder followed by λ_2. The measured net transmission for each data point of a projection as a

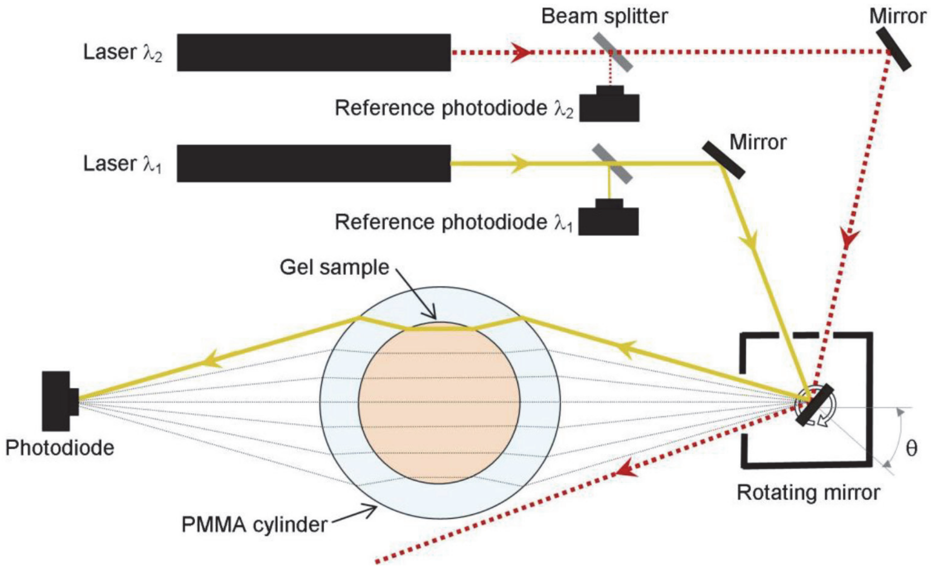

Figure 1. Schematic diagram of the RAH in-air optical CT with the addition of a second laser and reference detector.

function of dose, D and mirror angle, θ (refer figure 1), is:

$$T_{(\lambda_1-\lambda_2)}(\theta,D)=\frac{R_1(\theta,D_1)/R_1^{\mathrm{ref}}}{R_2(\theta,D_2)/R_2^{\mathrm{ref}}}\times\frac{R_2^{\mathrm{air}}/R_2^{\mathrm{ref}}}{R_1^{\mathrm{air}}/R_1^{\mathrm{ref}}} \tag{1}$$

where subscripts 1 and 2 correspond to λ_1 and λ_2, R and R^{ref} are the measurement and reference photodiode readings, and R^{air} is the measurement photodiode reading with the gel cylinder removed from the beam path. The measured net transmission is converted to attenuation and processed as usual, with conversion to dose via gel cuvette calibration samples, scanned by the optical CT.

Conceptually the net transmission comprises a number of elements that may be significant for this scanner configuration:

$$T_{(\lambda_1-\lambda_2)}(\theta,D)=\frac{T_1^{\mathrm{gel}}(\theta,D_1)}{T_2^{\mathrm{gel}}(\theta,D_2)}\times\frac{T_1^{\mathrm{refl}}(\theta)\times T_1^{\mathrm{contam}}(\theta)\times T_1^{\mathrm{defect}}(\theta)\times T_1^{\mathrm{int}}(\theta)}{T_2^{\mathrm{refl}}(\theta)\times T_2^{\mathrm{contam}}(\theta)\times T_2^{\mathrm{defect}}(\theta)\times T_2^{\mathrm{int}}(\theta)} \tag{2}$$

where there is a dosimetric component, T^{gel} for attenuation by the gel sample, and non-dosimetric components, T^{refl} for losses due to reflection at material interfaces, T^{contam} for losses due to contaminant particles in the gel or on the cylinder surfaces, T^{defect} for losses due to defects of gel cylinder, T^{int} for losses/gains due to optical interference. Since the intention is that the non-dosimetric terms will cancel, they need to be examined as a function of wavelength.

Change in refractive indices due to wavelength gives altered ray paths, which may affect all components of equation (2). T^{gel} changes if rays traverse gel differently. T^{refl} depends on ray angle and refractive indices. T^{contam} and T^{defect} change if rays do not intersect the particles or defects in the same way. T^{int} is affected by ray path change and wavelength. Because of these issues, the intent is to minimize change in ray paths rather than apply corrections. Ray paths and reflection losses were calculated using methods similar to previous [4][5], for λ_1 = 594 nm and λ_2 = 633 nm. Refractive indices used in calculations were $n_1^{\mathrm{gel}} = 1.342$, $n_2^{\mathrm{gel}} = 1.340$, $n_1^{\mathrm{PMMA}} = 1.491$ and $n_2^{\mathrm{PMMA}} = 1.489$. The gel PMMA cylinder dimensions were 76 mm outer diameter and 51 mm inner diameter, according to the existing scanner configuration [4][5].

3. Results and discussion

The existing RAH in-air scanner could incorporate an additional laser of different wavelength, while retaining a scan acquisition speed of 5 sec per slice due to the continuous 360° rotation of the scanning mirror. Alignment of the two lasers would be a fundamental aspect of the experimental setup, together with matching of polarization and spot sizes. Two sets of projection data would be acquired in a volumetric scan, one at the measurement wavelength of 594 nm and another at 633 nm, giving net transmission using equation (1). This has the advantage of removing inter-scan variability that may occur when the dosimeter is scanned on two separate occasions. It may be particularly advantageous where positioning reproducibility is limited. A guaranteed benefit is the convenience and time saving of a single scan.

A disadvantage of the proposed dual wavelength method is the loss of around 1/3 of the FXG dose sensitivity (T^{gel}). Some of this loss could be recovered by use of a higher wavelength than 633 nm, at the expense of greater ray deviations.

Calculated ray paths are similar for 594 and 633 nm as shown in figure 2. The differences between red and yellow ray locations at each of the four interfaces of the gel cylinder are given in figure 2(c). As expected, deviations are greater at the exit interfaces, reaching 0.13 mm at the gel-PMMA exit

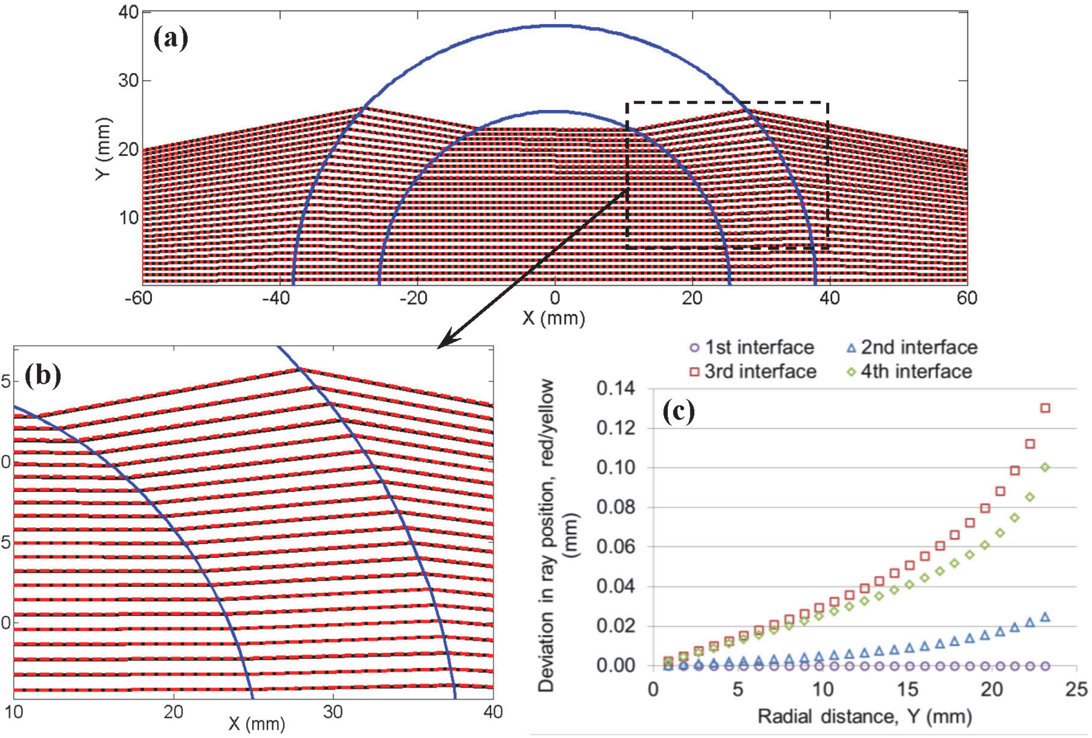

Figure 2. **(a)** Ray tracing through the gel cylinder from left to right for 594 nm (black lines) and 633 nm (dashed red lines). **(b)** Zoomed view of figure 2 (a) in the region of greatest path deviations between 633 and 594 nm (3rd and 4th interfaces). **(c)** Calculated differences in ray positions at each interface of the PMMA cylinder. Radial distance, Y is effectively proportional to the mirror angle, θ. The deviations are < 0.1 mm for the majority of rays and interfaces. Considering a laser beam FWHM of 0.4 mm, the largest deviations while not large, are not completely insignificant. However, their comparison to inter-scan spatial precision may be favourable. If so, both $T_1^{contam}/T_2^{contam}$ and $T_1^{defect}/T_2^{defect}$ could be closer to unity than that of pre-irradiation scanning.

8th International Conference on 3D Radiation Dosimetry (IC3DDose) IOP Publishing
Journal of Physics: Conference Series **573** (2015) 012057 doi:10.1088/1742-6596/573/1/012057

Reflection losses (T^{refl}) occurring as the beam scans across the cylinder must be accounted for as there is variation of at least several percent. A 633 nm beam may be used as a reference since there are small differences compared to 594 nm as shown in figure 3. The difference is 0.1 – 0.2 % at 90 % of the gel radius (where the data is usually truncated during processing). Therefore $T_1^{\mathrm{refl}}/T_2^{\mathrm{refl}}$ should be close to unity.

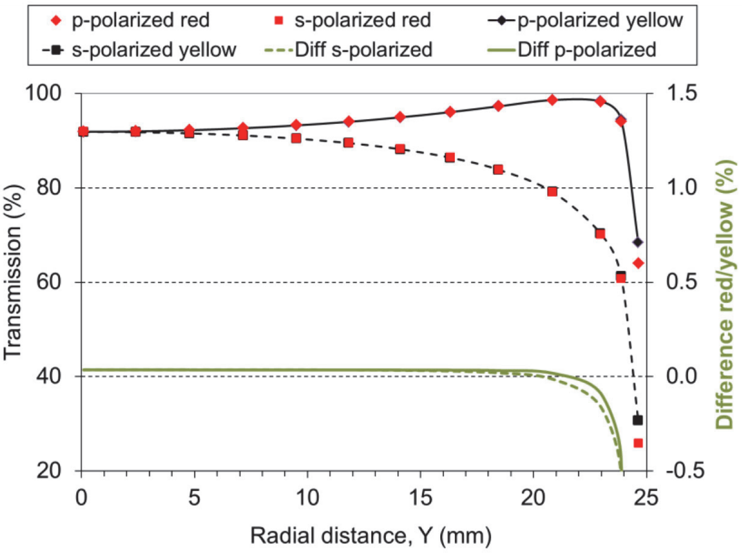

Figure 3. Calculated transmission through the gel cylinder, assuming 100 % transmission for the gel. The differences between 633 nm and 594 nm are given by the right y-axis.

Optical interference must be avoided since $T_1^{\mathrm{int}}/T_2^{\mathrm{int}}$ is unlikely to be unity. The gel cylinder hard coating has been previously noted to cause optical interference [5][6]. To avoid this, the cylinder should have a refractive index matched hard coating or be uncoated.

4. Conclusions

A dual wavelength optical CT scanner has been proposed, allowing both measurement and reference scans to be obtained in one scan, giving improved practicality for optical CT in gel dosimetry. There is the prospect of improved scan quality by better spatial registration of artifact generating flaws in reference and measurement projection data. The tradeoff between loss of gel measured sensitivity and potential improvement of artefacts is to be examined by experimental investigation. While this proposal is specific to the RAH in-air optical CT, it may also be suitable for other scanner configurations and gels/solids.

5. References

[1] Thomas A *et al* 2011 *Med. Phys.* **38** 4846-57
[2] Olding T *et al* 2011 *Phys. Med. Biol.* **56** 1259-79
[3] Xu Y *et al* 2013 *Phys. Med. Biol.* **58** 479-95
[4] Baldock C *et al* 2010 *Phys. Med. Biol.* **55** R1-63
[5] Ramm D *et al* 2012 *Phys. Med. Biol.* **57** 3853-68
[6] Ramm D 2012 *J. Phys.: Conf. Ser.* **444** 012078

5.3 Research publication on the development of the dual wavelength scanner

The following research paper was submitted to Physics in Medicine and Biology on the 20th June 2017 and accepted for publication on 24th January 2018.

A fast dual wavelength laser beam fluid-less optical CT scanner for radiotherapy 3D gel dosimetry I: Design and development

Daniel Ramm

Physics in Medicine and Biology **63** (2018) 045019
https://doi.org/10.1088/1361-6560/aaaa45

IOP Publishing Phys. Med. Biol. 63 (2018) 045019 (15pp) https://doi.org/10.1088/1361-6560/aaaa45

Physics in Medicine & Biology

IPEM Institute of Physics and Engineering in Medicine

RECEIVED
20 June 2017

REVISED
12 December 2017

ACCEPTED FOR PUBLICATION
24 January 2018

PUBLISHED
16 February 2018

PAPER

A fast dual wavelength laser beam fluid-less optical CT scanner for radiotherapy 3D gel dosimetry I: design and development

Daniel Ramm

Department of Medical Physics, Royal Adelaide Hospital Cancer Centre, South Australia, Australia
School of Physical Sciences, University of Adelaide, South Australia, Australia

E-mail: daniel.ramm@sa.gov.au

Keywords: gel dosimetry, optical CT, 3D dosimetry

Abstract

Three dimensional dosimetry by optical CT readout of radiosensitive gels or solids has previously been indicated as a solution for measurement of radiotherapy 3D dose distributions. The clinical uptake of these dosimetry methods has been limited, partly due to impracticalities of the optical readout such as the expertise and labour required for refractive index fluid matching. In this work a fast laser beam optical CT scanner is described, featuring fluid-less and dual wavelength operation. A second laser with a different wavelength is used to provide an alternative reference scan to the commonly used pre-irradiation scan. Transmission data for both wavelengths is effectively acquired simultaneously, giving a single scan process. Together with the elimination of refractive index fluid matching issues, scanning practicality is substantially improved. Image quality and quantitative accuracy were assessed for both dual and single wavelength methods. The dual wavelength scan technique gave improvements in uniformity of reconstructed optical attenuation coefficients in the sample 3D volume. This was due to a reduction of artefacts caused by scan to scan changes. Optical attenuation measurement accuracy was similar for both dual and single wavelength modes of operation. These results established the basis for further work on dosimetric performance.

1. Introduction

An accurate and reliable true 3D dosimetry system with high spatial resolution ($\leqslant 2$ mm) contiguous voxels would be a useful radiotherapy (RT) dosimetry verification tool. Efficiency of the system without the need for special conditions such as a dedicated laboratory or specific expertise would add appeal for routine clinical RT use. True 3D dosimetry provides complete visualisation of complex dose distributions in high spatial resolution (Skyt *et al* 2013, Thomas *et al* 2013). This can be beneficial for commissioning of treatment planning systems (TPS), delivery systems and new techniques, where comprehensive dosimetry data can increase confidence in the tested systems. Validation of treatment techniques such as stereotactic radiosurgery (SRS), stereotactic body RT (SBRT) and gating/tracking RT, particularly those involving use of modulation and requiring high geometric accuracy would ideally include end to end true 3D dosimetry (Schreiner 2015).

There has been widespread uptake of commercial semi-3D dosimetry instruments, claiming to be 3D or 4D, such as ArcCheck (Sun Nuclear Corporation), Octavius 4D (PTW Freiburg) and Delta^4 Phantom (ScandiDos AB). These devices are not complete 3D arrays and consequently do not continuously sample the entire 3D measurement space. They do however offer good practicality and efficiency in measurement and analysis. True 3D dosimetry systems can be used to verify the indirectly derived 3D dose distributions of semi-3D systems (Watanabe and Nakaguchi 2013).

Several main approaches have been developed for true 3D dosimetry by optical CT using radiochromic gel (Kelly *et al* 1998) and polymer gels (Gore *et al* 1996). Other optical CT compatible dosimeters include Presage plastic (Adamovics and Maryanski 2006) and silicone based dosimeters (De Deene *et al* 2015, Hoye *et al* 2015). The other principal readout methods investigated include MRI (Gore *et al* 1984) and x-ray CT (Hilts *et al* 2000). MRI and CT scanners are valuable clinical resources, while optical CT is a relatively inexpensive dosimetry dedicated option. Detailed reviews and details of general developments in true 3D dosimetry are provided in the proceedings for the International Conference on 3D Dosimetry/DOSGEL (De Deene and Baldock 2004, Schreiner 2006, Maris and Pappas 2009, Oldham 2010, Thwaites and Baldock 2013, Olsson *et al* 2015) and review paper by Baldock *et al* (2010).

Optical CT scanners have developed from first generation translating laser beam designs (Gore *et al* 1996) to broad beam scanners with cone beam (Wolodzko *et al* 1999) and parallel beam (Doran *et al* 2001) geometries, reducing scan times from hours to minutes. However, scattered light is more problematic for broad beam detection systems (De Jean *et al* 2006). The development of strategies to reduce scatter related effects is ongoing (Oldham *et al* 2010, Thomas *et al* 2011, Dekker *et al* 2016) as well as a recent return to laser scanning to avoid broad beam issues (Dekker *et al* 2017). Advances in laser beam scanners have decreased scan times to the order of those of broad beam scanners by use of a rotating mirror (Maryanski and Ranade 2001, van Doorn *et al* 2005) and dual galvanometer scanning mirrors (Krstajic and Doran 2007). Fan-beam geometry has also been proposed in an attempt to strike a good balance between scan speeds and scatter rejection (Campbell *et al* 2013).

All of the aforementioned optical CT scanners use a refractive index (RI) matching fluid bath to generate the appropriate light ray paths through the dosimeter for tomographic reconstruction, with the exception of Maryanski and Ranade (2001) whose scanner used a standard thin wall cylindrical gel container, collecting only the central 1/3 of complete projection data. Another prototype scanner has demonstrated a feasible approach to fluid-less scanning, acquiring projection data for 90% of the gel dosimeter diameter using a specifically proportioned PMMA cylinder (Ramm *et al* 2012). Manjappa *et al* (2016) discussed dry scanning using a cone beam scanner and a RI corrected algebraic reconstruction technique (ART), however few quantitative results were provided. Simulation studies of Presage dosimeters scanned in air using an ART have indicated useful reconstruction of up to 65% of the dosimeter diameter (Doran and Yatigammana 2012, Rankine and Oldham 2013). Minimisation of RI fluid volume has been investigated by simulation (Chisholm *et al* 2015) and experimentally (Bache *et al* 2016). While a reduction of RI fluid volume is useful, fluid RI matching and cleanliness issues remain.

Pre-irradiation reference scans have become a common part of quantitative optical imaging to provide a zero dose optical attenuation reference and to assist in reduction of reproducible artefacts (Doran *et al* 2001, Oldham *et al* 2001). In an attempt to simplify the scanning process by removal of the pre-irradiation scan step, a dual wavelength scanner has been proposed (Ramm and Rutten 2015). A second wavelength with reduced dose response may be used as the reference scan instead of a pre-irradiation scan. It was suggested that artefacts changing from scan to scan due to dust and marks on optical surfaces and positioning accuracy could potentially be reduced. Another approach to dual wavelength scanning has been reported for scanning deformable silicone dosimeters where pre-irradiation scans are not viable (De Deene 2015). Dual wavelength scanning was adopted for both laser beam and cone beam scanners featuring RI fluid baths.

This work presents the design and development of a fluid-less dual wavelength optical CT scanner (FDOCT). The basis for the fluid-less optical geometry has been described previously (Ramm *et al* 2012). The feasibility of dual wavelength operation was initially investigated by calculation of light ray paths and reflection losses (Ramm *et al* 2015). Here, design and setup issues are detailed and imaging performance is assessed using dyed water solutions. The measurement quality of optical attenuation in this paper provides indication of the potential for accurate radiation dosimetry. The second part of this work (Ramm 2018), hereafter referred to as Part II, addresses the calibration of optical attenuation to dose for ferrous xylenol-orange gel (FXG) and the quality of the resulting 3D dosimetry. All scanning and processing options (single/dual wavelength and pre-scanning) were performed to investigate the value of each method.

2. Materials and methods

2.1. Dual wavelength scanner design

The optical configuration of the FDOCT scanner was based upon a previous fluid-less optical CT scanner design (Ramm *et al* 2012). RI matching fluid was completely avoided by use of a specifically sized PMMA cylinder of 76 mm outer diameter (OD) and 51 mm inner diameter (ID) as detailed in Ramm *et al* (2012). Parallel rays (within 0.3°) pass through the gel sample by means of a unique combination of cylinder ID/OD ratio, refractive indices of PMMA and gel, and distance from the rotating mirror to cylinder.

For dual wavelength scanning a second set of components were included (laser, beam splitter, reference photodiode and mirror), with the optical arrangement shown in figure 1. The λ_1 (594 nm) and λ_2 (633 nm) laser beams were sequentially swept across the gel cylinder by a continuously rotating mirror. Optical trigger switches on the mirror rotating assembly enabled precise timing of projection data acquisition and synchronisation of the sample rotation stepper motor. Each laser had a reference photodiode detecting about 10% of the beam intensity via a beam splitter. All signals from the measurement PD were normalised to their respective reference PD signal to account for He–Ne laser output fluctuations of typically up to 1%.

Ray paths for the 2 wavelengths need to be coincident for the scanner to work well. Differences in ray paths of up to 0.13 mm (at the gel/PMMA exit interface) were previously determined by ray tracing calculations

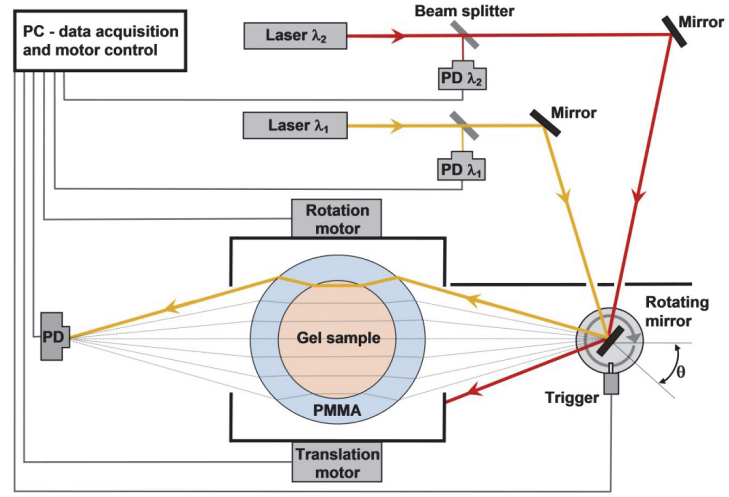

Figure 1. Schematic diagram of the fluid-less, dual wavelength, optical CT scanner (FDOCT). The He–Ne laser beam of λ_1 is swept by a rotating mirror, followed by the λ_2 beam, across a PMMA cylinder containing the gel sample. Photodiodes (PD) are used to measure beam intensities.

(Ramm *et al* 2015). Ray tracing results shown in figure 2 were calculated in a similar manner with the same refractive indices, using first principles of geometrical optics, computed using Matlab (The MathWorks Inc.).

The level of optical scatter detected with the laser beam and single detector configuration was assessed with a gel sample of 4% gelatin (300 Bloom, Type A, porcine) in water, prepared with similar methodology as FXG, minus the active ingredients. All light from the stationary FDOCT cylinder was blocked by a matte black foil sheet, except that allowed through a 4 mm diameter aperture. The sheet with the aperture was located 120 mm from the detector, close to the exit surface of the cylinder. This gave a detector acceptance cone in the gel of 6 mm diameter at the closest point to the detector, increasing to 12 mm at the other side of the gel. The signal detected with and without the aperture sheet was measured for the central rays, and for primary ray locations 10 mm and 20 mm offset from the optical axis. The stray light outside of the acceptance cone was measured by the reduction of detected signal with the aperture sheet in place relative to the unblocked signal.

2.1.1. *Components*

The He–Ne lasers were Melles Griot model 25 LYP 173-230 and 25 LHP 121-230 for 594 nm and 633 nm respectively. Specifications for $1/e^2$ beam diameter were 0.83 mm (594 nm) and 0.59 mm (633 nm) while divergence was 0.9 mrad (594 nm) and 1.35 mrad (633 nm). With a view to beam matching at the dosimeter location, a longer pathlength was used for the 633 nm beam, as per figure 1. Thorlabs model PDA100A silicon 9.8 mm diameter photodiodes (PD) were used for both measurement and reference detectors to maintain similar response characteristics.

The rotating mirror dc motor and drive (Toshiba LSM-206-8D) gave stable alignment and a constant rotation rate of 3600 rpm. Two optical switches (Sharp GP1A51HRJ00F) on the rotating mirror assembly precisely trigger the acquisition of projection data and the dosimeter rotation stepper motor. After 288 projections were acquired for a 360° sample rotation, the vertical translation stepper motor would drive to the next slice position. This resulted in a 10 slice min^{-1} acquisition rate.

LabView (National Instruments) software with a National Instruments model PCIe-6251 16 bit, 1.25 MS s^{-1} multifunction DAQ card was used for data acquisition and motion control. The combination of a 300 kS s^{-1} data acquisition rate, mirror rotation speed and the optical beam geometry provided a nominal 0.3 mm projection data point size within the gel sample.

PMMA gel cylinders were machined to 76.0 + 0.2 mm OD and 51.0–0.2 mm ID to allow refinishing 2 times in nominal steps of 0.2 mm while maintaining the ID/OD ratio within ±1%, which leads to ray deviations <0.1 mm from nominal. The internal and external cylinder walls were highly polished to give good quality optical surfaces. One cylinder was previously hard coated for improved durability (Ramm 2012) and another was left uncoated. Cylinder height of at least 60 mm provided standard 3D datasets comprising 50 slices at 1 mm thickness with a native axial resolution of 0.3 mm. Isotropic 0.3 mm voxels could be acquired however, a compromise between acquisition time and longitudinal resolution was made to limit acquisition time to 5 min in view of the application of imaging FXG samples.

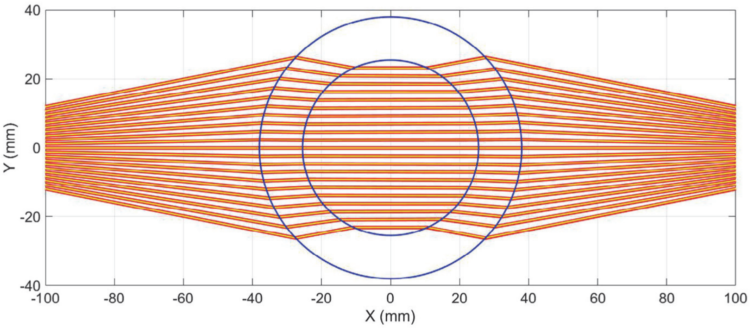

Figure 2. Results of ray tracing with 594 nm (thin yellow line) and 633 nm (thick red line). Light rays pass from left to right through a gel filled PMMA cylinder in air with OD 76 mm and ID 51 mm. The rays are parallel through the gel sample and the red and yellow rays are coincident to <0.2 mm.

2.1.2. Data processing

Optical intensity, I was measured by the PD as shown in figure 1. Measurements of I included dark signal correction for each projection. With a dual wavelength scanner, various scan and processing methodologies can be utilised to suit the application. In this work all scan and processing options were used to investigate the benefits and limitations of each. One option is the conventional single wavelength pre and post-irradiation scans to give the ratio of post-irradiation to pre-irradiation transmittance, as a function of radial position in the sample, Y (as shown in figure 2), at acquisition time points post-irradiation, t_{post} and pre-irradiation, t_{pre}:

$$T_{\mathrm{pre}}^{\mathrm{post}}(Y) = \frac{I(Y(t_{\mathrm{post}}))/I^{\mathrm{ref}}(t_{\mathrm{post}})}{I(Y(t_{\mathrm{pre}}))/I^{\mathrm{ref}}(t_{\mathrm{pre}})} \tag{1}$$

where I and I^{ref} are the measurement scan and reference scan optical intensities respectively. $T_{\mathrm{pre}}^{\mathrm{post}}$ could be calculated for either λ_1 or λ_2 to give a high or low measured dose response.

If pre-irradiation scanning is undesirable or unavailable, the pre-irradiation reference scan data can be replaced by the second wavelength scan data. We then have the ratio of transmittance for λ_1 and λ_2:

$$T_{\lambda_2}^{\lambda_1}(Y) = \frac{I_1(Y(t_{\mathrm{post}}))/I_1^{\mathrm{ref}}(t_{\mathrm{post}})}{I_2(Y(t_{\mathrm{post}}))/I_2^{\mathrm{ref}}(t_{\mathrm{post}})} \times \frac{I_2^{\mathrm{air}}/I_2^{\mathrm{ref}}}{I_1^{\mathrm{air}}/I_1^{\mathrm{ref}}} \tag{2}$$

where I_1 and I_2 are measurement scan intensities for λ_1 and λ_2 respectively, and I^{air} are measurements with the gel cylinder removed. The air scan data accounts for the differences between λ_1 and λ_2 laser outputs and PD response. An air scan was acquired for each scan session, however it potentially could be a periodic maintenance check for the system.

For dual wavelength scanning additional sets of projection data, I^{water} were applied to correct for a PD wavelength dependant angular response and other minor differences in the scans of the two beams. Scans of each gel cylinder filled with water instead of gel were acquired and saved to file for subsequent use as a cylinder specific correction. The water scans would only need reacquisition if the optical geometry or componentry were changed. The ray paths for the water filled cylinder were sufficiently close to that of gel for this purpose. The water scan corrected transmittance ratio is:

$$T\mathrm{w}_{\lambda_2}^{\lambda_1}(Y) = T_{\lambda_2}^{\lambda_1}(Y) \times \frac{I_2^{\mathrm{water}}(Y(t))/I_2^{\mathrm{ref}}(t)}{I_1^{\mathrm{water}}(Y(t))/I_1^{\mathrm{ref}}(t)}. \tag{3}$$

Another option with pre-irradiation scanning is normalisation of post-irradiation dual wavelength transmittance to pre-irradiation dual wavelength transmittance:

$$T_{\lambda_1/\lambda_2}{}_{\mathrm{pre}}^{\mathrm{post}}(Y) = \frac{T_{\lambda_2}^{\lambda_1}\left(Y(t_{\mathrm{post}})\right)}{T_{\lambda_2}^{\lambda_1}\left(Y(t_{\mathrm{pre}})\right)}. \tag{4}$$

The motivation for this approach revolves around the possibility of improved image quality due to the mitigation of artefacts caused by particulate contamination, marks on the gel cylinder and gel defects that change from scan to scan. Both pre and post scans have correction provided by the second wavelength scan.

Data processing and image reconstruction was performed using Matlab with the major steps shown in figure 4. Options were provided for the projection normalisation method and for down-sampling to increase the voxel size if desired. Pre-reconstruction signal processing included a 1D 5 × 5 median filter. Dose calibration was not required for the image analysis study in this paper. Maps of attenuation coefficients were used with post-reconstruction 5 × 5 pixel median filtering usually applied to each 2D reconstructed slice for analysis applications. Details of dose calibration are provided in Part II of this work (Ramm 2018).

The optical geometry of this scanner allows collection of projection data to approximately 90% of the gel diameter. The missing projection ends are extrapolated to the known physical cylinder ID ($r_{\text{gel}} \times 2$), mitigating a cupping artefact that can extend into the reconstructed 90% diameter (Jordan 1999, Ramm *et al* 2012). The extrapolation method assumes a constant optical attenuation coefficient from the line integral of optical attenuation at the projection end points, P_{end}, giving the extrapolated line integral optical attenuation, P_{extrap} as a function of radial distance, y in the missing data regions:

$$P_{\text{extrap}}\,(y) = P_{\text{end}} \frac{\sqrt{r_{\text{gel}}^2 - y^2}}{\sqrt{r_{\text{gel}}^2 - y_{\text{end}}^2}} \tag{5}$$

where y_{end} is the radial distance of the last measured projection point.

Filtered backprojection was by the Matlab inverse Radon transform function, using spline interpolation and the Shepp–Logan filter. Reconstructed pixel values were the difference in optical attenuation coefficient, $\Delta\mu_{\text{CT}}$ from post to pre-scan or λ_1 to λ_2:

$$\Delta\mu_{\text{CT}} = -\ln\left(T\right)/p \times 10\,(\text{cm}^{-1}) \tag{6}$$

where p is the reconstructed pixel size in mm and T is from equations (1), (3) or (4). The precise value for p was derived from digital calliper measurements of each cylinder and the data acquisition rate. The 'pre-scans' for the dyed water scans in this work were undyed water.

2.1.3. *Cuvette scanning in spectrophotometer mode*

For dose calibration purposes, 1 cm pathlength PMMA cuvettes were mounted on FDOCT instead of the gel cylinder as shown in figure 3(b). A removable adaptor plate located cuvettes reproducibly at the centre of the cylinder rotation mount, fixed at the zero rotational position. A 3 mm central axis portion of the laser beams' sweep at the cuvette was used to measure the transmittance of cuvette samples. Cuvette transmittance, T_{cuv} was calculated using equations (1), (2) or (4), matching the method for the cylinder projection data. Transmittance data was converted to optical attenuation coefficients:

$$\Delta\mu_{\text{cuv}} = -\ln\left(T_{\text{cuv}}\right)/l \times 10\,(\text{cm}^{-1}) \tag{7}$$

where l is the cuvette pathlength in mm. While the nominal value for l was 10 mm, each cuvette batch was measured with digital callipers to minimise the uncertainty in pathlength.

Using the cylinder scanning system for cuvette based optical attenuation measurements ensures the same beam spectrum and the same narrow beam geometry for both, avoiding differences in optical attenuation measurement that can occur when different instrumentation is used for calibration of an optical CT system.

Transmittance measurement accuracy and reproducibility was assessed with a set of neutral density filters (CF-VIS-ND, CVI Melles Griot) with NIST traceable calibration, utilising the cuvette scan configuration. Filter nominal transmittances were 0.8, 0.5, 0.3 and 0.1, with certified transmittance values at 590 nm and 635 nm differing by <0.1% for each filter.

2.1.4. *Gel dosimeter*

The optical CT scanner in this work can accommodate different hydrogels but is best performing when tuned to a particular gel RI and dose response spectra. Mirror and detector focal distances can be adjusted for specific gels to give best achievable ray paths, although there is not a high degree of sensitivity to RI in the range of standard dosimetry hydrogel RIs (Ramm *et al* 2012). For alternative gels, image quality would typically be comparable or better, depending on gel RI, to the results shown in figure 8(c) with the un-optimised extrapolation artefact. The FDOCT has been tuned for the ferrous xylenol-orange gelatine (FXG) dosimeter. FXG has been extensively studied (Schreiner 2004). It is optically absorbing, has high dose sensitivity and is simple to manufacture. Ferric ion diffusion is the clear major disadvantage, but the effects can be mitigated by scanning within 30 min of irradiation, with scan times of <10 min. This will typically limit penumbral broadening to the order of 1 mm for steep RT dose gradients, if no diffusion corrections are applied (Olding *et al* 2011, Babic *et al* 2009).

The peak dose response of FXG occurs at around 590 nm and beyond that, there is a steep drop in absolute optical attenuation and dose response spectra (Kelly *et al* 1998). At 633 nm, the dose response is 1/3 of the peak, thus reducing the dual wavelength dose sensitivity to 2/3 of the peak (Ramm *et al* 2015).

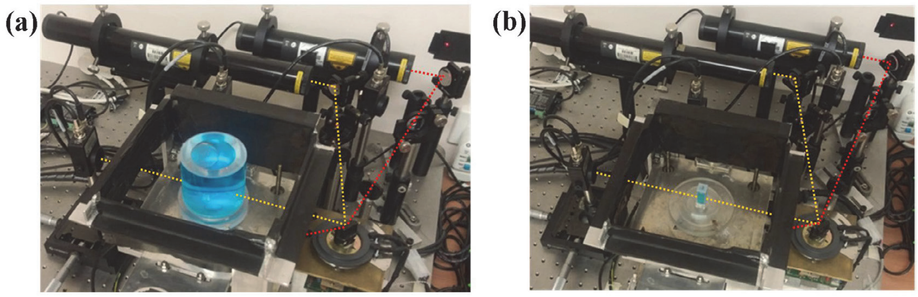

Figure 3. Photographs of the FDOCT scanner with (a) scanning cylinder in optical CT mode, and (b) cuvette in spectrophotometer mode. Both containing blue dyed water as used in this study. Laser beam paths are illustrated by dashed lines.

2.2. Scanner setup and tuning

For single laser operation, scanner tuning mainly consists of focal distance adjustments for rotating mirror and PD detector, and alignment of the beam to give a scan plane perpendicular to the cylinder axis. Lasers were always oriented to give a p-polarised beam as with previous work (Ramm *et al* 2015). A dual laser configuration requires laser beam size and position matching. Spot size matching was assisted by matching the laser type (He–Ne), and by setting the path length from laser to the gel cylinder centre to suit the beams' diameter and divergence. The second laser was aligned to the first, beginning with parallelism in the horizontal plane by measurement of beam height from the optical bench at locations separated by many times the gel diameter. Vertical alignment was obtained by sighting the beams' coincidence at the mirror, at the gel location and about 1 m beyond. Measurement of vertical alignment accuracy was made by translating a knife edge at the gel location vertically across the beams and recording PD output at each edge position. Horizontal alignment was achieved by scanning in air a 0.1 mm diameter wire fixed to the sample mount and then normalising the 594 nm projection to the 633 nm, where perfect beam matching would result in a completely cancelled wire from the normalised projection. Alignment to sub data point size (0.3 mm) was accomplished by fine adjustment of the fixed mirror kinematic mount.

During scanner development the PD angular dependence mentioned in section 2.1.2 was noted and while tilting the detector would change the response, a difference between the two beams would remain. Correction of the effect was made by use of water filled cylinder scans.

The extrapolation region of the reconstructed slices can be prone to artefact generation (Ramm *et al* 2012, Ramm 2013). This was due to sensitivities to the cylinder centre of rotation alignment, projection data distance calibration and alignment of projection data to the cylinder central axis. The accuracy of cylinder rotation was measured using a dial gauge. Distance calibration was tuned by adjustment of the mirror to cylinder focal distance to make the number of data points corresponding to the physical gel diameter close to a multiple of the data point size.

2.3. Image quality

While the imaging of complex objects may provide qualitative appeal, simple 3D uniform objects can be very informative of a system's imaging quality. Artefacts, uniformity, noise, reproducibility and quantitative accuracy can be assessed, and some of these imaging qualities tend to be the more problematic for optical scanners. In this work, uniform objects were created with water and dyed water solutions. Blue food dye (Queen Fine Foods P/L) was used to make a stock solution that was diluted to various nominal levels. The blue dye optical attenuation at 594 nm was 39% of that at 633 nm. This differential is comparable to that of FXG, albeit with the wavelengths reversed. Nonetheless it is a useful test of the dual wavelength scanning and reconstruction process, giving negative measured optical attenuation using unmodified data processing. These negative values were inverted to simplify presentation of results. Each test solution of given concentration was mixed and poured into scan cylinders and cuvettes, scanned immediately 4 times (4 × 5 min) and changed to the next concentration, without reliance on longer term stability of the solutions.

Geometric distortion and high contrast spatial resolution were assessed in the initial in-air scanner proof of concept (Ramm *et al* 2012). Geometric distortion is governed by the optical ray paths generated by the gel and cylinder. High contrast spatial resolution is primarily determined by source and detector characteristics. These imaging properties did not change significantly with the dual laser scanner build. In Part II (Ramm 2018), the imaging quality for low contrast objects was assessed using gel dose distributions since test objects created by irradiating gel samples provide high quality optical objects for imaging that are precisely relevant for the final application.

2.3.1. Artefacts

Early in scanner development, reasonable image quality was readily achieved for some slices of a complete volumetric scan (Ramm *et al* 2012), but rarely for every slice of the volume. Readily visible artefacts have been investigated and either minimised through setup or by correction of reproducible effects.

Some potential artefacts and those observed during scanner development are summarised by a conceptual expression of the total transmittance as the product of a number of transmittance components including non-dosimetric, potentially artefact generating components as follows:

$$T\,(\mathrm{OD}) = T^{\mathrm{gel}}\,(\mathrm{OD}) \cdot T^{\mathrm{path}}\,(\mathrm{OD}) \cdot T^{\mathrm{stray}} \cdot T^{\mathrm{refl}} \cdot T^{\mathrm{contam}} \cdot T^{\mathrm{defect}} \cdot T^{\mathrm{int}} \quad (8)$$

where T^{gel} is the internal transmittance for the ideal parallel ray path through the gel sample, T^{path} is a component for pathlength error due to non-ideal ray paths, T^{stray} is for losses or gains due to scattered and stray light, T^{refl} is for reflection losses at interfaces that change with angle of incidence, T^{contam} is for transmittance losses due to foreign contaminant particles or marks on surfaces, T^{defect} is for transmittance losses due to fixed defects of optical surfaces/materials and T^{int} is for optical interference effects (Ramm 2013).

Apart from T^{gel}, all components of equation (8) should ideally be unity, and if not, they can be cancelled by normalisation using equation (1) or (2) when the transmittance component matches in the reference data, such as T^{refl}, T^{contam} and T^{defect}. The level of success depends largely on the degree of repositioning accuracy for pre-irradiation scans, and beam and ray path matching for dual wavelength scanning. The dual wavelength water scan correction of section 2.1.2 provided point by point normalisation that gave improvement of T^{int} for the hard coated cylinder, similarly to the previous pre-irradiation reference scan approach (Ramm 2013). T^{stray} was not observed to be problematic since the scanner configuration of laser beam, single point detector and single lens component was designed to largely avoid issues due to reflected and scattered light.

T^{path} is a dose dependant artefact component and cannot be diminished by simple correction or normalisation. To understand the importance, this effect was modelled using ray tracing to calculate pathlengths in the gel sample and generate simulated projections, then used as input to the usual data processing/reconstruction routine. Reconstructed data was analysed using ImageJ (National Institutes of Health, USA) to assess the nature and extent of the T^{path} artefact.

The extrapolation artefact mentioned in section 2.2 was not included in equation (8) because it is a reconstruction artefact due to distance calibration and alignment rather than a transmittance measurement issue. It was addressed by scanner setup tuning and data processing as opposed to transmittance normalisation.

Light source stability and detector response characteristics are other sources of error in transmittance measurements. Residual uncorrected laser output fluctuations were observed because the measured reference PD signals were not completely adequate to remove all of the effects of laser output fluctuations. Low level, high frequency fluctuations were not fully accounted for with the present setup, likely due to sampling limitations of the data acquisition card and differences in PD amplified signal response times (refer to further details in section 3.2). For the PD detector, angular/positional dependence was noted. This effect cancels with pre-irradiation reference scans, however for dual wavelength scans, differences were corrected by the use of the water scans (equation (3)).

2.3.2. Uniformity and noise

At each step of dyed water optical density, random noise was quantified by 2 SD of reconstructed voxel values in a 45 mm (88% of diameter) FOV, and structured noise was defined as 2 SD of 3 × 3 (0.9 × 0.9 mm) binned pixel values in a 45 mm (88% of diameter) FOV for each reconstructed slice of 50 mm length volume. Uniformity was calculated using the maximum and minimum pixel values ((max − min)/(max + min)) of the 3D volume with 10 × 10 (3 × 3 mm) binned pixels in a 40 mm (78% of diameter) FOV for each reconstructed slice. Two dimensional reconstructed slices and 1D line profiles were used to visualise the nature of non-uniformities and noise.

2.3.3. Quantitative imaging accuracy

The accuracy of reconstructed linear optical attenuation coefficients was assessed by the average value of a cylinder central axis 40 mm diameter ROI for each reconstructed slice. Cuvette attenuation coefficients were determined as described in section 2.1.3 as the reference for the reconstructed attenuation coefficients.

2.3.4. Spatial resolution

The focus of this work was on accurate optical attenuation measurements with low noise and high uniformity, however spatial resolution was also assessed to verify that this scanner configuration and data processing had resulted in retention of suitable resolution for scanning radiotherapy dose distributions. A fine wire of 0.1 mm diameter was scanned and reconstructed and then line profiles across the wire were extracted to calculate the modulation transfer function (MTF) similarly to previous work (Ramm *et al* 2012). The intrinsic MTF was computed with de-convolution of sampling size and test object size. RT dose gradients were related to spatial

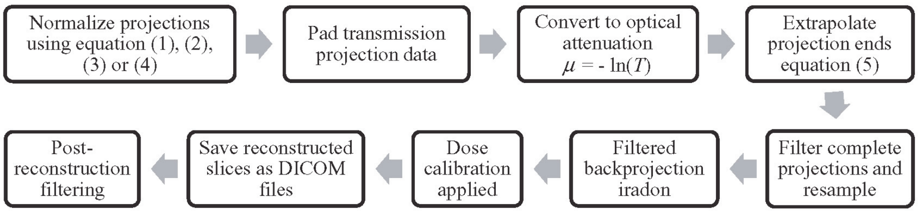

Figure 4. Data processing diagram for reconstruction of measured optical attenuation and gel dose in the optical CT scanning cylinder.

frequency by fitting normal cumulative distribution functions to dose penumbrae and using the σ fit coefficient values to calculate spatial frequencies.

3. Results and discussion

3.1. Optical CT scanner design

The addition of a second laser was possible without any reduction in scan speed for this fast laser beam optical CT technique. Scan speed was 10 slices min^{-1}, giving a 5 min acquisition time for a typical 50 slice scan of voxel size 0.3 × 0.3 × 1.0 mm, or 17 min for 0.3 mm isotropic voxels. This level of acquisition time is comparable to broad beam scanners (Olding *et al* 2010, Thomas *et al* 2011), although a sub-minute cone beam scanner has been recently reported (Chang *et al* 2016).

Some issues of stray light reaching the detector from reflections were addressed. The PD detector had a reflective surface, so it was tilted to avoid back-reflection into the sample that would then reflect back to the detector. All surrounding potentially reflecting surfaces were covered with matte black foil with a rectangular aperture for the light sources. Inter-reflections from optical surfaces in the beam path can be a source of inaccuracy in transmittance measurements, so the number of air to solid optical interfaces was minimised. The remaining inter-reflection from the cylinder back wall to front wall is less than 0.2% reaching the detector (Ramm *et al* 2012). Change of reflection losses (with angle of incidence) in the primary beam were experimentally accounted by use of normalisation reference scans as per section 2.1.2.

Parallel light ray paths through the gel were previously calculated and verified for 594 nm (Ramm *et al* 2012) and calculated for 633 nm (Ramm *et al* 2015). In this work the matching of 594 nm and 633 nm paths is demonstrated by alignment tuning results in section 3.1.1. The linearity of ray location in the gel sample as a function of scanning mirror angle is shown in figure 5. This means that for a constant data acquisition rate, projection data is spatially accurate without the need for correction as required by some oscillating mirror systems (Xu and Wuu 2013).

Optical interference effects when using coherent light sources can be reduced by using point by point normalisation for thin film interference and by filtering central axis interference (Ramm 2013). For samples of high quality (flat and parallel surfaces) and with small pathlengths such as cuvettes or filters, optical interference can be a significant effect. It is addressed by the averaging of interference fringes since the interference waveform is a modulation of the true signal (Mielenz *et al* 1973). This was required particularly for the neutral density filters in section 3.1.2.

Accurate quantitative imaging requires temporal and spatial stability of the light source. The He–Ne lasers used here have temporal fluctuations of output of up to about 1%. Correction was made by reference PD for each laser. Detector linearity is another major essential requirement. Both source and detector performance for simple transmittance measurements was confirmed in section 3.1.2 using the spectrophotometer mode of operation.

The magnitude of optical scatter was verified with a gelatin gel 'blank' sample as described in section 2.1. The stray light component of the total signal was determined at various primary ray locations. The mean stray light component was 0.2 ± 0.1% (1 SD) for both 594 and 633 nm beams. This indicates a low level of scatter detection and negligible variation over a projection.

3.1.1. Scanner tuning

Spot size matching was achieved by varying the pathlength distances from the exit of the laser to the centre of the scanner rotation stage. Figure 6 shows the matching of a scanned 0.1 mm wire where 594 nm and 633 nm scans gave wire FWHM's matched to 0.01 mm. The beams were translated to align within 0.01 mm in figure 6(a), from an initial 0.10 mm misalignment in figure 6(b). This level of beam matching was required to limit deviations of the 594 nm to 633 nm ratio to 1%. The residual ripple is of sufficiently high spatial frequency to be smoothed by pre-reconstruction filtering.

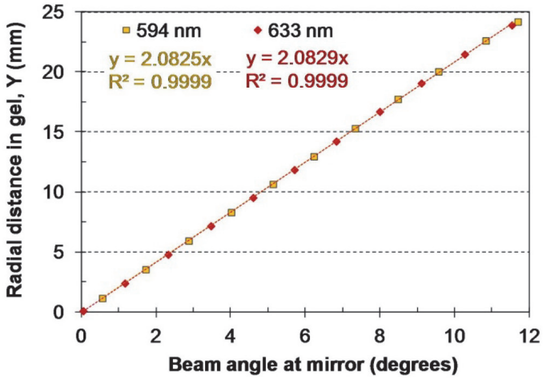

Figure 5. Linearity of ray location in gel with mirror angle, from ray tracing calculations. With the mirror rotating at constant angular velocity, ray locations in gel are linear with a uniform rate of data acquisition.

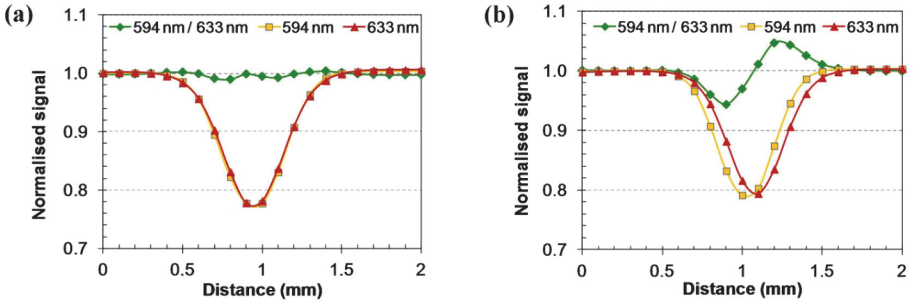

Figure 6. Laser beam alignment and spot size matching by horizontal scanning of a 0.1 mm diameter wire orientated vertically. (a) Final alignment giving maximum deviation of 1% for the 594 nm to 633 nm signal ratio. (b) Prior to displacement fine tuning with 5% deviations for the 594 nm/633 nm ratio at 0.1 mm misalignment of 594 nm and 633 nm beams.

To minimise an extrapolation artefact where the outer extrapolated region is visibly inaccurate, the pixel size calibration multiplied by the number of pixels corresponding to the gel sample diameter (cylinder ID) needs to close to the physical distance. The scanning mirror focal distance was fine-tuned to give a pixel size close to a multiple of the cylinder ID. This minimised the artefact and provided a very accurate pixel size calibration. A relative error in reconstructed pixel size gives the same relative error in reconstructed optical attenuation values when a non-reconstruction method is used for calibration. Section 3.2 provides illustration of the extrapolation artefact.

3.1.2. Spectrophotometer mode

Cuvette based optical attenuation measurements were possible with the scanner functioning as a 594 and 633 nm spectrophotometer. The accuracy and reproducibility of absolute optical transmittance using calibrated neutral density filters is shown in figure 7. The mean of 5 repeated measurements was within 0.8% for all filters, and 3 standard deviation random variations were 0.2% maximum. The ratios of 594 to 633 nm measurements were within 0.2% of the reference values. These results were achieved by addressing the considerations for accurate transmittance measurement such as light stability, detector linearity, sample obliquity, inter-reflections and optical interference.

Cuvette mounting was the same as the calibrated filters since they had the same 12 mm square external size as the filter holders. The cuvette pathlength was measured with digital callipers and confirmed within 0.2%. With the FDOCT calibrated by the reference filters, cuvette based measurements of relative optical attenuation were used as the reference for reconstructed attenuation coefficients of uniform water dye solutions in this study.

3.2. Artefacts

Optical artefacts in full 3D reconstructed volumes can be challenging to avoid in optical CT scanning. Artefacts are generally in the form of peripheral circular bands near sample edges, global cupping, rings, localised patches of non-uniformity, structured optical noise and streaking. For this scanner a number of sources of optical

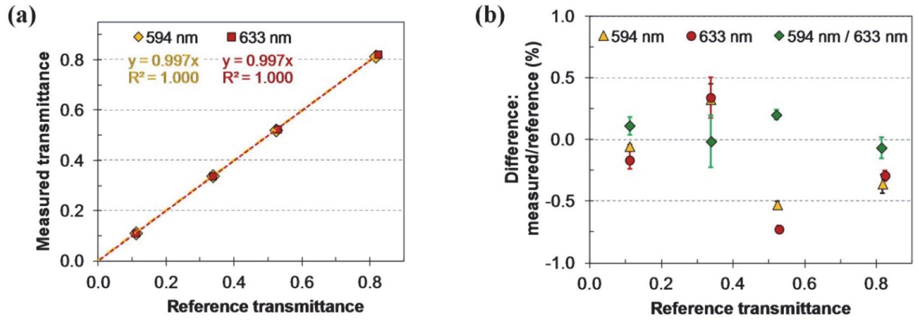

Figure 7. Measurement accuracy of the FDOCT in spectrophotometer mode using a set of calibrated spectrophotometer neutral density filters (reference transmittance). (a) Linearity of transmittance at 594 and 633 nm. (b) Differences between measured and reference transmittance, with error bars of 3 SD, $n = 5$.

artefacts were identified as given in equation (8). Artefact reduction is a continuous process of improvement by discovery of the next most significant artefact after the most obvious has been reduced.

Good spatial alignment of reference and measurement scans results in cancellation of the T^{refl} and T^{defect} components for both single wavelength and dual wavelength approaches. The T^{contam} component is prone to change from scan to scan so there can be improvement with the single scan dual wavelength method. Figure 8(a) shows streaking typical of T^{contam} if the cylinder has not been cleaned and the improvement with dual wavelength normalisation. Dual wavelength has an advantage if T^{contam} changes from scan to scan.

The T^{int} component can be avoided by use of an uncoated cylinder, while a cylinder with a thin film coating can give optical interference patterns that can be minimised by point by point normalisation (Ramm 2013). Since interference patterns differ for the different wavelengths, dual wavelength scans utilise an additional set of water scans as per equation (3). These water scans also provide correction for a small non-uniformity due to PD response that differs for the two wavelengths (section 2.3.1), and minor inter-reflection effects near the central axis, as shown in figure 8(b).

Aside from the interference patterns that were mitigated by water scans, the coated cylinder overall performance was comparable to that of the uncoated cylinder. Thus, hard coating was not viewed as distinctly beneficial since the cost of the coating may exceed that of cylinder minor refinishing by machining and polishing. However, increased scratch resistance may provide some benefit in the longer term, depending on usage.

Figure 8(c) illustrates the tuning of the extrapolation data. The unoptimised reconstruction is representative of water scans with the scanner tuned for the RI of gel. This minor artefact does not propagate into the non-extrapolated reliable FOV (rFOV), thus the scanner was not re-tuned from gel to water for the image quality scans of this work using dyed water solutions. While a good reconstruction of a uniform solution or gel including the extrapolated FOV (eFOV) can be achieved, the eFOV is unreliable due to the assumption of uniform optical attenuation coefficients in equation (5). A convenient benefit of the extrapolation optimisation is that an accurate distance calibration is obtained, i.e. reconstructed pixel size, which is required for accurate calibration using cuvettes. A pathlength error in either pixel size or cuvette pathlength gives a proportional error in optical attenuation and hence dose measurement.

After reduction of the aforementioned artefacts, the remaining notable effect is relatively low level structured noise giving a mottle pattern, shown in the optimised image in figure 8(c). This appears to be a residual difference in measurement and reference PD signals where high frequency laser output fluctuations of the order of the sampling rate (300 kHz) are sampled differently (the laser stability issue mentioned in section 2.3.1). The pattern is reduced with finer structure for the more stable 633 nm laser. This effect was not investigated in further detail due to the low level of deviations, however it was anticipated that improvements may be possible through closer examination of detector response times (using different gain levels) and performance of the analogue to digital converter regarding timing in multichannel acquisitions.

Another source of artefact in equation (8) is T^{path}, which is optical density dependant. The ray paths for this scanner are not exactly parallel (Ramm *et al* 2012) as the reconstruction algorithm assumes. An example of the effects of pathlength error due to the non-ideal ray paths is shown in figure 9. The minor bowing artefact is not typically visible in actual scans because the variations are of similar magnitude to the measurement noise and non-uniformity of real scans. Thus T^{path} does not limit the current system. Figure 9 shows that for some of the higher quality measurements achieved, the bowing artefact is somewhat apparent. For samples with greater attenuation, T^{path} may become more significant.

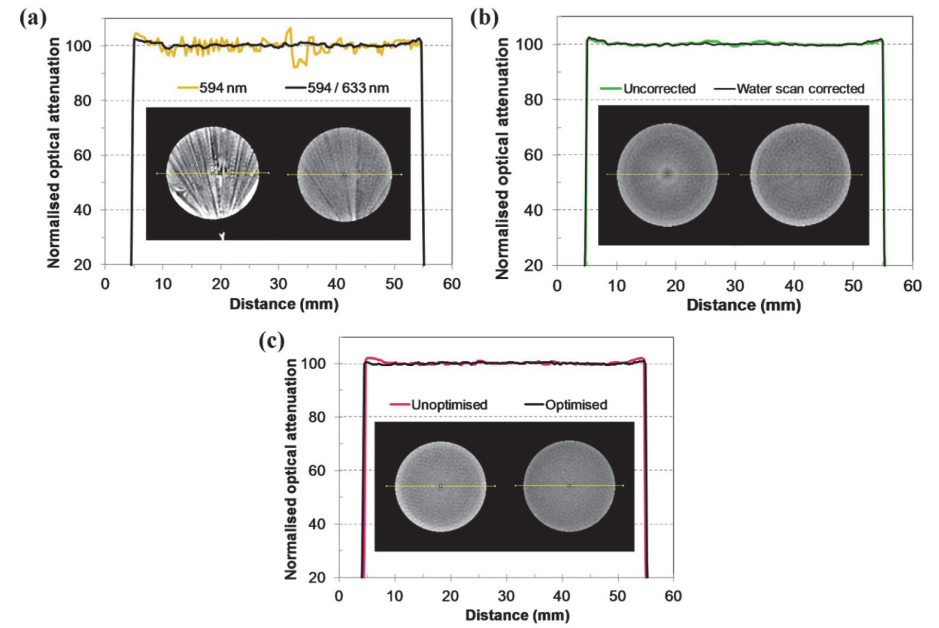

Figure 8. Reconstructed dyed water with (a) an example of streak artefacts caused by a foreign object on the cylinder outer surface. Streaking is clearly visible for a single wavelength (594 nm) scan while the dual wavelength scan (594/633 nm) is a substantial improvement. (b) Water scan correction of equation (3) for dual wavelength scanning with uniformity improvement. (c) Extrapolation artefact caused by imprecise extrapolated data. Optimisation of the extrapolation distance provided improvement. All windowing is 10% of the mean value and level is set to the mean.

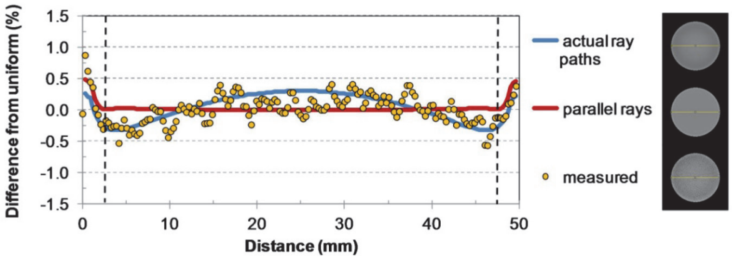

Figure 9. Reconstruction of simulated ray paths (dual wavelength) for a uniform gel with optical attenuation of 0.26 cm^{-1}. Profiles across the sample diameter show a subtle bowing artefact for the actual ray paths due to pathlength errors of slightly non-parallel rays. A high quality measurement gives some indication of the small (0.3%) non-uniformity. The dashed vertical lines indicate the boundary of the eFOV.

3.3. Accuracy of optical attenuation measurements

The mean optical attenuation coefficient measured by optical CT in a 40 mm diameter central volume of 50 mm length was compared to cuvette measurement of the same blue dye solution for several concentrations. Figure 10(a) shows good correlation of the optical CT measurements to cuvette for each of the processing options, single wavelength at 594 nm and 633 nm, and dual wavelength with and without pre-scanning. The detailed differences between optical CT and cuvette in figure 10(b) show that dual wavelength scanning is typically accurate to with 1%, with the single wavelength results similar.

The greater statistical uncertainties (combined cuvette and optical CT) for single wavelength were dominated by the cuvette measurements. Average 2 SDs were 0.8% and 0.1% for single wavelength cuvette and optical CT measurements respectively. Optical CT measurements were highly reproducible. Dual wavelength cuvettes SDs were improved at 0.4%. Cuvette scan to scan variations were greater for single wavelength scans because of limited transmission data (just a small central area of the cuvette) to average out defects in the transmission profile. Surface imperfections/cleanliness and optical interference were the main issues. The variability of cuvette based measurements was improved by dual wavelength scanning since scan to scan variations were reduced.

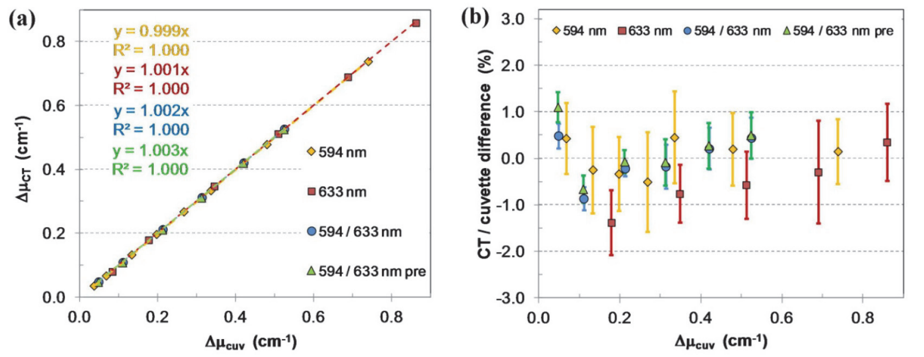

Figure 10. Quantitative accuracy of optical CT measured attenuation. (a) Correlation of optical CT to cuvette for each processing option of single and dual wavelength. (b) Local differences in optical CT versus cuvette with error bars for combined 2 SD errors of $\Delta\mu_{CT}$ and $\Delta\mu_{cuv}$ measurements ($n = 4$).

This is also seen in figure 7(b) for calibration filter scans. Increasing the cuvette pathlength would likely give improvements in accuracy and reproducibility, however 1 cm pathlength cuvettes are more readily available and convenient. Another potential improvement could be to position the cuvette closer to the detector to gain more transmission data for averaging.

3.4. Image noise and uniformity

Intra-scan analysis of the datasets of section 3.3 provided assessment of noise and uniformity for a range of optical densities. Line profiles across reconstructed slices of dual wavelength scans illustrate the uniformity and noise of measured optical attenuation coefficients in figure 11(a). Note that the extrapolation artefact was not optimised for these dyed water scans. Figure 11(b) gives an example of the ROIs and pixel binning used for the noise and uniformity analysis. Figure 11(b)(i) shows a raw reconstructed slice for a mid range OD with 1 SD noise of 0.8%, close to double that of figure 11(b)(ii) with the 2D 5 × 5 pixel median filter applied.

Results for random noise are not shown in figure 11 because they do not substantially differ from those for structured noise as the post reconstruction median filtering removes the majority of random noise. Structured noise results in figure 11(c) only gradually increase with decreasing $\Delta\mu_{CT}$, indicating that the main cause of the 'noise' largely scales with optical attenuation. This is consistent with the observation of laser instability as the dominant remnant artefact. Conversely, figure 11(d) reveals a sharp increase in non-uniformity for decreasing $\Delta\mu_{CT}$, suggesting that the artefacts responsible do not scale with $\Delta\mu_{CT}$, such as T^{contam} and T^{defect}. Particulate matter depositing on the outer optical surface of the scanning cylinder is an ever-present issue in a standard clinical environment (i.e. non-clean laboratory).

Dual wavelength scanning gave improvements in noise and uniformity, most notably for uniformity in the lower to mid-range $\Delta\mu_{CT}$ (0.1–0.3 cm^{-1}). This corresponds to FXG dose levels of approximately 1.5 to 4 Gy for dual wavelength. For 594 nm this dose range corresponds to $\Delta\mu_{CT}$ of 0.15–0.45 cm^{-1}. So we have uniformity (single versus dual wavelength) of around 2% versus 1% and 0.8% versus 0.5% at optical attenuation levels corresponding to 1.5 and 4 Gy respectively. This demonstrates a favourable trade-off between artefact reduction and loss of dose response sensitivity for dual wavelength scanning.

Ideal upper limits for FXG dose calibration would be about 5 Gy for dual wavelength ($\Delta\mu_{CT} \approx 0.4$ cm^{-1}), 5 Gy for 594 nm ($\Delta\mu_{CT} \approx 0.6$ cm^{-1}) and 15 Gy for 633 nm ($\Delta\mu_{CT} \approx 0.6$ cm^{-1}). These limits allow for typical FXG zero dose attenuation of the order 0.2 cm^{-1} at 594 nm (and less for 633 nm).

3.5. Spatial resolution

With the main focus of this paper on measurement of high quality uniform optical attenuation, it is pertinent to assess spatial resolution to verify the consequences of the data processing used to achieve the specified noise and uniformity results. Spatial resolution should not be degraded as to significantly affect measurement of the steepest dose gradients encountered in the intended radiotherapy application. The penumbrae of single small fields in Part II (Ramm 2018) have gradients of up to 25%/mm, and the composite dose distributions have gradients often around 10%/mm. Figure 12(a) shows the intrinsic MTF of this work is worse than previous work (Ramm *et al* 2012) which is expected due to increase of laser spot size from about 0.4 mm to 0.5 mm because of longer pathlengths for the dual wavelength configuration. The spatial resolution is further degraded by sampling (0.3 mm/sample), centre of rotation accuracy and filtering. The effect of the pre-construction 1D filtering was assessed as shown by the filtered and unfiltered results in figure 12. The final 2D 5 × 5 pixel median filter was

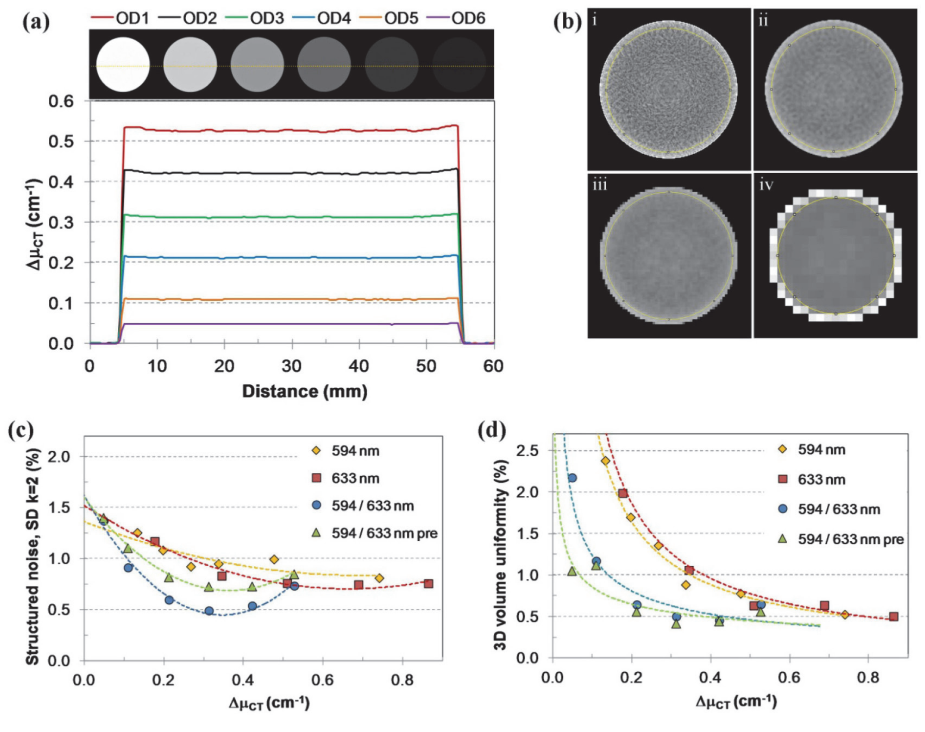

Figure 11. Optical CT image quality with a range of dyed water solutions. (a) Line profiles through each of the test optical densities (ODs) for dual wavelength (594/633 nm pre, filtered as per (b)(ii)). (b) Example of image analysis ROIs for a slice of OD3 (i) no post-reconstruction filtering of native 0.3 mm pixel size (not used in the analysis), (ii) 2D filtering by 5 × 5 pixel median, (iii) binned to 0.9 mm pixels for structural noise, (iv) binned to 3 mm pixels for uniformity, all windowed 10% of the mean value to make artefacts visible. (c) Structured noise (2 SD) as a function of optical attenuation. (d) Uniformity of complete 3D volume using maximum and minimum voxel values.

not applied in these cases since the consequences of this filtering are better assessed with dose profiles instead of a wire (refer to Part II). Figure 12(b) focuses on the lower spatial frequencies relevant to typical MV RT dose distributions. The MTF is >0.99 for 10%/mm gradients and 0.96 for 25%/mm. For un-normalised quantitative dosimetry we want no modulation of the imaged contrast, ie. MTF close to unity, so that the dose distribution is not significantly affected.

3.6. Limitations of the optical CT prototype

The prototype FDOCT scanner uses fixed optical geometry configured for a given gel dosimeter size. In this case the dosimeter comprises a 51 mm diameter gel sample with a 45 mm rFOV, and an inactive casing of PMMA that adds 25 mm to the overall diameter. The scanner does not have the flexibility to image different sized dosimeters. The dosimeter size was selected based upon a practical constraint of the requirement for the dosimeter to fit inside a pre-existing SRS head phantom, as an initial application. This highlights a disadvantage of the significant inactive volume of the dosimeter whereby only a 51 mm diameter of active volume could be achieved, given an opening in the phantom of about 80 mm. The plastic wall of the dosimeter also places limitations on the ability to conduct dosimetry at shallow depths, although slice-wise acquisition and a thin (or no) top cap for the cylinder provides some capacity for shallow measurements.

Linac based radiotherapy applications for the small 3D dosimeter described here are limited to SRS where targets are typically up to 30 mm in the largest extent and imaging of complete irradiated single tumour volumes are usually possible. For cases of multiple targets such as brain metastases, the small dosimeter size is limiting. Brachytherapy is another possible application where dose distributions delivered by small sources such as HDR ^{192}Ir could be measured, however patient target volumes may be larger than the rFOV of the FDOCT.

A larger active dosimeter than that of the work here would be required for a more general radiotherapy 3D dosimetry solution. Simple scaling up of the present optical CT scanning technique would likely present challenges that make the results of this small format scanner difficult or impossible to achieve. Of initial concern are the effects of increased scatter contributions and the increased detector dynamic range required to measure optical attenuation over a greater range of pathlengths, which are issues also common to other scanners. Increasing

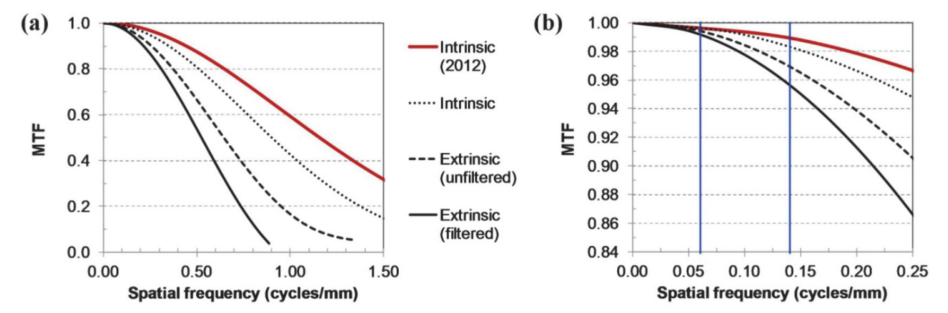

Figure 12. MTF calculated from the axial reconstruction of a 0.1 mm diameter wire. (a) Intrinsic resolution from previous work (Ramm *et al* 2012) compared to intrinsic for this work and the extrinsic with and without pre-reconstruction filtering. (b) Zoomed in view of (a), showing the high MTF values for spatial frequencies relating to radiotherapy dose distributions. Spatial frequencies of 0.14 and 0.06 cycles mm^{-1} equate to dose gradients of 25 and 10%/mm respectively.

the PMMA cylinder size becomes an ever increasing concern regarding material homogeneity and manufacturing processes. Additionally, the focussing of the laser beam onto a single photodiode detector may require additional optical elements, and the overall scanner footprint increases proportionally with dosimeter size. Iterative reconstruction techniques may provide more favourable results in terms of image quality and reconstruction accuracy in the eFOV instead of the simple backprojection and extrapolation methods employed.

As mentioned in earlier work, the active dosimeter is limited to hydrogels with RIs close to water in the range of 1.33–1.35, and high RI Presage is not suitable (Ramm *et al* 2012).

4. Conclusions

An optical CT scanner with practical operation for routine clinical true 3D dosimetry was developed. Minimal optical scanning expertise is required as the scanning process simply involves placing the dosimeter cylinder in its relocatable position on the scanning mount, which is similar to the level of know-how to scan film for film dosimetry. The simplicity of the design with the gel container acting as the sole optical lens for the system, offers favourable economy and potential for accurate absolute dosimetry. The dual wavelength mode of operation can provide greater robustness whereby minor cylinder scratching, particulate contamination and marks on optical surfaces can be better tolerated. In addition, pre-irradiation scanning of samples may be avoided. The reliable FOV of 85 to 90% of the gel diameter is comparable to scanners using RI fluid baths.

A number of issues causing optical artefacts were investigated and minimised or corrected, leading to improvements in image quality in terms of noise and uniformity. Dual wavelength scanning gave better results than single wavelength for both noise and uniformity, even with consideration of the net optical attenuation reduction at corresponding FXG dose levels. The most notable improvement was in uniformity at lower levels of optical attenuation. Cuvette measured optical attenuation was correlated to reconstructed cylinder 3D volume measurements within 0.5%.

Spatial resolution was verified and degradation compared to previous work was quantified. The reduction of spatial resolution was due to slightly larger laser spot sizes, a decrease in data sampling rates and filtering. The reduced resolution was still deemed acceptable for the spatial frequencies of the intended RT dose distributions.

Acknowledgments

This research was supported by the University of Adelaide and Royal Adelaide Hospital. Review of the manuscript and comments were gratefully received from Scott Penfold and Thomas Rutten.

References

Adamovics J and Maryanski M J 2006 Characterisation of presage: a new 3D radiochromic solid polymer dosemeter for ionising radiation *Radiat. Prot. Dosim.* **120** 107–12

Babic S, McNiven A, Battista J and Jordan K 2009 Three-dimensional dosimetry of small megavoltage radiation fields using radiochromic gels and optical CT scanning *Phys. Med. Biol.* **54** 2463–81

Bache S, Malcolm J, Adamovics J and Oldham M 2016 Optical-CT 3D dosimetry using Fresnel lenses with minimal refractive-index matching fluid *PLoS One* **11** e0152606

Baldock C, De Deene Y, Doran S, Ibbott G, Jirasek A, Lepage M, McAuley K B, Oldham M and Schreiner L J 2010 Polymer gel dosimetry *Phys. Med. Biol.* **55** R1–63

Campbell W G, Rudko D A, Braam N A, Wells D M and Jirasek A 2013 A prototype fan-beam optical CT scanner for 3D dosimetry *Med. Phys.* **40** 061712

Chang K H *et al* 2016 Development of a 3D optical scanner for evaluating patient-specific dose distributions *Phys. Med.* **31** 553–9

Chisholm K, Miles D, Rankine L and Oldham M 2015 Investigations into the feasibility of optical-CT 3D dosimetry with minimal use of refractively matched fluids *Med. Phys.* **42** 2607–14

De Deene Y 2015 Dual wavelength optical CT scanning of anthropomorphic shaped 3D dosimeters *J. Phys.: Conf. Ser.* **573** 012058

De Deene Y and Baldock C 2004 Third International Conference on Radiotherapy Gel Dosimetry (DOSGEL 2004) *J. Phys.: Conf. Ser.* **3**

De Deene Y, Skyt P S, Hill R and Booth J T 2015 FlexyDos3D: a deformable anthropomorphic 3D radiation dosimeter: radiation properties *Phys. Med. Biol.* **60** 1543–63

De Jean P, Senden R, McAuley K, Rogers M and Schreiner L J 2006 Initial experience with a commercial cone beam optical CT unit for polymer gel dosimetry I: optical dosimetry issues *J. Phys.: Conf. Ser.* **56** 179–82

Dekker K H, Battista J J and Jordan K J 2016 Stray light reduction in cone beam optical computed tomography: II. Reduction using a convergent light source *Phys. Med. Biol.* **61** 2910–25

Dekker K H, Battista J J and Jordan K J 2017 Scanning laser optical computed tomography system for large volume 3D dosimetry *Phys. Med. Biol.* **62** 2636–57

Doran S J and Yatigammana D N B 2012 Eliminating the need for refractive index matching in optical CT scanners for radiotherapy dosimetry: I. Concept and simulations *Phys. Med. Biol.* **57** 665–83

Doran S J, Koerkamp K K, Bero M A, Jenneson P, Morton E J and Gilboy W B 2001 A CCD-based optical CT scanner for high-resolution 3D imaging of radiation dose distributions: equipment specifications, optical simulations and preliminary results *Phys. Med. Biol.* **46** 3191–213

Gore J C, Kang Y S and Schulz R J 1984 Measurement of radiation dose distributions by nuclear magnetic resonance (NMR) imaging *Phys. Med. Biol.* **29** 1189–97

Gore J C, Ranade M, Maryañski M J and Schulz R J 1996 Radiation dose distributions in three dimensions from tomographic optical density scanning of polymer gels: I. Development of an optical scanner *Phys. Med. Biol.* **41** 2695–704

Hilts M, Audet C, Duzenli C and Jirasek A 2000 Polymer gel dosimetry using x-ray computed tomography: a feasibility study *Phys. Med. Biol.* **45** 2559–71

Hoye E M, Skyt P S, Yates E S, Muren L P, Petersen J B B and Balling P 2015 A new dosimeter formulation for deformable 3D dose verification *J. Phys.: Conf. Ser.* **573** 012067

Jordan K 1999 Developmental issues for optical CT and gel dosimetry *Canadian Organisation of Medical Physicists, Conf. Proc. DosGel99* pp 91–7

Kelly R G, Jordan K J and Battista J J 1998 Optical CT reconstruction of 3D dose distributions using the ferrous-benzoic-xylenol (FBX) gel dosimeter *Med. Phys.* **25** 1741–50

Krstajic N and Doran S J 2007 Fast laser scanning optical-CT apparatus for 3D radiation dosimetry *Phys. Med. Biol.* **52** N257–63

Manjappa R, Makki S S, Kumar R, Vasu R M and Kanhirodan R 2016 Fully 3D refraction correction dosimetry system *Phys. Med. Biol.* **61** 1722–37

Maris T G and Pappas E 2009 5th International Conference on 3D Radiotherapy Gel Dosimetry (DOSGEL 2008) *J. Phys.: Conf. Ser.* **164** 011001

Maryanski M J and Ranade M K 2001 Laser micro-beam CT scanning of dosimetry gels *Proc. SPIE* **4320** 764–7

Mielenz K D, Eckerle K L, Madden R P and Reader J 1973 New reference spectrophotometer *App. Opt.* **12** 1630–41

Oldham M 2010 6th International Conference on 3D Radiation Dosimetry (IC3DDose 2010) *J. Phys.: Conf. Ser.* **250** 011001

Oldham M, Siewerdsen J H, Shetty A and Jaffray D A 2001 High resolution gel-dosimetry by optical-CT and MR scanning *Med. Phys.* **28** 1436–45

Olding T and Schreiner L J 2011 Cone beam optical computed tomography for gel dosimetry II: imaging protocols *Phys. Med. Biol.* **56** 1259–79

Olding T, Holmes O and Schreiner L J 2010 Cone beam optical computed tomography for gel dosimetry I: scanner characterization *Phys. Med. Biol.* **55** 2819–40

Olsson L E, Bäck S and Ceberg S 2015 8th International Conference on 3D Radiation Dosimetry (IC3DDose 2014) *J. Phys.: Conf. Ser.* **573** 011001

Ramm D 2013 Laser beam optical CT scanner for in-air gel readout: imaging artefacts *J. Phys.: Conf. Ser.* **444** 012078

Ramm D 2018 A fast dual wavelength laser beam fluid-less optical CT scanner for radiotherapy 3D gel dosimetry II: dosimetric performance *Phys. Med. Biol.* **63** 045020

Ramm D and Rutten T P 2015 Feasibility of a dual wavelength laser optical CT scanner with in-air gel readout *J. Phys.: Conf. Ser.* **573** 012057

Ramm D, Rutten T P, Shepherd J and Bezak E 2012 Optical CT scanner for in-air readout of gels for external radiation beam 3D dosimetry *Phys. Med. Biol.* **57** 3853–68

Rankine L and Oldham M 2013 On the feasibility of optical-CT imaging in media of different refractive index *Med. Phys.* **40** 051701

Schreiner L J 2004 Review of Fricke gel dosimeters *J. Phys.: Conf. Ser.* **3** 9–21

Schreiner L J 2006 4th International Conference on 3D Radiotherapy Gel Dosimetry (DOSGEL 2006) *J. Phys.: Conf. Ser.* **56** 1

Schreiner L J 2015 True 3D chemical dosimetry (gels, plastics): development and clinical role *J. Phys.: Conf. Ser.* **573** 012003

Skyt P S, Petersen J B B, Yates E S, Poulsen P R, Ravkilde T L, Balling P and Muren L P 2013 Dosimetric verification of complex radiotherapy with a 3D optically based dosimetry system: dose painting and target tracking *Acta Oncol.* **52** 1445–50

Thomas A, Newton J and Oldham M 2011 A method to correct for stray light in telecentric optical-CT imaging of radiochromic dosimeters *Phys. Med. Biol.* **56** 4433–51

Thomas A, Niebanck M, Juang T, Wang Z and Oldham M 2013 A comprehensive investigation of the accuracy and reproducibility of a multitarget single isocenter VMAT radiosurgery technique *Med. Phys.* **40** 121725

Thwaites D and Baldock C 2013 7th International Conference on 3D Radiation Dosimetry IC3DDose 2012 *J. Phys.: Conf. Ser.* **444** 011001

van Doorn T, Bhat M, Rutten T P, Tran T and Costanzo A 2005 A fast, high spatial resolution optical tomographic scanner for measurement of absorption in gel dosimetry *Australas. Phys. Eng. Sci. Med.* **28** 76–85

Watanabe Y and Nakaguchi Y 2013 3D evaluation of 3DVH program using BANG3 polymer gel dosimeter *Med. Phys.* **40** 082101

Wolodzko J G, Marsden C and Appleby A 1999 CCD imaging for optical tomography of gel radiation dosemeters *Med. Phys.* **26** 2508–13

Xu Y and Wuu C-S 2013 Optical computed tomography utilizing a rotating mirror and Fresnel lenses: operating principles and preliminary results *Phys. Med. Biol.* **58** 479–95

5.4 Conclusions

The preliminary work in considering the feasibility of the addition of dual wavelength capability to the fluid-less optical CT scanner showed that it was readily achievable. However to minimise ray path differences due to the difference in wavelength, the wavelength difference was limited to < 40 nm. This difference would also lead to a dual wavelength dose response of 2/3 of the 594 nm response. The benefits of dual wavelength scanning in terms of artefact reduction were shown to outweigh the loss of dose response. Beam matching of spot size, alignment and ray paths was sufficient to provide improved image quality at optical attenuation levels equating to similar dose levels for single and dual wavelengths. Image quality and quantitative accuracy were assessed using dyed water solutions. Thus dual wavelength scanner operation had been established and optimised.

The next stage was to employ FXG dosimetry with the dual wavelength scanner and to investigate the measurement quality that could be achieved. This is detailed in the next Chapter.

Chapter 6

Performance of the gel dosimeter / optical CT system

6.1 Introduction

A dual wavelength optical CT scanner was previously developed and tested using dyed water solutions. In this work, FXG dosimetry was implemented with the dual wavelength scanner. This involved investigation of the dose response and confirmation of a suitable calibration procedure. The previously developed cuvette calibration method was adopted as one option, and a second option using a reconstructed gel volume for calibration was introduced. The benefits of each method were investigated. The dosimetric performance of the FXG / optical CT scanner system was established using a series of test irradiations. Measurement quality was quantified by comparisons to reference dosimeters. Finally, quality assurance guidelines to maintain performance in routine use were determined using insights obtained from the development of the system.

6.2 Research publication on dual wavelength scanner performance

The following research paper was submitted to Physics in Medicine and Biology on the 20th June 2017 and accepted for publication on 24th January 2018.

A fast dual wavelength laser beam fluid-less optical CT scanner for radiotherapy 3D gel dosimetry II: Dosimetric performance

Daniel Ramm

Physics in Medicine and Biology **63** (2018) 045020
https://doi.org/10.1088/1361-6560/aaaa46

IOP Publishing
Phys. Med. Biol. **63** (2018) 045020 (15pp)
https://doi.org/10.1088/1361-6560/aaaa46

Physics in Medicine & Biology

IPEM Institute of Physics and Engineering in Medicine

RECEIVED
20 June 2017

REVISED
10 January 2018

ACCEPTED FOR PUBLICATION
24 January 2018

PUBLISHED
16 February 2018

PAPER

A fast dual wavelength laser beam fluid-less optical CT scanner for radiotherapy 3D gel dosimetry II: dosimetric performance

Daniel Ramm
Department of Medical Physics, Royal Adelaide Hospital Cancer Centre, South Australia, Australia
School of Physical Sciences, University of Adelaide, South Australia, Australia
E-mail: daniel.ramm@sa.gov.au

Keywords: gel dosimetry, 3D dosimetry, optical CT

Abstract

New clinical radiotherapy dosimetry systems need comprehensive demonstration of measurement quality. Practicality and reliability are other important aspects for clinical dosimeters. In this work the performance of an optical CT scanner for true 3D dosimetry is assessed using a radiochromic gel dosimeter. The fluid-less scanner utilised dual lasers to avoid the necessity for pre-irradiation scans and give greater robustness of image quality, enhancing practicality. Calibration methods using both cuvettes and reconstructed volumes were developed. Dosimetric accuracy was similar for dual and single wavelength measurements, except that cuvette calibration reliability was reduced for dual wavelength without pre-irradiation scanning. Detailed performance parameters were specified for the dosimetry system indicating the suitability for clinical use. The most significant limitations of the system were due to the gel dosimeter rather than the optical CT scanner. Quality assurance guidelines were developed to maintain dosimetry system performance in routine use.

1. Introduction

Optical CT readout for true 3D dosimetry needs to be straightforward and efficient to be considered a viable option for routine work by clinical radiotherapy (RT) medical physicists. This would involve minimal optics expertise with simple standard operating procedures providing an efficient workflow. Measurement accuracy would be ideally at least comparable to accepted measurement methods such as film dosimetry. Advances towards a clinical true 3D dosimetry system with a fluid-less dual wavelength optical CT (FDOCT) were made in the companion paper for this work (Ramm 2018), hereafter referred to as Part I. The FDOCT scanner features a plastic cylinder containing a gel dosimeter that is placed on the scanner without the complications of immersing the dosimeter in refractive index (RI) matching fluid like other scanners (Doran 2013). The addition of a second wavelength provides an option to avoid the need for pre-irradiation scans. Furthermore, dual wavelength scanning was shown to be beneficial for image quality, particularly uniformity.

Part I of this work assessed imaging performance using dyed water solutions. In this part dosimetric performance is assessed using a ferrous xylenol orange gelatine (FXG) dosimeter (Kelly *et al* 1998). Resolution, time, accuracy and precision (RTAP) criteria were previously suggested (Oldham *et al* 2001) to indicate the suitability of gel dosimetry for a particular application (radiosurgery in that case). Criteria like these can provide a useful summary of performance. An alternative is proposed as follows. Time to acquire measurement data with resulting absolute dosimetric Accuracy, for voxels of a particular Resolution, for a given Volume (TARV). Ideally, the time component would be all-encompassing, including the time for reconstruction, preparation and quality assurance (QA) to give a better idea of overall system efficiency. However these additional items are more subjective than just the acquisition time. 'Absolute' dose accuracy provides an indication of measurement quality as an independent dosimetry technique. In this context absolute dose refers to dose measured by a dosimetry system via a calibration procedure using separate gel samples with a calibrated radiation beam. Specifying the volume provides further context for the time parameter since larger volumes usually result in longer acquisition times. In addition, dosimetric accuracy may be linked to the size of the volume.

There are few examples of studies of optical CT systems with detailed testing beyond proof of concept investigations or basic characterisations, such that they could be considered validated and commissioned for clinical use. Olding and Schreiner (2011) investigated the commercial VISTA (Modus Medical Devices Inc.) cone beam optical CT with FXG, generating imaging protocols designed to control measurement errors. Accuracy of 3–4% and 1% precision in scanning absorbing dye solutions was stated in prior work (Olding *et al* 2010b), however scanner/FXG system accuracy was not detailed. TARV parameters are interpreted to be 5 min, 4 ± 1%, 0.5 mm, dia. 100 × 100 mm.

Thomas *et al* (2011) assessed the Duke large field of view optical CT scanner (DLOS) with Presage dosimeters using a series of irradiations with various beam arrangements. The 3D measurements were normalised to treatment planning system (TPS) calculations and compared using a variant of the commonly used gamma analysis. Additionally small field output factors (OFs) (5–30 mm) were compared to commissioning data, EBT film and a first generation optical CT. TARV parameters appear to be 15 min, 5%, 2 mm, dia. 160 × 120 mm. The accuracy value is assumed from a statement of typical absolute dose agreement with the TPS.

Calibration methods for optically read 3D dosimeters have typically used calibration dosimeters of similar size to the measurement dosimeters, irradiated with a known dose distribution. Correlation of dose to optical attenuation has been achieved using distinct dose points (Kelly *et al* 1998, Oldham *et al* 2001), 1D data such as depth dose curves (Babic *et al* 2008a, Olding *et al* 2010a) and points from calibration dose patterns (Olding *et al* 2011). Optical attenuation measurements using an independent spectrophotometer with small vials or cuvettes filled with the dosimeter material have been problematic due to dosimeter size differences leading to physicochemical differences (Thomas *et al* 2011). Scatter and optical geometry differences due to use of various readout instrumentation can also contribute to discrepancies (Dekker *et al* 2016). If calibration via small samples could be successfully implemented there would be advantages in terms of reduction of dosimeter batch volumes and independence of methodology where transmission measurements are simply converted to attenuation coefficients without tomographic reconstruction.

In this work both cuvette based and volumetric reconstruction calibration methods were developed for the FDOCT scanner with FXG. This provided cross-checking of calibrations and provides the flexibility to select the calibration method of choice. The performance of the dosimetry system was verified for a number of irradiations with different beam geometries as characterised by reference dosimeters. Performance of the dosimetry system is summarised by specification of TARV values. QA recommendations for the system are provided for the purpose of maintaining measurement quality in routine use.

2. Materials and methods

2.1. Optical CT scanner and gel

The FDOCT scanner used 594 and 633 nm He–Ne lasers and a rotating mirror to sweep the beams across gel samples as detailed in Part I. There were two modes of operation, optical CT with a PMMA cylinder containing gel positioned on the scanning platform and secondly a spectrophotometer mode with cuvettes (without CT rotation). The CT cylinder size was 51 mm internal diameter (ID), 76 mm outer diameter (OD) and length 60 or 70 mm length. The PMMA cuvettes were 4 ml with a 10 mm pathlength. Figure 1 shows irradiated FXG cuvette and CT cylinder samples.

A scan acquisition time of 10 slices min^{-1} was the same for both single and dual wavelength scans since one mirror revolution sweeps the first laser beam across the sample followed by the second. Both single and dual wavelength data could be reconstructed, as was done in this work, to study the benefits of each method. Matlab (The MathWorks Inc.) was used to process the calibration scan and CT projection data, resulting in a stack of calibrated dose slices per cylinder scan and saved as DICOM files. Standard acquisition was fifty 1 mm slices with 0.3 mm axial resolution for a 5 min scan time. Post reconstruction 5 × 5 median filtering of the 2D slices was typically applied. Refer to Part I for full scanner details (section 2.1) and for discussion of scanner limitations (section 3.6).

For all irradiations in this work, FDOCT scans were conducted at 30, 50 and 70 min post irradiation, providing inter-scan variation data and the option to extrapolate measured data to the zero time point ($t = 0$ min) to mitigate the effects of diffusion. Linear extrapolation for each voxel using the time sequenced data was used similarly to Babic *et al* (2009). Pre-irradiation scans were conducted for all experiments so that comparisons of all processing options could be made.

Calibration cuvettes were scanned at the same post irradiation time ±1 min, and calibration cylinders at the calibration slice ±1 min. Measurement scans were timed such that the centre of the 50 mm scan length was the timed point, giving ±2.5 min deviations at the extremities. This was to match dose development of the different samples so that errors would be minimised even with measurable change in dose development occurring. Dose development refers to the increase of optical attenuation of the gel dosimeter with time as the radiation induced chemical reactions proceed.

Table 1 defines the classifications of scan and processing options used in this work. Both single and dual wavelength scans were calibrated by both the cuvette and volumetric pattern methods described in section 2.2.

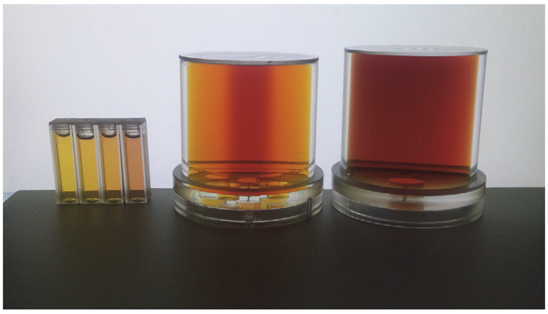

Figure 1. Photograph of FXG in cuvettes for calibrations (0–4 Gy), one CT cylinder with a small field irradiation down the cylinder axis and the other with a large field irradiation.

Table 1. Classification of scan/processing options.

	Y_c	Y_p	DW_c	DW_p	DWP_c	DWP_p
Wavelength (nm)	594	594	594/633	594/633	594/633	594/633
Pre-irradiation scan	Yes	Yes	No	No	Yes	Yes
Calibration	Cuvette	Pattern	Cuvette	Pattern	Cuvette	Pattern

A standard FXG recipe (Bero *et al* 2001, Babic *et al* 2008a) was adopted for the FDOCT. The gel was prepared with deionised water and final concentrations of 50 mM sulphuric acid, 0.05 mM xylenol-orange, 0.3 mM ammonium ferrous sulphate and 4% gelatin. Warm gel was passed through a 2 μm filter before filling scanning cylinders and cuvettes. Cuvettes were placed in a water-filled cylindrical container, approximating the thermal mass of a gel-filled FDOCT cylinder. All gel samples of the batch were placed together in an insulated container with lid and were set overnight in a refrigerator at about 10 °C. On the day of use the samples all together were slowly (over 4–5 h) stabilised to ambient room temperature. These procedures were aimed at avoiding large temperature gradients within gel samples and to closely match the thermal histories of all samples.

Aside from temperature related manufacturing differences, temperature dependence of FXG optical readout has been noted in this work and by others (Olding and Schreiner 2011). Thermochromic behaviour was verified by repeat scanning of irradiated cuvette and cylinder samples while warming from fridge to room temperature.

The other main properties of FXG to be controlled to achieve accurate dosimetry are auto-oxidation and the balance between dose development and ferric ion diffusion, as discussed by Olding and Schreiner (2011). Auto-oxidation was addressed in the calibration procedures. The optimal post-irradiation scan time was determined by the practicalities of carrying out the readout process, allowing enough time for dose development and minimising the time allowing diffusion to occur. Dose development and diffusion were characterised by repeat scanning from an early post-irradiation time point (2 min). The FDOCT cylinder was irradiated with a 2 × 2 cm field and the dose development was measured by a small region of interest (ROI) at the field centre, and diffusion was assessed by measurement of the 80/20% penumbra distance for each scan.

2.2. FXG dose calibration

The dose range for calibration was guided by the accuracy, noise and uniformity analysis in Part I. Two different dose calibration methods were developed, aiming for both dose accuracy and practicality. There is also the benefit of cross-checking for validation. The first method was cuvette, non-reconstruction based, and the second was by reconstruction of optical attenuation in a FDOCT scanning cylinder. The two calibration methods were substantially independent while attempting to achieve the same objective. The gel sample size was small for the cuvette versus the larger CT cylinder. Optical attenuation measurement was single point transmission versus 3D reconstruction and dose delivery was a simple reference condition versus a MLC derived dose pattern.

All irradiations in this work were conducted using a Varian Trilogy linac 6 MV beam with HDMLC at 600 MU min^{-1}. Source to surface distance (SSD) was 100 cm, except where indicated otherwise.

2.2.1. Cuvette based method

Cuvettes were irradiated in a full scatter solid water phantom at $d_{\max}$ for the standard reference condition (10 × 10 cm field size and 100 cm SSD), delivering well known doses with low gradients to the centre of the cuvettes. Characterisations of the dose responses were made with a set of 3 × 10 polystyrene 10 mm pathlength, 4 ml cuvettes. For routine calibrations of FDOCT cylinders, 4 PMMA 10 mm pathlength, 4 ml cuvettes were irradiated to 0, 1, 2.25 and 4.5 Gy and the FDOCT scan sequence was timed to match the post-irradiation time for all cuvettes and cylinders to minimise uncertainties due to auto-oxidation and dose development. Cuvettes were removed from their water bath and quickly returned after scanning, to minimise readout uncertainties due to FXG thermochromic behaviour. The 0 Gy sample was used to correct for auto-oxidation. Calibration data processing was integrated into the Matlab reconstruction code. The cuvette transmission data was processed according to the chosen single or dual wavelength option (see Part I for details of processing options) giving measured optical attenuation coefficients for known doses. Calibration curve fitting used a power fit, $y = ax^b$ to account for slight non-linearity in the dose response, as the linear fitting typically used for FXG dosimetry was deemed too inaccurate at the wavelengths used in this work. Lower wavelengths such as 540 nm green have improved linearity (Babic *et al* 2008b).

2.2.2. *Reconstructed pattern method*

The alternative calibration method used a calibration pattern irradiation of a FXG-filled FDOCT cylinder, followed by scanning and reconstruction. The calibration pattern comprised two overlapping MLC fields, 27.5 × 15 mm, with 15 mm overlap, using 160 MU for one field and 320 MU for the other. The beam central axis was parallel to, and centred on the cylinder axis. The relatively small field sizes were selected to give a condition with sufficient phantom material surrounding the irradiated area thus providing full scatter to the measurement points, without having to insert or immerse the FDOCT cylinder in another phantom. Four discrete dose steps were identified as calibration dose points.

The calibration pattern was characterised by film (ISP EBT3 and Epson V700) and ion chamber (IBA CC01) measurements, traceable to the linac reference absolute dosimetry calibration. Film results were used to quantify the relative dose distribution. The film dose distributions were obtained using FilmQA Pro (ISP) software with triple channel processing, sampled at the FDOCT axial resolution of 0.3 mm and filtered using the same 5 × 5 median filter as the gel data. The ion chamber results were used to give the best absolute dose value available for the central dose point and the other dose points measured by film were scaled accordingly. Prior to renormalisation the film absolute dosimetry results agreed with the ion chamber to 1%.

In axial slices of the cylindrical gel, the calibration pattern gave three relatively uniform regions with distinct dose values, plus near zero dose regions. The maximum dose gradients within 3 × 3 mm ROIs centred on each dose point were 0.6, 0.4 and 0.2%/mm for the two intermediate dose points and the high dose point respectively. The near zero dose point was the average of two low dose values. Reconstructed optical attenuation coefficients in the slice corresponding to the $d_{\max}$ depth for the central high dose area of the axial dose distribution were extracted by 0.9 × 0.9 mm ROIs at each of the dose points. The dose points were automatically located relative to the centroid of the central high dose area by Matlab processing code, accurate to 0.5 mm, for both the film characterisation and routine gel calibrations. Similarly to the cuvette based method, calibration curve fitting was a power fit, $y = ax^b + c$, with the inclusion of an offset coefficient since there was no zero dose measurement.

2.3. Test irradiation fields

A number of irradiations were used to test the dosimetric performance of the system. A separate batch of FXG was made for each of the seven test fields. The first was the simplest most well characterised condition, the linac reference condition, followed by several smaller field irradiations relevant to the intended application of stereotactic RT. The standard square single fields were previously well characterised by ion chamber and diode scans and OFs for linac commissioning. The composite beam test irradiations were characterised using an ion chamber and radiochromic film similarly to the calibration test pattern. That is, gold standard (lowest uncertainty) measurement data was the reference to determine dosimetric accuracy of the FDOCT/FXG system. Comparisons to TPS calculations provide full 3D to 3D analysis however there are additional uncertainties in the TPS data. In fact, the intended application for the FDOCT/FXG system is to verify stereotactic RT TPS predicted doses.

2.3.1. *Uniform single field*

The linac reference condition, a jaw defined field of 10 × 10 cm at 100 cm SSD in a full scatter phantom was used by placing the FDOCT cylinder in a water phantom with the top surface flush with the water surface as indicated in figure 2(a). With this dose distribution the lateral profiles are uniform to ±0.5% over the 50 mm gel diameter. The dose delivered to $d_{\max}$ was 4.00 Gy. The beam output was known from the routine reference calibration using a NE2611 ion chamber. The reference data for profiles and percentage depth dose (PDD) curves was ion chamber commissioning data (IBA CC04) measured in a scanning water tank. Uniformity and noise analysis was conducted similarly to that described in Part I. Line profiles were single pixel width as indicated in the results figures except for the PDD curves which were averaged over a 30 pixel (9 mm) width on the 2D lateral view of the 3D dataset.

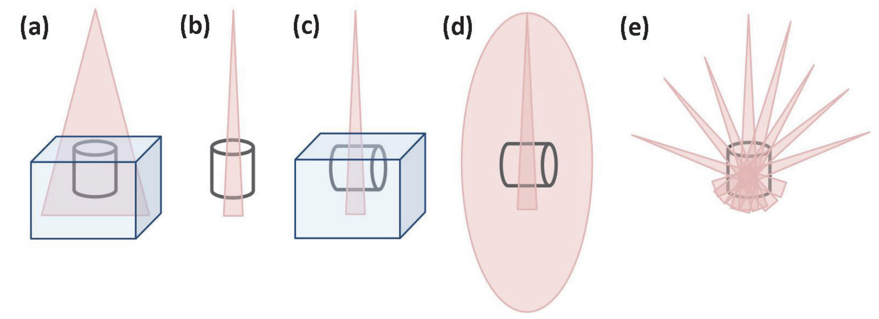

Figure 2. Schematic diagrams of linac beam deliveries for the test fields. (a) Uniform field (10 × 10 cm) in full scatter water phantom. (b) Small single fields (1×1, 2×2, 3×3 cm) with cylinder top entry. (c) Small single field (2 × 2 cm) in water phantom with cylinder side entry. (d) Small field (2 × 2 cm) 360° arc. (e) Eight static non-coplanar beam plan giving a *C*-shape dose distribution. Each of the seven test irradiations used separate FXG batches, conducted on different days as independent experiments.

2.3.2. Small single fields

These test fields were MLC defined in the range of routine stereotactic RT field sizes, 1 × 1, 2 × 2 and 3 × 3 cm, with delivery geometry shown in figure 2(b). These exact fields were previously measured for linac commissioning. OFs were measured by SRS diode (PTW 60018) corrected by Monte Carlo derived small field correction factors and daisy chaining to a 5 × 5 cm field. Ion chambers (IBA CC01, CC04) had also been used for cross checking the larger 2 and 3 cm fields. The SRS diode was also used for PDD data. In this work EBT3 films were used to acquire 2D data in the beam axial plane. Film processing was as described in section 2.2.2. Analysis included profile comparison and 2D gamma analysis using PTW Verisoft commercial software with criteria 2% absolute dose, 1.5 mm distance to agreement (DTA) and 10% threshold.

The delivery of the 2 × 2 cm field was repeated, but with side entry of the cylinder as shown in figure 2(c). A water phantom was used to maintain the condition of a perpendicular surface for beam entry of figure 2(b). This side entry delivery was compared to the top entry to confirm the measured dose distributions were consistent regardless of differences such as irradiation through the FDOCT cylinder wall (12.5 mm PMMA) versus the top (2 mm PMMA), and axial plane scanning versus perpendicular views by stacking of slices. For comparison of PDDs and profiles, depths though PMMA were scaled according to the electron density of PMMA for the radiation beam central axis. No normalisations or other corrections were applied.

2.3.3. Composite fields

Multiple beam irradiations were delivered isocentrically to the gel centre. One delivery was a 360° arc around the FDOCT cylinder and the other was an eight static beam plan as shown in figures 2(d) and (e) respectively. The arc delivery used a 2 × 2 cm MLC defined field and the eight beam plan used various MLC apertures generated by a Brainlab iPlan TPS to produce a *C*-shaped dose distribution in the centre of the gel volume. While the *C*-shape was arbitrary, the plan was similar to clinical SRS plans with multiple non-coplanar MLC beams shaping the dose distribution to conform to a target shape.

The reference dosimetry for the arc plan was an IBA CC01 ion chamber in a water filled FDOCT cylinder as shown in figure 3(a). Additionally EBT3 film was precisely cut and fitted to the water filled cylinder as shown in figure 3(b). For the eight beam plan EBT3 film was used. Figure 3(c) shows an irradiated film with the *C*-shape. Analysis was similar to that of section 2.2.2.

2.4. Summary of dose accuracy

A value of overall absolute dosimetric accuracy was calculated from the seven independent test irradiations of section 2.3. The dose distributions had maximum doses ranging from 3 to 4 Gy. The mean dose of a small ROI in a low gradient, high dose area provided the dose value. The ROI was 5 mm diameter in the selected 2D plane for the 10 × 10 cm field and 3 mm diameter for all others. The dose values for multiple post irradiation scans were averaged, except for the 1 × 1 cm field where only the dataset extrapolated to the zero post-irradiation time point was used. The differences between the FXG dose values and the doses at corresponding points with reference dosimeters (ion chamber, diode or film) were calculated. The mean dose difference and standard deviation for the seven irradiations were obtained for each scan type of table 1.

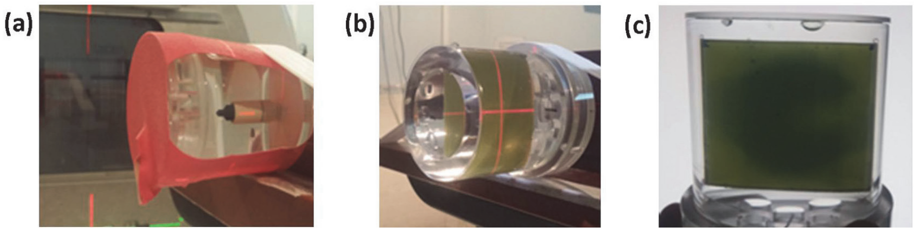

Figure 3. Photographs of the reference dosimeters for gel comparisons of the composite field irradiations. Water filled FDOCT cylinder with (a) CC01 ion chamber, (b) EBT3 radiochromic film, and (c) EBT3 film irradiated with the *C*-shape of section 2.3.3.

3. Results and discussion

3.1. Dosimetry system standard operation

Diffusion of ferric ions is a key concern for FXG dosimetry and was addressed by fast FDOCT scanning however, a balance is required with dose development. Selection of a standard post-irradiation scan time was assisted by the data shown in figure 4(a). Dose development is largely stabilised after 20 min, while the penumbra is continuously blurred. Twenty to 30 min was identified as the ideal post-irradiation scan time, similarly to Olding and Schreiner (2011). The temperature dependence of irradiated FXG was found to be 1%/°C as shown in figure 4(b). Olding and Schreiner (2011) found a greater temperature dependence of 2.5%/°C. The difference may be due to the different light sources used and different suppliers of the ferrous and xylenol orange dye active components, as dependencies on wavelength and chemical composition have been observed. FDOCT cylinder and cuvettes were maintained at matching temperatures, within 0.5 °C during irradiation and readout. Differences between cuvette samples and between FDOCT cylinders of the same batch were matched to better than 0.3 °C.

3.2. Dose calibration

3.2.1. FXG dose response

Calibration of optical attenuation coefficients to dose for a series of cuvette measurements is shown in figure 5(a). While the dose response curves are approximately linear, a more accurate fit to the measured data was obtained with a power fit of the form, $y = ax^b$. The difference between curve fitting and measured in figure 5(b) gives deviations of up to -3 to 2% for linear fitting, reducing to $<0.5\%$ for power fitting. The relative root mean squared error (RMSE) was 1.5–1.6% for linear fitting and 0.1–0.2% for power fitting. This non-linear behaviour for yellow light has been previously investigated where it appeared as a 'dose threshold' effect when using a linear fit (Babic *et al* 2008b). The general curve shape for 594 nm He–Ne light reported by Babic *et al* (2008b) is in agreement with this work. The non-linearity for red 633 nm light is slightly greater as shown by the values of the power coefficient b in figure 5(a). For dual wavelength, linearity is slightly improved from the yellow. The intended applications for the system only involve single use—prepare, irradiate and read, so non-linearity (with an accurate curve fit) is not problematic. A small priming dose as recommended by Babic *et al* (2008b) to improve linearity was avoided as it adds an extra step to the overall process and brings additional uncertainties.

For best accuracy each batch of FXG needs to be calibrated, so a reduction of cuvette dose measurement points was sought to minimise the routine calibration effort. Figure 5(c) gives the results of three point power curve fitting using the 1, 2 and 4 Gy dose points, and the differences from the full nine point fitting are shown in figure 5(d). Three point fitting gave negligible increase in dose calibration uncertainty and was thus adopted for the standard cuvette calibration procedure.

3.2.2. Reconstructed dose calibration pattern

The characterisation of the calibration pattern with film and ion chamber resulted in the relative and absolute dose levels in table 2. The absolute dose values correspond to the nominal linac output and daily output variations were accounted in the calibration procedure. The ROIs for the dose points as measured by film are shown in figure 6(a) and figure 6(b) for FXG. Profiles across the dose patterns are given in figure 6(c), showing the plateaus at the dose point ROIs (arrowed). The film measurement was the un-normalised average of five films, and the gel result was from a 30 min post-irradiation FDOCT calibration scan (DWP_c as defined in table 1) for one of the test irradiations (section 3.3), calibrated by cuvette to illustrate comparison to film. There is good agreement at the dose points, unaffected by FXG diffusion in the high dose gradients. A profile from a 70 min post-irradiation FXG scan is included in figure 6(c), also showing negligible diffusion effects at the dose points, although diffusion is clearly evident. Thus the method of extrapolation to $t = 0$ min was not required for the calibration data. Extrapolation was used in sections 3.4 and 3.5.

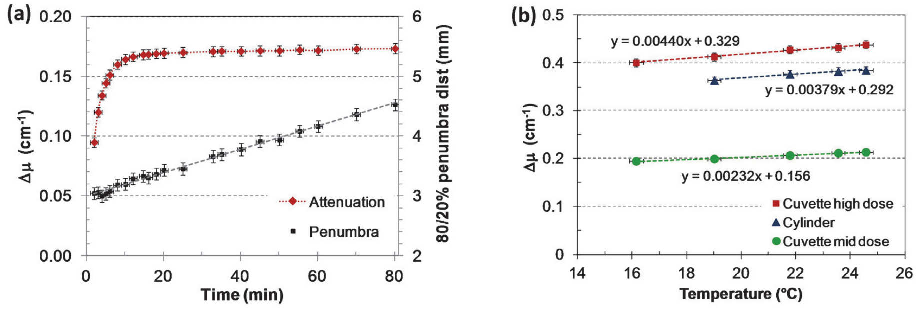

Figure 4. Properties of FXG at 594 nm readout. (a) Changes in optical attenuation (dose development) and diffusion (80/20% penumbra distance) with time post-irradiation. (b) FXG readout temperature dependence measured with cuvette and FDOCT cylinder volumes. The three datasets indicate temperature dependence of 1.0, 1.0 and 1.1%/°C.

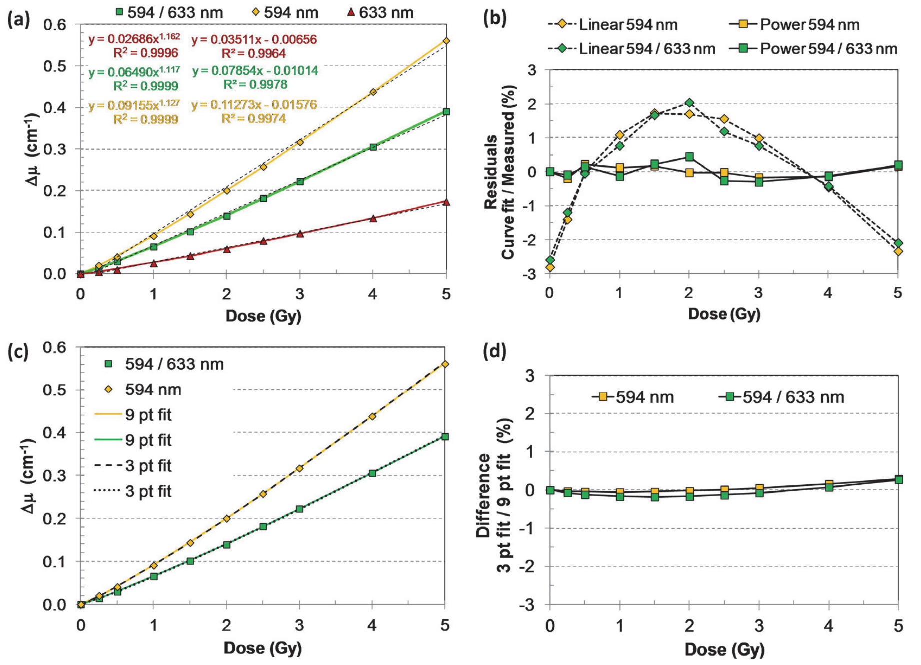

Figure 5. (a) FXG dose calibration curves for yellow, red and dual wavelength cuvette scans. Dashed lines are linear fitting and solid lines are power curve fitting to the nine measured data points. Error bars of 2SD ($n = 3$) are smaller than the data point sizes. (b) Residuals for linear and power curve fitting. (c) FXG dose calibration curves from figure (a) with three point power curve fitting using only the 1, 2 and 4 Gy measured dose points. (d) Differences between the three point and nine point curve fits.

Table 2. Dose levels for the calibration pattern with 6 MV beam output calibrated to 1.000 cGy/MU.

Dose point	Relative dose (%)	Absolute dose (Gy)
1	100.0 ± 0.3	4.262 ± 0.013
2	68.7 ± 0.3	2.926 ± 0.013
3	36.0 ± 0.3	1.534 ± 0.012
4	3.1 ± 0.2	0.132 ± 0.010

For routine calibrations, the reconstructed optical attenuation coefficients at the dose points were assigned the known dose values of table 2 and power curve fit coefficients were obtained for the calibration. QA of the system includes periodic verification of the dose points to ensure ongoing accuracy of the calibration dose values (Test 7 in table 9).

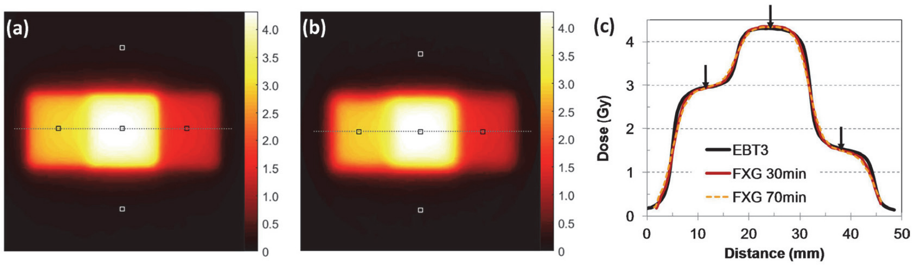

Figure 6. Dose calibration pattern (in Gy) with calibration ROIs. (a) EBT3 film in solid water at 14 mm depth, and (b) FXG at 14 mm depth, DWP_c 30 min scan. (c) Profiles across the EBT3 and FXG dose patterns, and a 70 min FXG scan profile.

3.2.3. Comparison of calibration methods

Cuvette and calibration pattern methods were conducted and compared for seven batches of gel in the dose measurement verifications of sections 3.3–3.5. For each batch there were 3 post-irradiation scans at different time points between 20 min and 90 min. The calibration methods were compared by calculating the RMSE from the differences between the calibration curves over the entire dose range, relative to a nominal maximum of 4.5 Gy. Figure 7 is an example set of calibration curves, close to the mean of all results. This shows a significant difference between DW_c and DW_p, while there is good agreement of cuvette and pattern calibrations for Y and DWP. Table 3 summarises six of the gel batches, showing greater average and inter-batch differences for DW. These results gave confidence in both cuvette and pattern calibration methods for the scan options utilising pre-irradiation scans, however they revealed inconsistencies between DW_c and DW_p calibrations.

The calibration curves of figure 7 were plotted without the zero dose attenuation subtracted, helping to identify where the differences actually occur. The zero dose difference between DW_c and DW_p was 3.4%, however it is not just a simple offset, there are also differences in curve shape. DWP processed scans removed the inherent (i.e. zero dose) difference in optical attenuation at 594 nm and 633 nm by normalisation to pre-irradiation scans, giving improvement to the level of results for single wavelength (Y). Pre-irradiation scans effectively discard the gel physicochemical history from manufacture to the pre-irradiation scan time point. This mitigates effects due to gel sample to sample variations by setting a sample specific zero for optical attenuation, relatively close to the time of post-irradiation scans. As DW scans do not have this 'zeroing' and correction of sample to sample variations, accurate calibrations become more difficult, as indicated the results in table 3.

The differences between DW_c and DW_p calibration curves raise the question of which method is more accurate. If the zero dose optical attenuation for each method is subtracted from the curves, the DW_p curve more closely matches the DWP curves than does the DW_c. Thus the cuvette based method appears subject to greater uncertainty than the pattern calibration method where pre-irradiation scans are not used. This is consistent with the fact that cuvette calibrations use multiple samples of different size (volume) to the sample to be calibrated. Confirmation of calibration accuracy for each calibration method is provided by the tests of section 3.3.

One of the total of seven gel batches was excluded from the table 3 data since the handling of the gel samples differed from the other six. These gel samples were subject to an extra day of room temperature and then returned to refrigeration, compared to the standard process of prepare, refrigerate overnight and use the following day. The RMSE differences between pattern and cuvette calibrations were around double the mean values given in table 3. This indicated systematic worsening of all cuvette based calibrations with increasing time and conditions for physicochemical differences in gel samples to occur, illustrating the importance of controlling the standard process. This occurred even though the cuvettes were maintained in the water bath mimicking the thermal load of a gel filled FDOCT cylinder.

3.3. Uniform dose distribution

A dose distribution was delivered to FXG with uniformity of 0.5% in the FDOCT cylinder axial slice plane. This was a very well characterised 10 × 10 cm 6 MV beam, giving a reliable reference for the FDOCT/FXG system comparisons. A reconstructed FXG (DWP_p) axial slice (14 mm depth) and the central axis lateral dose plane are given in figure 8(a). Figure 8(c) illustrates the uniformity with profiles at 3 depths. The profiles are flat to ±0.5%, but a subtle dip was noted in the centre. Detailed comparisons to ion chamber data in figure 8(d) show this is the actual beam profile due to flattening filter and beam characteristics. It is also observed that the small ($<0.5\%$) difference between beam profile shapes at 14 mm versus 50 mm was detectable by the FXG measurements.

Table 4 summarises the intra-scan image quality of the uniform irradiation. These results are consistent with the dyed water solution results of Part I, although the uniformity results were marginally worse. Considering some of this non-uniformity is due to the true beam profile, the FXG result is very close to the dyed water

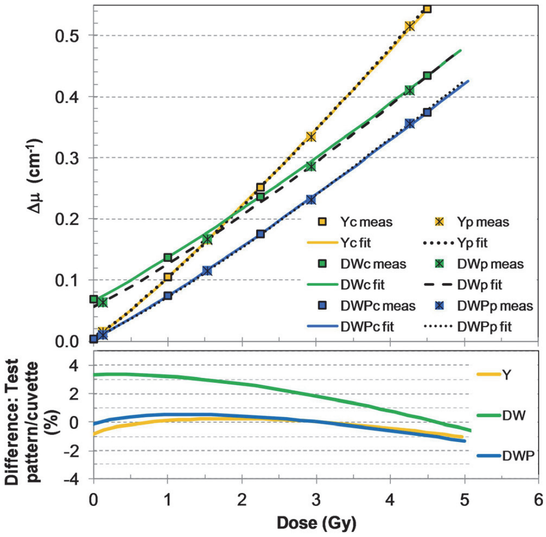

Figure 7. Example of typical calibration curves for single (Y) and dual wavelength (DW and DWP) comparing cuvette '*c*' and calibration pattern '*p*' methods. Measured points and power curve fitting lines are shown. Differences between pattern and cuvette methods are shown in the lower plot. These differences give RMSE for Y, DW and DWP of 0.4, 2.3 and 0.6% respectively.

Table 3. Differences between cuvette and pattern calibration for six batches of gel and repeat scans at three post-irradiation time points.

	Mean RMSE (%)	Inter-batch SD (%)	Intra-batch SD (%)
Y	0.6	0.2	0.2
DW	2.1	1.3	0.1
DWP	0.5	0.2	0.1

scans at around 0.8%, thus indicating no significant loss of image quality going from dyed water to irradiated FXG scanning.

Absolute dose accuracy is shown in table 5 for each scan and calibration method. The dose values were the average in a 5 mm diameter ROI on the central axis of the $d_{\max}$ slice. All results were within 1% and on average were <0.5%.

With absolute dose accuracy established at a reference point ($d_{\max}$), PDD curves were compared as shown in figure 8(b). Better than 0.5% agreement with ion chamber over 10–60 mm depths was achieved for all scan methods except for DW_c. This confirmed both cuvette and pattern calibration methods were accurate when used with pre-irradiation scanning. Dual wavelength without pre-irradiation scanning was accurate with pattern calibration but not with cuvette calibrations as shown in figure 8(b). This was expected as discussed in section 3.2.3. It was noted that the DW_c calibration for this batch was better than the average illustrated in figure 7, thus the $d_{\max}$ dose accuracy was within 1% however, deviation in accuracy was revealed by the PDD curves.

3.4. Small single fields

Dose distributions were measured for 1, 2 and 3 cm field sizes as illustrated in figure 9. Standard beam characteristics, PDDs and profiles were measured by extracting line profiles from the 3D datasets. OFs were measured from the single beam irradiations. Other optical scanner systems have measured OFs by irradiating a sample with multiple beams and normalising the smaller beams to the largest (Babic *et al* 2009, Thomas *et al* 2011), that is, relative dosimetry within a sample. With the FDOCT/FXG system, dose calibration accuracy and scan precision provides the ability to measure OFs using absolute dose to 1.1% accuracy as shown in table 6. This level of accuracy for the 1 cm field size could only be achieved by diffusion correction to $t = 0$ min (approximately 2% correction at 30 min post-irradiation). At this field size the beam profile is sufficiently peaked that diffusion lowers the peak level of optical attenuation with post-irradiation time. For 2 cm field sizes and above, peak levels were not affected by diffusion. This can be seen in the beam profiles of figure 9(b) where 30 min scans and 0 min extrapolated scan data is shown. While diffusion correction largely recovers the 1 cm field peak dose, there is still some disagreement in penumbral regions. It has been observed in studies beyond the scope of this work that high dose gradients in FXG cannot be fully recovered by linear extrapolation methods, even though the data obtained

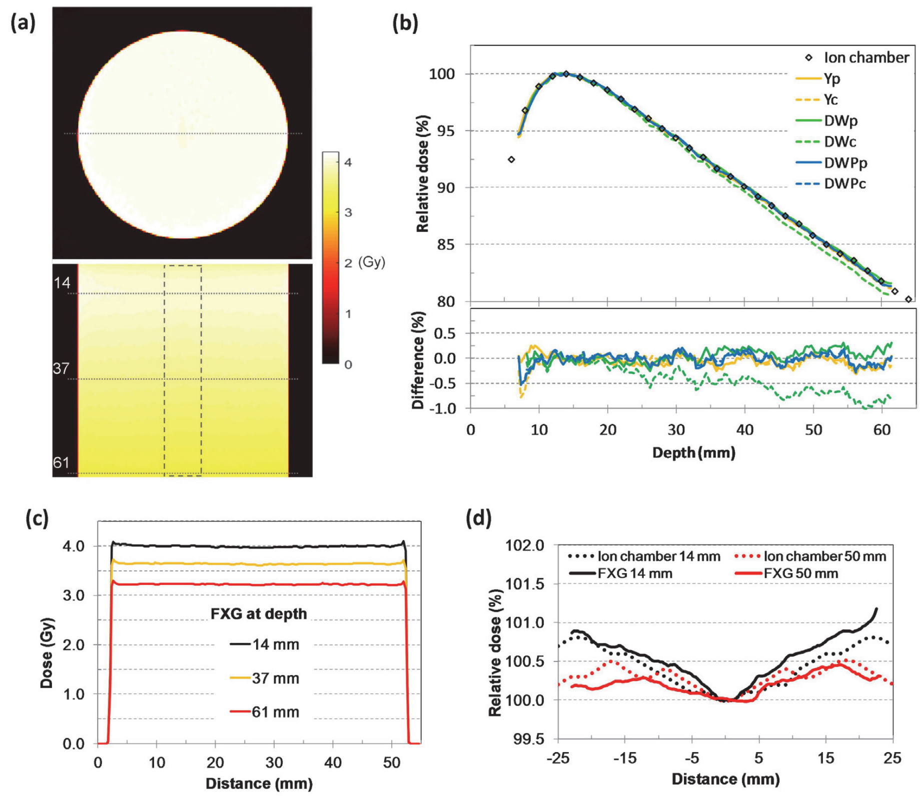

Figure 8. Irradiation of FXG down the cylinder axis, giving near uniformity in axial slices. (a) Reconstructed dose (DWP_p) axial plane at 14 mm depth and lateral plane. (b) PDD curves from averaged line profiles (30 pixel (9 mm) width as shown in (a)) down the cylinder central axis. (c) Profiles across the gel at different depths. (d) Close-up view of FXG relative profiles compared to ion chamber. Both FXG and ion chamber data were smoothed to show the subtle differences of profile flatness with depth.

Table 4. Intra-scan uniformity and noise analysis from uniform FXG irradiation.

Scan type	Noise (%)	Structured noise (%)	3D uniformity (%)
Y	0.4	0.4	1.1
DW	0.4	0.4	1.2
DWP	0.4	0.4	1.2

Table 5. FXG dose accuracy at $d_{\max}$ for a 4 Gy uniform dose. Assessment from three separate post-irradiation FDOCT scans.

Scan type	Dose (Gy)	Difference (%)	Inter-scan SD (%)	Intra-scan SD (%)
Y_c	3.986	−0.3	0.6	0.2
Y_p	3.977	−0.6	0.3	0.1
DW_c	3.967	−0.8	0.2	0.2
DW_p	3.988	−0.3	0.4	0.2
DWP_c	3.993	−0.2	0.2	0.2
DWP_p	3.982	−0.4	0.4	0.2

beyond $t = 0$ is substantially linear (shown in figure 4(a)). Nevertheless, penumbral dose point agreement is within 0.5 mm for diffusion corrected and 1 mm for 30 min scans as shown in figure 9(b). The penumbral gradients of around 25%/mm are higher than those typically encountered in composite dose distributions.

Film to FXG 2D comparisons are shown in figure 9(c) with ⩾95% pass rates at 2% dose/1.5 mm DTA criteria. FXG diffusion was the source of the greatest differences, especially for the corners of the square dose distributions. The measurement uncertainties of both FXG and film contribute to differences, and film uniformity and

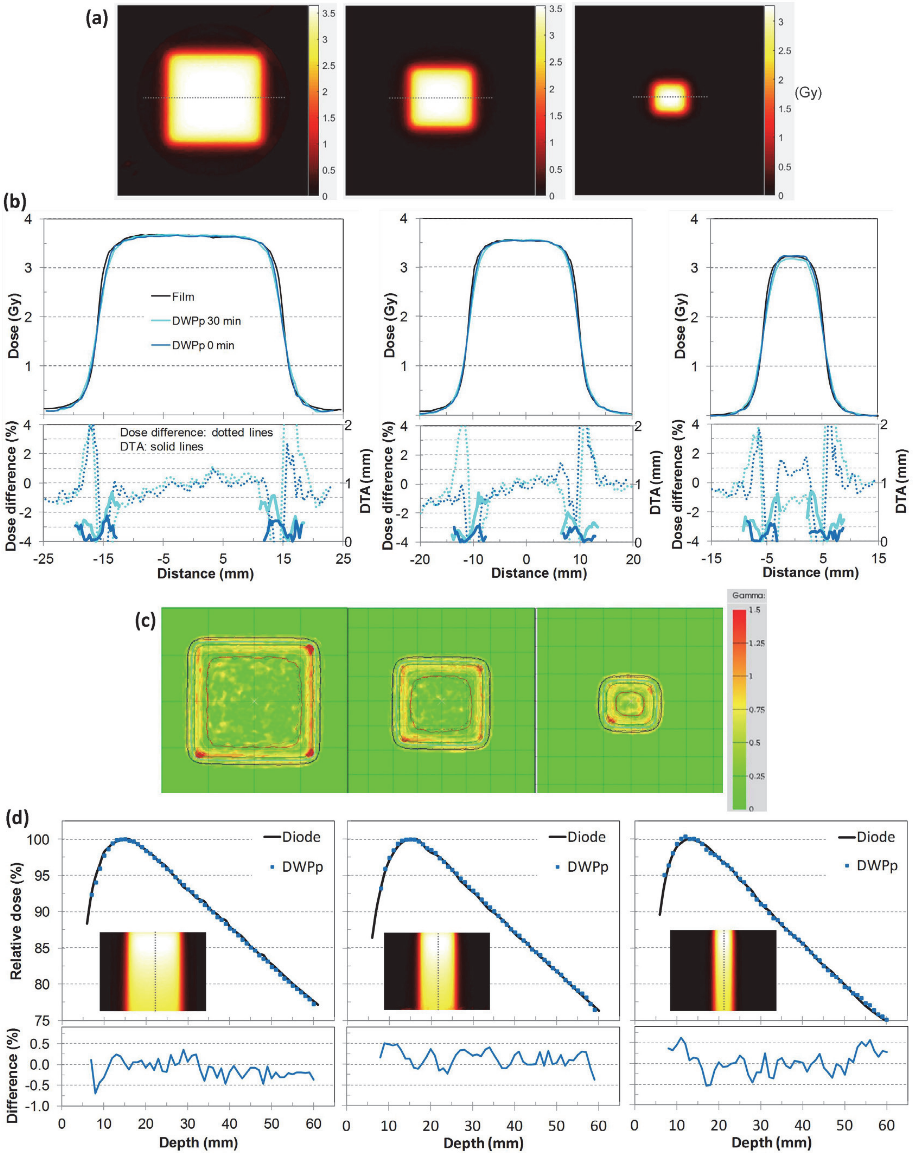

Figure 9. FXG dose measurement (DWP$_p$) of 3 × 3, 2 × 2 and 1 × 1 cm fields. (a) Axial slices at $d_{\max}$. (b) Profiles across the axial slices for the 30 min scan, extrapolated data and film. (c) Gamma analysis maps with isodose lines (solid for FXG and dotted for film) with 2% dose and 1.5 mm DTA criteria. Pass rates were 95.0, 96.2 and 96.8% for 3, 2 and 1 cm fields respectively. At 2%/2 mm, all pass rates were >99%. (d) FXG measured PDDs compared to diode measured in a scanning water tank.

Table 6. FXG measured OFs for small MLC fields from three post-irradiation FDOCT scans compared to beam commissioning data (diode/ion chamber). Combined 1SD errors from intra and inter-scan variations.

	MLC field size (mm)					
	10 × 10		20 × 20		30 × 30	
Measurement type	OF	Difference (%)	OF	Difference (%)	OF	Difference (%)
Beam data	0.8188	0.0 ± 0.8	0.8875	0.0 ± 0.4	0.9136	0.0 ± 0.3
Y_p	0.8106	−1.0 ± 1.3	0.8895	0.2 ± 0.2	0.9148	0.1 ± 0.2
DW$_p$	0.8101	−1.1 ± 1.2	0.8915	0.4 ± 0.2	0.9203	0.7 ± 0.2
DWP$_p$	0.8104	−1.0 ± 1.4	0.8893	0.2 ± 0.2	0.9154	0.2 ± 0.2

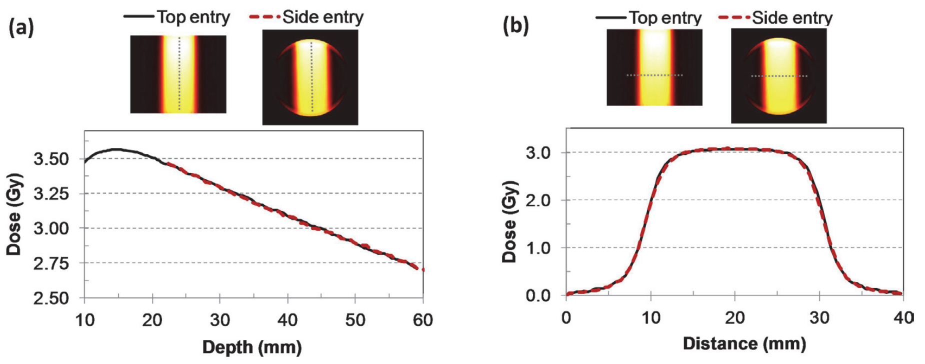

Figure 10. FXG measurements of a 2 × 2 cm field with beam entry through the cylinder top, compared to side entry. (a) Depth dose curves, and (b) profiles at depth of 40 mm.

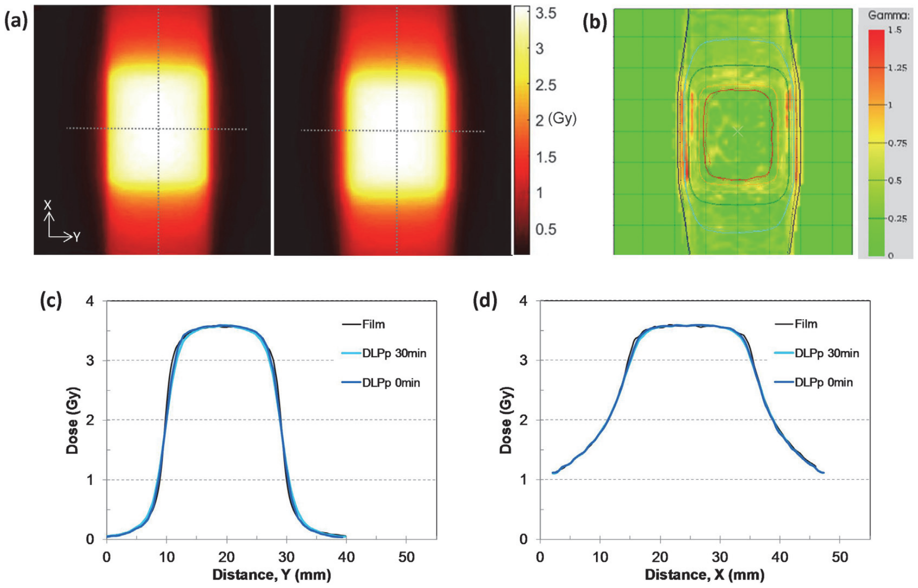

Figure 11. Dose measurements of a 2 × 2 cm field, 360° arc around the FDOCT cylinder. (a) Central lateral plane for film (left) and FXG (right). (b) Gamma map with isodose lines (solid for FXG and dotted for film) with 2% dose and 1.5 mm DTA criteria. Pass rate was 97.3%, and >99% at 2%/2 mm. (c) FXG and film dose profiles in the cylinder longitudinal (*Y*) direction, and (d) transverse (*X*) direction.

noise was not typically better than that of FXG. In fact, film non-uniformity appeared to be the second most significant source of differences.

The three field sizes differ in PDD curve shape and figure 9(d) shows that the FXG measured PDDs were within 0.5% of reference diode data beyond the buildup region.

The beam entry for the irradiations in this section was through the cylinder top and down the axis, so different irradiation geometry was tested by beam entry through the cylinder side. There was good agreement of side versus top entry as shown in figure 10, giving the same depth dose curve and profiles to within 1% absolute dose or 0.2 mm DTA. The profiles from the side entry dataset excluded the 5 mm periphery of the cylinder axial view to avoid edge artefacts.

3.5. Composite dose distributions

The 360° arc irradiation provided a flat region of dose in the centre and varying dose gradients in orthogonal planes as shown in figure 11. Both ion chamber and film were used to verify the dose distribution. FXG measurements agreed with the ion chamber point dose as given in table 7. Line profile comparisons with film in figure 11(c) for the longitudinal profile gave similar results to the same size (2 × 2 cm) static field in section 3.4.

Table 7. Measured isocentre dose for a 2 × 2 cm MLC 360° arc around the FDOCT cylinder. FXG combined 1SD errors from intra and inter-scan variations.

Measurement type	Dose (Gy)	Difference (%)
CC01 ion chamber	3.590	0.0 ± 0.4
EBT3 film	3.574	-0.4 ± 0.6
Y_p	3.594	0.1 ± 0.2
DW_p	3.596	0.2 ± 0.5
DWP_p	3.588	-0.1 ± 0.2

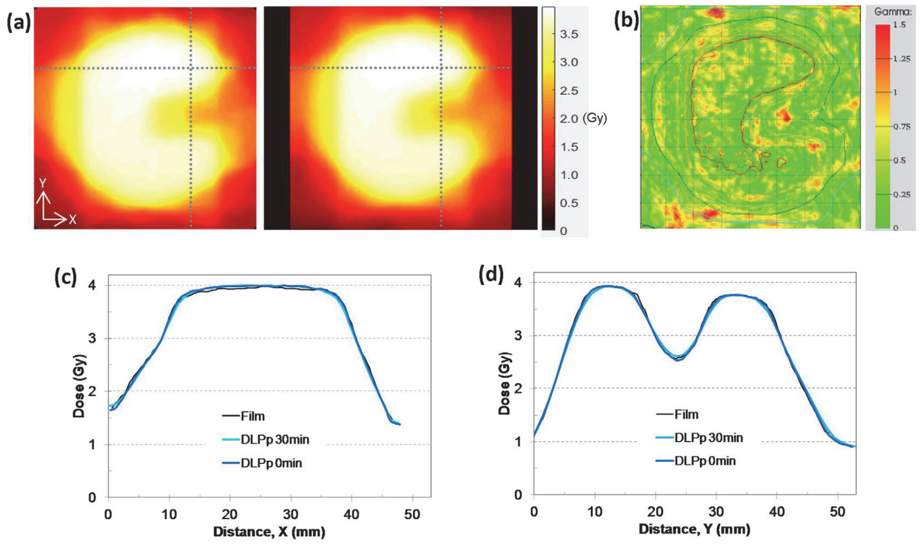

Figure 12. *C*-shape dose distribution delivered by eight static MLC beams. (a) Dose measured by a central lateral plane of film (left) and FXG (right). (b) Gamma map with isodose lines (solid for FXG and dotted for film) with 2% dose and 1.5 mm DTA criteria. Pass rate was 97.4%, and 98.8% at 2%/2 mm. (c) FXG and film dose profiles in the cylinder transverse (*X*) direction, and (d) longitudinal (*Y*) direction.

The profile in the transverse plane (figure 11(d)) has reduced dose gradients of between 10 and 2%/mm in the dose falloff regions. There is general agreement of 1% or 0.5 mm in the lower gradients, and 1 mm in the higher gradients for the 30 min scan. The 2D gamma analysis confirmed the weakest areas of agreement in the highest gradients to the same level as section 3.4, while in the lower gradients no failures were detected.

The *C*-shape dose distribution as measured by film and FXG is shown in figure 12. Profiles had general agreement of 1–1.5% or 0.5 mm DTA. The gamma analysis gave a 97.4% pass rate with 2%, 1.5 mm criteria, with differences primarily caused by both film and FXG non-uniformities. As mentioned in section 3.4, film non-uniformities appeared greater than those of FXG due to film and flatbed scanner limitations. Re-sampling by binning 2 × 2 pixels to give a 0.6 mm pixel size resulted in a 2%/1 mm pass rate of 98.6%. The influence of measurement structured noise, particularly for the film, was reduced by the re-sampling.

These dose distributions provided clinically relevant tests with the maximum range of gradients likely to be encountered with MLC defined radiosurgery treatment plans. The FDOCT/FXG results were equivalent to film in 2D and close to ion chamber point dose measurement, therefore indicating the gel dosimetry system to be a useful dosimetry tool for clinical RT verifications.

3.6. Summary of dose accuracy

Absolute dose accuracy measured by the FXG/FDOCT system using each scan/processing method as defined in table 1 is summarised in table 8. The mean of the dose differences between FXG and the reference dosimetry for the seven test irradiations were $<0.5\%$ for all scan options except for DW_c. Inter-experimental variations at the 1 SD level were $\leqslant 1.0\%$. The much larger deviations for DWc were due to volumetric differences between cuvette and cylinder as mentioned in sections 3.2.2 and 3.3.

Table 8. FXG/FDOCT dose accuracy for dual and single wavelength scanning for moderate dose levels (3–4 Gy) and dose gradients <5%/mm. Dose differences from the seven test irradiations of sections 3.3–3.5 compared to the reference dosimeters at the nominal maximum of each dose distribution.

Scan type	Mean dose difference (%)	1 SD (%)
Y_c	−0.1	1.0
Y_p	0.0	0.7
DW_c	−2.6	2.1
DW_p	0.1	0.7
DWP_c	−0.3	0.9
DWP_p	−0.1	0.6

Table 9. QC tests for the FDOCT scanner in routine use (e.g. weekly).

Test no.	Test description	Limit	Frequency
1	Visual inspection of scanning cylinders	If defect test 4 and 5	Before use
2	Optical transmission accuracy with calibrated filters (section 3.1.2 Part I)	1%	Monthly
3	Laser alignment by in air scan of 0.1 mm wire (section 3.1.1 Part I)	0.05 mm or 2% signal ratio	3 monthly
4	Water scan uniformity, $\Delta\mu$ (section 2.1.2 Part I)	0.0002 cm^{-1}	3 monthly
5	Uniformity, noise, accuracy of dyed water solution (section 3.3 and 3.4 Part I)	1%	3 monthly
6	Spatial resolution by scan of 0.1 mm wire in gel (section 3.5 Part I)	0.1 mm FWHM difference	Annually
7	Gel calibration by pattern method versus cuvette (section 2.2 herein)	1%	Annually

The dose accuracies specified are valid down to a 1 × 1 cm field size only if extrapolation to post-irradiation time zero is used. At 30 min post-irradiation for the 1 × 1 cm field, an additional 2% error results due to reduction of the dose peak by diffusion. The other fields maintained their peak doses with post-irradiation time.

3.7. Scanner QA

Routine periodic quality control (QC) tests of scanner performance should be employed to maintain the performance of the system close to that specified by the performance analysis. A suggested routine test regime from experience gained through scanner development and more than a year of scanner operation is provided in table 9. These tests have been determined specifically for the FDOCT scanner, however they may also help provide some guidance for other systems. In non-routine situations such as maintenance, repair or re-location of the scanner, all of the tests in table 9 should be conducted. If the scanner is used less often than the test frequencies, then the respective tests would be recommended before use.

4. Conclusions

A true 3D dosimetry system with a completely fluid-less, dual wavelength optical CT scanner was developed and tested for clinical application. The practicalities of optical CT scanning were improved by eliminating fluid altogether from the scanner and the option to avoid pre-irradiation scans by dual wavelength scanning. The FDOCT/FXG system gave typical agreement with reference dosimeters to 1%. This was achieved with both cuvette based and reconstructed dose pattern calibration methods for single and dual wavelength techniques, except for cuvette calibrations with the dual wavelength method without pre-irradiation scans. Therefore the most efficient approach with high accuracy was found to be dual wavelength scanning without pre-irradiation scans, calibrated by a reconstructed dose pattern. The most robust approach was dual wavelength with pre-irradiation scanning as it can best deal with artefacts generated by unclean FDOCT cylinder and cuvette optical surfaces. Single wavelength scanning provided comparable quality dose measurements thus represents the most economical scanner configuration. Cuvette calibrations are independent of reconstructed dose measurements however, are more prone to physicochemical differences compared to larger volume cylinder samples, resulting in greater uncertainties if the gel samples are not handled according to standard procedure.

A summary of system performance via the TARV parameters comprised values, 5 min, 0.5 ± 1.0%, 0.3 × 0.3 × 1.0 mm, dia. 50 × 50 mm. The benchmarking of dosimetric performance, independent of TPSs, provides evidence of the system's ability in the intended application of true 3D verification of computed dose distributions in radiosurgery treatment planning. The quoted dose accuracy is limited to field sizes 10 mm or greater due to FXG diffusion. Therefore adoption of a minimally diffusing gel dosimeter with this type of scanner could extend use to the most challenging very small (4 or 5 mm) collimated radiosurgery beams. The lack of diffusion would also provide greater flexibility with respect to prolonged delivery times and post-irradiation scan timing. Extending the range of doses of suitable measurement quality would provide the ability to test clinical hypo-fractionated dose levels used in modulated treatment plans without changing trajectories or rates of modulation.

Acknowledgments

This research was supported by the University of Adelaide and Royal Adelaide Hospital. Review of the manuscript and comments were gratefully received from Scott Penfold and Thomas Rutten.

References

Babic S, Battista J and Jordan K 2008a Three-dimensional dose verification for intensity-modulated radiation therapy in the radiological physics centre head-and-neck phantom using optical computed tomography scans of ferrous xylenol-orange gel dosimeters *Int. J. Radiat. Oncol. Biol. Phys.* **70** 1281–91

Babic S, Battista J and Jordan K 2008b An apparent threshold dose response in ferrous xylenol-orange gel dosimeters when scanned with a yellow light source *Phys. Med. Biol.* **53** 1637–50

Babic S, McNiven A, Battista J and Jordan K 2009 Three-dimensional dosimetry of small megavoltage radiation fields using radiochromic gels and optical CT scanning *Phys. Med. Biol.* **54** 2463–81

Bero M A, Gilboy W B and Glover P M 2001 Radiochromic gel dosemeter for three-dimensional dosimetry *Radiat. Phys. Chem.* **61** 433–5

Dekker K H, Battista J J and Jordan K J 2016 Stray light reduction in cone beam optical computed tomography: II. Reduction using a convergent light source *Phys. Med. Biol.* **61** 2910–25

Doran S J 2013 How to perform an optical CT scan: an illustrated guide *J. Phys.: Conf. Ser.* **444** 012004

Kelly R G, Jordan K J and Battista J J 1998 Optical CT reconstruction of 3D dose distributions using the ferrous-benzoic-xylenol (FBX) gel dosimeter *Med. Phys.* **25** 1741–50

Oldham M, Siewerdsen J H, Shetty A and Jaffray D A 2001 High resolution gel-dosimetry by optical-CT and MR scanning *Med. Phys.* **28** 1436–45

Olding T and Schreiner L J 2011 Cone beam optical computed tomography for gel dosimetry II: imaging protocols *Phys. Med. Biol.* **56** 1259–79

Olding T, Darko J and Schreiner L J 2010a Effective management of FXG gel dosimetry *J. Phys.: Conf. Ser.* **250** 012028

Olding T, Holmes O and Schreiner L J 2010b Cone beam optical computed tomography for gel dosimetry I: scanner characterization *Phys. Med. Biol.* **55** 2819–40

Olding T, Holmes O, DeJean P, McAuley K B, Nkongchu K, Santyr G and Schreiner L J 2011 Small field dose delivery evaluations using cone beam optical computed tomography-based polymer gel dosimetry *J. Med. Phys.* **36** 3–14

Ramm D 2018 A fast dual wavelength laser beam fluid-less optical CT scanner for radiotherapy 3D gel dosimetry I: Design and development *Phys. Med. Biol.* **63** 045019

Thomas A, Newton J, Adamovics J and Oldham M 2011 Commissioning and benchmarking a 3D dosimetry system for clinical use *Med. Phys.* **38** 4846–57

6.3 Conclusions

The dosimetric performance of the FXG / optical CT system featuring fluid-less, dual wavelength operation was detailed. It was shown that calibration methodology should be considered more carefully for dual wavelength scanning without pre-irradiation scans, where cuvette calibrations are not recommended. With a calibration sample of the same size as the measurement sample, using a reconstruction based calibration method, accuracy was maintained without pre-irradiation scanning. It was shown that different scanning options have various benefits. A single wavelength scanner would provide the cheapest, simplest scanner configuration. A dual wavelength scanner has additional complexity but provides the most practical and efficient normal operation. Measurement quality was largely similar, except in the case of sub-optimal cylinder cleanliness where dual wavelength scanning can be superior. This adds to the practicality for routine use since less diligence in cylinder cleaning prior to scanning can be tolerated. Thus a dual wavelength fluid-less optical CT scanner providing a practical option for clinical true 3D dosimetry has been developed. Measurement accuracy was validated, ready for clinical application.

Chapter 7

Summary

7.1 Conclusions

This research commenced with an overall objective of development of a true 3D dosimetry system for radiotherapy dosimetry. Optical CT scanning of a radiochromic gel dosimeter was the method of choice. It was proposed that optical CT scanning could be made more practical and efficient with dosimetric accuracy competitive with established dosimeters. To achieve greater practicality in optical CT scanning, the scanning process was simplified by conceiving optical geometry that did not require RI matching fluid. The design used the gel cylindrical container as a lens to provide parallel ray geometry over most of the gel sample and resulted in a simple, cost effective scanner with a minimal number of optical components. Fundamental geometrical optics calculations led to the discovery of conditions whereby parallel rays through the gel sample were generated by just the gel and its container. It was found that a PMMA cylinder containing gel with a ratio of inner to outer diameters of 0.67 could provide suitable ray paths for tomographic reconstruction.

A prototype scanner was constructed using a laser beam and rotating mirror sweeping the beam across the sample. The high speed of the beam’s sweep yielded acquisition times on the order of typical broad beam scanners which have been favoured by other researchers due to their fast acquisition rates. The prototype scanner was shown to provide suitably accurate reconstructions with minimal distortion and sub-millimetre spatial resolution. A dosimetry system was developed using FXG radiochromic gel. The gel dose response was characterised using a simple power function to account for slight, but significant, non-linearity. This, together with mitigation of FXG readout temperature dependence, and accurate optical attenuation measurements of the scanner, provided high quality true 3D absolute dosimetry. The accuracy of the scanner and gel dosimetry system was determined by comparisons to conventional detectors considered to be the best reference for given conditions.

Clinical application of the 3D dosimetry system was demonstrated for SRS dose distributions delivered by linac. The value of true 3D measurements was shown by quantification of dose levels and 3D spatial accuracy of dose distributions with a single delivery and measurement. Calculated doses of a SRS treatment planning system were verified by 3D dosimetry, which was the main intended application for the system. Versatility was shown by implementation of another application using an ^{192}Ir brachytherapy source. A surface applicator was placed on an exposed gel surface to deliver the superficial dose distribution. True 3D measured dose distributions provided verification of Monte Carlo derived planning data.

A well performing, completely fluid-less, fast laser beam optical CT scanner had been developed, however, further increases in practicality and efficiency of operation were sought by the addition of a second laser beam of differing wavelength. It was found that a second wavelength could be used to give a reference dataset to replace the usual pre-irradiation scan data. The difference in wavelength was minimised to avoid changes in refractive indices that would result in ray path deviations. Competing with this was the effect of reduced net dose response with less difference in wavelength. It was shown that the negative effect of a 1/3 reduction in dose response was offset by positive effects of improved image quality. The second wavelength could better correct for artefacts due to particles and defects on the cylinder optical surfaces. This was only possible with precise beam matching and alignment.

An alternative calibration method for FXG was developed using the reconstruction of a known dose pattern delivered to a gel cylinder. The original cuvette based method was found to be deficient when pre-irradiation scans were not used with dual wavelength scanning. This was attributed to the different gel volumes undergoing different physico-chemical changes from manufacture to the pre-irradiation time point. By matching volumes, the dose pattern method proved to be a suitable solution for an accurate calibration method. The dual wavelength scanner was benchmarked against reference detectors. Thus, a fluid-less dual wavelength optical CT scanner had been developed to a stage where it was ready for clinical application.

The main limitation of the 3D dosimetry system was found to be the FXG dosimeter. Ion diffusion was the well-known issue that limited dose measurement accuracy in high gradient regions. Additionally for small field sizes (< 10 mm) the peak dose could drop significantly with post irradiation time. Due to the speed and quality of optical CT scanning, multiple scans could be acquired and then used to correct for diffusion. This would however only provide partial correction with a small residual difference remaining. Nevertheless the non-diffusion corrected differences were of the order of dose gradient blurring due to volume averaging by other detectors such as micro ionisation chambers.

7.2 Future

The fluid-less dual wavelength optical CT scanner was successfully developed with a 51 mm diameter gel sample size. The size was constrained by the requirement that the cylinder overall size would allow fitment to an existing head phantom. This would provide a useful solution for 3D dosimetry of small SRS dose distributions, however, a larger gel dosimeter would be required for other applications such as SBRT or more general RT treatments. Smaller 3D dosimeters can produce accurate dosimetry more easily than larger dosimeters since detector dynamic range and scatter are more significant issues at larger sizes. Thus scaling up the present scanner design would not necessarily be straightforward. In principle scaling to, for example, double the size should be feasible. If the reconstructed pixel size was scaled in proportion, then scan acquisition time per slice could remain the same. In this case FXG ion diffusion may be a sub-pixel effect. Beam wander at the detector may need to be addressed by additional lenses or an alternative detector. A larger PMMA cylinder is a more substantial mass of plastic that may be more difficult to produce. Application of a hard surface coating for larger cylinders could be beneficial to preserve the quality of the larger optical surface area. RI matching of hard coating is recommended to avoid optical interference effects. Anti-reflective coatings may be useful to reduce stray light, especially for scanners with array detectors.

Alternative light source and detector arrangements may be possible with a next generation design using a laser line source and linear array detector. This approach would attempt to balance the competing effects of decreased stray light rejection with increased scan speed. The aim would be to reduce scan acquisition time significantly otherwise the change from point to array detector may not be worthwhile. Faster data acquisition products are now available at the time of completion of this work, thus scan speed improvements can be made from that reason alone. Sub-minute scan times would be a goal to further improve the appeal of optical CT scanning.

The choice of chemical dosimeter for this work, FXG, with well-known characteristics, provided the sound basis for a 3D dosimetry system, notwithstanding the shortcoming of ion diffusion. Optical CT scanner development was the main focus of this work and the use of a consistent gel dosimeter was useful to develop scanner performance. With an efficient and accurate optical scanner developed, the FXG gel dosimeter was the weaker aspect, since it placed limits on the performance of the dosimetry system. Thus, different gel dosimeters could be the subject of further investigations. Gels with low diffusion such as polymer gels and micelle gels could be used with the scanner developed in this work, however, they also have their own issues to address. For example, micelle gels have low dose sensitivity and are typically used with higher doses to give adequate optical attenuation. Improved optical CT imaging quality could help offset the lower dose sensitivity. Re-usable dosimetric gels could provide a significant improvement by the reduction of gel manufacturing efforts, making optical CT gel dosimetry methods more clinically compatible.

It is therefore concluded that there are further options, to build upon the work conducted here, continuing to strive for more practical, efficient, reliable and accurate true 3D dosimetry systems based upon optical CT scanning.

Appendix A

Matlab code for ray tracing with a gel filled cylinder as per the geometry in figure 2.1. Only refraction was considered here, while reflection effects were considered separately using recognised equations.

```
%% Ray tracing for optical CT gel cylinder

clear all

% Cylinder size
D1=input('Outer diameter of cylinder:');
D2=input('Inner diameter of cylinder:');
R1=D1/2;
R2=D2/2;

GW=input('Gel or water (g/w) : ','s');

ffl=input('Focal length:');
DetPos=input('Detector position:');

% Refractive indices
n1=1.000;        % Air

%% YELLOW 594nm RIs
n2=1.491         % PMMA
if GW=='g'
  n3=1.342       % Gel
elseif GW=='w'
  n3=1.333       % Water
end

NumRays=10;

step=0.194/NumRays;  % alphai1 = 0.1880  Y2=22.48mm    0.194 = Y2 23.0mm
alphai1=-step;

% Calculate each ray
for i=1:(NumRays+1);
   alphai1=alphai1+step;
   alpha1=asin((ffl*tan(alphai1)+R1*tan(alphai1))/(R1*sqrt(1+(tan(alphai1))^2)))-alphai1;
   Y1=R1*sin(alpha1);
   f1=ffl+(R1-Y1/tan(alpha1));
   theta1=alpha1+alphai1;
   theta2=asin(n1/n2*sin(theta1));
   alphat1=alpha1-theta2;
   dt1=(2*R1*cos(theta2)-sqrt((2*R1*cos(theta2))^2-4*(R1^2-R2^2)))/2;
   d21=dt1*cos(alphat1);
   Y2=Y1-d21*tan(alphat1);
   alpha2=asin(Y2/R2);
   theta3=alpha2-alphat1;
   theta4=asin(n2/n3*sin(theta3));
   alphat2=theta4-alpha2;
```

```
  dc=2*R2*cos(theta4);
  d32=dc*cos(alphat2);
  Y3=Y2+d32*tan(alphat2);
  alpha3=asin(Y3/R2);
  theta5=alpha3+alphat2;
  theta6=asin(n3/n2*sin(theta5));
  alphat3=alpha3-theta6;
  dt2=(2*R2*cos(alphat3-alpha3+pi)+sqrt((2*R2*cos(alphat3-alpha3+pi))^2-4*(R2^2-R1^2)))/2;
  d43=dt2*cos(alphat3);
  Y4=Y3+d43*tan(alphat3);
  alpha4=asin(Y4/R1);
  theta7=alpha4-alphat3;
  theta8=asin(n2/n1*sin(theta7));
  alphai2=theta8-alpha4;
  f2=Y4/tan(alphai2);
  bfl=f2-(R1-Y4/tan(alpha4));

  X0=-(ffl+R1);
  X1=X0+f1;
  X2=X1+d21;
  X3=X2+d32;
  X4=X3+d43;
  X5=X4+f2;
  Y0=0;
  Y5=0;

  % Ray coordinates
  X(:,i)=[X0,X1,X2,X3,X4,X5];
  Y(:,i)=[Y0,Y1,Y2,Y3,Y4,Y5];

  A(1,i)=alphai1;

  % Deviation at gel centre and at detector
  DevInGelY(:,i)= (Y3-Y2)/2;
  DevDetectorY(:,i)=(bfl-DetPos)*tan(alphai2);
  Y2plot(:,i)=Y2;

end
```